

Christoph Josef Backi

Modeling, Estimation and Control of Freezing and Thawing Processes

Theory and Applications

Thesis for the degree of philosophiae doctor
Trondheim, December 2015

Norwegian University of Science and Technology
Faculty of Information Technology, Mathematics and Electrical Engineering
Department of Engineering Cybernetics



NTNU

Norwegian University of Science and Technology

Thesis for the degree of philosophiae doctor

Faculty of Information Technology, Mathematics and Electrical Engineering
Department of Engineering Cybernetics

© 2015 Christoph Josef Backi.

ISBN 978-82-326-1302-1 (printed version)

ISBN 978-82-326-1303-8 (electronic version)

ISSN 1503-8181

ITK Report 2015-8-W

Doctoral theses at NTNU, 2015:323

Printed by Skipnes

To my parents.

Summary

Fisheries and aquaculture are very important sectors in the Norwegian industry. Fish and its by-products are considered wholesome foodstuff and are popular especially due to their nutritional value. Therefore, consumer safety is a very important topic and methods for prolonging shelf-life play a vital role in the fishing and aquaculture industries. These methods are mostly based on cooling and freezing techniques, as bacteriological and enzymatic activities are generally reduced at low temperatures. However, freezing and cooling are quite energy- and time-consuming. Freezers are often designed as batch-operations, especially on board fishing vessels, and thus act as bottlenecks in the production chain. Therefore, an optimal operation should be imposed in order to minimize the time the good is spending in the freezer. If a good is in the freezer longer than necessary, this operation can be denoted as *overfreezing*. Hence, the aim is to monitor and operate the freezing processes in an optimal way with respect to quality, but also with regards to energy use and environmental impact. This can be achieved by a better understanding of the factors that influence the quality of fish and seafood during freezing and thawing. Furthermore, comprehension of the actual processes that happen during phase change are of importance; this includes the derivation of a mathematical model to describe the temperature evolution in the food. This model can also be used to monitor and operate the reversed freezing process, namely thawing. Considering not only freezing but also the thawing process as an additional and often inevitable production step makes sense due to the fact that it is difficult to process frozen fish.

The thesis is structured into five parts, which are divided thematically: *Introduction and Preliminaries, Mathematical Modeling, Freezing and Thawing Applications, Experiments and Closing Remarks*.

Part I gives an introduction to the context of this thesis. The importance of the fishing industry for the Norwegian economy is highlighted. Furthermore, preliminaries about topics related to freezing and thawing of foodstuff in general, and fish and fish products in particular, are presented. These preliminaries include methods of industrial applicable and more theoretical nature. Furthermore, a Chapter is dedicated to the concise introduction to quality aspects of fish, in a general way, but also with respect to freezing and thawing applications and processes.

In Part II, a mathematical model for freezing and thawing processes is derived from the diffusion equation, a partial differential equation (PDE). This model represents a form of a linear heat equation, which is extended by a nonlinear term. This nonlinear term enters the equation due to the fact that phase change occurs in both freezing and thawing, and

therefore the parameters of the diffusion equation are modeled state- and thus temperature-dependent. Similarities between this model and other types of PDEs, in particular the Burgers' equation and its potential form, are investigated. However, due to the state-dependency of the coefficients, known transformations can not be applied in order to use already established stability results for this kind of heat equation. Therefore, the stability of the model is investigated. This is conducted in order to show that the model can be used for describing freezing and thawing applications, which are in fact known to be stable due to the laws of thermodynamics.

Part III presents applications of the model derived in Part II for freezing and thawing processes, respectively. Firstly, an observer based on an Extended Kalman Filter (EKF) is developed for both, freezing in plate freezers and thawing in contact thawing devices. The aim is to estimate the temperatures in the inner domain of a block of foodstuff. Therefore, some assumptions have to be imposed, e.g. that temperatures on the surface of the block are measurable. Secondly, the models are subject to Optimal Control Problems (OCP), where an optimal input function, meaning the temperature at the boundaries, is calculated in order to either optimally freeze or thaw blocks of foodstuff. This is done for open loop Optimal Control (OOC), which holds for perfect knowledge of the process with no measurement and estimation disturbances. Furthermore, closed loop Model Predictive Control (MPC) is applied, where measurement / estimation errors as well as discrepancies between the model and the real process are taken into account.

In Part IV experimental results for a freezing process in a horizontal plate freezer and a thawing process in a rebuilt horizontal plate freezer adapted for thawing purposes (*plate thawer*) are shown. Both of these experiments have been conducted at Matís Food Research in Reykjavík, Iceland. The freezing experiments were conducted with a rectangular tray made of aluminum, which was placed in between the plate freezer walls and filled with tap water. Temperature loggers were placed in several positions inside the tray to log the temperature during phase change from liquid to solid. Ammonia was used as the refrigerant in the plate freezer. For the thawing process the same tray was used. Blocks of frozen headed and gutted (H/G) cod were placed inside the tray and between the walls of the re-built plate freezer. The medium to thaw the fish blocks was tap water. Temperature loggers were attached to the fish blocks, namely in the center, half-way to the center and just below the surface.

In Part V the thesis is closed with the conclusion and an outlook on future work.

Contents

Summary	iii
Contents	v
List of figures	ix
List of tables	xv
Abbreviations	xvii
Preface	xix
I Introduction and Preliminaries	1
1 Introduction	3
1.1 Motivation	4
1.2 Main contributions	4
1.3 Publications	5
1.4 Organization of the thesis	6
2 Nomenclature	9
2.1 The environment	9
2.2 Parameters and variables	9
2.3 Chemical substances	10
2.4 Notation	11
2.5 Important Lemmas	11
3 Preliminaries on freezing technology	13
3.1 Methods acting through the boundary	15
3.2 Methods acting in the inner domain	18
3.3 Conclusion	20
4 Preliminaries on thawing technology	21
4.1 Methods acting through the boundary	22
4.2 Methods acting in the inner domain	26
4.3 Conclusion	29

5	Fish as foodstuff	31
5.1	Quality of fish	31
5.2	Shelf Life	37
5.3	Actions and precautions to preserve quality and extend shelf life	38
II	Mathematical Modeling	41
6	Modeling	43
6.1	Mathematical model for heat transfer	43
6.2	Parameters	44
6.3	Simulations	47
6.4	Comment on the chosen boundary conditions	54
7	Transformations	57
7.1	Similarities to Burgers' and potential Burgers' equation	57
7.2	Motivation for stability analysis	59
8	Stability	61
8.1	Steady state solution	61
8.2	Stability for asymmetric boundary conditions $u_0 \neq u_L$	64
8.3	Symmetric boundary conditions $u_0 = u_L$	66
8.4	Simulation examples	67
III	Freezing and Thawing Applications	69
9	Problem formulation and introduction to estimation	71
9.1	Problem formulation	71
9.2	Estimation of unmeasurable states	72
10	Full model inner-domain temperature estimation for freezing	75
10.1	Observer model	75
10.2	Observer	77
10.3	Comments on the upcoming Chapters	80
10.4	Simulations	81
11	Reduced model inner-domain temperature estimation for freezing	89
11.1	Observer model	89
11.2	Simulation examples	90
12	Full model inner-domain temperature estimation for thawing	105
12.1	Simulation examples	105
13	Reduced model inner-domain temperature estimation for thawing	113
13.1	Simulation examples	113
13.2	Real-time applicable observer	121

14	Introduction to Optimal control and problem formulation	125
14.1	Introduction to Optimization	125
14.2	Introduction to Optimal Control	126
14.3	ACADO Software Package	127
14.4	Parameters	128
14.5	Assumptions and comments on the OOC and MPC simulations and the controller performances	133
15	Optimal boundary control for freezing	135
15.1	Introduction	135
15.2	Open loop Optimal Control	137
15.3	Model Predictive Control	141
16	Optimal boundary control for thawing	145
16.1	Introduction	145
16.2	Open loop Optimal Control	146
16.3	Model Predictive Control	148
IV	Experiments	157
17	Freezing	159
18	Thawing	165
V	Closing Remarks	169
19	Conclusion	171
19.1	Contributions in the field of modeling and analysis	171
19.2	Contributions in the field of applications	172
20	Future Work	175
20.1	Future work regarding modeling and model analysis	175
20.2	Future work regarding the observer designs	175
20.3	Future work regarding the optimal control designs	176
20.4	Further comments on freezing, thawing and other applications	176
	Appendices	179
A	Comparative plots for the chosen discretization schemes	181
B	Proof of Lemma 8.1	187
C	Proof of Lemma 8.2	191
D	Illustration of the full model observer design case	195

E	Illustration of the reduced model observer design case	199
F	Further simulation results for the observer design cases	201
G	Design of a 1-dimensional observer	205
	References	211

List of figures

3.1	Vapor-compression refrigeration process with separator unit	14
3.2	Fish blocks on a conveyor belt	15
3.3	Vertical plate freezer	16
3.4	Sketch of the pressure-temperature phase diagram for water	18
4.1	Air-blast batch thawer	23
4.2	Thawing in a water bath with air bubbles	24
4.3	Thawing in water in a cylindrical thawing tank	25
5.1	Quality as a function of freshness and other factors	31
5.2	Graphical Representation of a quality score for iced cod	33
6.1	Thermal properties as functions of temperature	45
6.2	Freezing curve	46
6.3	A sketch of the parameters $c(T)$ and $\lambda(T)$ as obtained by equations (6.9) and (6.10)	47
6.4	A sketch of the parameters $c(T)$ and $\lambda(T)$ as obtained by equations (6.11) and (6.10)	48
6.5	Solutions of the discretization scheme for freezing (dashed), thawing (dotted) and the MATLAB [®] solver pdepe (solid) for $N = 29$ at positions $n = 1$ (blue) $n = 7$ (green) and $n = 15$ (red)	50
6.6	Plot of the temperature distribution along the spatial direction x over time for the freezing case	51
6.7	Plot of different temperatures at fixed spatial points over time for the freezing case	52
6.8	Illustration of the discretization points along the spatial variable for $N = 199$ cells	52
6.9	Plot of the temperature distribution along the spatial direction x over time for the thawing case	53
6.10	Plot of different temperatures at fixed spatial points over time for the thawing case	53
8.1	The parameter functions $c(T)$ and $\lambda(T)$ as defined for the stability investigation	62
8.2	Steady state solutions	64
8.3	Noisy initial condition for the simulation	67
8.4	Temperature evolution over space and time	68

8.5	Temperature evolution over space and time - the first 50 s	68
10.1	Discretization scheme for the observers	76
10.2	Design schematic for the observers	80
10.3	Comparison between the dynamics of the plant (blue) and those of the observer (red) at $m = 5$ and different positions along the x -axis	82
10.4	Results for the full model observer at $m = 1$ and different positions along the x -axis for constant Q and R	83
10.5	Results for the full model observer at $m = 1$ and $n = 5$ for constant Q and R , zoom into the latent zone	84
10.6	Results for the full model observer at $m = 3$ and different positions along the x -axis for constant Q and R	84
10.7	Results for the full model observer at $m = 3$ and $n = 5$ for constant Q and R , zoom into the latent zone	85
10.8	Results for the full model observer at $m = 5$ and different positions along the x -axis for constant Q and R	86
10.9	A 3-dimensional plot of the estimation error for the full observer at $m = 5$ for constant Q and R	86
10.10	Results for the full model observer at $m = 3$ and different positions along the x -axis for switched Q and R	87
10.11	Results for the full model observer at $m = 5$ and different positions along the x -axis for switched Q and R	87
10.12A	A 3-dimensional plot of the estimation error for the full observer at $m = 5$ for switched Q and R	88
11.1	Parameter function definitions for the reduced observer case	89
11.2	Comparison between the dynamics of the plant (blue) and those of the observer (red) at $m = 5$ and different positions along the x -axis	90
11.3	Results for the reduced model observer at $m = 3$ and different positions along the x -axis for constant Q and R	91
11.4	Results for the reduced model observer at $m = 5$ and different positions along the x -axis for constant Q and R	92
11.5	A 3-dimensional plot of the estimation error for the reduced observer at $m = 5$ for constant Q and R	93
11.6	Results for the reduced model observer at $m = 3$ and different positions along the x -axis for switched Q and R	93
11.7	Results for the reduced model observer at $m = 5$ and different positions along the x -axis for switched Q and R	94
11.8	A 3-dimensional plot for the reduced model observer at $m = 5$ for switched Q and R	94
11.9	Comparison between the dynamics of the plant (blue) and those of the observer (red) at $m = 5$ and different positions along the x -axis for parameter functions with identical values	95
11.10	Results for the reduced model observer at $m = 3$ and different positions along the x -axis for switched Q and R and identical parameter definitions	96
11.11	Results for the reduced model observer at $m = 5$ and different positions along the x -axis for switched Q and R and identical parameter definitions	97

11.12	A 3-dimensional plot for the reduced model observer at $m = 5$ for switched Q and R and identical parameter definitions	97
11.13	Step-wise definition of the parameter function definitions for the real-time applicable reduced observer case	98
11.14	Comparison between the dynamics of the plant (blue) and those of the observer (red) at $m = 5$ and different positions along the x -axis for the parameters as defined in Figure 11.13 and identical parameter definitions	98
11.15	Results for the real-time applicable observer at $m = 3$ and different positions along the x -axis for switched Q and R and identical parameter definitions . . .	99
11.16	Results for the real-time applicable observer at $m = 5$ and different positions along the x -axis for switched Q and R and identical parameter definitions . . .	99
11.17	A 3-dimensional plot for the real-time applicable observer at $m = 5$ for switched Q and R and identical parameter definitions	100
11.18	Results for the real-time applicable observer at $m = 3$ and different positions along the x -axis for switched Q and R and differing parameter definitions . .	101
11.19	Results for the real-time applicable observer at $m = 5$ and different positions along the x -axis for switched Q and R and differing parameter definitions . .	101
11.20	A 3-dimensional plot for the real-time applicable observer at $m = 5$ for switched Q and R and differing parameter definitions	102
12.1	Comparison between the dynamics of the plant (blue) and those of the observer (red) at $m = 5$ and different positions along the x -axis for differing parameter definitions	106
12.2	Results for the full model observer at $m = 1$ and different positions along the x -axis for constant Q and R	107
12.3	Results for the full model observer at $m = 1$ and $n = 5$ for constant Q and R , zoom into the latent zone	108
12.4	Results for the full model observer at $m = 3$ and different positions along the x -axis for constant Q and R	109
12.5	Results for the full model observer at $m = 3$ and $n = 5$ for constant Q and R , zoom into the latent zone	109
12.6	Results for the full model observer at $m = 5$ and different positions along the x -axis for constant Q and R	110
12.7	A 3-dimensional plot of the estimation error for the full observer at $m = 5$ for constant Q and R	110
12.8	Results for the full model observer at $m = 3$ and different positions along the x -axis for switched Q and R	111
12.9	Results for the full model observer at $m = 5$ and different positions along the x -axis for switched Q and R	112
12.10	A 3-dimensional plot of the estimation error for the full observer at $m = 5$ for switched Q and R	112
13.1	Comparison between the dynamics of the plant (blue) and those of the observer (red) at $m = 5$ and different positions along the x -axis for parameter definitions that can be found in Table 12.1	114
13.2	Results for the reduced model observer at $m = 3$ and different positions along the x -axis for constant Q and R	115

13.3	Results for the reduced model observer at $m = 5$ and different positions along the x -axis for constant Q and R	115
13.4	A 3-dimensional plot of the estimation error for the reduced observer at $m = 5$ for constant Q and R	116
13.5	Results for the reduced model observer at $m = 3$ and different positions along the x -axis for switched Q and R	117
13.6	Results for the reduced model observer at $m = 5$ and different positions along the x -axis for switched Q and R	117
13.7	A 3-dimensional plot for the reduced model observer at $m = 5$ for switched Q and R	118
13.8	Comparison between the dynamics of the plant (blue) and those of the observer (red) at $m = 5$ and different positions along the x -axis for parameter functions with identical values	119
13.9	Results for the reduced model observer at $m = 3$ and different positions along the x -axis for switched Q and R and identical parameter definitions	119
13.10	Results for the reduced model observer at $m = 5$ and different positions along the x -axis for switched Q and R and identical parameter definitions	120
13.11	A 3-dimensional plot for the reduced model observer at $m = 5$ for switched Q and R and identical parameter definitions	120
13.12	Results for the real-time applicable observer at $m = 3$ and different positions along the x -axis for switched Q and R and identical parameter definitions . . .	121
13.13	Results for the real-time applicable observer at $m = 5$ and different positions along the x -axis for switched Q and R and identical parameter definitions . . .	122
13.14	A 3-dimensional plot for the real-time applicable observer at $m = 5$ for switched Q and R and identical parameter definitions	122
13.15	Results for the real-time applicable observer at $m = 3$ and different positions along the x -axis for switched Q and R and differing parameter definitions . .	123
13.16	Results for the real-time applicable observer at $m = 5$ and different positions along the x -axis for switched Q and R and differing parameter definitions . .	123
13.17	A 3-dimensional plot for the real-time applicable observer at $m = 5$ for switched Q and R and differing parameter definitions	124
14.1	Parameter $c(T)$ as defined in (6.11) (blue) compared to the approximation defined in (14.3) (red)	129
14.2	Parameter $\lambda(T)$ as defined in (6.10) (blue) compared to the approximation defined in (14.4) (red)	130
14.3	Parameter $\lambda_T(T)$ as defined in (14.5)	130
14.4	Parameter $k(T)$ as defined with (6.10) and (6.11) (blue) compared to the approximation calculated with (14.3) and (14.4) (red)	131
14.5	Parameter $\kappa(T)$ as defined with (6.10) and (6.11) (blue) compared to the approximation calculated with (14.3) and (14.5) (red)	131
14.6	Parameter $k(T)$ as defined with (6.10) and (6.11) (blue) compared to the approximation defined in (14.6) (red)	132
14.7	Parameter $\kappa(T)$ as defined with (6.10) and (6.11) (blue) compared to the approximation defined in (14.7) (red)	132
15.1	Temperature vs. pressure for the refrigerants NH_3 and CO_2	136

15.2	State evolution over time - OOC case	139
15.3	Boundary temperature (top) and its rate of change over time (bottom) - OOC case	139
15.4	States T_1 to T_{25} at the end of the time horizon - OOC case	140
15.5	A 3-dimensional plot of the temperatures - OOC case	140
15.6	State evolution over time - MPC case	142
15.7	Boundary temperature (top) and its rate of change over time (bottom) - MPC case	143
15.8	A 3-dimensional plot of the temperatures - MPC case	143
16.1	Functional principle	146
16.2	Boundary temperature (top) and its rate of change over time (bottom) - OOC case for large rates of change	149
16.3	State evolution over time (top) and temperatures at the end of the time horizon (bottom) - OOC case for large rates of change	150
16.4	Boundary temperature (top) and its rate of change over time (bottom) - OOC case for small rates of change	151
16.5	State evolution over time (top) and temperatures at the end of the time horizon (bottom) - OOC case for small rates of change	152
16.6	Boundary temperature (top) and its rate of change over time (bottom) - MPC case for large rates of change	153
16.7	A 3-dimensional plot of the temperatures (top) and temperatures at the end of the time horizon (bottom) - MPC case for large rates of change	154
16.8	State evolution over time - MPC case for large rates of change	154
16.9	Boundary temperature (top) and its rate of change over time (bottom) - MPC case for small rates of change	155
16.10	State evolution over time and space (top) and temperatures at the end of the time horizon (bottom) - MPC case for small rates of change	156
16.11	State evolution over time - MPC case for small rates of change	156
17.1	The horizontal plate freezer used for the experiments	159
17.2	The positions of the loggers	160
17.3	The measured freezing curves	160
17.4	The measured freezing curves - the first 1800 s	161
17.5	The measured freezing curves compared with the simulation results	162
17.6	The measured freezing curves compared with the simulation results for reduced heat transfers at the boundaries	163
18.1	Two frozen fish blocks on the aluminum tray	165
18.2	The aluminum tray with the fish blocks in between the plate thawer walls	166
18.3	The measured thawing curves	166
18.4	The measured thawing curves compared with the simulation results	167
A.1	N=5 discretization steps	181
A.2	N=9 discretization steps	182
A.3	N=49 discretization steps	182
A.4	N=99 discretization steps	183

A.5	N=199 discretization steps	183
A.6	N=5 discretization steps	184
A.7	N=9 discretization steps	184
A.8	N=49 discretization steps	185
A.9	N=99 discretization steps	185
A.10	N=199 discretization steps	186
F.1	Results for the reduced model observer at $m = 1$ and different positions along the x -axis for constant Q and R	201
F.2	Results for the reduced model observer at $m = 1$ and $n = 5$ for constant Q and R , zoom into the latent zone	202
F.3	Results for the reduced model observer at $m = 3$ and $n = 5$ for constant Q and R , zoom into the latent zone	202
F.4	Results for the reduced model observer at $m = 1$ and different positions along the x -axis for constant Q and R	203
F.5	Results for the reduced model observer at $m = 1$ and $n = 5$ for constant Q and R , zoom into the latent zone	203
F.6	Results for the reduced model observer at $m = 3$ and $n = 5$ for constant Q and R , zoom into the latent zone	204
G.1	States for the 1-dimensional real-time applicable observer for identical parameter definitions	207
G.2	Error plot for the 1-dimensional real-time applicable observer for identical parameter definitions	208
G.3	States for the 1-dimensional real-time applicable observer for differing parameter definitions	208
G.4	Error plot for the 1-dimensional real-time applicable observer for differing parameter definitions	209

List of tables

- 6.1 Simulation parameters for the illustrative examples 51
- 10.1 Simulation parameters for the observer design cases for freezing 83
- 12.1 Simulation parameters for the observer design cases for thawing 107
- 15.1 Simulation parameters for the OOC freezing case 138
- 15.2 Simulation parameters for the MPC freezing case 142
- 16.1 Simulation parameters for the OOC thawing case 148
- 16.2 Simulation parameters for the MPC thawing case 153
- 17.1 Simulation parameters for the freezing experiment 161

Abbreviations

ATP	Adenosine triphosphate
BC	Boundary condition
CrP	Creatine phosphate
DAE	Differential Algebraic Equation
EKF	Extended Kalman Filter
FIR	Far infrared
GDP	Gross domestic product
HPF	Horizontal plate freezer
HTC	Heat transfer coefficient
H/G	Headed and gutted
IC	Initial condition
KKT	Karush-Kuhn-Tucker conditions
MPC	Model Predictive Control
MWT	Micro wave thawing
NLP	Nonlinear Programming
NMPC	Nonlinear Model Predictive Control
OCP	Optimal Control Problem
ODE	Ordinary Differential Equation
OOC	Open loop Optimal Control
PAF	Pressure Assisted Freezing
PAT	Pressure Assisted Thawing
PDE	Partial Differential Equation
PIT	Pressure Induced Thawing
PSF	Pressure Shift Freezing
RFT	Radio frequency thawing
SQP	Sequential Quadratic Programming
VPF	Vertical plate freezer
WGN	White Gaussian noise

Preface

This thesis is submitted in partial fulfillment of the requirements for the degree of philosophiae doctor (PhD) at the Norwegian University of Science and Technology (NTNU).

It presents the results of my doctoral studies which have been carried out at the Department of Engineering Cybernetics at NTNU and at SINTEF Fisheries and Aquaculture, both located in Trondheim, Norway, from April 2011 to August 2015. My supervisor has been Professor Jan Tommy Gravdahl of the Department of Engineering Cybernetics and my co-supervisor has been Dr. Karl Johan Reite of SINTEF Fisheries and Aquaculture.

During my time as a PhD Candidate I was given the opportunity to visit Professor Jakob Stoustrup at the Department of Electronic Systems (Control and Automation group) at Aalborg University, Denmark, from August 2013 to December 2013. I am very grateful for the hospitality and the fruitful collaboration with Associate Professors Jan Dimon Bendtsen and John-Josef Leth.

My PhD work was funded by the Norwegian Research Council as part of the project DAN-TEQ (Development and assessment of novel technologies improving the fishing operation and on board processing with respect to environmental impact and fish quality - project number 199447/I10) of SINTEF Fisheries and Aquaculture. In addition, some of the results that are presented in this work were obtained working in the project QualiFish (New technology for a profitable white fish industry - project number 233709), also of SINTEF Fisheries and Aquaculture and funded by the Norwegian Research Council.

Acknowledgments

I would like to thank all the people who, in some way or another, contributed so I could write this thesis.

First of all I want to thank my supervisor Professor Jan Tommy Gravdahl for his big support, his encouragement (especially when yet another dead end was reached), his patience, his “go for it”-mentality and for his willingness to hire me in the first place. In addition, I thank my co-supervisor Dr. Karl Johan Reite and my project leader Dr. Ida Grong Aursand, both of SINTEF Fisheries and Aquaculture, for their support and for always having an open door.

There are many people at the Department of Engineering Cybernetics who deserve to receive my deepest gratitude, starting with the administrative and technical staff whose help was appreciated (and needed) many times: Tove Johnsen, Unni Johansen, Eva Amdahl,

Bente Lindquist, Janne Hagen, Stefano Bertelli, Torkel Hansen, Jan Leistad and Åsmund Stavadahl, just to name a few. Additionally I want to thank Professor Lars Imstrand, Dr. Arnfinn Aas Eielsen and Dr. Giancarlo Marafioti for the fruitful discussions, Dr. Esten Ingar Grøtli for the good cooperation, Dr. Milan Milovanović for introducing me to the world of partial differential equations, Dr. Christian Holden for his help with computer problems and of course my long-time office mate Dr. Marialena Vagia for making the office days a little brighter (not necessarily by singing with her headphones on). Furthermore, I would like to thank all of my colleagues, particularly Serge, Hodjat, Eleni, Mark, Andres, Tor Aksel, Brage, Mikkel, Mladen, Mutaz, Kristoffer, Lorenzo, Anne Mai, Mansoureh, Torstein, Sergey, Konstanze and Leif as well as all the guys who left the department over the years, especially Aleksander, Joakim, Anders, Anton and Walter for all the (more or less) meaningful discussions during lunch and coffee breaks and the overall great atmosphere at the department.

In addition, I would like to thank some people at SINTEF Fisheries and Aquaculture, Professor Marit Aursand, Dr. Hanne Digre, Dr. Ulf Erikson, Leif Grimsmo, Dr. Lars Tandle Kyllingstad and Dr. Ekrem Misimi for their help, encouragement and collegiality during my time as part-time employee from March 2014 to June 2015.

Moreover, I want to thank several people at the Department of Electronic Systems at Aalborg University, Denmark: Professor Jakob Stoustrup (currently at the Pacific Northwest National Laboratory, Richland, WA, USA), Associate Professors Palle Andersen and Tom Pedersen for the important and inspiring discussions, Associate Professors Jan Dimon Bendtsen and John-Josef Leth for the outstanding cooperation and my colleagues Jesus, Mert, Karl, Tomasz, Rasmus and Kasper for making my stay in Aalborg a remarkable experience (“Christmas party”).

I am grateful for the valuable comments of Professor Turid Rustad of the Department of Biotechnology and Professor Elena Celledoni of the Department of Mathematical Sciences, both at NTNU, as well as the possibility to conduct experiments at the laboratories of Matís Food Research in Reykjavík, Iceland together with Dr. Magnea Guðrún Karlsdóttir and Ásbjörn Jónsson.

Finally, I would like to thank my family and friends in Germany. First of all my parents Mechthild and Josef for always being there for me, supporting me in every possible way and their sacrifices not only towards me, but also towards my siblings, to enable us to receive the best possible education, my sister Myriam with her partner Thomas and their lovely son Emil and my brother Alexander with his wife Cornelia and their three wonderful children Theo, Paula and Ida for their inspiration, as well as my countless friends back home for their lasting friendship, especially Florian Brenner and Christian Opitz.

Last but not least I am deeply grateful towards the committee for their effort and time to evaluate my thesis: Dr. Berit Floor Lund, Professor Laurent Di Meglio and Professor Ole Morten Aamo.

*Christoph Josef Backi
Trondheim, December 2015*

Two things are indispensable for our research work: untiring persistence and the readiness to dispose of something in which we have invested a lot of time and hard work.

Albert Einstein

Part I

Introduction and Preliminaries

Chapter 1

Introduction

Fish and fish-products are an important dietary component in many countries and cultures. Among others, the main reasons are the nutritional values and the availability, as fish can be found in sea as well as in fresh water. In the recent 30 – 40 years the availability was increased by efforts in the aquaculture industry, especially for salmon, for which Norway had and still has a leading role since its beginning in the 1970s.

In Norway the consumption of fish and its by-products in 2010 was about 45 kg per capita per year while in the European Union it was in average about half that value, as mentioned by Failler [40]. Not only in terms of consumption, but also as an economical factor fish is of significant importance for the Norwegian industry. This can be recognized by the fact that the fish industry is the largest economy branch in Norway, next to the oil and gas sector. It has always been of considerable significance for the country, as it has already been an important sector well before the discovery of oil at the Norwegian continental shelf. As stated by Sandberg et al. [99], the fisheries and the aquaculture sector contributed with 2.5 – 3 % to the Norwegian GDP over the last ten years. This is small compared to the mineral oil and natural gas sectors, which, in 2008, contributed with about one third to the Norwegian GDP, according to Statistics Norway. In the future, however, fisheries and aquaculture will be of even higher importance as the primary energy carriers, in particular oil and gas, are finite. If harvested sustainably and responsibly, the fishing resources can be made infinitely available. Therefore, a sustainable, strong and innovative fishing and aquaculture industry can contribute to Norway's success also in the future when oil and gas are topics of the past. Automation and automatic control can contribute to reach these goals by developing solutions in order to make the fishing and aquaculture sector stronger and more profitable.

Fish is a foodstuff that is susceptible to rapid spoilage. This is caused by enzymatic as well as bacteriological changes. Thus it is essential to extend its shelf life in order to guarantee a product that is safe to consume whilst holding high quality standards. This implies that along the production chain – from catch via processing to consumption – techniques aiming on quality preservation and thus shelf life extension have to be imposed. There are many preservation techniques used in the fishing and aquaculture industries and their application varies depending on the nature of the final product; even a mix of different techniques is applied. Preservation techniques like cooking, drying, salting

or smoking have extensively been used in past times. However, these techniques have a direct influence on the taste, odor and texture of the product and are thus not applicable if the fish should be processed in different ways or sold as a natural product. Nowadays these techniques are mostly considered as refinement only. Other preservation techniques, mainly cooling and freezing, lower the rate of spoilage while not excessively affecting the physical properties of the fish. If applied correctly, cooling and freezing can extend the shelf life in time ranges of several days to several months, respectively; under perfect storage conditions even years seem possible. In these times they are considered as standard ways of preservation. The following scenario can be mentioned as an example of a chain of different preservation techniques: A trawler cruises several weeks, during which the catch gets headed and gutted (H/G) and then frozen to blocks on board. Back on shore these blocks get unloaded, thawed and cooled again while waiting for filleting and final refinement, for example smoking. This example already includes three of the earlier mentioned preservation techniques, namely freezing, cooling and smoking.

As can be seen, freezing is an essential part in fish processing if direct refinement is not possible or wished. In the aforementioned example, the reversed freezing process, namely thawing, is introduced. Thawing is also an essential part of fish processing as it is impossible to process and refine fish in frozen state (for example filleting H/G fish). Freezing and thawing can be used to dampen out seasonal fluctuations in order to provide a product all year long and not only during catch season, e.g. white fish. There exist broad varieties of freezing and thawing methods, differing by means of practicality as well as resulting quality with respect to fish species and final product.

1.1 Motivation

As mentioned before, the processes of freezing and thawing of foodstuff are essential parts in the production chain. The impact of these processing stages on the final quality of the product is of significant importance. Therefore the monitoring and estimation of the freezing process and especially of the freezing times are important. This also contributes to a more energy-efficient operation as *overfreezing* can be avoided, which describes the case when the product is in the freezer longer than necessary. From an economical point of view this is also of significant relevance due to the fact that freezing and thawing often are conducted as batch processes, meaning that they act as bottlenecks in the processing stages. Fast freezing without overfreezing helps to widen up this bottleneck. Thus, the overall quality of the whole catch / harvest can be enhanced as the time before freezing is reduced. As the thawing process takes significantly longer than freezing, conducting thawing in a controlled manner can also widen up the bottleneck in further processing and refinement stages.

1.2 Main contributions

The main contributions of this thesis can be split into two main parts. Firstly, development and theoretical stability investigation of a mathematical model describing phase change phenomena during freezing and thawing. Secondly, applications of this model to monitor and optimally control the freezing and thawing processes.

The model is a partial differential equation (PDE) with state-dependent parameter functions and describes the spatial and time-dependent temperature distribution inside regular shaped blocks of foodstuff for both, freezing and thawing. A first description of the state-dependent parameter functions can be found in [10]. The stability investigation results in global asymptotic stability for the one-dimensional version of the PDE. The results for this analysis are presented in [15], [17] and [18], respectively. The stability properties for the linear heat equation are known and have been presented e.g. by Krstić and Smyshlyaev [69]. The stability analysis in this thesis is inspired by the analysis of Krstić and Smyshlyaev [69], however, for state-dependent parameter functions. Furthermore, similarities between Burgers' equation, its potential form and the introduced heat equation with state-dependent parameters are pointed out.

The applications are based on a spatial discretization of the PDE resulting in a set of coupled nonlinear ordinary differential equations (ODEs). An observer design to estimate inner-domain temperatures is developed based on an Extended Kalman Filter (EKF), introduced in [16] and [12]. This is conducted for a two-dimensional representation of the PDE for freezing and thawing, respectively. Thereby, several definitions of the parameter functions are investigated for the observer in order to reduce the computational calculation effort and yield a real-time applicable observer. Another application study has the aim to optimally control the boundary temperature, both for freezing and for thawing processes modeled by the PDE. This is performed solving both, open loop Optimal Control Problems (OCPs) as presented in [14] and [13] as well as closed loop Model Predictive Control (MPC) problems shown in [19].

1.3 Publications

The work conducted during my PhD studies has resulted in 11 international publications, of which all, except the results of [11], are included in this thesis. The latter mentioned is the outcome of one of the PhD courses (*Nonlinear Observer Design*) and has been presented at an international conference. The remaining 10 publications are split up into two journal articles, three extended abstracts with poster presentations and five conference papers. One of the journal articles is published in an international journal whereas the second is submitted to an international journal, the extended abstracts have all been presented at international workshops, four conference papers have been presented at international conferences as well, whereas one conference paper is submitted to an international conference. In the sequel all publications are listed.

1.3.1 Journal papers

- [18] C. J. Backi, J. D. Bendtsen, J. Leth, and J. T. Gravdahl. A heat equation for freezing processes with phase change: Stability analysis and applications. *International Journal of Control*, 2015, DOI: 10.1080/00207179.2015.1102327.
- [9] C. J. Backi. Methods for (industrial) thawing of fish blocks - a review. Submitted to the *Journal of Food Engineering*, 2015.

1.3.2 Conference papers

- [19] C. J. Backi, J. Leth and J. T. Gravdahl. Optimal boundary control of a contact thawing process for foodstuff. Submitted to the *11th IFAC Symposium on Dynamics and Control of Process Systems, including Biosystems (DYCOPS-CAB 2016)*, Trondheim, Norway, 2016.
- [17] C. J. Backi, J. D. Bendtsen, J. Leth, and J. T. Gravdahl. Stability properties of a heat equation with state-dependent parameters and asymmetric boundary conditions. In *Proceedings of the 1st Conference on Modelling, Identification and Control of Nonlinear Systems (MICNON 2015)*, Saint-Petersburg, Russia, 2015.
- [15] C. J. Backi, J. D. Bendtsen, J. Leth, and J. T. Gravdahl. The nonlinear heat equation with state-dependent parameters and its connection to the Burgers' and the potential Burgers' equation. In *Proceedings of the 19th IFAC World Congress*, Cape Town, South Africa, 2014.
- [16] C. J. Backi, J. D. Bendtsen, J. Leth, and J. T. Gravdahl. Estimation of inner-domain temperatures for a freezing process. In *Proceedings of the 2014 IEEE Multi-Conference on Systems and Control*, Antibes, France, 2014.
- [11] C. J. Backi, J. T. Gravdahl, and E. I. Grøtli. Nonlinear observer design for a Greitzer compressor model. In *Proceedings of the 21st Mediterranean Conference on Control and Automation*, Chania, Greece, 2013.
- [14] C. J. Backi, and J. T. Gravdahl. Optimal boundary control for the heat equation with application to freezing with phase change. In *Proceedings of the 2013 Australian Control Conference*, Perth, Australia, 2013.

1.3.3 Conference abstracts and presentations

- [12] C. J. Backi, and J. T. Gravdahl. A reduced observer design for a freezing process in plate freezers. In *Proceedings of the 19th Nordic Process Control Workshop*, Trondheim–Bodø, Norway, 2015.
- [13] C. J. Backi, and J. T. Gravdahl. Optimal Neumann boundary control for a freezing process with phase change. Presented at the *18th Nordic Process Control Workshop*, Oulu, Finland, 2013.
- [10] C. J. Backi, and J. T. Gravdahl. Modeling of the Freezing Process for Fish in Vertical Platefreezers. In *Proceedings of the 17th Nordic Process Control Workshop*, Copenhagen, Denmark, 2012.

1.4 Organization of the thesis

The thesis is divided into five parts, namely *Introduction and Preliminaries*, *Mathematical Modeling*, *Freezing and Thawing Applications*, *Experiments* and *Closing Remarks*.

Part I is structured into five Chapters, namely an *Introduction*, where the industrial context in which this thesis is written, is presented, *Nomenclature*, where the used notations, chemical abbreviations and functional spaces are listed, *Preliminaries on freezing technology*, where state-of-the-art methods for industrial freezing of foodstuff are presented,

Preliminaries on thawing technology, where state-of-the-art technologies for (industrial) thawing of foodstuff are outlined and finally *Fish as foodstuff*, in which topics about quality and quality changes in fish, as well as methods to extend its shelf life are presented.

Part II is a theoretical part introducing the mathematical model for freezing and thawing, which is based on the diffusion equation with state-dependent parameters. The model for freezing and thawing is a heat equation and has certain similarities to other classes of (nonlinear) PDEs, especially the Burgers' equation and its potential form. In addition, a stability investigation is conducted for the model.

Part III presents applications for the system introduced in Part II, both for freezing and thawing. It is divided into eight Chapters, where Chapters 9–13 present an introduction to and designs of observers for estimation of inner-domain temperatures for freezing and thawing based on Extended Kalman Filters with different definitions of the parameter functions. Chapters 14–16 introduce and develop optimal control strategies to find boundary inputs for freezing and thawing processes. Both, open loop Optimal Control (OOC) and closed loop Model Predictive Control (MPC) are discussed.

Part IV delivers experimental results conducted both for freezing (Chapter 17) and thawing (Chapter 18) in order to validate the models for both cases.

Part V provides the conclusion in Chapter 19 and some comments on future work in Chapter 20.

Chapter 2

Nomenclature

2.1 The environment

$T \geq 0 \in \mathbb{R}$	The absolute temperature in [K]
$\rho(T) > 0 \in \mathbb{R}$	The density of the considered material in [kg m ⁻³]
$c(T) > 0 \in \mathbb{R}$	The specific heat capacity at constant pressure of the considered material in [J kg ⁻¹ K ⁻¹]
$\lambda(T) > 0 \in \mathbb{R}$	The thermal conductivity of the considered material in [W m ⁻¹ K ⁻¹]
H	Height of a block in [m]
$k(T) > 0 \in \mathbb{R}$	The thermal diffusivity of the considered material in [m ² s ⁻¹]
L	Length of a block in [m]
$\kappa(T) < 0 \in \mathbb{R}$	The derivative of the thermal conductivity divided by the specific heat capacity and the density of the considered material with respect to temperature in [m ² K ⁻¹ s ⁻¹]
$t \geq 0 \in \mathbb{R}$	The time in [s]
$x \in \mathbb{R}$	Spatial coordinate in [m]
$y \in \mathbb{R}$	Spatial coordinate in [m]

2.2 Parameters and variables

2.2.1 Modeling and stability investigation

$I_{\Delta T}, I_{\Delta u}$	Neighborhood around the freezing point
S, Γ	Parameters of the linear function $Sx + \Gamma$
T_0, T_L	Boundary conditions
$V > 0, V_1 > 0, \Lambda > 0$	Lyapunov candidates
u	State variable representing temperature
w	Error variable for the temperature
x_i	Mass fraction of substance i
$\alpha > 0, \beta > 0$	Bound variables
ε	Parameter

2.2.2 Observer

A	(Linearized) system matrix
$A_{\hat{s}}$	Linearized system matrix of the observer
B	Input matrix
C	Output matrix
D	Feedthrough matrix
I	Identity matrix
K	Observer feedback gain
P	Solution to the matrix Riccati differential equation
$Q > 0$	Noise covariance matrix of the model error; positive definite
$R \geq 0$	Noise covariance matrix of the measurement error; positive semi-definite
p, q	Parameters of the linear function $pT + q$
v	White Gaussian noise representing modeling errors
z	White Gaussian noise representing measurement errors

2.2.3 Optimal Control

E	Weight matrix to penalize deviations of T from T_{ref} in the OOC / MPC
F	Weight matrix to penalize deviations of a from a_{ref} in the OOC / MPC
G	Weight matrix to penalize deviations of b from b_{ref} in the OOC / MPC
J	Objective functions in the OOC / MPC
T	The state variable in the OOC / MPC
T_{ref}	Reference value for the state variable in the OOC / MPC
U	Weight matrix to penalize deviations of Z from Z_{ref} in the OOC
W	Terminal cost matrix to penalize deviations of T from T_{ref} at the end of the time horizon Z in the OOC
Z	Variable time horizon in the OOC
Z_{ref}	Reference value for the variable time horizon in the OOC
a	The boundary temperature in the OOC / MPC
a_{ref}	Reference value for the boundary temperature in the OOC / MPC
b	The time-derivative of the boundary temperature in the OOC / MPC
b_{ref}	Reference value for the time-derivative of the boundary temperature in the OOC / MPC
$\underline{\gamma}$	Lower bound on a variable γ in the OOC / MPC
$\overline{\gamma}$	Upper bound on a variable γ in the OOC / MPC
τ	Time horizon in the MPC

2.3 Chemical substances

NH_3	Ammonia
CO_2	Carbon dioxide
O_2	Oxygen
$(\text{CH}_3)_3\text{NO}$	Trimethylamine oxide
$\text{N}(\text{CH}_3)_3$	Trimethylamine
N_2	Nitrogen
CaCl_2	Calcium Chloride
NaCl	Sodium Chloride
$\text{C}_2\text{H}_6\text{O}_2$	Ethylene glycol

2.4 Notation

The subscript x , in particular f_x , defines the (partial) derivative of the function f with respect to the spatial variable x . The same holds for the double subscript xx , specifically f_{xx} , which represents the double (partial) derivative of the function f with respect to x . In the same fashion, the subscript t indicates a (partial) derivative of the function f with respect to time t .

Let $L^2([0, 1])$ denote the space of real-valued, square integrable functions f defined on $[0, 1]$ with finite L^2 -norm; $\|f\|^2 = \int_0^1 f(x)^2 dx < \infty$.

The space $H^1([0, 1])$ is the subspace of $L^2([0, 1])$ consisting of functions g with finite H^1 -norm; $\|g\|_{H^1} = \|g\|^2 + \|g_x\|^2 < \infty$.

Functions $w = w(t, x)$ are dependent on time t and space x (the spatial variable). To ease notation, frequently the dependency on t and $/$ or x are left out, e.g., $\|w(t)\|$ is the L^2 -norm of the function $x \mapsto w(t)(x) = w(t, x)$.

2.5 Important Lemmas

The following two well-known lemmas are taken from the book of Krstić and Smyshlyaev [69] and are needed in Sections 8.2 and 8.3.

Lemma 2.1 (Poincaré's Inequality). *For any continuously differentiable function $\omega = \omega(x)$, where $x \in [0, 1]$, the following inequalities hold:*

$$\begin{aligned} \|\omega\|^2 &\leq 2\omega(0)^2 + 4\|\omega_x\|^2, \\ \|\omega\|^2 &\leq 2\omega(1)^2 + 4\|\omega_x\|^2. \end{aligned}$$

Lemma 2.2 (Agmon's Inequality). *For any function $\omega = \omega(t, x)$ with $\omega(t) \in H^1([0, 1])$, the following inequalities hold:*

$$\begin{aligned} \max_{x \in [0, 1]} |\omega(t, x)|^2 &\leq \omega(0)^2 + 2\|\omega(t)\| \|\omega_x(t)\|, \\ \max_{x \in [0, 1]} |\omega(t, x)|^2 &\leq \omega(1)^2 + 2\|\omega(t)\| \|\omega_x(t)\|. \end{aligned}$$

Chapter 3

Preliminaries on freezing technology

Freezing is the most common method of shelf life extension over long periods for either transport or storage. Especially for rapidly spoiling foodstuff, like for example fish and its products, extension of shelf life is inevitable in order to guarantee a high quality and safe product. If done properly, freezing extends the shelf life without influencing quality attributes excessively, meaning that for example changes in texture, taste and freshness are negligible compared to the advantage of storing it over long times. Of course, when talking about freezing in terms of quality and shelf life extension one has to talk about the reversed freezing process as well, namely thawing. In each of these stages quality degrades, however, this degradation processes can be reduced to a minimum by applying the right techniques for specific applications. Issues concerning quality and quality changes of fish are presented in Chapter 5, whereas freezing and thawing are outlined in Chapters 3–4 from an engineering perspective.

From a theoretical point of view, the process of freezing an object down to a specific temperature requires the removal of a particular amount of energy. This amount of energy is defined by the temperature difference between initial and final temperature multiplied by the object's specific heat capacity plus the latent heat of fusion

$$\Delta h = c(T)(T_{init} - T_{final}) + h_{latent}.$$

However, removing only this amount of heat will not lead to a uniform and equal distribution of temperature, as for most freezing methods the cold front propagates through the spatial domain from the boundaries towards the interior.

Freezing techniques, especially in the fishing industry, can be divided into methods acting via the boundary of either blocks of fish or fillets, single fish or fillets and methods that act instantly also in the inner domain of the object to be frozen. This means that the phase change of water from liquid to solid happens either by a frozen front, which moves from the boundary layers to the inner domain (boundary methods) or instantly all over the fish (inner domain methods). All forms of freezing methods presented in the sequel rely on the same principles of heat exchange, namely evaporation of a refrigerant extracting heat from the object to be frozen, either directly or by a secondary freezing medium, like for example air or brine. Typical refrigerants are ammonia (NH_3) and carbon dioxide (CO_2), to name but a few. After evaporation, these refrigerants have to be regenerated by extracting the

added heat in a compression – condensation – expansion procedure. The overall process is called *vapor-compression cycle* including four stages: Evaporation, compression, condensation and expansion.

There are several possibilities of designing these processes. One relies on the principle that the refrigerant vaporizes partially while pulling heat off the product directly or off the secondary freezing medium. However, liquid fractions of ammonia in the compressor can lead to destruction, especially at the blades. Therefore, vapor and liquid phases for this specific process have to be separated in a so called separator. A sketch of such a process can be seen in Figure 3.1. The functional principle can be considered to be a decoupling of the refrigeration cycle into two loops, namely an outer *regeneration loop* and an inner *evaporation loop*, which are connected by the separator. In the *evaporation loop* liquid ammonia from the separator gets pumped through the evaporator, where it partly vaporizes taking heat off the object to be frozen. In the *regeneration loop* the heat that has been added to the refrigerant gets removed.

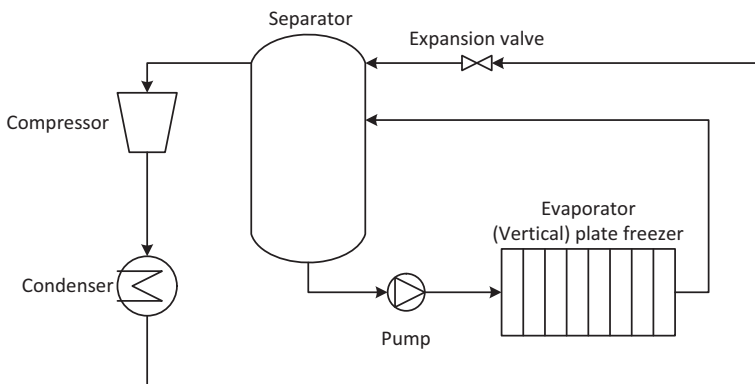


Figure 3.1: A sketch of a typical freezing process, as it is used on board fishing vessels. The evaporator is a vertical plate freezer and the two phases of the refrigerant leaving the evaporator are separated in the separator.

In the setup presented in Figure 3.1, which can be found on fishing vessels, the compressor is mostly chosen to be a screw compressor. The reason for this is its robustness in unsteady conditions on fishing vessels. The functional principle behind a screw compressor are two helical screws (one male and one female), which rotate against each other and whose cavities become narrower as the medium is propagated through the spatial direction. However, in more stationary applications, like e.g. in factories, all sorts of compressors can be used. The condenser is often a heat exchanger (counter current or parallel flow) with sea-water as secondary medium. In refrigeration systems, where no water is available, air is often used as a cooling medium in the condenser.

Another possibility is to fully vaporize the refrigerant in the evaporator. Here, one does not need the separator and a decoupling of the evaporation loop is, in theory, not necessary. However, after the condenser you can often find a so called receiver, which ensures that the expansion valve receives a steady head of liquid. There exist several forms of these cycles, for example one-stage or two-stage compression cycles, one-loop or two-loop (separator-

based) cycles, and many more. Çengel and Boles [23] provide an overview over different types of refrigeration cycles, including vapor-compression cycles.

3.1 Methods acting through the boundary

These methods are the most common ones when it comes to large-scale industrial application. Reasons for this are the rather easy implementation and maintenance and that they, to some degree, can be operated and used on board fishing vessels.

3.1.1 Plate freezers

In plate freezers the objects will be frozen to rectangular blocks of different sizes. A typical size is $0.5\text{ m} \times 0.5\text{ m} \times 0.1\text{ m}$, which gives a weight of roughly 25 kg. Such a block can be seen in Figure 3.2, which is displayed with kind permission of SINTEF Fisheries and Aquaculture, Trondheim, Norway.



Figure 3.2: Fish blocks on a conveyor belt after having been frozen in vertical plate freezers (left and right from the conveyor belt) on board a fishing vessel

Plate freezers come in two main constructive forms, namely vertical and horizontal. The latter thereby has the advantage that the size of the block can be varied easily. Vertical plate freezers are mostly produced with fixed block sizes and can be used on fishing vessels due to their robustness in unsteady weather conditions off shore. A typical vertical plate freezer is shown in Figure 3.3 by courtesy of MMC Kulde AS, Ålesund, Norway.

However, the principle of extracting heat is the same for both types of plate freezers. A liquid refrigerant flows through the plate freezer walls, where it evaporates and takes heat off the objects to be frozen. A manifold assures thereby that the same refrigerant characteristics are available in all the parallel walls. That means that there are no significant temperature differences in different walls in the plate freezer. In this setup, the plate freezer itself is the evaporator, compare to Figure 3.1. The heat exchange at the boundary is mainly driven by conduction.



Figure 3.3: Vertical plate freezer as produced by MMC Kulde AS, Ålesund, Norway

3.1.2 Air blast freezers

In these methods air serves as a secondary freezing medium and is cooled down by passing finned coils, in which a refrigerant evaporates and extracts heat from the air. The cold air then takes heat off the objects to be frozen while flowing over it. The heat transfer coefficient (HTC) is thereby significantly depending on the speed with which the air is flowing over the objects, see e.g. Footit and Lewis [43]. Here, the heat exchange at the boundary is mainly driven by convection.

There are several forms of these freezers, which all rely on the same principle. One group are continuous freezers, namely so called spiral belt freezers or tunnel freezers. In the first case, a spiral conveyor belt is moving upward in a freezing chamber while the cold air flows downwards in the opposite direction. In the second case a conveyor belt is moving horizontally through a freezing chamber, while the air typically flows in opposite direction to the belt's movement. Another group are batch blast freezers, where trolleys loaded with fish or fish blocks are loaded into the freezing chamber. In order to obtain best possible freezing results, the trolleys should fit the chamber in an optimal way such that good air flow is obtained. Furthermore, the blocks should be loaded on the trolleys in such a way that optimal air flow is not hindered. A description about how this can be achieved is provided by Kolbe and Kramer [65].

Advantages of these methods are relatively high freezing rates. Disadvantages can be that the use of cold, dry air can dry out the product's surface and lead to oxidation of fats, so called lipid oxidation.

3.1.3 Air impingement freezers

The functional principle of air impingement freezers is similar to that of air blast freezers. However, the cold air is shot at high velocities directly onto the product's surface using air impingement jets obtaining speeds up to seven times higher than conventional air blast freezers. Kolbe and Kramer [65] report about freezing times approaching those of cryogenic freezing (see Section 3.1.5) and reduced weight loss during freezing.

3.1.4 Brine freezers

Brines are mostly referring to solutions of salts, however, glycols and other fluids can fall into this category as well. After flowing over the freezing product the brines give up the added heat in a heat exchanger to a vaporizing medium, thus the brine has to be steadily regenerated. For safety reasons it is of high importance to wrap the freezing product in sealed packages to prevent direct contact with the brine. This does especially hold for glycol-based brines, as they can pose a possible health threat if consumed in large quantities. The same holds for Calcium Chloride (CaCl_2), while Sodium Chloride (NaCl) does not pose a health threat to the consumers, however, the taste of the objects to be frozen might change.

The freezing points of the latter two mentioned can be brought to around $-20\text{ }^\circ\text{C}$, although these temperatures are impractical. Kolbe and Kramer [65] mention that viscosity might be a problem for CaCl_2 at these temperatures leading to higher required pumping power. NaCl might freeze at this temperature at the tube walls in the heat exchanger. Therefore slightly higher temperatures of about $-15\text{ }^\circ\text{C}$ seem to be more practical. For glycol-based brines the freezing point can be lowered to about $-50\text{ }^\circ\text{C}$, however, viscosity poses a problem at these temperatures as well. Therefore, a practical temperature is about $-15\text{ }^\circ\text{C}$ as well, according to Kolbe and Kramer [65], limiting the gradient necessary for heat exchange as well as the final temperature. It is also this relatively high operating temperature, which makes these methods best suited for the freezing of individual fish or fillets. From a practical point of view, the cold brine is either sprayed onto the freezing objects, or the objects are submerged in the brine.

3.1.5 Cryogenic freezers

Cryogenic freezing methods have, to some degree, the same functional principle like methods using brines. The most common refrigerants are liquid nitrogen (N_2) and liquid carbon dioxide (CO_2). With both of them very low temperatures can be achieved; liquid N_2 vaporizes at atmospheric pressure at $-196\text{ }^\circ\text{C}$ whereas liquid CO_2 first turns into “snow” (a mixture of solid and vapor) when pressure is reduced to atmospheric pressure and then vaporizes at $-78.5\text{ }^\circ\text{C}$. However, the refrigerant cannot be regenerated, like for example brine solutions can. This means that, after it has been used for freezing and thus vaporized, the vapor will be released into the atmosphere.

There exist several technical solutions, mostly based on methods spraying the refrigerant onto the freezing object. This can be realized in tunnel freezers (continuous operation) or in cabinet freezers (batch operation). The storage of liquid N_2 has to happen in well-isolated, pressurized tanks. However, due to the large temperature difference between the stored N_2 and the surroundings, boiling losses will occur when stored over long periods. These losses can exceed 1 % per day, according to Kolbe and Kramer [65]. Also losses during transport from the storage tank to the processing plant can be quite significant. Storage of CO_2 on the other hand is not that problematic. At a pressure of around 2 MPa it can be stored at about $-18\text{ }^\circ\text{C}$. This reduces the losses compared to liquid N_2 by far.

Advantages for liquid N_2 are that the temperature gradient between the freezing object and the refrigerant is so high that the heat is extracted rapidly, making it the fastest freezing method available. However, this poses a disadvantage as well, as the freezing object is

likely crack into several pieces when thrown into a bath of liquid N_2 . The large significant losses during storage and transport are also a disadvantages. The use of liquid CO_2 seems more reasonable compared to liquid N_2 , however, as it is released into the atmosphere after use one should also consider its impact on the climate.

3.2 Methods acting in the inner domain

These methods rely on the principle of undercooling, where one exploits the lowered freezing point of water for high pressures as well as the effects of a rotating magnetic field, which hinders the water molecules to nucleate around a core to form ice crystals.

3.2.1 Pressure freezers

Pressure freezers rely on the fact that the freezing point of water is lower than $0\text{ }^\circ\text{C}$ for high pressures. In the phase diagram for water, see e.g. Figure 3.4, one can see that at about 210 MPa the freezing temperature of water is about $-21\text{ }^\circ\text{C}$.

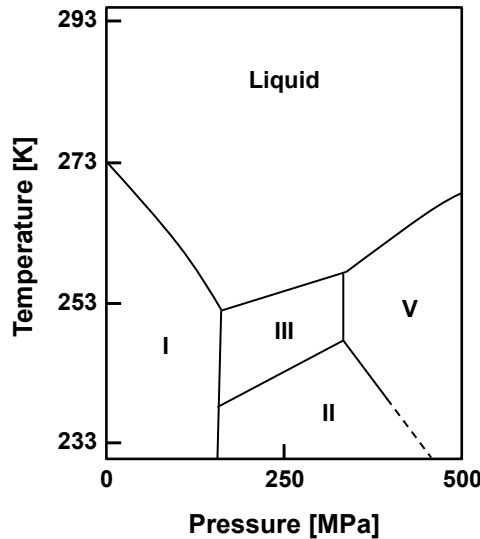


Figure 3.4: Sketch of the pressure-temperature phase diagram for liquid water and different ice formations, compare to e.g. Cheftel et al. [24, Figure 2]

There exist basically two different ways of using pressure in freezing applications, namely Pressure Shift Freezing (PSF) and Pressure Assisted Freezing (PAF). A comparative study of these two methods is presented by Fernández et al. [41]. In principle these two pressure freezing methods differ in the way the phase change from liquid to solid occurs. However, there are different modes of operation, as e.g. described in Norton and Sun [85], Otero and Sanz [88] and LeBail et al. [73]. In all the cases the heat has to be extracted via an external freezing medium, which surrounds the pressurized chamber.

In PAF the phase change happens at a constant pressure while the temperature is being

lowered. This is to some degree comparable to a boundary method, as at first the boundary layers will be frozen as the cold front propagates through the freezing object. However, if a specific temperature below the freezing point at this particular pressure is reached, the pressure is reduced to ambient pressure and the product will freeze more or less instantly also in the inner domain.

For PSF, on the other hand, temperature reduction occurs at a constant pressure such that the water at the specific end-temperature is still in liquid form. Then the pressure is reduced to ambient pressure, which causes the freezing to occur throughout the whole spatial domain. Thereby the latent heat of fusion is removed at atmospheric pressure followed by a tempering phase down to the desired storage temperature.

Both, PAF and PSF have their advantages and disadvantages. PSF provides a fast and evenly distributed freezing pattern throughout the object, but at the cost that the pressure needed is significantly higher than for PAF and that only temperatures of at most $-21\text{ }^{\circ}\text{C}$ can be achieved. However, the product can be cooled down even more at ambient pressure. PAF works with lower pressures, but at the cost that the object undergoes freezing of the boundary layer first, before the inner domain freezes due to the pressure release.

Pressure freezing methods are not (yet) practical for industrial use, as the sizes of the pressurized chambers are by now limited to some liters. However, they provide large freezing rates, which leads to small ice crystal formation and thus to reduced drip loss, according to Li and Sun [75]. Furthermore, they offer a great potential for storing fresh products at low temperatures without freezing, as the water at high pressures remains liquid even below $0\text{ }^{\circ}\text{C}$.

3.2.2 Cell Alive System freezers

Freezers working with the principle of so called *Cell Alive System (CAS)* are often designed as conventional air blast freezers (cabinets), in which the product gets frozen by convection. In this cabinet a weak magnetic field is used to keep the water molecules (inside the object to be frozen) spinning in order to avoid forming ice crystals. Thus the water will still be liquid even though the temperature is below the freezing point. This phenomenon is comparable to the principle of supercooling, or often called undercooling, where pure water can be cooled down at standard pressure to a minimum of around $-48\text{ }^{\circ}\text{C}$. The water may not offer any nucleation sites, which means that water molecules should not be able to nucleate and form ice crystals. This equilibrium, however, is very unstable and a slight disturbance may cause instant nucleation and forming of ice.

The advantages of this method are that, while in the cool cabinet with the magnetic field, the product can be stored unfrozen at low temperatures. If the magnetic field is turned off, ice crystals start to form both intra- and extracellular in the object and freezing will happen instantly, comparable to PSF. If one compares the effort with the quality after thawing, CAS might be best for large and valuable fish, like for example tuna. This might also be the reason why some Japanese tuna boats use CAS.

Nevertheless, a study conducted by Erikson et al. [39] showed no significant differences in quality comparing Atlantic cod frozen pre-rigor in CAS, air-blast and cold storage freezers.

3.3 Conclusion

Methods that act in the inner-domain of the object to be frozen are not yet applicable in large scale industrial applications. However, they offer great potential when it comes to freezing times and ice-crystal size, meaning quality with respect to drip loss and thus possible yield. Drip loss denotes the liquid that leaves the object after being thawed and is directly related to the water holding capacity. The water holding capacity, however, has to do with the speed of freezing. Thus, fast inner-domain methods are beneficial for the water holding capacity. If these methods can be made applicable in larger scales, they could take over from the methods that act via the boundaries. These processes are established in industry at a large scale and thus capable of delivering high outputs. The freezing times are generally larger than those for the inner-domain methods, however, sufficiently large to obtain good qualities for most of the methods. An exception might be the brine freezing methods, which are too slow due to small temperature gradients between freezing medium and initial temperature of the objects to be frozen.

But like mentioned before, for every application there might be a different freezing method delivering optimal results, not also with respect to quality, but also to a cost-benefit analysis.

Chapter 4

Preliminaries on thawing technology

As introduced before, freezing is an essential part of shelf life extension for fish and its by-products. For most of the cases the raw material cannot be processed if still in frozen state. An exception to this is the cutting of fish sticks out of large blocks of frozen fillets after a short tempering phase of these blocks, described e.g. by Jason [57]. But if fish is frozen as H/G (headed and gutted)-fish on board a trawler and shall be filleted and processed in a factory on shore, gentle and effective thawing techniques are required in order to obtain a high quality product. It is nearly impossible to cut fillets of good quality out of a frozen H/G-fish. Thawing represents therefore a vital part for further processing of frozen fish.

To understand the process of thawing it is inevitable to understand the process of freezing, as thawing is the reversed freezing process. Like already introduced in Chapter 3, freezing occurs when removing a specific amount of heat, and thus of energy, Δh from the freezing object. However, as known from Chapter 3, by only adding Δh one does not obtain a uniformly distributed final temperature throughout the fish block, as no spatial and time dependent dynamics of the temperature are taken into account. The amount of heat added has to be enough to thaw the interior of the fish block such that the phase change of water from solid to liquid has just passed, or in other words, the amount of latent heat of fusion has been added.

It must be mentioned that the freezing process runs faster compared to the thawing process as frozen water is a better conductor of heat than liquid water. After the process started, the outer layers of the fish block act like a resistance to the heat flow, with decreasing value for the freezing case and increasing value for the thawing case. There exists a broad variety of thawing techniques, differing by means of practicality as well as resulting quality with respect to fish species and final product. Thawing methods can be divided into two main groups, namely methods that add heat to the fish through the boundary layers and methods that distribute and generate heat all over the (inner) spatial domain of the fish (block).

It generally holds that the quality of the thawed product will be highest if the thawing process proceeds slowly; in fact, drip loss will be minimized during slow thawing, as mentioned by Nilsson [83]. As will be seen in the subsequent listing of different thawing methods, this relationship must not hold for all methods, as problems like lipid oxidation and drying of the tissue might arise. General rules for thawing define limits in which thawing temperatures can be chosen. According to Jason [57] the quality of the fish will suffer

if its temperature exceeds 20 °C and for temperatures above 30 °C the fish will cook.

Good outlines over different thawing methods were introduced by Jason [57], who focuses on established and applied techniques used by industry as well as more advanced, theoretical methods, which are not applicable for large scale thawing, and Li and Sun [75], who reviewed novel techniques for freezing and thawing altogether. The thesis of Haugland [47] provides some new insights over industrial thawing methods, in particular for Atlantic salmon, not covered by Jason [57].

4.1 Methods acting through the boundary

The methods mentioned in this section are methods that affect the fish block only via its boundary layers. This means that heat can only be imposed to the fish block by introducing a heat source at these boundaries. Thus the heat front must propagate all the way through the fish block in order to reach the center and thaw it completely.

4.1.1 Thawing in air

Air thawing can come in several forms and can be considered a cheap solution to thawing blocks of fish. The thermodynamic phenomenon underlying these techniques is heat transfer through convection, which can be divided into natural and forced convection. Natural convection is simply heat exchange between a medium and a body without any external interaction, whereas forced convection is heat exchange with exterior interaction (mostly by letting the air flow over the frozen object).

A disadvantage of all these methods is that they have a high probability of lipid oxidation and drying out the surface as air is the thawing medium and in direct contact with the fish. Especially drying of the surface is a problem for forced convective thawing whereas lipid oxidation may impose problems particularly to fatty fish. These two disadvantages can be reduced by using humid air, as it contains less oxygen and a higher fraction of water vapor, see for example Jason [57] and Archer et al. [5].

Thawing in still air

Thawing in still air means that a fish block is being thawed only by non-moving air surrounding it, which is an example for natural convection. The heat exchange rate is very low and thus it takes a long time to thaw the entire fish block. Jason [57] reports that it can take up to 20 hours to thaw a 100 mm thick block of frozen whole cod in air at 15 °C.

The process can be accelerated by putting the fish block on a grate, such that the air surrounding it can be acting also on the underside of the block. Further acceleration can be achieved by separating single fish from the block leading to a larger area and thus to faster thawing. This should be done with minimal force as the use of excessive force can damage the fish resulting in parts of the fillet and / or skin to remain sticking on the block.

However, the relatively slow rate of thawing can lead to a high rate of lipid oxidation, as the fish is exposed to air for a long time. Like mentioned before, the use of humid air with a high fraction of water vapor can reduce lipid oxidation and drying of the surface.

Air blast thawing

Air blast thawing is a method widely used in industrial applications. It follows the same principles like thawing in still air, but in contrast the air is forced to move over and around the fish (block)'s surface; this is an example for forced convection. Compared to thawing in still air, flowing air leads to a higher rate of heat exchange. A crucial parameter hereby is the speed of the air flowing over the fish. The heat transfer coefficient (HTC) is dependent on the air speed; typical speeds are $6 - 10 \text{ m s}^{-1}$, see e.g. Footit and Lewis [43]. It takes about 4 – 4.5 hours to thaw a 100 mm thick block of frozen whole cod in humid, $20 \text{ }^{\circ}\text{C}$ warm air moving at 8 m s^{-1} , according to Jason [57].

In practice both, continuous and batch thawers can be found. However, due to the cheaper costs of batch thawers, they are mostly used. In one type, fish blocks or single fish are put on trays which can easily be stacked on trolleys with enough space in between. This is important in order to have a uniform flow of air inside the chamber into which the trolleys are moved. Not only the space between trays, but also the space between trolleys is important for the air to flow in an optimal way. For a uniform thawing of all blocks inside the batch thawer it is important to have a reversible fan blowing air from both directions along the length of the chamber. Water is added to the air by nozzles and heat is provided by hot water pipes, for example. A schematic of such a thawing process can be seen in Figure 4.1, which is displayed by courtesy of Her Majesty's Stationary Office under the Open Government Licence (OGL) of the United Kingdom's National Archives.

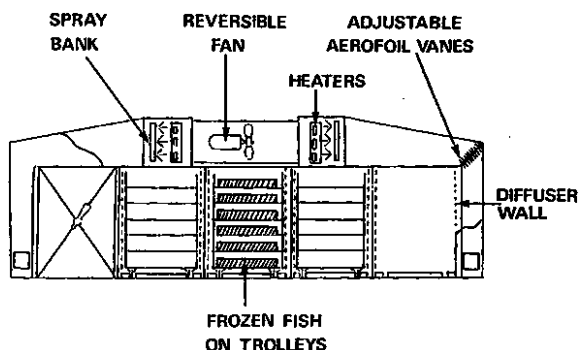


Figure 4.1: Air-blast batch thawer, taken from Jason [57]

The rate of lipid oxidation for the described setup is naturally lower than for thawing in still air, due to the shorter thawing time and the addition of water. A small danger of drying of the surface, however, remains present. In addition, overheating can occur if the temperature is not perfectly controlled and therefore in practice the fish is taken out of the thawer prior to complete thawing and brought to a cold storage room where it completely thaws covered in ice (prevention for lipid oxidation and drying).

4.1.2 Thawing in water

Besides air thawing techniques, water thawing techniques are widely used in industrial applications. They are often called immersion thawers, as the fish block is immersed inside

4. Preliminaries on thawing technology

a water container. However, as the density of ice is slightly lower than that of liquid water, it has to be assured that the fish block remains under water to achieve best possible heat transfer. With this technique, the aforementioned dangers of lipid oxidation and surface drying during thawing are naturally not present or at least reduced to a minimum.

There exist several different methods, which rely on the same principle, namely heat exchange between the thawing medium water and the fish block by means of heat conduction. The majority of all water-based thawing techniques are notably faster than air thawing methods as the heat exchange rate in heat conduction problems is higher than for heat convection problems. It has to be mentioned that these methods in optimal operation require the thawing medium to be consistently exchanged and / or regenerated, due to the fact that the thawing capacity gets reduced as a result of the water being cooled. Furthermore, contamination with bacteria poses a threat to the quality of the thawed product. Principally there are two different kinds, namely batch and continuous operations.

One method is to use rectangular tanks of varying sizes (roughly $0.3 - 1 \text{ m}^3$), which are filled with water and fish blocks. This method represents a batch thawer as it is no continuous operation. They can be operated in two ways, either by exchanging the thawing medium consistently or by conducting thawing with a fixed amount of water. For the first operation a water hose is consistently pumping (heated) water into the tank and thereby exchanging the water present in the tank, as for example presented in Haugland [47]. A way to enhance heat exchange for both operational modes is to pump small air bubbles into the tank, enhancing heat transfer. Gradually, single fish will separate from the block leading to an increased area of heat exchange, a further acceleration factor. A picture of such a thawing process in a tank with water bubbles can be seen in Figure 4.2.



Figure 4.2: Thawing of two blocks of frozen H/G cod in a tank with enhanced heat transfer due to air bubbles - the aluminum frame hinders the fish blocks from being lifted up

Among continuous operations many different constructive forms can be found. One of these consists of a large cylindrical tank, which is divided into several compartments. The fish blocks are filled into one compartment, which turns around the cylinder's rotational axis. When one full turn is achieved the fish should be fully thawed. In the final stage there

will only be single thawed fish present in the tank. This method has a high volumetric efficiency and is shown in Figure 4.3 by kind permission of Melbu Systems AS, Melbu, Norway. Other methods work with helical screws in big tanks, where the frozen fish gets loaded in the one end and unloaded at the other - fully thawed. A method following the same principle consists of big tanks with a conveyor belt on the bottom. Thawed fish will sink to the bottom and can be transported out of the tank with the conveyor belt.



Figure 4.3: A cylindrical thawing tank as built by Melbu Systems AS, Melbu, Norway

A further method are so called continuous immersion thawers. They are usually composed of conveyor belts with attached open grid baskets, into which the fish blocks get loaded. First the baskets with the fish blocks run along an array of water sprayers before going into a water bath upside down. Just before coming back to the loading point the baskets get unloaded. Due to the fact that in the final stage of the operation single thawed fish are to be found in the baskets, their grid should be sufficiently fine-meshed so the fish will not slide through.

4.1.3 Vacuum thawing

Vacuum thawing relies on the principle that the boiling temperature of water is lowered as the pressure is decreased. Furthermore, it is based upon the fact that condensation of water emits heat. Thus a desired thawing temperature can be chosen equal to the boiling temperature of water at a certain pressure. Then steam is released into the vacuum chamber at this preset pressure and will condense at the surface of the fish block releasing its heat of condensation. The close-to-vacuum operation allows the water vapor to get into air cavities in between single fish. For this method it is required to control the pressure and steam very carefully, otherwise heat damage might occur. If done properly, this method is equal to air blast or water thawing by means of speed. According to Jason [57], 65 mm thick blocks of shrimps and 50 mm thick blocks of plaice can be thawed in under 80 minutes.

Commercial vacuum thawers work with trolleys, just like for air blast thawing. A liquid

ring pump empties the air out of the thawing chamber. Water in a small container at the bottom of the chamber is heated by different means (e.g. steam, electrical, heat exchangers) such that it boils and becomes water vapor (at low temperatures as the pressure is low). The operation itself is clean as the water only condensates on the fish's surface, the chamber walls remain dry. Furthermore, no bacteria are present, the operation is hygienic and there is almost no cleaning to be done.

4.1.4 Contact thawing

Contact thawers typically consist of parallel metal plates. In between these plates a block of fish can be placed such that the block has contact to the plates on both sides. The metal plates are heated up in order to thaw the fish block. This has similarities to freezing fish to blocks in plate freezers, however, it is the reversed process. Therefore, one could imagine plate freezers specifically rebuilt as “plate thawers” working with thawing media such as water or glycol-water mixtures. Even electrical heaters inside the plates are possible. These thawers have two advantages, firstly, the fish block is not in direct contact to the thawing medium and secondly, the process is controllable in a better way compared to other thawing techniques, especially the ones mentioned earlier. Better ability to monitor and control the process is achievable due to the fact that heat transfer in plate freezers and, by implication, in plate thawers, are well understood. This better understanding is one of the outcomes of this thesis.

4.2 Methods acting in the inner domain

The second big group of methods act directly in the inner domain of the fish / fish block. In general, all of these methods are faster compared to conventional thawing methods relying on air or water as thawing media. However, they are only available in small scale and thus not (yet) applicable in large-scale industrial applications. A big problem imposes so called local overheating or thermal runaway, especially in dielectric methods, whereas the small size of apparatuses using high pressure (not more than 5 dm³) limits it to (professional) kitchen use for high quality fish products.

4.2.1 High pressure thawing

The principle behind high pressure thawing is the same as already introduced for high pressure freezing in Section 3.2.1. The freezing and thus the thawing temperature of water is lowered as the pressure rises. As already described in Section 3.2.1, the lowest freezing temperature for water of $-21\text{ }^{\circ}\text{C}$ is obtained at 210 MPa, whereas for ambient pressure of around 0.1 MPa the freezing temperature of water is around $0\text{ }^{\circ}\text{C}$, see Figure 3.4.

There are two methods conducting the thawing under high pressure, namely Pressure Assisted Thawing (PAT) and Pressure Induced Thawing (PIT). PAT means that thawing happens at constant pressure while the driving force is the temperature difference between the pressurized chamber and a thawing medium (mostly water bath). This method is more or less the reversed Pressure Assisted Freezing (PAF) from Section 3.2.1. In PIT applications on the other hand, the thawing occurs while the pressure is applied along the melting curve of ice I, see Figure 3.4. The differences between these two techniques are well

explained in Otero and Sanz [88] and Norton and Sun [85]. LeBail et al. [73] provide a review over applications for high pressure freezing and thawing both for microscopic preparation and foodstuff, whereas Li and Sun [75] deliver a review over high pressure applications for freezing and thawing of foodstuff.

For high pressure freezing it is inevitable to have the refrigerant / freezing medium around the pressurized chamber in order to decrease the temperature of the product inside the chamber. For high pressure thawing this is not necessarily needed, as the ideal gas law states that the temperature rises if the pressure rises. However, to control the temperature inside the pressurized chamber, a steady temperature on the outside should be imposed. The size of these applications are limited to very small scales. Schubring et al. [100], for example, describe experiments, where the chamber had a volume of 0.6 dm^3 .

Schubring et al. [100], Zhu et al. [111] and Rouillé et al. [96] discuss properties of quality, like color, drip loss, texture and pH-value after high pressure thawing treatments and compare these to conventional thawing methods under ambient pressure. High pressure freezing and thawing reduces drip loss, according to Rouillé et al. [96] whereas Zhu et al. [111] mention that the freezing part is of higher significance than the thawing part. Discoloration and hardening of the tissue are reported by Schubring et al. [100] and Zhu et al. [111]. All of the aforementioned articles noticed faster thawing times compared to conventional thawing methods.

4.2.2 Electrical methods

Electrical methods use electric fields in order to generate heat throughout the spatial domain of the objects to be thawed. In Zhao et al. [110] some methods get introduced, such as electrical resistance thawing and dielectric thawing.

Dielectric thawing

Dielectric thawing is a collective term for all sorts of thawing methods that use high-frequency waves in order to thaw foodstuff. The most common among these techniques are radio-frequency- (RF) and microwave- (MW) based methods, which differ in the used frequency band. Depending on applications, different limits for these frequency-bands can be found in literature, however, as a rough classification one can define RF in the MHz and MW in the GHz range, respectively. Another important factor is the voltage applied and thus the electrical power.

Dielectric thawing exclusively works for materials that are electrical insulators and can be polarized by an electric field. In an oscillating electric field, the molecules start rotating and colliding with other molecules and thus heat is generated inside the objects. The penetration depth (meaning thawing impact) depends on the applied frequency of the method. For foodstuff it is known that lower frequencies reach deeper into the objects than higher frequencies, making RF methods more suitable for large-scale industrial applications, see e.g. Wang et al. [107]. As an indicator for which frequencies are best to apply to a specific foodstuff one can find the frequency where the imaginary permittivity of this foodstuff has its maximum value - the so called *Debye resonance*. However, foodstuff consist mostly of water and therefore the known value for water is a first good choice.

Problems with these methods can be local overcooking due to irregular shapes and / or entrapped air. Furthermore Zhao et al. [110] report about possible overheating or even burning of packaging materials due to multiple Debye resonance frequencies, when foodstuff is thawed while being boxed / wrapped.

Microwave techniques use microwave radiation in order to thaw fish. They rely on the same principle like common microwave ovens for domestic use. The frequencies of these microwaves lie between those of radio waves and infrared light. However, as the penetration depth is depending on the frequency and the tissue composition itself, local thermal runaway can occur. That means that due to the limitations in penetration only the boundary layers get affected by the microwaves, whereas the inner layers remain frozen and will be thawed by regular thermal conduction. The heating gradient with microwaves is larger than that for conduction and thus the boundary layers will heat up faster than the inner layers. This phenomenon is intensified by the fact that liquid water absorbs more energy than ice, which even enhances thermal runaway. Common penetration depths for domestic use microwave ovens (2.45 GHz and 1–2 kW) are not more than a few centimeters - enough for private use, but not necessarily for industrial applications.

Radiowave thawing relies on the use of waves with low frequencies and thus large wavelengths. Theoretically, this leads to larger penetration depths. With the right power input it is supposed to be safer and better in terms of overheating and uniform temperature distribution than microwave heating. However, local thermal runaway still imposes a possible disadvantage.

Far-infrared thawing

Far-infrared thawing (FIR-thawing) relies to some extent to the same principles as dielectric thawing. The spectrum of the infrared waves ensues the microwave spectrum and thus the frequencies are higher and the wavelengths smaller. In Sakai and Hanzawa [97] thawing procedures using FIR waves are introduced as an alternative to microwave thawing. Although having even higher frequencies and smaller wavelengths than microwaves, Sakai and Hanzawa [97] claim that the danger of local overheating (thermal runaway) is reduced (or almost zero) due to the fact that the absorption coefficient of the FIR waves for ice and water are almost the same. However, the penetration depths for the FIR waves are even smaller than those for microwaves and thus local overheating imposes a threat to thick foodstuff.

Electrical resistance thawing

The principle behind electrical resistance thawing is that heat is generated inside foodstuff when electric current passes through. This is due to the fact that food imposes electrical resistance to the current. Further names for this technique are *Ohmic thawing* or generally *Joule heating*.

The lower the resistance, the faster the thawing time. Therefore, Jason [57], Li and Sun [75] and de Alwis and Fryer [33] mention that a first thawing stage should not include electrical resistance thawing, but conventional thawing techniques. The reason for this is the high specific resistance of frozen fish muscle at very low temperatures (e.g. $25 \cdot 10^6 \Omega \text{ cm}^{-1}$ at $-30 \text{ }^\circ\text{C}$) which makes it a poor conductor of electricity. However, frozen

fish at these temperatures is a good conductor of heat, which makes it applicable for conventional thawing techniques. When the specific electrical resistance is reduced (e.g. $800 \Omega \text{ cm}^{-1}$ at 0°C), then electrical resistance thawing can be used to thaw it completely (for example to remove the latent heat of fusion). According to Li and Sun [75] frozen foodstuff (tuna, beef and eggs) are thawed rapidly by means of high voltage electrostatic field in the temperature region from -3°C to 3°C using a patented method from Tatsukiyo Ohtsuki¹.

Compared to dielectric thawing, electrical resistance thawing has two big advantages in terms of efficiency. Firstly, almost all the energy put into the process enters the food as heat and secondly there is no limitation of the penetration depth. However, local overheating imposes constraints on the operation and the foodstuff should be in rectangular regular shapes in order to be put between two parallel metal plates.

4.3 Conclusion

Methods that act via the boundary of the object to be thawed are practically applicable for industrial use, whereas methods acting in the inner domain of the object are not yet suitable for large scale applications. Main reasons are the rather small volumes (e.g. for high pressure methods) as well as the dangers of local overheating (mainly for dielectric heating). Electrical resistance thawing is applicable for larger scales along with a boundary method, for example thawing in a water bath, which should precede the electrical resistance thawing. A promising technology in terms of increased ability to control the thawing process are the so-called contact thawing methods. The underlying thermodynamic phenomena are well understood and thus (local) overheating can be avoided, as shown in Chapter 16.

¹US Patent 5,034,236 and European Patent 0409430

Chapter 5

Fish as foodstuff

In this Chapter different aspects of fish quality as well as changes in fish quality are presented. It is illustrated that fish quality is subject to a broad variety of influences and parameters, making a simple definition impossible. This Chapter is aiming to provide an overview over the most important phenomena regarding fish quality and has therefore no intention of being highly detailed or being complete.

5.1 Quality of fish

Quality of fish is a term that is difficult to describe as it is influenced by many factors and parameters. Thus it needs further clarification and definition. Ólafsdóttir et al. [86] describe quality as a function of many other factors. Probably the most important one among these factors is freshness as it describes quality in the sense as consumers understand it. Freshness itself, however, is a function of other factors, like e.g. lipids, ATP (adenosine triphosphate)-levels, microbiology, etc.; as can be seen in Figure 5.1.

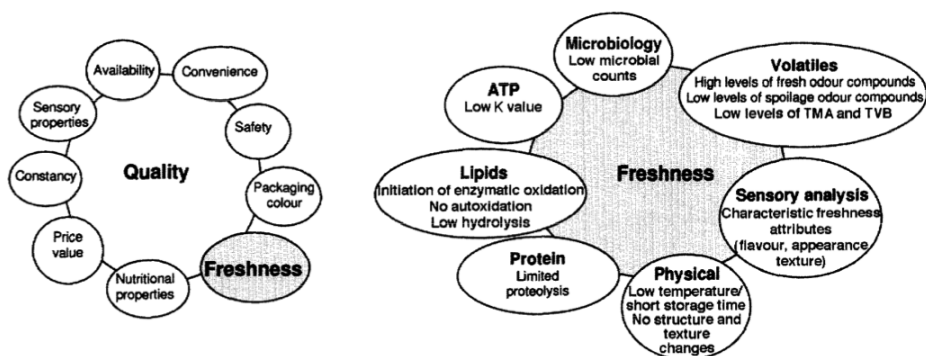


Figure 5.1: Quality as a function of freshness and other factors, taken from Ólafsdóttir et al. [86]

Figure 5.1 is reprinted from Trends in Food Science and Technology, 8(8), G. Ólafsdóttir,

E. Martinsdóttir, J. Oehlenschläger, P. Dalgaard, B. Jensen, I. Undeland, I. M. Mackie, G. Henehan, J. Nielsen and H. Nilsen, Methods to evaluate fish freshness in research and industry, 258–265, Copyright 1997, with permission from Elsevier.

It must be mentioned that freshness is a necessary, but not sufficient condition for high quality scores. Further important quality aspects besides of freshness are for example the nutritional properties and hygienic aspects, which are correlated with sensory properties. However, freshness is the most important condition regarding consumer safety. One basic rule in food production is food safety in the sense that a product should be safe to be consumed and not cause any sicknesses or diseases among the consumers. If this is assured, other quality aspects can be taken into account, like for example the appearance of the product, etc. However, spoilage can occur even without the presence of pathogenic bacteria, meaning that eating a spoiled fish might not necessarily make the consumer sick.

It has to be mentioned that in this Section, quality and freshness are solely subject to fresh fish stored in flake ice or slurry ice. Slurry ice is a refrigerant consisting of a large number of ice crystals within a solution of water and a freezing point depressant (most commonly salt). Quality changes during freezing and frozen storage are presented in Section 5.1.3. Many publications cover quality and freshness of fresh, chilled fish. Dawood et al. [32] give results about quality changes due to delayed icing of rainbow trout whereas Barros-Velázquez et al. [21] conclude that better quality can be obtained by using slurry ice rather than flake ice. However, flake ice is mostly used in industry.

5.1.1 Assessment of fish quality

There exist several methods to assess fish quality. These can be divided into two main groups, namely sensory and instrumental (i.e. machine-based) analysis. Sensory analysis means that a person assesses the quality (mainly freshness) of whole fish or fish fillets by using his senses, evaluating appearance, texture, odor and sometimes taste. Machine-based analysis tries to automatize and therefore replace sensory analysis.

Sensory analysis

Assessment of quality / freshness by means of sensory analysis requires highly trained professionals, as it is important to do so in an objective way. This can be supported by standardized methods, for example the *EU scheme* or the *Quality Index Method (QIM)*, which is based upon a grading system, where different attributes get rated with a score from 0 – 3 points. The QIM grades attributes like e.g. color / appearance, odor, form and mucus for specific parts of the fish, namely the skin, the eyes, the gills and the abdomen, however, there are slightly different QIM-schemes for different fish species. The QIM determines fish freshness and is supposed to deliver a measure regarding food safety - briefly speaking it can give information about the current freshness and predict how many days an acceptable freshness level can be preserved. An introduction to sensory analysis methods and principles can be found in Vaclavik and Christian [106].

Machine-based analysis

Machine-based analysis tools use physical measurements in order to evaluate quality and freshness. Present techniques measure electrical parameters (conductance and capacitance

of fish muscle and skin), the color of the skin and muscle and the texture. Latter is measured by devices providing force-deformation curves. Furthermore, tools like image analysis, VIS-spectroscopy (absorption spectroscopy of visible light) and electronic noses are used. Ólafsdóttir et al. [87] deliver an overview over different techniques and propose the design of a multisensor device that can be used to deliver more than one physical measurement at once. This multisensor provides a so called *Artificial Quality Index (AQI)* and is supposed to replace the *Quality Index Method (QIM)* - the aforementioned sensory analysis method.

5.1.2 Postmortem changes in fish

A fish undergoes a number of changes after it has died. The driving forces for these changes are due to enzymatic (autolytic) and bacteriological activities. Thereby, enzymatic and autolytic changes precede bacteriological changes. In Figure 5.2, Huss [55] presents a graph of a sensory analysis scheme including four different phases of spoilage and the dominant causes for changes of freshness (autolytic and bacteriological). The rejection level is to be found in phase 4 (quality score lower than 4); for reference: a quality score of 6 indicates neutral, tasteless fish. For further explanation about this scheme, see Huss [55].

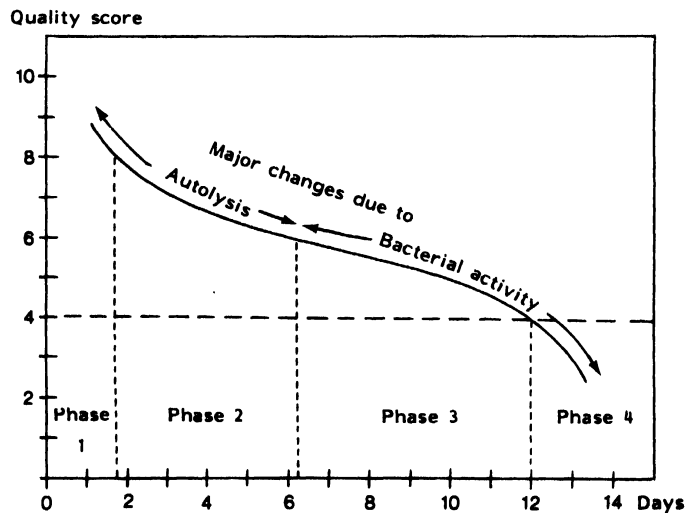


Figure 5.2: Graphical Representation of a sensory analysis scheme for iced cod (0 °C), taken from Huss [55]

Source of Figure 5.2: Food and Agriculture Organization of the United Nations. 1995. Quality and quality changes in fresh fish, by H. H. Huss, Technical Report 348, FAO Fisheries. Rome, Italy. Reproduced with permission.

Sensory changes

Sensory changes, like mentioned before, can directly be perceived by senses checking the appearance, odor, texture and taste of the fish. According to Huss [55], the first occurring changes are those in appearance and texture. Furthermore, a characteristic taste of a species is developed after some days of storage on ice. Change in odor is the most significant evidence of degraded freshness: If a fish smells “fishy”, it is not fresh anymore; a fresh fish has clear eyes, dark red gills and has no characteristic smell, except for the smell of seaweed.

Rigor mortis

In fish and other species energy is produced by either burning glycogen (stored carbohydrates) or fat with oxygen, which is provided by the blood. This chemical reaction leads to the production of mainly carbon dioxide (CO₂), water (H₂O), adenosine triphosphate (ATP) and creatine phosphate (CrP). ATP is responsible for the transportation of chemical energy within cells for metabolism. If the fish dies and its heart stops pumping blood through its veins, the oxygen supply ceases and glycogen can no longer be oxidized. Instead, the glycogen is metabolized anaerobically to lactic acid. ATP levels drop dramatically for dead fish, as the body is using the present ATP. Furthermore, CrP is able to rapidly transfer its phosphates to adenosine diphosphate (ADP) in order to maintain the ATP levels and keep the metabolism running. However, when glycogen is broken down anaerobically, far less ATP is produced. Drop of ATP production below a certain level results in onset of rigor mortis, meaning that the muscle stiffens and cannot be resolved mechanically without damaging the tissue. A short summary of the muscle chemistry post mortem: Levels of glycogen, ATP and CrP are reduced, while lactic acid, creatine and degradation products of ATP increase.

Several factors influence the onset of rigor mortis, the most significant are the stress level and exhaustion as they have a dramatic effect on the glycogen levels. It is known that the onset of rigor mortis happens earlier for stressed and exhausted fish compared to non-stressed / rested fish. This is due to the fact that the ATP levels of the latter are significantly higher, see e.g. Skjervold et al. [101], who investigated rigor mortis for farmed Atlantic salmon. Also species, temperature, handling, size and physical condition have an effect on the onset of rigor mortis, according to Huss [55]. The stronger rigor mortis, the more likely is gaping and destruction of the tissue. Gaping denotes the separation of single flakes of the fillet from one another so that slits or holes appear. A comparative study on processing farmed Atlantic salmon pre-, in- or post-rigor is presented by Mørkøre et al. [79], with the conclusion that pre-rigor filleting gives the best quality results.

Resolution of rigor mortis happens after some time, which is also depending on the stress level and exhaustion. Freezing pre-rigor gives good results when the rigor mortis phase can pass in the frozen state. That means that ATP should be used up before being thawed in order to avoid rigor mortis during thawing. Thaw rigor can be avoided by thawing the fish at low temperatures and is a bigger problem for fillets than for whole or H/G fish, see for example Stroud [104] and Einen et al. [38].

Enzymatic changes

Enzymatic or autolytic changes begin directly after the fish has died. Autolysis (self-digestion) connotes destruction of components by their own enzymes. The first autolytic changes in dead fish result in the aforementioned rigor mortis. As it is of crucial importance for fish quality, it has been presented separately above.

Further enzymatic changes cause softening and weakening of the tissue. In particular, proteolytic enzymes, such as cathepsins and calpains cause tissue softening especially in places where the fish has been handled roughly and on the belly tissue. In addition to the already mentioned autolytic changes which affected the muscle cell per se, collagenases cause deterioration of connective tissue and lead to gaping of fillets. Moreover, acids which are produced after the fish died, lead to a lower pH level compared to live fish. This has a negative influence on the water holding capacity and thus the yield for fresh fish will be lower due to increased drip loss.

Bacteriological changes

Bacteriological changes occur parallel to enzymatic changes. However, as can be seen in Figure 5.2, quality degradation induced by enzymes precedes that induced by bacteria. Bacteria can be found in live, healthy or newly-caught fish, more precisely on the skin, in the gills and in the intestines. However, the flesh is sterile, meaning that the immune system hinders bacterial growth. Furthermore, slime layers with antibacterial components prevent bacteria from growing and getting into the flesh. After the fish died, the immune system collapses, the bacteria number increases and after some time they will reach the flesh. The bacterial flora depends on the environment rather than the species.

Bacterial growth is divided into phases as described in Huss [55]. These phases mostly depend on the storage temperature and generally it holds that, the warmer the temperature, the faster the rate of growth of bacteria. The principle of bacteriological spoilage can be best described by the term *Specific Spoilage Organisms (SSO)*, as pictured by Gram and Dalgaard [44] and Huss [55]. The SSO principle relies on the fact that not all species of microflora are responsible for spoilage, but that only specific bacteria are causing off-flavors and -odors (to name but a few effects). This leads to the conclusion that using total bacterial counts may not give a good indication of spoilage.

Off-odors originate in the reduction of trimethylamine oxide (TMAO) ((CH₃)₃NO) to offensively smelling trimethylamine (TMA) (N(CH₃)₃) by oxygen-consuming bacteria. TMA is responsible for the “fishy” smell in fish of degraded freshness and quality. TMA itself constitutes so called total volatile bases (TVB), also called TVBN, where N stands for nitrogen. These TVB(N) still rise after TMA reached its maximum level due to the formation of ammonia (NH₃) and other volatile amines. Furthermore, there exist volatile sulfur components which are produced by most SSO. As both, ammonia and the volatile sulfur components are noticeable in the ppm¹ range, they play a significant role in terms of freshness.

¹parts per million

Lipid oxidation and hydrolysis

Lipid oxidation occurs when unsaturated fatty acids react with oxygen and leads to rancid tastes and smells. Moreover, it can lead to changes in texture. The same holds for lipid hydrolysis. The formation of free fatty acids (FFA) and glycerol caused by enzymatic activity, however, can lead to soapy off-flavors and is more problematic to ungutted, than to gutted fish.

5.1.3 Quality changes during freezing and frozen storage

Quality changes during freezing and frozen storage are almost exclusively caused by autolytic changes, as bacterial growth is nearly zero in these temperature regions. However, the earlier described reduction of TMAO is not only done by bacterial activity, but can also be caused by enzymes. In some species TMAO is reduced to dimethylamine (DMA) and Formaldehyde (FA), where FA is of bigger significance as it contributes to both, toughening of the muscle and reduction of the water holding capacity. The enzymes responsible for the reduction of TMAO get active when cell walls get disrupted by freezing and they are highly concentrated in the kidney. The effect of FA is even enhanced by rough handling and temperature fluctuations during storage. Therefore, one can conclude that gentle handling, gutting before freezing, fast freezing and storing at a steady temperature without fluctuations help reducing the production of FA.

Lipid oxidation and freezer burn (sublimation of frozen water) are also problems during frozen storage if the fish is not packed properly, meaning air-tight, vacuum or atmospheric packing, as described by Aberoumand and Jooyandeh [1].

During formation of external ice, the myofibrils within the muscle fibers start clumping and thus their water holding capacity becomes lower. Alizadeh et al. [2] report about changes in texture, drip loss and even color for Atlantic salmon frozen in high-pressure and air blast applications. It is known that slow freezing causes the formation of large ice crystals and, in addition, the freezing of extracellular liquid prior to intracellular liquid. Both have a negative effect on drip loss due to the fact that cell walls get disrupted and intracellular liquid is set free. Further effects of slow freezing can be lipid oxidation and protein denaturation.

Stroud [104] delivers an overview over advantages and disadvantages for freezing whole fish and fillets in, pre- and post-rigor with respect to quality factors, such as drip loss and gaping, but also on difficulties during further processing after thawing. He concludes that there is no easy and general rule and that the decision has to be made case-by-case.

5.1.4 Effect of thawing on fish quality

Thawing is the reversed freezing process and is inevitable for further processing as the fish for most applications cannot be processed in frozen state. An exception is the cutting of fish sticks out of blocks of fillets, which, after a short tempering phase, can be cut in frozen state. Thawing is not able to enhance quality losses that occurred during freezing and frozen storage, it can at best preserve the quality level. As for all stages in the processing line, lipid oxidation is a problem also in thawing.

Haugland [47] points out that drip loss can be a problem if the thawing happens too slowly.

However, if thawed too rapidly, meaning with high temperatures ($> 20\text{ }^{\circ}\text{C}$), increased denaturation of proteins can occur.

Alizadeh et al. [2] compare different freezing and thawing techniques and their impact on quality factors of Atlantic salmon, such as texture, color and drip loss. They conclude that the rate and temperature of freezing has a bigger influence on the quality attributes, like texture, color and drip loss, compared to thawing. However, this must not hold for all species.

Einen et al. [38] conclude that for slow thawing processes or thawing with low temperatures, rigor mortis during thawing is not a problem if storage temperatures are less than $-20\text{ }^{\circ}\text{C}$. ATP is degraded below this temperature and rigor mortis passes in the frozen state. The study was conducted for pre-rigor fillets of Atlantic salmon. Archer et al. [5] provide an overview over maximal thawing temperatures (between $12\text{ }^{\circ}\text{C}$ and $25\text{ }^{\circ}\text{C}$) recommended by different sources (e.g. Torry Research Station or International Institute of Refrigeration) and also state maximal product temperatures (between $0\text{ }^{\circ}\text{C}$ and $7\text{ }^{\circ}\text{C}$).

5.2 Shelf Life

In this Section several effects on the shelf life of fish are presented. It has to be mentioned that there exist trade-offs between several effects, meaning that extending shelf life with one effect can cause another effect to lose its influence on shelf life extension. This is for example the case for gutting fish, explained in Section 5.2.3, which is then more susceptible to lipid oxidation. Therefore, one has to decide from case to case, meaning that there is no general rule for shelf life extension. Like the previous Section, this Section does not have the intention of being highly detailed nor of being complete as it is only intended to provide a brief overview.

5.2.1 Effect of storage temperature

Both, enzymatic and microbiological activity depend on temperature, where latter is responsible for spoilage of most fresh fish. It holds that the lower the temperature, the lower the enzymatic and microbiological activity and thus the longer shelf life. Therefore, the storage temperature is one of the most important influences on the shelf life. However, it is not only the storage temperature that has to be regarded, but also the delay before chilling. This “initial spoilage” cannot be reversed and should be minimized by all means.

There exist several ways of storing fish in order to prevent it from spoiling rapidly. First there is chill storage which, according to Huss [55] holds for temperatures between $0\text{ }^{\circ}\text{C}$ and $25\text{ }^{\circ}\text{C}$. However, this temperature range refers to fish from tropical waters, as Huss [55] provides a broad overview. In the western world, chill storage is defined in the temperature range $0\text{ }^{\circ}\text{C}$ to $4\text{ }^{\circ}\text{C}$. This implies storage on flake ice, which is state of the art in the fishing industry in the western world.

Extended shelf life is obtained by superchilling which happens in the temperature range between $-4\text{ }^{\circ}\text{C}$ and $0\text{ }^{\circ}\text{C}$. Kaale et al. ([60], [61] and [62]) present a whole series of studies on ice-crystal development and growth during superchilling and superchilled storage of Atlantic salmon (vacuum-packed and air-packed, respectively). They conclude that faster superchilling delivers smaller ice crystals and that there are differences between the ice

crystal sizes (smaller on the outer layers, bigger in the inner layers). However, superchilling and storing at the superchilling-temperature leads to slow partial freezing in the inner layers and all its arising problems, such as extracellular prior to intracellular ice crystal formation. Kaale and Eikevik [59] conducted a study on the microstructure of red and white muscles of Atlantic Salmon during superchilling and they conclude that this technique provides interesting results for the food industry. Partial freezing can be obtained by storing fish in Refrigerated Seawater (RSW), which provides the advantages of longer shelf life due to low exposure to oxygen and reduced pressure marks. However, disadvantages can be corrosion on the vessel due to the use of salts to lower the freezing point as well as changes in texture and taste of the fish.

5.2.2 Effect of hygiene and anaerobic conditions

According to Huss [55], excessive hygiene, like aseptic handling does not have a large effect compared to the standards that are already established in the western world. Here quick and effective chilling or freezing are of bigger relevance. In other countries, however, hygiene is of far greater importance as for example bacteria grow more quickly if hygienic precautions are lacking or are not strictly imposed.

It is known that anaerobic conditions or high concentrations of CO₂ can reduce microbial growth. This is already implemented, for example in Modified Atmospheric Packing (MAP). However, MAP and storing under anaerobic conditions must not necessarily be beneficial for any species.

5.2.3 Effect of gutting

Gutting is important for shelf life extension as the intestines contain many bacteria. Moreover digestive enzymes are produced in the guts which lead to violent, post mortem autolysis. On the other hand gutting means that a larger area of the fish is exposed to air which can lead to oxidation and discoloration. In addition one has to differ between fatty and lean fish. Small and medium sized, fatty fish are not eviscerated directly after the catch due to their large numbers and the dangers of discoloration and rancidity. Lean fish, however, should be gutted after catch due to the fact that shelf life extension outweighs discoloration and rancidity in this case.

5.2.4 Effect of species, fishing ground and season

In general it holds that large fish spoil slower than small fish, flat fish keep better than round fish, lean fish keep longer than fatty fish and bony fish have a longer shelf life than cartilaginous fish. An exception from these rules is for example that salmon keeps longer than cod. Huss [55] mentions that fish from tropical waters have a longer shelf life than fish from temperate waters, when stored on ice. This can lead to the conclusion that bacteria on tropical fish grow slower when the temperature is reduced.

5.3 Actions and precautions to preserve quality and extend shelf life

After the fish has been caught it should not wait a long time before being killed. If the catch is large and it can be foreseen that the time to slaughter is long, the fish should be

kept in water. This will reduce the stress levels significantly and thus the onset of rigor mortis will happen later, which is important if the fish should be frozen after slaughtering. In addition, the killing should be done fast and thoroughly to reduce stress levels even more.

During all stages, but especially during slaughtering, the fish should be handled with care. Removing the intestines is crucial if the fish will not be subject to oxidation to a large extent. This is due to the fact that the intestines contain both enzymes and bacteria, which cause degradation, especially proteolytic, nucleotide and lipoidal breakdown. Nevertheless, for small and fatty fish, like already mentioned before, the intestines could remain in the body, as oxidation poses a bigger threat to quality degradation. Oxidation, however, is not a problem only in the slaughtering stage, but in all stages, especially during storage.

The fish should be frozen quickly as this causes smaller ice crystals and less drip loss (as described earlier). Kolbe and Kramer [65] compare freezing processes with regard to their freezing speed, whereas Nilsson [83] points out that a freezing process can be considered fast if the ice front propagates through the medium with $15 - 30 \text{ mm h}^{-1}$. However, the positive effects of fast freezing can be destroyed by temperature fluctuations during storage, as it is well-known that temperature gradients during storage cause recrystallization and growth of initially small ice-crystals. Therefore, storage at constant, sufficiently low temperatures is to prefer.

Thawing should be conducted in a way such that drip loss is minimized and the overall yield of the product is enhanced. Haugland [47] reports that the temperature band for thawing of salmon should be between $5 \text{ }^{\circ}\text{C}$ and $10 \text{ }^{\circ}\text{C}$. Too slow thawing can have the effect of high drip loss, whereas too fast thawing (meaning with temperatures $> 20 \text{ }^{\circ}\text{C}$) can lead to protein denaturation. Thus there exist trade-offs and a general rule cannot be stated; it is rather a case-by-case decision.

With me, everything turns into
mathematics.

René Descartes

Part II

Mathematical Modeling

Chapter 6

Modeling

The modeling of freezing processes has drawn the attention of researchers over the last decades. As mentioned before, freezing is an essential part of shelf life extension and therefore of high interest for industry and thus for the scientific community.

As the temperature-dynamics during freezing depend both on space and time, a good approach to model these dynamics is to use distributed parameter systems (DPS), in particular partial differential equations (PDEs). The most common PDE for thermal problems is the so called heat equation, a parabolic PDE. As available computational power grows, it is possible to simulate complex heat exchange processes modeled by PDEs. Even if finding an explicit analytical solution to the PDE is hard or impossible, simulations can provide qualitative and quantitative results. The process of freezing foodstuff is described in a whole range of publications, where Pham ([92] and [93]) give an overview over how to model heat and mass transfer in frozen foods. Delgado and Sun [34] present models for heat and mass transfer, whereas Woinet et al. [108] compare experimental and theoretical results of freezing with a simplified heat equation model. Costa et al. [31] present numerical results for a latent heat thermal energy storage system modeled by a diffusion equation. Cleland et al. [29] give experimental data for freezing and thawing of multi-dimensional objects modeled by finite element techniques.

6.1 Mathematical model for heat transfer

The equation modeling heat transfer is the one-dimensional diffusion equation, a parabolic PDE:

$$\rho(T) c(T) T_t = [\lambda(T) T_x]_x \quad (6.1)$$

subject to Dirichlet boundary conditions

$$\begin{aligned} T(t, 0) &= T_0, \\ T(t, L) &= T_L, \end{aligned} \quad (6.2)$$

where $\rho(T) > 0$ describes the density, $c(T) > 0$ denotes the specific heat capacity at constant pressure and $\lambda(T) > 0$ indicates the thermal conductivity of the medium to be frozen. Note that $\rho(T)$, $c(T)$ and $\lambda(T)$ can be regarded as thermodynamic alloys of substances

like water, fat, etc., as explained in Section 6.2. The boundary conditions T_0 and T_L are given by the refrigerant temperatures at $x = 0$ and $x = L$, respectively. Furthermore, the two subscripts $(\cdot)_t$ and $(\cdot)_x$ denote derivatives with respect to time t and the spatial variable x , respectively.

Since λ depends on T , differentiation yields

$$\lambda_x(T) = \lambda_T(T) T_x$$

and thus the diffusion equation (6.1) can be rewritten in the following form

$$\rho(T) c(T) T_t = \lambda_T(T) T_x^2 + \lambda(T) T_{xx}, \quad (6.3)$$

where two new parameters, the thermal diffusivity $k(T)$ and $\kappa(T)$ are introduced as

$$k(T) = \frac{\lambda(T)}{\rho(T) c(T)}, \quad (6.4)$$

$$\kappa(T) = \frac{\lambda_T(T)}{\rho(T) c(T)}. \quad (6.5)$$

This leads to a rewritten form of (6.3):

$$T_t = \kappa(T) T_x^2 + k(T) T_{xx}, \quad (6.6)$$

which is still subject to the boundary conditions in (6.2).

6.2 Parameters

As already mentioned before, the parameters $\rho(T)$, $c(T)$ and $\lambda(T)$ are state- and thus temperature-dependent and can be regarded as thermodynamic alloys of the basic components (water / ice, protein, fat, carbohydrates and ash), which a freezing good consists of. The overall parameters can thus be calculated by adding up the component's parameters multiplied by the respective mass fractions x_i

$$c(T) = \sum_i c_i(T) x_i,$$

$$\rho(T) = \sum_i \rho_i(T) x_i,$$

$$\lambda(T) = \sum_i \lambda_i(T) x_i.$$

The calculations of $c_i(T)$, $\rho_i(T)$ and $\lambda_i(T)$ have been introduced by Harðarson [45] and take the following form

$$c_i(T) = a_{c0,i} + a_{c1,i}(T - 273.15) + a_{c2,i}(T - 273.15)^2, \quad (6.7a)$$

$$\rho_i(T) = a_{\rho0,i} + a_{\rho1,i}(T - 273.15) + a_{\rho2,i}(T - 273.15)^2, \quad (6.7b)$$

$$\lambda_i(T) = a_{\lambda0,i} + a_{\lambda1,i}(T - 273.15) + a_{\lambda2,i}(T - 273.15)^2, \quad (6.7c)$$

where the coefficients $a_{j,i}$ are constant for a specific material / object to be frozen. Mass fractions are considered constant, except that for water. Based on Johnston et al. [58], an approximated function for the iced fraction of water is chosen to

$$x_{ice}(T) = -1.4256 e^{\frac{2}{3}(T-273.15)} + 0.9 \quad (6.8)$$

and holds for the temperature region $233 \text{ K} \leq T \leq 272 \text{ K}$. The reason for not all water being frozen, even at as low temperatures as $243 \text{ K} \approx -30^\circ \text{C}$ is that the concentration of salt and other solutes is increased in the unfrozen water, suppressing its freezing point.

Figure 6.1 shows different plots of parameter functions for Atlantic cod, which are calculated using (6.7). The values are taken from Harðarson [45]. Ice fraction denotes the fraction of ice compared to the total amount of water.

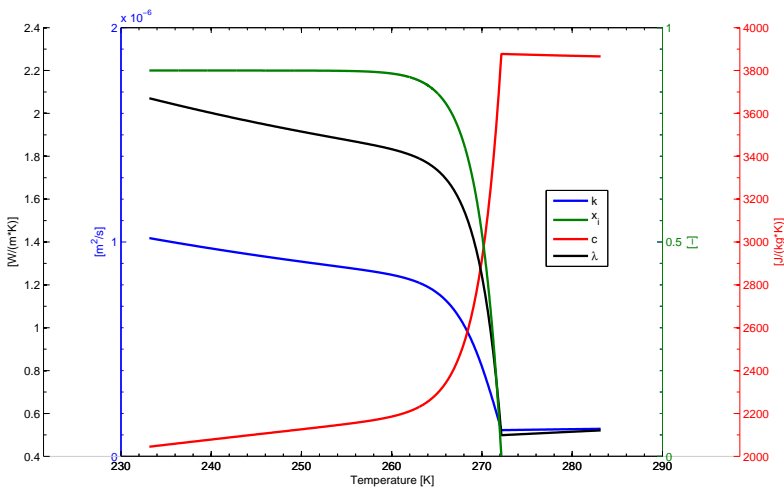


Figure 6.1: Thermal conductivity (black), thermal diffusivity (blue), ice fraction (green) and specific heat capacity (red) as functions of temperature, based on (6.7) and values from Harðarson [45]

It must be mentioned that the density $\rho(T)$ is considered constant over the whole temperature range, thus $\rho(T) = \rho = \text{const}$. This can be justified by the fact that the variations in the considered temperature range are very small compared to the other two parameters $c(T)$ and $\lambda(T)$. Therefore, it does not make sense to model the ice fraction as presented in (6.8). Although not correct from a stringent mathematical and engineering point of view, the water is therefore considered to be ice below the freezing point T_F .

The partial differential equation (6.3) does not model for phase change phenomena directly. In the particular case, *thermal arrest* caused by the presence of *latent heat of fusion* is the noticeable phenomenon of phase change. *Latent heat of fusion* is a hidden amount of energy in the water fraction, which has to be removed in order for the water molecules

to crystallize. This has the effect that when the temperature of the good to be frozen is reduced and approaches the freezing temperature, it remains constant at this temperature until the amount of *latent heat of fusion* is removed. Only after this is done, the temperature can drop below the freezing temperature - thus the term *thermal arrest*. Figure 6.2 displays a typical freezing curve for the inner domain of foodstuff.

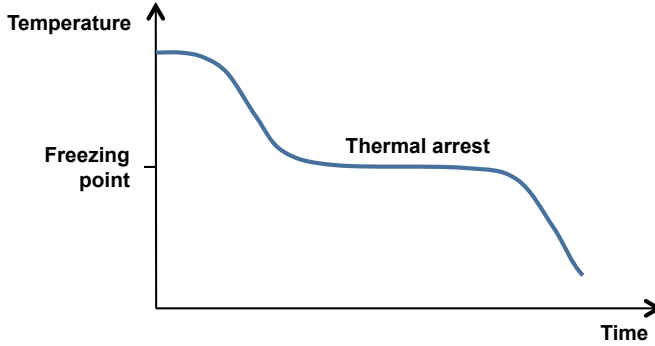


Figure 6.2: A typical freezing curve, as it can be found in e.g. Johnston et al. [58]

There are methods to adapt equations in order to model phase change behavior, as presented e.g. in Muhieddine et al. [80]. In this work an approach is chosen, which artificially adapts the parameter functions, the so called *apparent heat capacity method*. This means that the parameters presented in Figure 6.1 do not model for a process with phase change. Therefore, new parameter definitions must be introduced, which are calculated using the following equations described by Muhieddine et al. [80]

$$c(T) = \begin{cases} c_s, & T < T_F - \Delta T \\ c_l = \frac{c_l + c_s}{2} + \frac{LH}{2\Delta T}, & T_F - \Delta T \leq T \leq T_F + \Delta T \\ c_l, & T > T_F + \Delta T, \end{cases} \quad (6.9)$$

$$\lambda(T) = \begin{cases} \lambda_s, & T < T_F - \Delta T \\ \lambda_s + \frac{(\lambda_l - \lambda_s)[T - (T_F - \Delta T)]}{2\Delta T}, & T_F - \Delta T \leq T \leq T_F + \Delta T \\ \lambda_l, & T > T_F + \Delta T, \end{cases} \quad (6.10)$$

where the index l defines liquid state, the index s stands for solid state and LH denotes the amount of *latent heat of fusion*, which depends on the amount of water in the good to be frozen.

The new definitions for $c(T)$ and $\lambda(T)$ are held constant above and below a region around the freezing point $I_{\Delta T} =]T_F - \Delta T, T_F + \Delta T[$. This is shown in the sketch in Figure 6.3, which is a simplification compared to Figure 6.1. Inside $I_{\Delta T}$ the specific heat capacity $c(T)$ is overestimated, following the *apparent heat capacity method* principle. This has the effect, that the values for both, $k(T)$ (6.4) as well as $\kappa(T)$ (6.5) become very low inside $I_{\Delta T}$ and thus heat transfer is also very low in this region. The parameter ΔT has thereby the role of an open design parameter, which can be chosen by comparing simulation results to measured freezing curves. As can be seen in (6.9), choosing ΔT small has

the effect that the overestimated value of $c(T)$ is larger than for a bigger chosen ΔT . In this work, $\Delta T = 0.5$ K such that the overestimated value of $c(T)$ is roughly that of the latent heat of fusion LH . Thus, ΔT can be chosen such that simulated freezing curves fit to measured freezing curves.

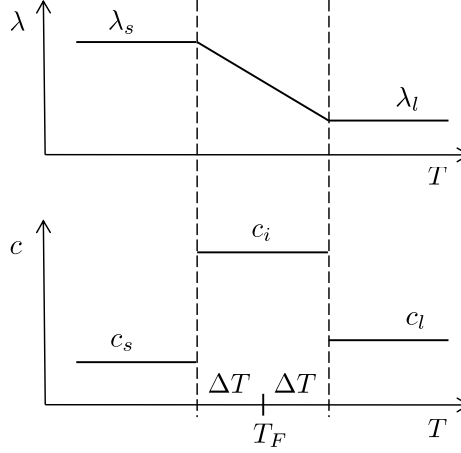


Figure 6.3: A sketch of the parameters $c(T)$ and $\lambda(T)$ as obtained by equations (6.9) and (6.10)

However, the parameter $c(T)$ is defined as a step-function when entering and leaving $I_{\Delta T}$. Now, a new definition of this parameter will be introduced, which does not rely on a step-wise change of values. This is achieved by defining additional temperature ranges δT connected to ΔT , in which the constant values c_s and c_i as well as c_i and c_l are interconnected. This leads to a quasi-continuous definition of $c(T)$ in a similar fashion like for $\lambda(T)$:

$$c(T) = \begin{cases} c_s, & T < T_F - \Delta T - \delta T \\ c_s + \frac{c_i - c_s}{\delta T} [T - (T_F - \Delta T - \delta T)], & T_F - \Delta T - \delta T \leq T < T_F - \Delta T \\ \frac{c_l + c_s}{2} + \frac{LH}{2\Delta T}, & T_F - \Delta T \leq T \leq T_F + \Delta T \\ c_i - \frac{c_i - c_l}{\delta T} [T - (T_F + \Delta T)], & T_F + \Delta T < T \leq T_F + \Delta T + \delta T \\ c_l, & T > T_F + \Delta T + \delta T. \end{cases} \quad (6.11)$$

A sketch of the parameter definitions obtained by (6.10) and (6.11) is displayed in Figure 6.4.

6.3 Simulations

The PDE (6.6) together with the boundary conditions (6.2) is simulated using a semi-discretization approach, which means that it is discretized in the spatial domain only. This leads to a set of interdependent (coupled) ordinary differential equations (ODEs), which are solved with the MATLAB[®] solver `ode45`. There are two main challenges when discretizing the PDE (6.6).

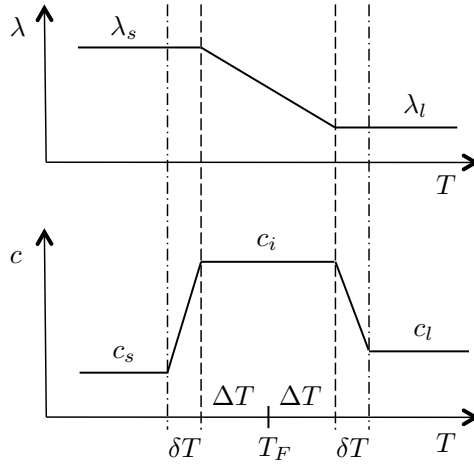


Figure 6.4: A sketch of the parameters $c(T)$ and $\lambda(T)$ as obtained by equations (6.11) and (6.10)

Firstly, the discretization schemes should not be too computationally intensive as the application studies in Part III require continual recalculation, especially the Extended Kalman Filter, whose feedback gain vector has to be updated for every new operating point. Therefore, simple schemes are preferred over more advanced schemes.

Secondly, the schemes should deliver satisfactory results also for low discretization resolutions, meaning for a small number of discretization points. The choice of low discretization resolutions is accounted for by the required low computational effort for the application studies as well.

The discretization for the term T_{xx} will be performed by a center difference approach, whereas that for the term T_x^2 will be conducted using a so called downwind discretization scheme, which, in order to compute a gradient between two cells, uses the value of the cell with index n and the value of the cell that lies ahead of this cell in the direction of the flow, here in direction of the heat flow. Schemes of this sort are especially known from problems concerning hyperbolic PDEs, see e.g. Iannelli [56]. This means that the scheme will be changed, depending on in which direction the heat is flowing. For freezing the heat will be flowing from the inner domain towards the boundaries, whereas for thawing the heat will flow from the boundaries towards the inner domain.

It must be mentioned that based on simulation results two discretization schemes get introduced, one for freezing and one for thawing, respectively. The difference between these two schemes is that for freezing the boundary conditions have been regarded in the discretized version of T_x^2 . For thawing the boundary conditions have not been incorporated into this term, but enter the equation exclusively through the discretized version of the term T_{xx} , meaning that T_x^2 in this case is passive. This was found to fit the results of the commercial MATLAB[®] solver pdepe best. Nevertheless, for test purposes the scheme for thawing was also implemented for a freezing case, however, delivered worse convergence results, meaning that the dynamics were not accurate compared to pdepe, especially for

low discretization numbers.

For the freezing case, the discretization of the two terms T_x and T_{xx} for $n = 1 \dots N$ looks as follows

$$T_x = \begin{cases} \frac{T_n - T_{n-1}}{\Delta x}, & \text{if } n < \frac{N+1}{2} \\ \frac{T_{n+1} - T_{n-1}}{2\Delta x}, & \text{if } n = \frac{N+1}{2} \\ \frac{T_{n+1} - T_n}{\Delta x}, & \text{if } n > \frac{N+1}{2}, \end{cases} \quad (6.12)$$

$$T_{xx} = \frac{T_{n+1} - 2T_n + T_{n-1}}{\Delta x^2},$$

whereas for the thawing case the discretization scheme for two terms T_x and T_{xx} for $n = 1 \dots N$ has been defined as

$$T_x = \begin{cases} \frac{T_{n+1} - T_n}{\Delta x}, & \text{if } n < \frac{N+1}{2} \\ \frac{T_{n+1} - T_{n-1}}{2\Delta x}, & \text{if } n = \frac{N+1}{2} \\ \frac{T_n - T_{n-1}}{\Delta x}, & \text{if } n > \frac{N+1}{2}, \end{cases} \quad (6.13)$$

$$T_{xx} = \frac{T_{n+1} - 2T_n + T_{n-1}}{\Delta x^2},$$

where for both cases in (6.12) and (6.13), T_0 and T_{N+1} represent ghost cells introducing the boundary conditions to the equation.

Figure 6.5 shows an exemplary plot of the solutions for the two discretization schemes for freezing and for thawing compared to the solution of the MATLAB[®] solver `pdepe` for a freezing simulation at positions $n = 1$, $n = 7$ and $n = 15$ for $N = 29$ discretization steps. As can be seen the scheme for freezing (6.12) (dashed lines) is close to the solid lines, which display the solution of the `pdepe`-solver. The dotted lines visualize the solution of the scheme for thawing (6.13).

Comparisons between the discretization schemes (6.12) as well as (6.13) and the commercial MATLAB[®] solver `pdepe` for different discretization resolutions are presented in Appendix A.

For the freezing case it can be seen that for small numbers of discretization points ($N = 5$ and $N = 9$ in Figures A.1 and A.2) the discretization scheme (6.12) captures the latent zone, whereas the MATLAB[®] solver `pdepe` has a constant temperature at other temperature levels, which explicitly differ from $T_F \pm \Delta T$. For the other cases displayed in Figures A.3, A.4 and A.5, the solution of (6.12) is delayed compared to that of `pdepe`, but represents the overall dynamics and thermal arrest in an acceptable manner with respect to applications. All in all, (6.12) shows good convergence and is even superior to the MATLAB[®] solver `pdepe` in detecting the latent zone for small discretization numbers.

In the thawing case for $N = 9$, $N = 49$ and $N = 99$ in Figures A.7, A.8 and A.9, respectively, the convergence of the scheme (6.13) is somewhat accelerated compared to that of `pdepe`. For $N = 5$ in Figure A.6 the opposite behavior can be observed. However, for $N = 199$ the solution of (6.13) converges almost perfectly to the solution obtained by `pdepe`, as can be seen in Figure A.10. All in all, (6.13), like (6.12), captures the overall

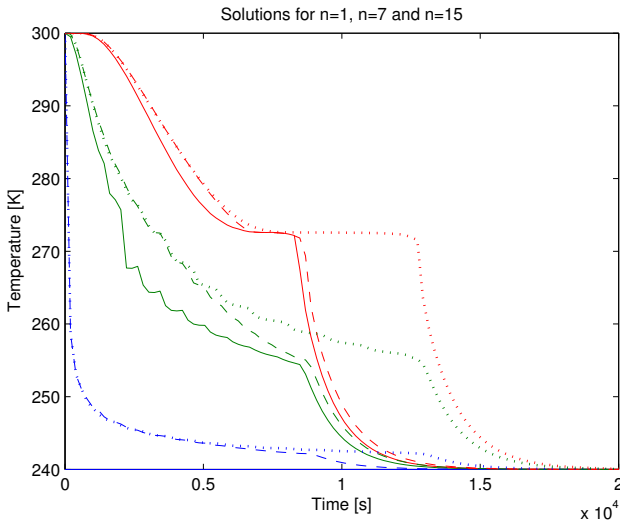


Figure 6.5: Solutions of the discretization scheme for freezing (dashed), thawing (dotted) and the MATLAB[®] solver pdepe (solid) for $N = 29$ at positions $n = 1$ (blue) $n = 7$ (green) and $n = 15$ (red)

dynamics and thermal arrest in a sufficiently well way with regards to applications, as can be seen in the aforementioned comparative plots. This holds especially for the case when $N = 9$, which is of interest for the observer design.

6.3.1 Freezing case

The freezing technology, which is the foundation for the presented simulations is plate freezer technology, as introduced in Section 3.1.1. A plate freezer is demonstrated in Figure 3.3 in particular.

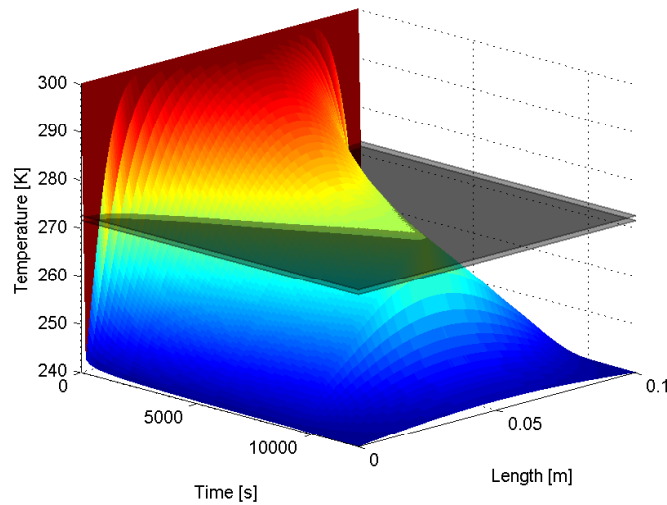
The parameters that have been chosen for the simulations can be found in Table 6.1. The space in between the freezer plates is $L = 0.1$ m, the initial temperature is evenly distributed $T_{init} = 300$ K, the boundary temperatures are alike and constant at $T_0 = T_L = 240$ K and the simulation time is $1.2 \cdot 10^4$ s. Furthermore, the mass in between the freezer plates is considered to be homogeneous with no entrapped air and perfect contact to the plates.

The plots in Figure 6.6 and Figure 6.7 illustrate that the model (6.3) delivers the desired results. In Figure 6.6 a plot of the temperature distribution along the spatial direction x over time is presented. One can clearly see the stationary behavior indicating thermal arrest, especially in the very center of the domain. The region $I_{\Delta T}$ is visualized in between the two grey planes.

In Figure 6.7 different temperatures at fixed spatial points are illustrated over time. They are to be found at discretization points $n = 1$ (boundary layer - blue), $n = 5$ (green), $n = 10$ (red), $n = 20$ (cyan), $n = 30$ (magenta), $n = 50$ (yellow), $n = 70$ (black) and $n = 100$ (center layer - blue). Also here the phenomenon of thermal arrest is perceivable especially in

T_F	272	K
ΔT	0.5	K
δT	0.1	K
LH	280000	$\text{J kg}^{-1} \text{K}^{-1}$
c_s	2200	$\text{J kg}^{-1} \text{K}^{-1}$
c_i	283000	$\text{J kg}^{-1} \text{K}^{-1}$
c_l	3800	$\text{J kg}^{-1} \text{K}^{-1}$
ρ	950	kg m^{-3}
λ_s	1.8	$\text{W m}^{-1} \text{K}^{-1}$
λ_l	0.5	$\text{W m}^{-1} \text{K}^{-1}$

Table 6.1: Simulation parameters for the illustrative examples

Figure 6.6: Plot of the temperature distribution along the spatial direction x over time for the freezing case

the very center of the domain. The discretization points are illustrated in Figure 6.8.

6.3.2 Thawing case

The corresponding thawing method for the illustrative simulation example, which is presented here, is contact thawing, as already introduced in Section 4.1.4.

For the simulations, the same parameters as already introduced for the freezing case in Table 6.1 are used. Again, the initial temperature is assumed to be evenly distributed, but now at $T_{init} = 240$ K, whereas the boundary temperatures are alike and held constant at $T_0 = T_L = 300$ K. The simulation time is now five times longer, namely $6 \cdot 10^4$ s due to the

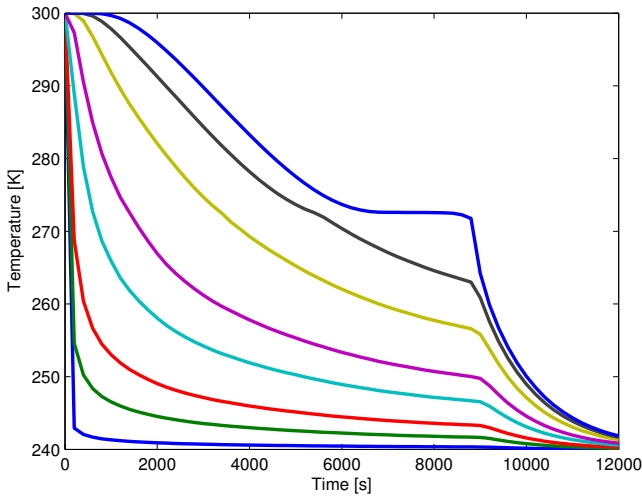


Figure 6.7: Plot of different temperatures at fixed spatial points over time for the freezing case

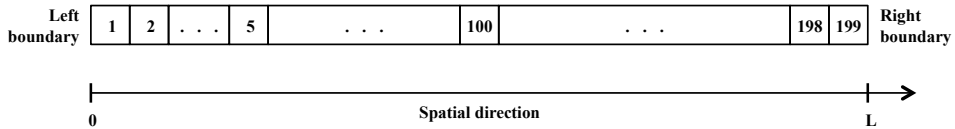


Figure 6.8: Illustration of the discretization points along the spatial variable for $N = 199$ cells

fact that thawing takes longer than freezing.

In Figure 6.9 a plot with the same properties as in Figure 6.6 is presented. Figure 6.10 presents the temperatures at the same fixed spatial points as in Figure 6.7. By comparing Figures 6.9 and 6.10 with Figures 6.6 and 6.7 it can be noticed that it takes excessively longer to reach the desired temperature imposed by the boundary conditions. The reason for this is the lower thermal diffusivity of liquid water compared to that of ice. During freezing, the initially built ice-layer on the outer layers of the object has an accelerating effect due to the larger thermal diffusivity compared to that of liquid water. During thawing, however, the opposite effect can be seen, namely that the initially built layer of liquid water at the boundary acts as an insulation due to the lower thermal diffusivity compared to that of ice.

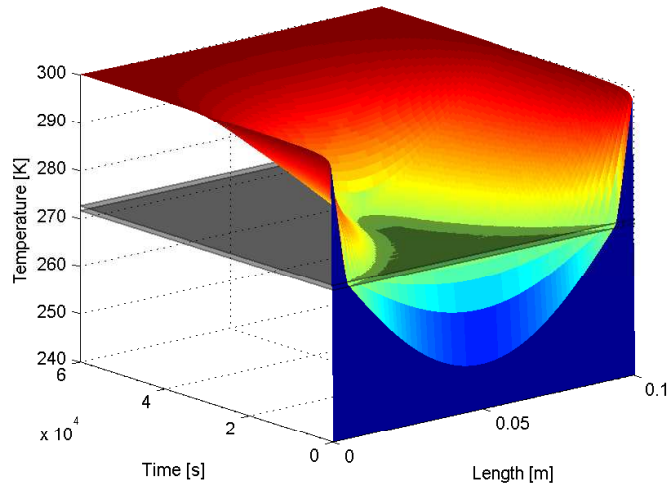


Figure 6.9: Plot of the temperature distribution along the spatial direction x over time for the thawing case

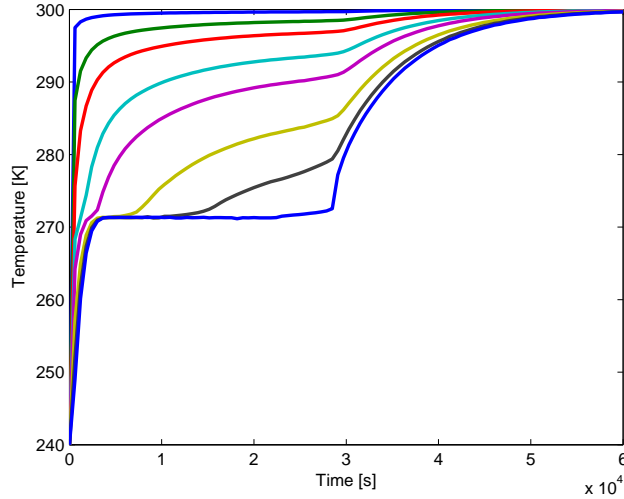


Figure 6.10: Plot of different temperatures at fixed spatial points over time for the thawing case

6.4 Comment on the chosen boundary conditions

The boundary conditions, which are chosen for the freezing and thawing cases are of Dirichlet kind as defined in (6.2). It has to be mentioned that there exist other relevant boundary conditions for these cases, namely Neumann boundary conditions, which are defined as a heat flow through the boundary. Often these boundary conditions are used to describe insulation by setting the heat flow to zero. Sometimes also a constant heat flow through the boundary is imposed to a problem. These two approaches are known to be boundary conditions of the second kind as introduced in Cleland and Earle [25, Equation 3]. The latter, however, is not practical for the application of freezing and thawing of foodstuff as the heat flow through the boundary cannot be a constant value: The driving force for heat flow is the temperature difference at the boundaries, meaning the difference between the temperature of the freezing / thawing medium and the boundary of the food to be frozen / thawed. This is known to be a boundary condition of the third kind, see e.g. Cleland and Earle [25, Equation 4].

A formal definition of the Neumann boundary conditions for the present problem is as follows

$$\nabla T \cdot \mathbf{n} = \frac{1}{K} \dot{q},$$

where ∇ is the differential operator, \mathbf{n} defines the normal vector with respect to the boundary, \cdot is the inner product, K is a factor (which can be a constant, but also a function of e.g. time) and \dot{q} is a heat flow. In the one-dimensional case the Neumann boundary conditions have the following definition

$$\frac{\partial T}{\partial x} = \frac{1}{K} \dot{q}.$$

A heat flow \dot{q} can be defined by Fourier's law similar to the definition of the Neumann boundary condition

$$\dot{q} = \lambda A T_x,$$

where λ is the material's thermal conductivity, A is a cross-sectional area and T_x is a temperature gradient; but also in another form mostly used for convective boundary conditions

$$\dot{q} = h A \Delta T,$$

where h is the heat transfer coefficient (HTC), A is a cross-sectional area and ΔT is a temperature difference. Combining the definition of the Neumann boundary condition with $\dot{q} = h A \Delta T$ leads to the conclusion that

$$K = h A \Delta x.$$

Understanding the physics of the problem, both types of boundary conditions (BCs), those of Dirichlet and those of Neumann type, can, in this special case and for the present discretization schemes, be transformed into one another. The Dirichlet BCs define the refrigerant temperature at ghost cells just outside the spatial domain. For the definition of the Neumann BCs these ghost cells must be defined as well. The reason for this is that the driving force for the heat flow is a temperature gradient, here specifically that between the freezing / thawing medium (temperature at the ghost cell) and the boundary cell of the

spatial domain. Therefore, the two boundary conditions are implementation-wise (meaning for the used discretization methods) the same and might only differ in a scaling factor.

Looking at the center difference formulation at the left boundary one receives

$$\frac{k(T_1)}{\Delta x^2} (T_2 - 2T_1 + T_0)$$

with Neumann BCs

$$\frac{\partial T}{\partial x} = \frac{T_1 - T_0}{\Delta x} = \frac{1}{K} \dot{q}.$$

Thus,

$$\frac{k(T_1)}{\Delta x^2} (T_2 - T_1 - \frac{1}{K} \dot{q} \Delta x),$$

where putting in the convective heat flow leads to

$$\frac{k(T_1)}{\Delta x^2} (T_2 - T_1 - \frac{hA\Delta x}{K} (T_1 - T_0)),$$

which, for $hA\Delta x = K$, represents the initial center difference formulation. This closes the argumentation that using Dirichlet BCs in this special case is valid and might only differ in a factor compared to the Neumann BCs.

It must be mentioned that the Dirichlet boundary conditions can be interpreted as Neumann boundary conditions with an infinite HTC. However, in the discretization schemes used in this work, the implementation of the boundary condition is slightly different, namely of Dirichlet-like kind. This can especially be seen in Figures A.1–A.5 and A.6–A.10, where the solution at the boundaries of the commercial solver `pdepe` instantly jumps to the boundary condition (infinite gradient). The solutions at the boundaries using the discretization schemes (6.12) and (6.13), however, have a finite slope and approach the boundary conditions asymptotically. This gradient and therefore the heat flux through the boundaries is furthermore inversely proportional to the spatial resolution Δx .

In two-phase flows the HTC of the refrigerant is highly dependent on the local conditions. It will rise together with the vapor quality (i.e. the mass fraction of the vapor phase) due to the increase in flow velocity. In addition, with an increase of the vapor quality, usually the nucleate boiling contribution decreases and the two-phase evaporation increases, what in sum leads to an increased HTC. Furthermore, the nucleate boiling contribution to the HTC is a strong function of the local heat flux, which again is a function of the HTC.

Therefore, Dirichlet boundary conditions are chosen for the models for freezing and thawing. Further reasons for this approach are to be found in the following assumptions:

1. The pressure loss in the evaporator is small and thus the evaporation temperature over the whole evaporator length is assumed constant
2. The overall thermal resistance (i.e. the inverse of the HTC) is constant over the length of the evaporator
3. The freezing medium is only partially evaporated, meaning that a good fraction of the mass flow is still liquid and thus the medium is far away from the dry-out point (i.e. fully evaporated)

Chapter 7

Transformations

This Chapter intends to provide insights concerning similarities between the model introduced in Chapter 6 and other parabolic PDEs, in particular Burgers' equation and its potential form.

7.1 Similarities to Burgers' and potential Burgers' equation

The viscous Burgers' equation,

$$u_t(t, x) = \varepsilon u_{xx}(t, x) + u(t, x)u_x(t, x) \quad (7.1)$$

with subscript referring to partial derivative with respect to the argument, e.g., $u_t(t, x) \equiv \partial u(t, x)/\partial t$, is commonly used to describe turbulent flows and closely related to the Navier-Stokes equations. The Burgers' equation is one of the very few nonlinear partial differential equations that can be solved exactly (for a restricted set of initial functions only, and for a constant parameter ε). In the context of gas dynamics, Hopf [53] and Cole [30] independently showed that this equation can be transformed into the linear diffusion equation and solved exactly for arbitrary initial conditions (but again for constant ε). The study of the general properties of the Burgers' equation has motivated considerable attention due to its applications in fields as diverse as number theory, gas dynamics (Korshunova and Rozanova [66]), heat conduction (Hills [51]), elasticity (Sugimoto and Kakutani [105]) and in special cases even transport phenomena (Hasan et al. [46]), etc.

The stability properties of the Burgers' equation with constant and time-varying parameters have been studied previously. Krstić [68] presents stability results for both viscous and inviscid Burgers' equation by defining control laws satisfying a Lyapunov analysis in the L^2 -norm. Balogh and Krstić [20] introduce H^1 -stability for the Burgers' equation with nonlinear boundary feedback, whereas Krstić et al. [71] show results in nonlinear stabilization of shock-like unstable equilibria in the viscous Burgers' equation. Moreover, Krstić et al. [72] go a step further and present results for the same problem in trajectory generation, tracking and observer design, whereas Liu and Krstić [76] attend the topic of adaptive control for a Burgers' equation with unknown viscosity.

However, as explained in Chapter 6, the model considered in this work represents freezing and thawing cases with phase transition. This change in phase is the reason for introducing

state-dependent parameters due to the fact that the physical properties of the material to be frozen change significantly around and after crossing the freezing point.

This means that the parameter ε depends on the state variable itself, namely $\varepsilon = \varepsilon(u(t, x))$, which is a more challenging case than the situations outlined above. This problem was initially introduced in Backi et al. [14] for an application that describes the freezing of fish in a vertical plate freezer. Inspired by this problem, the present work, among other things, attempts to investigate the stability properties of the Burgers' equation with specific functional forms of ε and its derivatives, see Chapter 8.

First of all, let us introduce the diffusion equation for a constant parameter ε . Let $u = u(t, x)$ be a function of two variables, time $t \in \mathbb{R}_+$ and space x . For simplicity and without loss of generality, only one spatial dimension $x \in [0, L] \subset \mathbb{R}$ is considered. The function u must satisfy a partial differential equation of the form

$$\begin{aligned} u_t &= [\varepsilon u_x]_x, \\ u(0, x) &= U(x), \end{aligned} \tag{7.2}$$

where ε is a parameter and $U(x)$ denotes an initial condition.

For the problem to be well posed, u must also satisfy various relevant boundary conditions. With constant ε , the diffusion equation (7.2) can be rewritten as the linear heat equation

$$u_t = \varepsilon u_{xx}. \tag{7.3}$$

The stability properties of (7.2) and thus of (7.3) have been studied extensively in many publications, for example by Krstić and Smyshlyaev [69]. In particular, it is known that the heat equation is stable in the sense that $u(t, x) \rightarrow \bar{u}(x)$ for any $\varepsilon > 0$, where $\bar{u}(x)$ describes the steady-state solution.

If the parameter ε depends on the spatial variable x , i.e. $\varepsilon = \varepsilon(x)$, a slightly more complicated expression for (7.2) is obtained

$$u_t = \varepsilon_x u_x + \varepsilon u_{xx}. \tag{7.4}$$

This may be handled by means of so-called *gauge transformations*, which eliminate the spatial dependency of $\varepsilon(x)$, see e.g. Smyshlyaev and Krstić [102]. In addition, the spatial derivative of the parameter, ε_x , vanishes after transforming the system; hence system (7.4) can be transformed into system (7.3) for which the stability properties mentioned above are known to hold.

Similar techniques can be applied to the previously introduced Burgers' equation (7.1). Heredero et al. [49] show that the standard Burgers' equation with $\varepsilon = 1$,

$$u_t = u_{xx} + 2uu_x \tag{7.5}$$

can be transformed into the potential Burgers' equation by using the transformation $u = v_x$, resulting in

$$v_{tx} = v_{xxx} + 2v_x v_{xx}.$$

After integrating this expression one obtains

$$v_t = v_{xx} + v_x^2,$$

which represents the potential form of the Burgers' equation. After introducing the transformation $w = e^v$ the potential Burgers' equation then boils down to the linear heat equation, as outlined above.

Finally, if the coefficient ε is a known function of time, Burgers' equation becomes

$$u_t = \varepsilon(t)u_{xx} + uu_x. \quad (7.6)$$

For this case, it was shown by Sophocleous [103] that a *time*-dependent gauge transformation exists, which transforms the nonlinear PDE into a linear one.

7.2 Motivation for stability analysis

Differentiating (6.6) with respect to x yields

$$\begin{aligned} T_{tx} &= [\kappa T_x^2 + k T_{xx}]_x \\ &= \kappa_T T_x^3 + 2\kappa T_x T_{xx} + k_T T_x T_{xx} + k T_{xxx} \\ &= \kappa_T T_x^3 + 2T_x T_{xx} \left(\kappa + \frac{k_T}{2} \right) + k T_{xxx}. \end{aligned} \quad (7.7)$$

After introducing a change of variable $\varphi = T_x$ the following equation is obtained:

$$\varphi_t = \kappa_T \varphi^3 + 2\varphi \varphi_x \left(\kappa + \frac{k_T}{2} \right) + k \varphi_{xx} \quad (7.8)$$

which, apart from the additional term $\kappa_T \varphi^3$, has similarities to the standard Burgers' equation in (7.5).

As mentioned, the stability properties of the Burgers' equation have been subject to many publications. However, these results are not applicable to (7.8) due to the fact that an additional term φ^3 is present and also that the effect of the non-constant, state-dependent parameters κ_T , κ , k_T and k on the stability properties of the overall PDE are unknown. Thus, the earlier described transformations from Burgers' equation to linear heat equation cannot be applied, making a stability investigation necessary. Furthermore, the system considered in Backi et al. [14] is quite limited in actuation, meaning that only limited Dirichlet or Neumann boundary control can be applied. The main contribution of the upcoming Chapter 8 is thus to generalize Backi et al. [14] and show that under certain assumptions, the version of the (potential) Burgers' equation that is considered in this work converges to a stationary solution determined by (constant) boundary conditions.

Particularly it must be pointed to Kreiss and Kreiss [67], who treat stability analysis for the Burgers' equation in terms of convergence to steady state solutions and to Argomedeo et al. [6], who attend the topic of input-to-state stability of a time-varying non-homogeneous diffusion equation.

Chapter 8

Stability

In this Chapter the stability properties of the model introduced in Chapter 6 are investigated. It is known that the processes of freezing and thawing are indeed stable. Laws of thermodynamics, specifically the second law, dictate that heat always flows in the direction from the warmer to the cooler medium, until both temperatures are in an equilibrium. In a freezing case this means that the heat in the warmer freezing good will always flow to the colder refrigerant in the evaporator (here the plate freezer walls) and cause it to evaporate. Thus the boundary of the freezing object cools down, causing a temperature gradient in the object itself. For thawing the opposite is the case, namely that heat flows from the thawer walls into the frozen good. Therefore, a model describing these phenomena must be stable in order to describe these processes correctly.

For the stability investigation the definitions of the parameter functions $c(T)$ and $\lambda(T)$ as shown in Figure 8.1 are introduced. Note that the transitions between c_s and c_i as well as between c_i and c_l in the regions δT are modeled by functions in the shape $c(T) = \frac{o_1}{o_2+T}$, respectively, where o_1 and o_2 are constants.

8.1 Steady state solution

Before conducting the stability analysis of the model (6.6), it is necessary to derive an explicit formula for its steady-state solution. This is done by setting $T_t = 0$, which results in

$$\kappa(T) T_x^2 + k(T) T_{xx} = 0. \quad (8.1)$$

For general $\kappa(T)$ and $k(T)$ the solution to the nonlinear ODE (8.1) can be found by evaluating the following expression:

$$C_1 x + C_2 = \int^{T(x)} \exp\left(\int \frac{\kappa(\zeta)}{k(\zeta)} d\zeta\right) d\zeta. \quad (8.2)$$

Now from physical considerations it follows that the steady state solution must be within the interval $[T_0, T_L]$ (or $[T_L, T_0]$ depending on which of T_0 and T_L is smaller) for all values of the spatial coordinate. Also, inspired by the qualitative sketch shown in Figure 8.1, it will

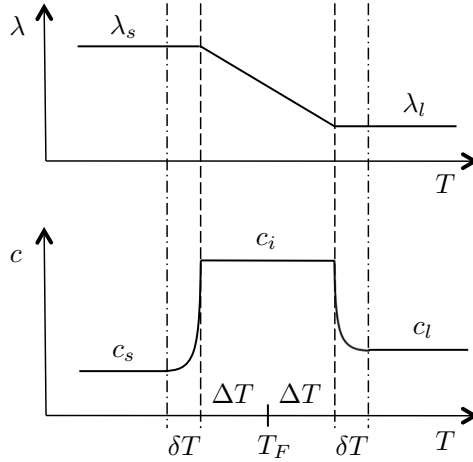


Figure 8.1: The parameter functions $c(T)$ and $\lambda(T)$ as defined for the stability investigation

be stated henceforth that $\kappa(T) = 0$ outside $I_{\Delta T}$. Based on this and due to the assumption that both boundary conditions, T_0 and T_L , are strictly below $T_F - \Delta T$, it can be concluded that $\kappa(T)$ is zero along the steady state solution. From (8.1) it then follows that the steady-state solution can be described as the solution of the ODE

$$k(T) T_{xx} = 0, \quad (8.3)$$

which, since $k(T) > 0$ for all T , has the solution

$$T(x) = C_1 x + C_2. \quad (8.4)$$

The coefficients can be found by applying the boundary conditions (6.2) to (8.4) leading to $C_2 = T_0$ and $C_1 = \frac{1}{L}(T_L - T_0)$ and thus

$$T(x) = \frac{1}{L}(T_L - T_0)x + T_0, \quad (8.5)$$

which represents a straight line between the two boundary values T_0 and T_L .

Now an investigation of the steady state solution follows for the case when both boundary temperatures are inside $I_{\Delta T}$. Thus, the steady state solution for the case when $\kappa(T) \neq 0$ is derived. From (6.4) and (6.5) it can be seen that both, $\rho(T)$ and $c(T)$ get cancelled out in (8.1). Therefore it is enough to represent the remaining parameter $\lambda(T)$ as a linear function, compare to Figure 8.1, as $\lambda(T) = -p T + q$ and $\lambda_T(T) = -p$ with $p > 0$ and $q > 0$ leading to the steady state expression

$$-p T_x^2 + (-p T + q) T_{xx} = 0. \quad (8.6)$$

This yields the solutions

$$T(x) = \frac{1}{p} \left(q \pm \sqrt{q^2 + 2p(C_1 x + C_2)} \right), \quad (8.7)$$

where, again, the coefficients C_1 and C_2 can be found using the boundary conditions (6.2), and thus

$$\begin{aligned} C_2 &= \frac{1}{2} T_0^2 p - T_0 q, \\ C_1 &= \frac{1}{2L} \left(T_L^2 p - 2 T_L q - T_0^2 p + 2 T_0 q \right). \end{aligned} \quad (8.8)$$

Note that only one solution in (8.7) provides the correct coefficient values, depending on if the respective boundary condition T_0 or T_L is bigger or smaller than $\frac{q}{p}$.

Steady state simulation examples

In order to calculate the steady state solutions numerically, $\lambda(T)$ and $\lambda_T(T)$ inside $I_{\Delta T}$ are taken from the actual freezing case presented in Chapter 6. The parameter $\lambda(T)$ inside $I_{\Delta T}$ is therefore represented by the linear function

$$\lambda(T) = -1.3 T + 354.75. \quad (8.9)$$

Hence, $\frac{q}{p} = \frac{354.75}{1.3} \approx 272.9$. Furthermore, the pair of BCs is defined to be located inside $I_{\Delta T}$ as $T_0 = 271.7$ K and $T_L = 272.3$ K. It holds that $T_0 < \frac{q}{p}$ and $T_L < \frac{q}{p}$. In addition, $L = 0.1$ m, $T_F = 272$ K and $\Delta T = 0.5$ K.

The numerical simulation indicating the steady state solution can be seen in Figure 8.2. The plot on the top left position shows the simulated steady state solution of the MATLAB® solver pdepe for 99 discretization steps after 10^7 s. On the top right plot the analytical steady state solution calculated with (8.7) is presented, whereas the error between simulated and analytical solution is displayed in the bottom left plot. The error is very small with magnitudes in the range of 10^{-10} . On the bottom right the state evolution at different time instances is shown. The initial condition for the simulation is 300 K, equally distributed along the spatial domain.

For the freezing and thawing applications, there is no need to have the boundary conditions inside $I_{\Delta T}$. Thus the result presented in Figure 8.2 is of no significance for the subsequent stability analysis. Hence, the steady state solution can be defined to have the shape of a straight line between the two BCs as defined in (8.5).

The PDE (6.6) is specific for freezing and thawing applications. As showing stability for this system is intended, a more general view on the problem is chosen in the sequel. To indicate this, the state variable is changed from T to u in the upcoming two Sections 8.2 and 8.3.

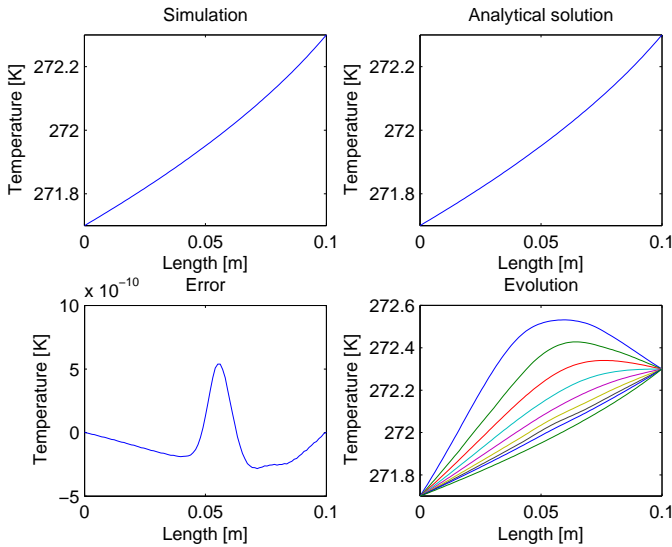


Figure 8.2: Simulated (top left) and analytical (top right) steady state solutions, error between simulated and analytical steady state solution (bottom left) and simulated state evolution (bottom right)

8.2 Stability for asymmetric boundary conditions $u_0 \neq u_L$

First, an investigation of the stability properties of (6.6) for asymmetric boundary conditions as defined in (6.2) will be conducted. This defines a more general case than symmetric boundary conditions.

In general, the function u can be expressed as the sum of a transient part $w(t, x)$ and a stationary part $\bar{u}(x)$, i.e. $u(t, x) = w(t, x) + \bar{u}(x)$. Here, $\bar{u}(x)$ is a function of x due to the asymmetric boundary conditions in the form $\bar{u}(x) = Sx + J$, where S and J are constants. Furthermore, the spatial coordinate is normalized to belong to $[0, 1]$. With these conventions, the following equivalent form of (6.6) is studied:

$$\begin{aligned} w_t &= \frac{\kappa}{L^2} (w_x + S)^2 + \frac{k}{L^2} w_{xx} \\ &= \frac{\kappa}{L^2} (w_x^2 + S^2 + 2Sw_x) + \frac{k}{L^2} w_{xx} \end{aligned} \quad (8.10a)$$

with boundary conditions

$$w(t, 0) = w(t, 1) = 0. \quad (8.10b)$$

Remark 8.1. It must be pointed out that the focus lies on continuously differentiable solutions with finite H^1 -norm only. From a rigorous mathematical point of view, the question of existence of such solutions is a crucial aspect, however, this will not be addressed here. Be advised that Prüss et al. [95] provide a treatment of this topic for the (related) Stefan

problem. Nevertheless, the application studies indicate that at least some solutions of this form exist.

With this remark, the following Lemma is stated.

Lemma 8.1. *Let w satisfy (8.10). Suppose that there exists constants $\beta > \alpha > 0$ such that $\alpha \leq k \leq \beta$. If*

$$(\kappa + k_u)^2 < 2(\kappa k_u - k_{uu}k + k_u^2) \quad (8.11a)$$

$$k_{uu}k < k_u^2 + \kappa k_u \quad (8.11b)$$

$$w > 0 \quad \forall u \in I_{\Delta u} \quad (8.11c)$$

$$\kappa k_u \geq 0 \quad (8.11d)$$

$$k_{uu} \leq 0 \quad \forall u \in I_{\Delta u} \quad (8.11e)$$

$$\kappa < 0 \quad \forall u \in I_{\Delta u} \quad (8.11f)$$

$$\kappa \equiv 0 \quad \forall u \notin I_{\Delta u} \quad (8.11g)$$

then the origin is globally asymptotically stable (with respect to $\|\cdot\|$). In particular, $\|w(t)\| \rightarrow 0$ as $t \rightarrow \infty$.

The proof of Lemma 8.1 can be found in Appendix B. The details of the assumptions in Lemma 8.1 will be discussed in Remark 8.2.

Now, Lemma 8.1 will be extended to the H^1 -case.

Lemma 8.2. *Suppose that the assumptions of Lemma 8.1 hold true. If moreover*

$$\kappa_u \leq 0 \quad (8.12a)$$

$$w_x(t, 1)w_{xx}(t, 1) - w_x(t, 0)w_{xx}(t, 0) \leq 0 \quad (8.12b)$$

$$\kappa S\left(w_x^2(t, 1) - w_x^2(t, 0)\right) \leq 0 \quad (8.12c)$$

$$\kappa\left(w_x^3(t, 1) - w_x^3(t, 0)\right) \leq 0 \quad (8.12d)$$

then the origin is globally asymptotically stable (with respect to $\|\cdot\|_{H^1}$). In particular, $\|w(t)\|_{H^1} \rightarrow 0$ as $t \rightarrow \infty$.

The proof of Lemma 8.2 can be found in Appendix C. The details of the assumptions in Lemma 8.2 will be discussed in Remark 8.2.

Together with Lemma 2.2 (*Agmon's Inequality*), Lemma 8.2 now immediately implies the following main result.

Theorem 8.3. *Let w satisfy (8.10). Suppose that the assumptions of Lemma 8.2 hold true. Then $w(t, x) \rightarrow 0$ as $t \rightarrow \infty$, hence $u(t, x) \rightarrow \bar{u}(x)$ as $t \rightarrow \infty$.*

Remark 8.2. The assumptions in Lemma 8.1 and Lemma 8.2 impose limitations to the parameter functions $k(u)$ and $\kappa(u)$ and their respective derivatives.

In Lemma 8.1 assumptions (8.11d)–(8.11g) hold true due to definition of the parameter functions in Figure 8.1. Assumption (8.11c) holds true due to the fact that the boundary conditions are chosen constant below the region $I_{\Delta u}$ and the definition of w in the beginning of this subsection. Assumptions (8.11a)–(8.11b) have to be imposed to the problem and hold actually true, also due to the definition of the parameter functions.

In Lemma (8.2) assumption (8.12a) holds true, due to the definition of the parameter functions, again see Figure 8.1. Assumptions (8.12b)–(8.12d) define conditions for the temperature change with respect to the spatial domain and its derivative, both evaluated at the respective boundaries.

8.3 Symmetric boundary conditions $u_0 = u_L$

In the case of symmetric boundary conditions, which represents a special case of the one with asymmetric boundary conditions, one can use the same fundamentals of the previously conducted proofs. Note that the boundary condition in (8.10b) will stay the same, but the boundary condition in (6.2) can be reformulated as

$$u(t, 0) = u(t, L) = u_B$$

in terms of u as state variable.

In fact, to prove stability for symmetric boundary conditions, the same Lyapunov functions can be used and thus almost identical versions of Lemma 8.1 and Lemma 8.2 can be stated, but with a reduced amount of assumptions on the parameter functions.

In Lemma 8.1 particularly, assumptions (8.11c)–(8.11g) can be removed. This is due to the fact that all terms including S disappear, as $S = 0$. This is valid due to the fact that the steady state solution is now represented by a straight line between the two boundary values

$$u(x) = u_B = \text{const.}$$

That this is actually true can be shown using the results presented in Section 8.1 and solving them for equal boundary values. Therefore, (B.6) in Appendix B can be rewritten in a reduced form

$$\dot{V} = \frac{1}{L^2} \int_0^1 \frac{1}{k} A w_x^2 dx$$

with A defined in (B.7a) and thus only (8.11a)–(8.11b) are required to hold in order for the origin to be globally asymptotically stable (with respect to $\|\cdot\|$) and $\|w(t)\| \rightarrow 0$ as $t \rightarrow \infty$.

For (C.9) in Appendix C the terms containing S can be eliminated due to the same argument as used above and thus the equation is reduced to

$$\dot{V}_1 = \frac{1}{L^2} \int_0^1 \left(\frac{\kappa_u}{3} w_x^4 - k w_{xx}^2 \right) dx + \frac{1}{L^2} \left[k w_x w_{xx} + \frac{2\kappa}{3} w_x^3 \right]_0^1.$$

It can be directly seen that now only assumptions (8.12a), (8.12b) and (8.12d) have to be fulfilled in order for the origin to be globally asymptotically stable (with respect to $\|\cdot\|_{H^1}$) and $\|w(t)\|_{H^1} \rightarrow 0$ as $t \rightarrow \infty$.

The argumentation in Theorem 8.3 is untouched by these changes, as the reduced versions of both, Lemma 8.1 and Lemma 8.2, hold for the case with symmetric boundary conditions. However, it must be pointed out that $w(t,x) \rightarrow 0$ as $t \rightarrow \infty$, but now $u(t,x) \rightarrow u_B$ as $t \rightarrow \infty$, meaning that $u(t,x)$ now tends to the steady state value $u(x) = u_B$, which is constant over the whole spatial domain.

8.4 Simulation examples

Exemplary for the two stability investigations for asymmetric and symmetric boundary conditions, respectively, only the first mentioned case is presented as a simulation example. The boundary conditions are chosen to $T_0 = 240$ K and $T_0 = 260$ K, whereas the initial condition is defined to be a noisy function consisting of a sum of sinusoidal functions of different frequencies around $T = 280$ K plus added white Gaussian noise as demonstrated in Figure 8.3.

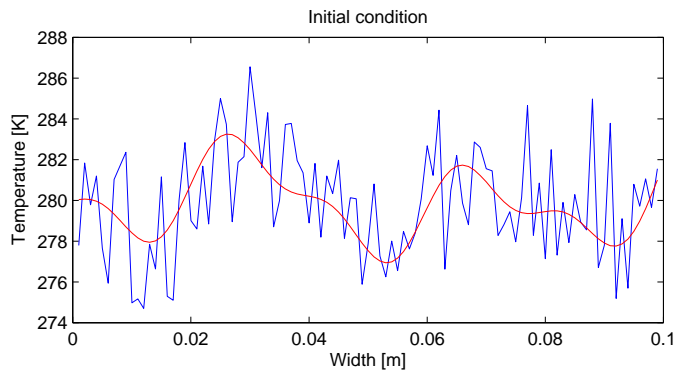


Figure 8.3: Noisy initial condition for the simulation

The red line illustrates the sinusoidal function whereas the blue line represents the overall noisy IC. The simulations were accomplished in the same fashion like in Section 6.3.1 using the ode45-solver in MATLAB[®]. The simulation parameters are shown in Table 6.1

In Figure 8.4, the simulation results are presented in a 3-dimensional plot showing temperature evolution over space and time. As can be seen the temperature converges towards the steady state solution, which is a straight line between the two boundary values $T_0 = 240$ K and $T_0 = 260$ K, according to Section 8.1.

Figure 8.5 displays the first 50 s of Figure 8.4 in order to illustrate the damping character of the model. It can be seen that the high-frequency white Gaussian noise is flattened out quite quickly, whereas the low-frequency sinusoidal function remains present longer.

The simulation results emphasize the stability results established above. It is obvious that

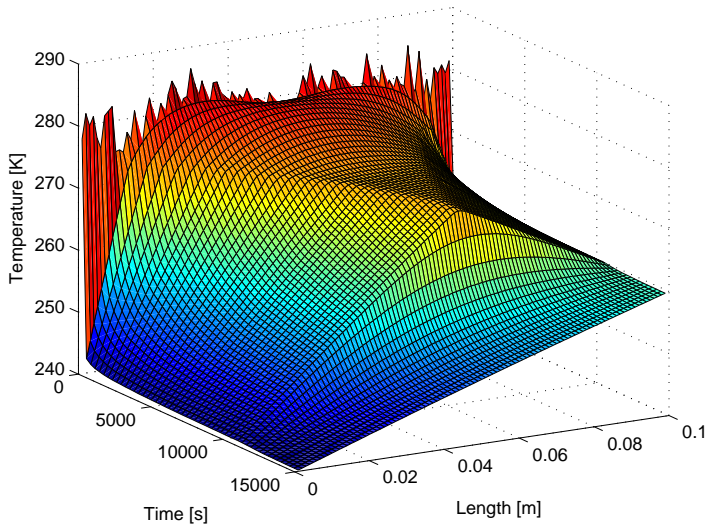


Figure 8.4: Temperature evolution over space and time

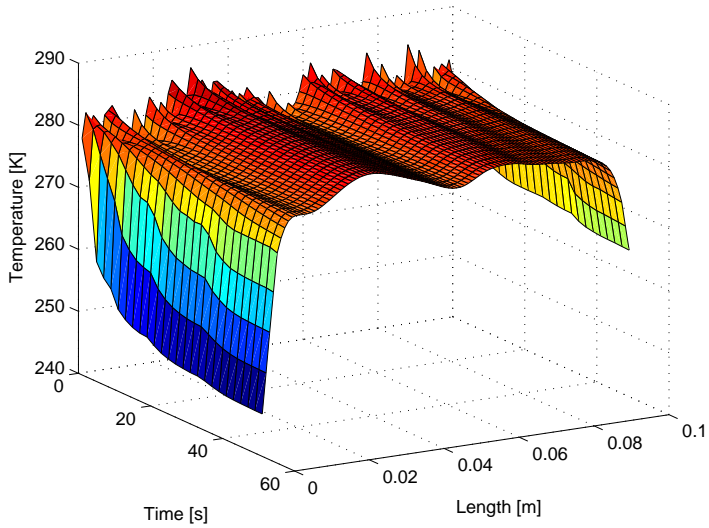


Figure 8.5: Temperature evolution over space and time - the first 50 s

the model (6.6) in fact holds for a freezing case, even in the presence of the nonlinear term $\kappa(T)T_x^2$.

Nothing burns like the cold.

George R.R. Martin

Part III

Freezing and Thawing Applications

Chapter 9

Problem formulation and introduction to estimation

The overall aim for the applications presented in the upcoming Chapters is to estimate the inner-domain temperatures inside a block of foodstuff and thus to monitor the processes of freezing in plate freezers as well as thawing in contact thawing devices.

9.1 Problem formulation

It is of significant importance for the whole production chain to predict the freezing and thawing times of foodstuff. This holds especially for batch processes, where one batch is forced to wait until the other batch has left the freezer / thawer. Overestimation of freezing and thawing times may therefore lead to unnecessary waiting times with arising consequences such as quality degradation. Underestimation of freezing times, e.g., can lead to too high final temperatures with consequences such as higher load of the storage freezer, which then has to compensate for the difference in temperature; a storage freezer should run constantly with small variations in temperature. Underestimation of thawing times, however, can imply difficulties when processing the fish further, e.g. when filleting.

Freezing time denotes the time it takes to freeze the ‘worst point’ (the point hardest to affect – depending on geometry and freezing method) down to the safe temperature (mostly $-18\text{ }^{\circ}\text{C}$). In theory it should suffice to remove a ‘theoretical’ amount of energy, which is defined by the difference between initial and desired temperature plus latent heat of fusion, as already introduced in Chapter 3. But as the cold front propagates throughout the spatial domain, the removal of this ‘theoretical’ amount of energy will not lead to a uniform distribution of temperature. In fact the temperature of the ‘worst point’ will be higher than the desired temperature. Due to the laws of thermodynamics the overall temperature will uniformly converge to the desired temperature (without disturbances acting on the systems, meaning perfect insulation). However, this procedure is not allowed by some authorities, e.g. the ‘regulation of deep-frozen foodstuff’ (*Forskrift om dyperfrysede næringsmidler*) of the Norwegian Ministry of Health and Care Services states that before being transported to the storage freezer, the goods must be $-18\text{ }^{\circ}\text{C}$ at the warmest point.

Analytical and numerical models for the freezing of foodstuff have been described by a

whole range of publications, for example by Delgado and Sun [34], who give an overview about different techniques. Analytical methods deliver freezing time predictions and are often based on *Plank's equation*¹, see Plank [94] and Lopez-Leiva and Hallström [77]. Pham [91] describes freezing time predictions for rectangular blocks of foodstuff, whereas Pham [89] introduces an extension of Plank's equation for simple shapes. Analytical functions to predict freezing and thawing times for regular and irregular shapes are presented by Cleland et al. ([27] and [28]). Numerical modeling methods have been described in various publications. A finite-difference scheme for freezing foodstuff is introduced by Pham [90], while Cleland et al. [26] present results for freezing and thawing time prediction by numerical methods. These numerical methods mostly rely on temperature predicting models described by partial differential equations.

Due to the fact that freezing time estimation is often done by simplified analytical means and prior-to-freezing-calculations, the freezing time is often 'overestimated'. Since energy-efficiency has become a big topic in the last two decades due to the finiteness of primary energy carriers as well as their impact on the climate, it is important to gain more knowledge of energy-consuming processes, such as freezing processes. In that sense better estimation of freezing time could help terminate the freezing process even before the above mentioned analytical methods would suggest.

The same as described for freezing times before holds for the estimation of thawing times as well.

9.2 Estimation of unmeasurable states

As computational power has grown significantly in the last decades, it makes sense to introduce real time monitoring and estimation of freezing time; that is, to design state-observers which provide estimates of the non-measurable temperature field in the interior of the good's volume. With this knowledge, the freezing time can be estimated.

Observer designs are not possible for any arbitrary system, in fact the possibility of recovering the states of a physical process from a process model depends highly on what kind of measurements are available. For a linear system

$$\begin{aligned}\dot{x} &= Ax + Bu \\ y &= Cx + Du\end{aligned}\tag{9.1}$$

with A denoting the system matrix, B indicating the input matrix, C labeling the output matrix and D describing the feedthrough matrix as well as $x \in \mathbb{R}^n$ being the state vector and $y \in \mathbb{R}^m$ labeling the output vector, the so-called observability condition has to be fulfilled. This means that the observability matrix O has to be of rank n in order for (9.1)

¹Note that in literature both versions of the name, *Plank* and *Planck*, are used; the correct full name is *Rudolf Plank*, however.

to be observable:

$$O = \begin{bmatrix} C^T \\ C^T A \\ C^T A^2 \\ \vdots \\ C^T A^{n-1} \end{bmatrix}. \quad (9.2)$$

This is known as the *Kalman rank condition*. There are, however, weaker forms of observability, where only the unstable modes are required to be observable; this is known as detectability.

Observability for nonlinear systems has e.g. been described in the works of Marino and Tomei [78] and Nijmeijer and van der Schaft [82], who present Lie-derivative-based approaches to check observability for classes of nonlinear systems.

9.2.1 Observer Design methods for ordinary differential equations

Many observer design methods exist; the most well-known of these is undoubtedly the Kalman Filter for discrete-time systems. It has shown itself valuable in many fields of control engineering practice and is a very important tool for control engineers due to its known robustness properties. There exists also a continuous-time version of the Kalman Filter, the so-called Kalman-Bucy-Filter (KBF). Both of these designs rely on linear or linearized system equations with added noise (commonly white Gaussian noise) to compensate for modeling and measurement errors.

Furthermore there exist so called Extended Kalman Filters (EKF), which utilize the same principle as the aforementioned filters, but instead of linearizing around a fixed setpoint, the linearized system matrix gets updated with full state information at each time-step. Like the Kalman Filter, the EKF has formulations both in discrete and continuous time.

In addition, nonlinear observer design methods have been developed in the recent years, where a broad overview is provided by Nijmeijer and Fossen [81]. Specific nonlinear observers have been introduced by Arca and Kokotovic [4], who present an observer based on a circle criterion design. Further observer design methods include high gain observers as e.g. described by Khalil [63], (adaptive) backstepping observers as introduced by Krstić et al. [70] and adaptive observers as developed in the work of Zhang [109].

9.2.2 Observer Design methods for partial differential equations

Observers for partial differential equations have received more and more attention in the scientific community in the recent years. In general there exist two ways to attack these problems: *Early lumping* and *late lumping*. In the former approach, the spatial domain is discretized prior to the observer design, which is then finite-dimensional. In the latter approach the observer is designed for the PDE itself, meaning it will be an infinite-dimensional description. *Early lumping* can be seen as a technique to approximate the PDE by a set of ODEs and then use established techniques as described in Section 9.2.1. An example of an *early lumping* design has been introduced by Kobayashi and Hitotsuya

[64], where the observer is split up into a finite- and an infinite-dimensional part. Examples of *late lumping* approaches are presented by Sallberg et al. [98], where an infinite-dimensional sampled data Kalman Filter is introduced and by Krstić and Smyshlyaev [69], where transformations are used in order to reduce the system's complexity prior to designing the observer by PDE-backstepping methods. Hidayat et al. [50] deliver a broad overview over different types of PDE observers.

All of the above mentioned designs have one thing in common, namely that all rely on system descriptions with constant parameters or on linear PDEs, such that transformations (e.g. gauge-transformations) can be used to obtain simplified system structures with known properties. As the system, which is investigated in this work, is defined by state-dependent parameter functions, however, the already established methods cannot be used here. This motivates the investigations in the subsequent chapters.

Chapter 10

Full model inner-domain temperature estimation for freezing

In this Chapter an observer for estimation of the temperature field in the inner domain of a block of foodstuff, in particular fish, is developed. Furthermore an outlook is given on different forms of this observer, which are introduced in the upcoming Chapters 11–13. These forms include observers for both, freezing and thawing as well as designs that are based on reduced dynamics in order to reduce the computational effort.

10.1 Observer model

The model for the observer design is based upon (6.6), but in a two-dimensional formulation. It describes the temperature distribution $T = T(t, x, y)$ throughout a block of foodstuff that is frozen inside a plate freezer,

$$\begin{aligned}\rho(T)c(T)T_t &= (\lambda(T)T_x)_x + (\lambda(T)T_y)_y \\ &= \lambda_T(T)(T_x^2 + T_y^2) + \lambda(T)(T_{xx} + T_{yy}),\end{aligned}\tag{10.1}$$

where $\rho(T)$, $c(T)$ and $\lambda(T)$ are introduced in Section 6.1. Rewritten, (10.1) becomes

$$T_t = \kappa(T)(T_x^2 + T_y^2) + k(T)(T_{xx} + T_{yy})\tag{10.2}$$

where $k(T)$ and $\kappa(T)$ are defined in (6.4) and (6.5), respectively.

In order to be well-posed, boundary and initial conditions have to be defined for distributed parameter systems. For the present case it is practical to either choose Dirichlet or Neumann boundary conditions, representing temperature or heat flow at l through the boundaries, respectively. Initial conditions represent the initial state of the system. Here it is convenient to choose them evenly distributed throughout the whole spatial domain.

The effects of the freezing medium (vaporizing liquid ammonia) at $x = 0$ and $x = L$ as well as of exposure to air ($y = 0$) are modeled by Dirichlet boundary conditions, whereas presumed perfect insulation at the bottom of the fish block ($y = H$) is modeled by Neumann boundary conditions.

Note that the boundary inputs at $x = 0$ and $x = L$ are not actively controlled. As an introduction to the upcoming investigation, Figure 10.1 illustrates how the spatial domain is discretized and furthermore which of the states are measurable (orange) and which are not (blue). In addition Figure 10.1 shows how the boundary conditions are chosen and the way they act on the system; the arrows indicate the direction of heat flow.

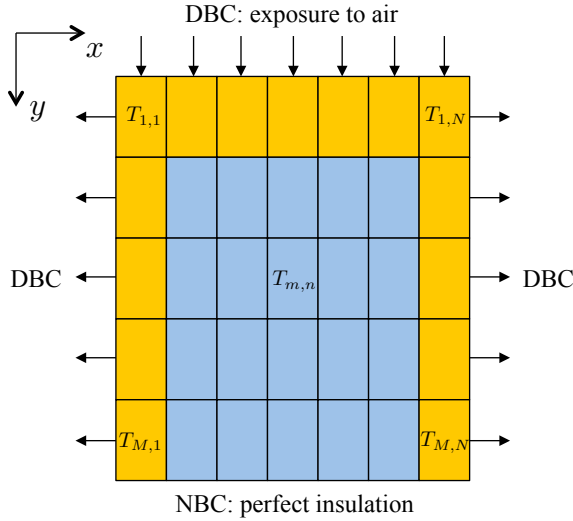


Figure 10.1: DBC denotes Dirichlet boundary conditions and NBC denotes Neumann boundary conditions

10.1.1 Parameters

The parameter distribution functions $k(T)$ and $\kappa(T)$ are introduced in Chapter 6, whereas the parameters $c(T)$, $\lambda(T)$ and $\rho(T)$, which form the parameter functions $k(T)$ and $\kappa(T)$ are described in Section 6.2. A sketch of these parameters is shown in Figure 6.4, while the values are demonstrated in Table 6.1.

10.1.2 Discretization

Discretization is performed by means of finite difference methods for the spatial derivatives only. This corresponds with an *early lumping* approach and will lead to an approximation of the PDE by a set of interdependent (coupled) ODEs. For discretization it is necessary to use uneven discretization numbers N and M in x - and y -direction, in order to be able to define central layers for both spatial domains.

The terms T_x , T_y , T_{xx} and T_{yy} will be approximated by the discretization scheme introduced in (6.12). Hence, the following discretizations hold for fixed y - and x -positions, respectively

$$T_x = \begin{cases} \frac{T_{m,n} - T_{m,n-1}}{\Delta x}, & \text{if } n < \frac{N+1}{2} \\ \frac{T_{m,n+1} - T_{m,n-1}}{2\Delta x}, & \text{if } n = \frac{N+1}{2} \\ \frac{T_{m,n+1} - T_{m,n}}{\Delta x}, & \text{if } n > \frac{N+1}{2}, \end{cases} \quad (10.3)$$

$$T_y = \begin{cases} \frac{T_{m,n} - T_{m-1,n}}{\Delta y}, & \text{if } m < \frac{M+1}{2} \\ \frac{T_{m+1,n} - T_{m-1,n}}{2\Delta y}, & \text{if } m = \frac{M+1}{2} \\ \frac{T_{m+1,n} - T_{m,n}}{\Delta y}, & \text{if } m > \frac{M+1}{2}. \end{cases} \quad (10.4)$$

$$T_{xx} = \frac{T_{m,n+1} - 2T_{m,n} + T_{m,n-1}}{\Delta x^2}, \quad (10.5)$$

$$T_{yy} = \frac{T_{m+1,n} - 2T_{m,n} + T_{m-1,n}}{\Delta y^2}. \quad (10.6)$$

The discrete expressions (10.3), (10.4), (10.5) and (10.6) are defined for $1 \leq n \leq N$ and $1 \leq m \leq M$, where the values at $T_{m,0}$, $T_{m,N+1}$, $T_{0,n}$ and $T_{M+1,n}$ represent the fictional states (ghost cells) where the boundary conditions enter the equations. The discretization step sizes are $\Delta x = \frac{L}{N}$ and $\Delta y = \frac{H}{M}$.

This discretization procedure will lead to $N \cdot M$ coupled ordinary differential equations. For $1 \leq n < \frac{N+1}{2}$ and $1 \leq m < \frac{M+1}{2}$, a general description of this ODE has the form

$$\begin{aligned} \dot{T}_{m,n} = & \kappa(T_{m,n}) \left[\left(\frac{T_{m,n} - T_{m,n-1}}{\Delta x} \right)^2 + \left(\frac{T_{m,n} - T_{m-1,n}}{\Delta y} \right)^2 \right] \\ & + k(T_{m,n}) \left[\frac{T_{m,n+1} - 2T_{m,n} + T_{m,n-1}}{\Delta x^2} + \frac{T_{m+1,n} - 2T_{m,n} + T_{m-1,n}}{\Delta y^2} \right]. \end{aligned} \quad (10.7)$$

10.1.3 Boundary conditions

As mentioned before, Dirichlet boundary conditions are imposed on the system at $T_{m,0}$, $T_{m,N+1}$ and $T_{0,n}$. It must be pointed out that these boundary conditions are assumed constant and can therefore be defined as $T_{m,0} = T_{m,N+1} = T_{Boundary}$ for all m (temperature of ammonia) and $T_{0,n} = T_{Air}$ for all n (temperature of air). Furthermore, perfect insulation at the bottom of the fish block is defined by Neumann boundary conditions at $T_{M+1,n}$, leading to the expression $T_{M+1,n} - T_{M,n} = 0$ for all n . It has to be pointed out that the heat transfer with air at $y = 0$ models for a disturbance with a constant air temperature using Dirichlet boundary conditions as a worst-case scenario.

10.2 Observer

The observer is designed to estimate the unmeasurable states inside the spatial domain of the fish block. Inner-domain measurements are neither practical nor possible for the system setup. The estimation of the unmeasurable states is important to predict when the desired temperature is reached inside the inner layers of the spatial domain. Thus it can replace simpler, approximative freezing time prediction methods, as already mentioned in

the beginning of this Chapter.

A first choice for a practical observer design is often a Kalman Filter based design. Due to the fact that a Kalman Filter is a well-established observer in engineering practice, it is often used as a benchmark in order to compare other observer designs with regard to performance. The Kalman Filter has certain robustness properties which are based on the fact that modeling and measurement errors are introduced to the system model by adding up white Gaussian noise signals v and z to the state derivatives and the outputs, respectively. Here, the possibility of implementing an Extended Kalman Filter (EKF) will be investigated.

10.2.1 Design

The design relies on a nonlinear model running in parallel to the plant. Both, plant and model base on the same spatially discretized equations of the PDE (10.2) and are fed with the same inputs, namely the boundary conditions at $x = 0$, $x = L$ ($T_{Boundary}$) and $y = 0$ (T_{Air}). The boundary conditions at $y = H$ are directly embedded in the spatially discretized equations of the plant and the model. The plant's equations look therefore as follows:

$$\begin{aligned}\dot{T} &= f_1(T), \\ y &= CT,\end{aligned}\tag{10.8}$$

where in fact $f_1(T)$ is given by equations in the form (10.7) with the respective difference expressions for distinct values for n and m . In order to introduce the design of the proposed EKF, firstly the standard Kalman-Bucy-Filter is introduced. Let the plant be in the form

$$\begin{aligned}\dot{x} &= f(x, u) + v, \\ y &= Cx + z,\end{aligned}\tag{10.9}$$

and thus the observer dynamics become

$$\begin{aligned}\dot{\hat{x}} &= A\hat{x} + Bu + KC(x - \hat{x}), \\ y &= Cx,\end{aligned}\tag{10.10}$$

where $A = \left. \frac{\partial f}{\partial x} \right|_{(x_0, u_0)}$ and $B = \left. \frac{\partial f}{\partial u} \right|_{(x_0, u_0)}$ are the Jacobians of $f(x, u)$ with respect to the state variables x and the input u , respectively, around an equilibrium point (x_0, u_0) . C defines the output matrix and K is the observer feedback gain calculated by the Riccati differential equation

$$\dot{P} = AP + PA^T - PC^T R^{-1} CP + Q,\tag{10.11a}$$

$$K = PC^T R^{-1},\tag{10.11b}$$

where $Q = Q^T \geq 0$ and $R = R^T > 0$ denote the covariance matrices of the white Gaussian noise signals v representing errors in the model and z indicating measurement noise, respectively.

The following observer dynamics for the EKF are proposed

$$\begin{aligned}\dot{\hat{T}} &= f_2(\hat{T}) + KC(T - \hat{T}), \\ y &= CT,\end{aligned}\tag{10.12}$$

where a nonlinear model is used for the observer, as can be seen by comparing (10.12) and (10.10). In (10.12), $f_2(T)$ is also given by equations in the form (10.7), just like $f_1(T)$. This means that A in the proposed design will only be used to calculate the solutions to the Riccati equation and thus to compute the observer feedback gain K .

10.2.2 Linearization

In contrast to the above mentioned standard design (10.10), the Jacobian in the proposed observer is not linearized around a fixed setpoint, but around the actual setpoints defined by the solutions to the ODEs, \hat{T}_S , meaning $A_{\hat{T}_S} = \left. \frac{\partial f_2}{\partial T} \right|_{\hat{T}_S}$. Thus the system matrix $A_{\hat{T}_S}$ represents the linearized system's behavior at particular points in state-space and changes as the system is progressing in time.

The state vector is defined as

$$T = [T_{1,1} \ \cdots \ T_{1,N} \ T_{2,1} \ \cdots \ T_{2,N} \ \cdots \ T_{M,N}]^T,$$

which leads to a sparse matrix $A_{\hat{T}_S}$ with a regular pattern of diagonal and side-diagonal entries. Note that the system matrix can be subject to change due to the definition of the chosen parameter functions and also to the discretization scheme.

10.2.3 Measurements

It is assumed that no in-domain measurements are available, compare to Figure 10.1 and thus only temperatures at the boundaries are available for measurement. This means that the output is

$$y = [T_{1,1} \ \cdots \ T_{1,N} \ T_{2,1} \ T_{2,N} \ \cdots \ T_{M,1} \ T_{M,N}]^T,$$

which results in an output matrix on the following form

$$C = \text{blockdiag} [C_1 \ C_2 \ \cdots \ C_M],$$

where $C_1 = I_{(N \times N)}$ and $C_k = \begin{bmatrix} 1 & 0_{(1 \times (N-1))} \\ 0_{(1 \times (N-1))} & 1 \end{bmatrix}$ for $2 \leq k \leq M$.

10.2.4 Riccati equation

In this setup the matrix Riccati differential equation is in the same form like (10.11)

$$\dot{P} = A_{\hat{T}_S} P + P A_{\hat{T}_S}^T - P C^T R^{-1} C P + Q, \quad (10.13a)$$

$$K = P C^T R^{-1}, \quad (10.13b)$$

where Q and R are introduced in Section 10.2.1. Note that no correlation between single states and outputs is assumed. Note that the feedback gain K is actually a function of time and the linearization point \hat{T}_S .

A schematic of the overall design can be seen in Fig. 10.2.

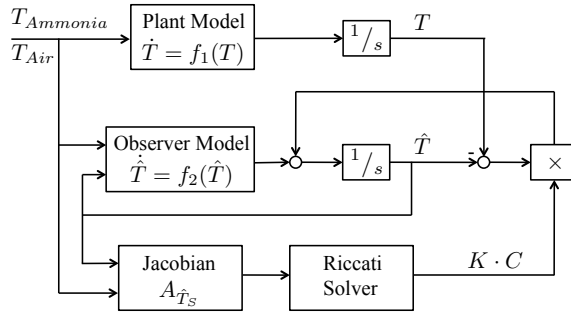


Figure 10.2: Design schematic for the observers

10.2.5 Observability

The question of observability of the system (6.6) in its discretized and linearized form presented in Section 10.1.2 is a crucial point. Due to the fact that the parameter functions are depending on the state itself and thus the linearized system matrix $A_{\hat{T}_S}$ is changing its values with each iteration, a calculation of the observability matrix \mathcal{O} beforehand is not possible. Therefore the observability matrix is calculated for all instances of the linearized system matrix $A_{\hat{T}_S}$ after the simulation is conducted. For all presented cases in Chapters 10, 11, 12 and 13 the observability matrix showed full rank and therefore all of the designs are valid as observers.

10.3 Comments on the upcoming Chapters

In this short Section some comments concerning different observer designs as well as general remarks on the simulation results are given.

10.3.1 Comments on the different observer designs

As mentioned before, different observer designs will be introduced in this and the upcoming Chapters 11–13. All in all three different observer designs will be presented, namely a full model observer relying on the full system description as well as two models based upon reduced system descriptions, one of them a real-time applicable observer. Furthermore, the possibility of switching the covariance matrices Q and R will be investigated and compared to results obtained by constant covariance matrices.

Finally, the observers will be tested for differing parameter functions, in particular the parameters of the observers will be chosen to be double the size compared to those of the plant (denoted S_{Sys}), namely $k_{\text{EKF}} = 2k_{\text{Sys}}$, $\kappa_{\text{EKF}} = 2\kappa_{\text{Sys}}$ and $\Delta T_{\text{EKF}} = 2\Delta T_{\text{Sys}}$. The parameter functions of the plant are calculated with the coefficients in Table 10.1 and are the same for Chapters 10, 11, 12 and 13. However, the responses of the reduced observers are quite different and depend highly on the size of the parameter functions. Therefore also simulations for perfect knowledge of the parameters are conducted for the reduced designs, namely $k_{\text{EKF}} = k_{\text{Sys}}$, $\kappa_{\text{EKF}} = \kappa_{\text{Sys}}$ and $\Delta T_{\text{EKF}} = \Delta T_{\text{Sys}}$.

10.3.2 Comments on the simulations in general

In the Chapters 10, 11, 12 and 13 the results are presented in Figures, where blue curves denote the response of the plant, green curves indicate noisy measurements and red curves label the response of the observers.

The most important results denote the observer dynamics in the center and the bottom of the spatial domain, namely at $m = 3$ and $m = 5$. The main focus lies therefore on plots showing these results. However, more plots for other positions can be found in Appendix F for completeness.

10.4 Simulations

In order to show observer performance for the described setup, it is essential to conduct simulations for both, the dynamics of the plant and the observer dynamics and compare these to each other. The reason for this is that both systems will converge to the steady state solution dictated by the boundary conditions, however, the time for convergence will differ. Simulations are conducted in MATLAB[®] Simulink using the ode45-solver with variable step size, but with a maximal step size of 0.1 s.

In Figure 10.3 a comparative plot between the dynamics of the plant and those of the observer can be found for the case $N = 9$ and $M = 5$ and the simulation parameters listed in Table 10.1. The values for N and M present a trade-off between accuracy and performance, as spatial resolution is limited by computational power. In addition, temperature variations along the y -coordinates for fixed x -positions are small, but not negligible due to the heat exchange with air at $y = 0$. This justifies to choose M quite small, but greater than 1 ($M = 1$ represents a 1-dimensional PDE).

It can be seen that the observer converges faster to the steady state dictated by the boundary conditions. This is due to the fact that the parameters $k(T)$ and $\kappa(T)$ are chosen to be twice as big compared to the plant.

The following values are chosen for the covariance matrices Q and R , respectively and hold in this Chapter, as well as in the upcoming Chapter 11.

$$\begin{aligned}
 R_1 = 10^4 \begin{bmatrix} \Gamma & 0 & 0 & 0 & 0 \\ 0 & \Sigma & 0 & 0 & 0 \\ 0 & 0 & \Sigma & 0 & 0 \\ 0 & 0 & 0 & \Sigma & 0 \\ 0 & 0 & 0 & 0 & \Sigma \end{bmatrix}, & \quad R_2 = 10^2 \begin{bmatrix} \Gamma & 0 & 0 & 0 & 0 \\ 0 & \Sigma & 0 & 0 & 0 \\ 0 & 0 & \Sigma & 0 & 0 \\ 0 & 0 & 0 & \Sigma & 0 \\ 0 & 0 & 0 & 0 & \Sigma \end{bmatrix} \\
 Q_1 = 10^1 \begin{bmatrix} \Gamma & 0 & 0 & 0 & 0 \\ 0 & \Phi_1 & 0 & 0 & 0 \\ 0 & 0 & \Phi_1 & 0 & 0 \\ 0 & 0 & 0 & \Phi_1 & 0 \\ 0 & 0 & 0 & 0 & \Phi_1 \end{bmatrix}, & \quad Q_2 = 10^0 \begin{bmatrix} \Gamma & 0 & 0 & 0 & 0 \\ 0 & \Phi_2 & 0 & 0 & 0 \\ 0 & 0 & \Phi_2 & 0 & 0 \\ 0 & 0 & 0 & \Phi_2 & 0 \\ 0 & 0 & 0 & 0 & \Phi_2 \end{bmatrix}
 \end{aligned}$$

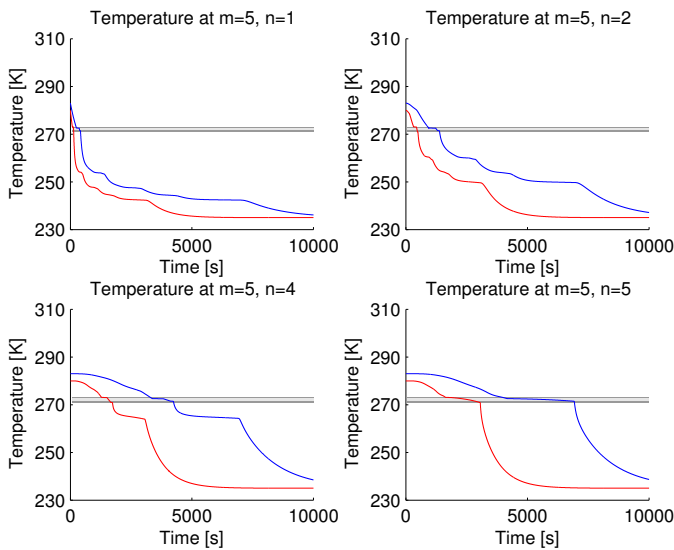


Figure 10.3: Comparison between the dynamics of the plant (blue) and those of the observer (red) at $m = 5$ and different positions along the x -axis

$$\begin{aligned}\Gamma &= I_{(9 \times 9)} \\ \Sigma &= \begin{bmatrix} 10 & 0 \\ 0 & 10 \end{bmatrix} \\ \Phi_1 &= \text{diag}([1 \ 10 \ 10 \ 10 \ 10 \ 10 \ 10 \ 10 \ 1]) \\ \Phi_2 &= \text{diag}([1 \ 1 \ 10 \ 100 \ 100 \ 100 \ 10 \ 1 \ 1])\end{aligned}$$

10.4.1 Results for constant covariance matrices Q and R

Figure 10.4 presents results for $m = 1$ and different positions along the x -axis. All measurements are available and thus the states can be estimated correctly, even in the presence of added measurement noise.

In Figure 10.5 a zoom into the latent zone at $m = 1$ and $n = 5$ is shown and it can be seen that the state is estimated correctly, even for differing parameter functions. The reason for this is of course to be found in the available measurements. What happens if the measurements are not available can be seen in Figure 10.7.

Figure 10.6 depicts similar plots like in Figure 10.4, but now at $m = 3$. It can be seen that at position $m = 3$ and $n = 1$ the estimation has very low error. This is again due to the fact that the measurement at this position is available. For the other positions the error becomes larger the further the specific position is away from the measurement. However, convergence of the observer states towards the states of the plant is obvious. The latent zone is estimated well for all of the cases, but after crossing the latent zone there remains an estimation error.

L	0.1	m
H	0.5	m
T_F	272	K
$T_{init,EKF}$	280	K
$T_{init,Sys}$	283	K
ΔT_{EKF}	1	K
ΔT_{Sys}	0.5	K
δT	0.1	K
$T_{Boundary}$	235	K
T_{Air}	278	K
c_s	2200	J kg ⁻¹ K ⁻¹
c_l	3800	J kg ⁻¹ K ⁻¹
c_i	283000	J kg ⁻¹ K ⁻¹
ρ	950	kg m ⁻³
λ_s	1.8	W m ⁻¹ K ⁻¹
λ_l	0.5	W m ⁻¹ K ⁻¹

Table 10.1: Simulation parameters for the observer design cases for freezing

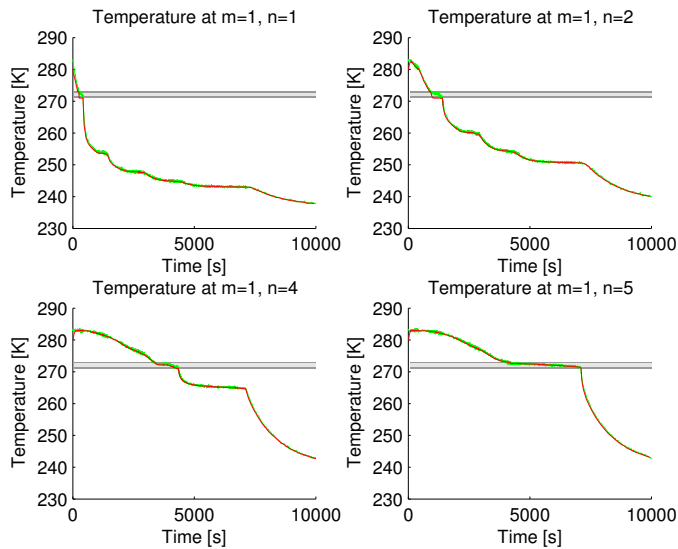
Figure 10.4: Results for the full model observer at $m = 1$ and different positions along the x -axis for constant Q and R

Figure 10.7 shows a zoom into the latent zone at $m = 3$ and $n = 5$. Convergence can clearly be seen, however, the estimated state is off the real state due to the fact that the latent zone for the observer is chosen to be double the size compared to the plant.

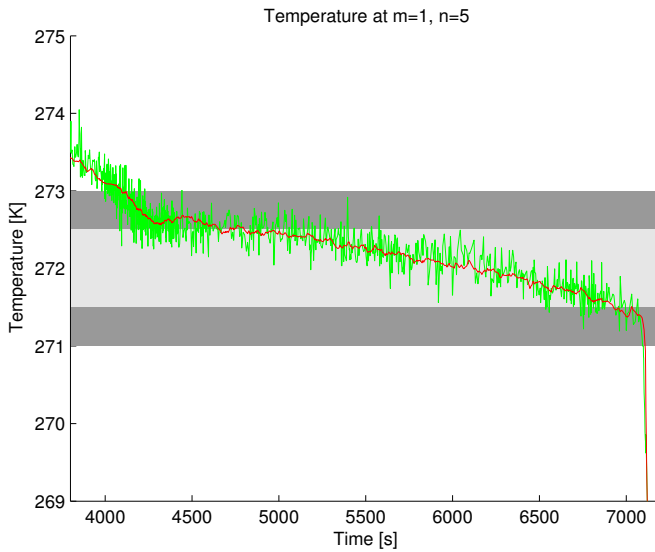


Figure 10.5: Results for the full model observer at $m = 1$ and $n = 5$ for constant Q and R , zoom into the latent zone

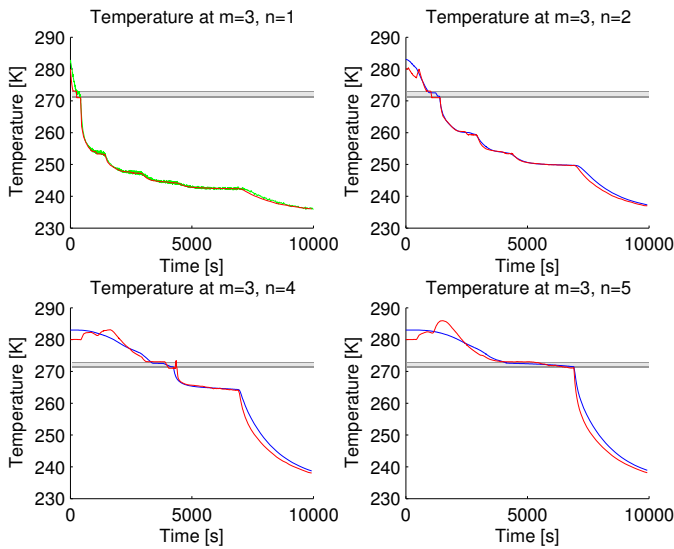


Figure 10.6: Results for the full model observer at $m = 3$ and different positions along the x -axis for constant Q and R

In Figure 10.8 similar plots compared to those shown in Figures 10.6 and 10.4 are presented. The latent zone is captured quite well by the observer, but there is a larger estima-

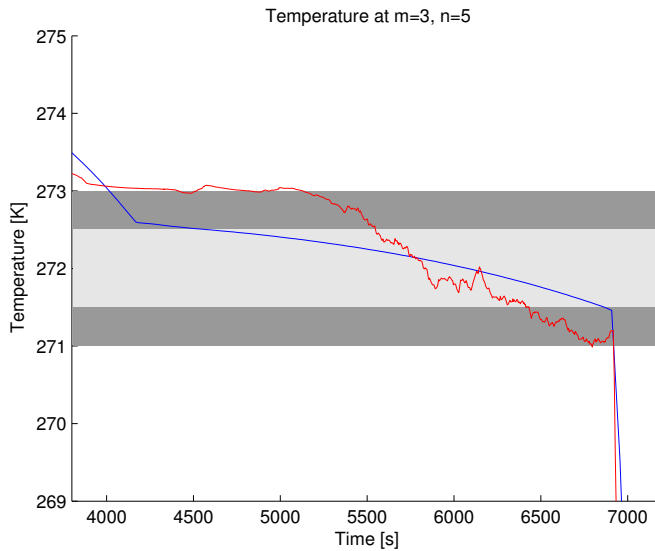


Figure 10.7: Results for the full model observer at $m = 3$ and $n = 5$ for constant Q and R , zoom into the latent zone

tion error than for the case presented in Figures 10.6 after crossing the latent zone. However, if compared to the open-loop simulations in Figure 10.3, the estimation is clearly an improvement. Figure 10.9 depicts a 3-dimensional plot of the estimation error at $m = 5$ to illustrate convergence at this position along the whole x -axis.

10.4.2 Results for switched covariance matrices Q and R

Observer performance can be enhanced by switching the observer covariance matrices Q and R after crossing the latent zone $I_{\Delta T}$. The switching from Q_1 to Q_2 and R_1 to R_2 occurs after the measurable state $T_{1,5}$ is smaller than 271 K. This is important due to the fact that accurate estimation is crucial after having crossed the latent zone. The estimate indicates the time when freezing is done, meaning that the desired temperature is reached. The results visualized in this Subsection represent a comparative study to the results presented in Section 10.4.1 and therefore only three Figures will be presented to show the improved estimation.

Figure 10.10 shows the results obtained for switched covariance matrices at $m = 3$ for different positions along the x -axis and can directly be compared to Figure 10.6. It can be seen that the switching of the covariance matrices has a positive effect on the estimation error as it is brought back to zero faster than for constant covariance matrices in Figure 10.6, especially for the important cases $n = 4$ and $n = 5$ in the inner domain. This can be seen at the respective peaks bringing the red line (observer) to the blue line (plant).

In Figure 10.11 the same behavior as already described in Figure 10.10 can be seen. Compared to Figure 10.8 it gets clear that also for $m = 5$ the states get estimated more precisely

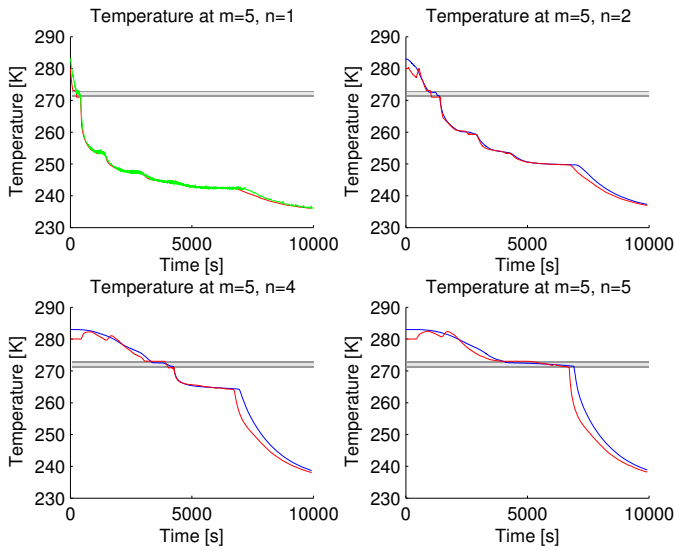


Figure 10.8: Results for the full model observer at $m = 5$ and different positions along the x -axis for constant Q and R

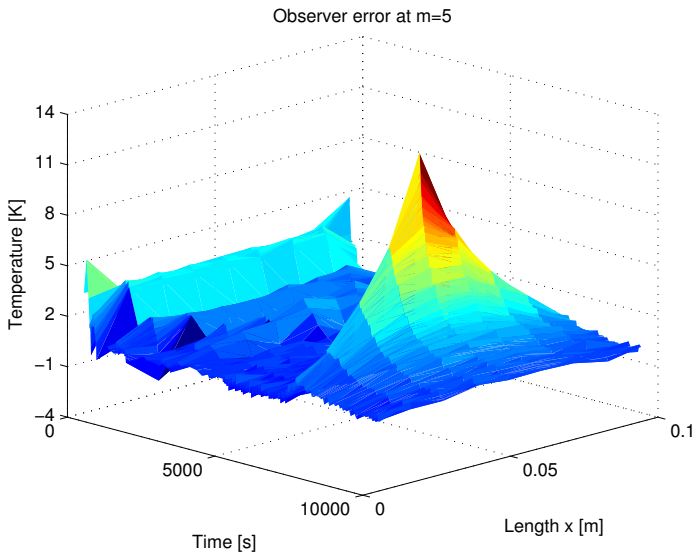


Figure 10.9: A 3-dimensional plot of the estimation error for the full observer at $m = 5$ for constant Q and R

after crossing the latent zone.

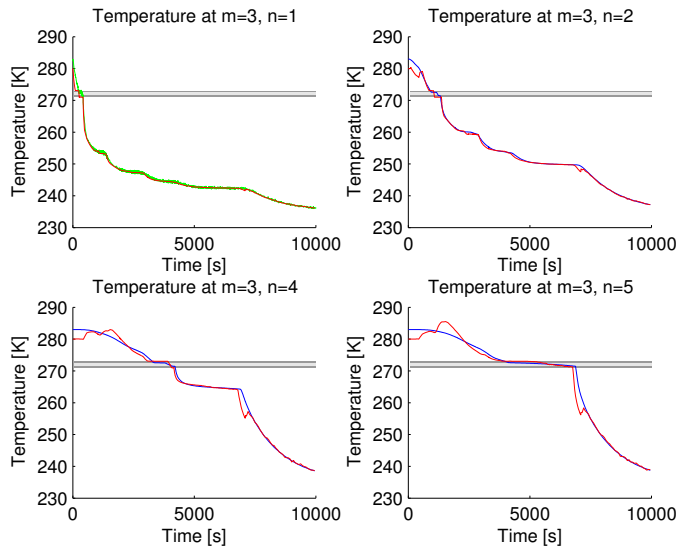


Figure 10.10: Results for the full model observer at $m = 3$ and different positions along the x -axis for switched Q and R

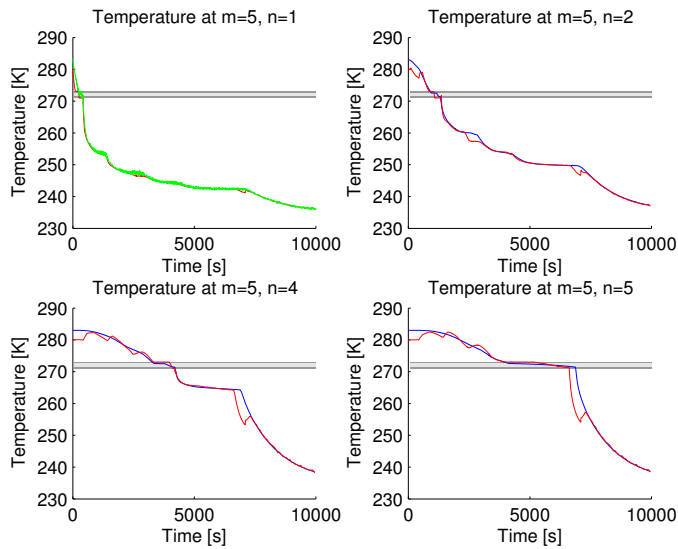


Figure 10.11: Results for the full model observer at $m = 5$ and different positions along the x -axis for switched Q and R

Figure 10.12 shows a 3-dimensional plot of the estimation error at $m = 5$ along the x -axis. By comparing it to Figure 10.9 it can be perceived that the large peak flattens out more

rapidly for the case with switched covariance matrices.

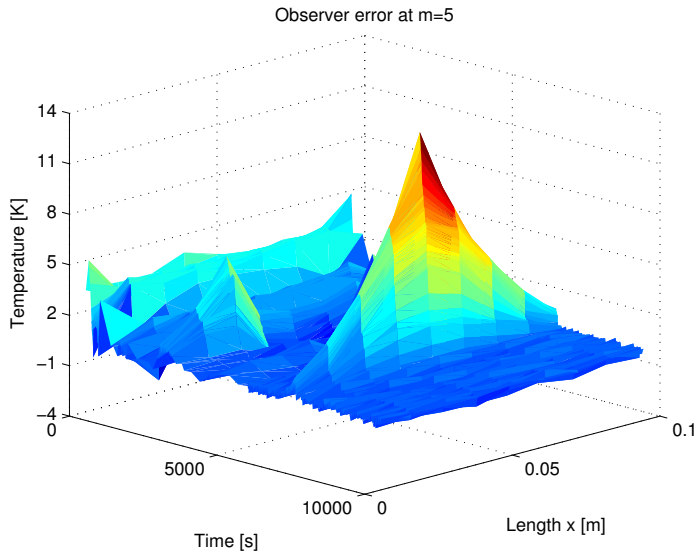


Figure 10.12: A 3-dimensional plot of the estimation error for the full observer at $m = 5$ for switched Q and R

Chapter 11

Reduced model inner-domain temperature estimation for freezing

In this Chapter an observer design similar to that presented in Chapter 10 is introduced. The difference between these two designs is to be found in the fact that the one presented in this Chapter is based upon a reduced system description. This reduced system description is the basis for the observer dynamics, however, the full system description as presented in Chapter 10 remains valid for the plant's dynamics.

11.1 Observer model

The model for the reduced model observer relies on the same modeling principles like already described in Chapter 10. This includes the chosen methods for discretization, the boundary conditions as well as the measurements. The differences in the models are based in differing definitions of the parameter functions, in particular of the thermal conductivity $\lambda(T)$, which is now defined to be piecewise constant as can be seen in Figure 11.1. Still, $\rho(T)$ is assumed constant over the considered temperature range.

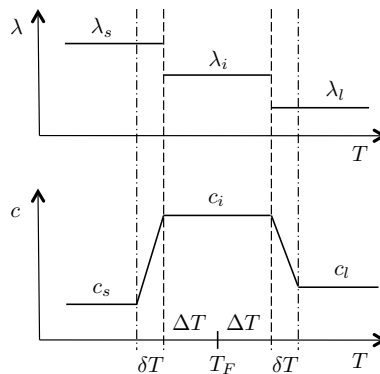


Figure 11.1: Parameter function definitions for the reduced observer case

The definition of $\lambda(T)$ as shown in Figure 11.1 leads to the system dynamics in the following form (compare (10.2))

$$T_t = k(T)(T_{xx} + T_{yy}). \quad (11.1)$$

This is due to the fact that $\lambda_T(T) = 0$ for all T .

11.2 Simulation examples

Simulations have been carried out in the same fashion like in Chapter 10. Firstly, examples with constant covariance matrices Q and R get presented. Secondly, examples for which these covariance matrices change values after a specific condition is fulfilled, are visualized. As the values for Q and R from Chapter 10 have delivered good results, also the reduced observer design will be based on these definitions.

Like before, in order to show observer performance, simulations for both, the dynamics of the plant and the observer dynamics are conducted. Both systems will converge to the steady state solution dictated by the boundary conditions, but at different rates. In Figure 11.2 a comparative plot between the dynamics of the plant (10.2) and those of the observer (11.1) can be found. The plots show results at $m = 5$ for different positions along the x -axis. The simulation parameters can be seen in Table 10.1, where in addition $\lambda_i = 1.15 \text{ Wm}^{-1}\text{K}^{-1}$ holds.

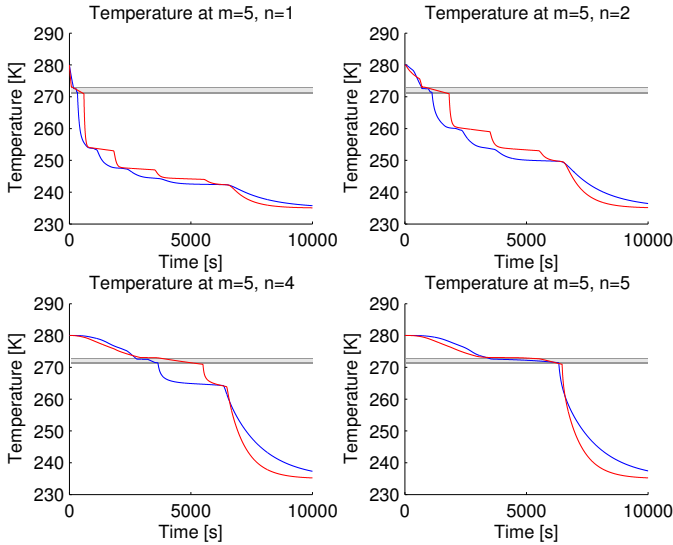


Figure 11.2: Comparison between the dynamics of the plant (blue) and those of the observer (red) at $m = 5$ and different positions along the x -axis

It can be seen that the dynamics are somewhat similar. This might be due to the fact that on the one hand the terms $\kappa(T)(T_x^2 + T_y^2)$ are not present in the observer model, but that on the other hand $k_{EKF} = 2k_{Sys}$ holds.

11.2.1 Results for constant covariance matrices Q and R

For these simulations the values for $Q = Q_1$ and $R = R_1$ were chosen constant for the whole simulation time. Plots for the same positions as already presented in Section 10.4.1 for the full observer design case with constant Q and R are presented for direct comparison.

Thus, Figure F.1 shows simulation results for $m = 1$ at different x -positions. Still, the states are estimated accurately due to the fact that the (noisy) measurements are available.

Figure F.2 presents a zoom into the latent zone at $m = 1$ and $n = 5$. The white Gaussian noise added to the measurement signals is clearly visible in the green curve.

In Figure 11.3 results for $m = 3$ and different positions along the x -axis can be seen. Convergence to the real states is obvious, however, the estimation error becomes larger, the further the particular position is away from the measurement at the boundary $m = 3$ and $n = 1$. The estimation error is larger in the beginning of the simulation, but gets smaller over time. The latent zone is captured quite well, however, there is an estimation error present towards the end of the simulation.

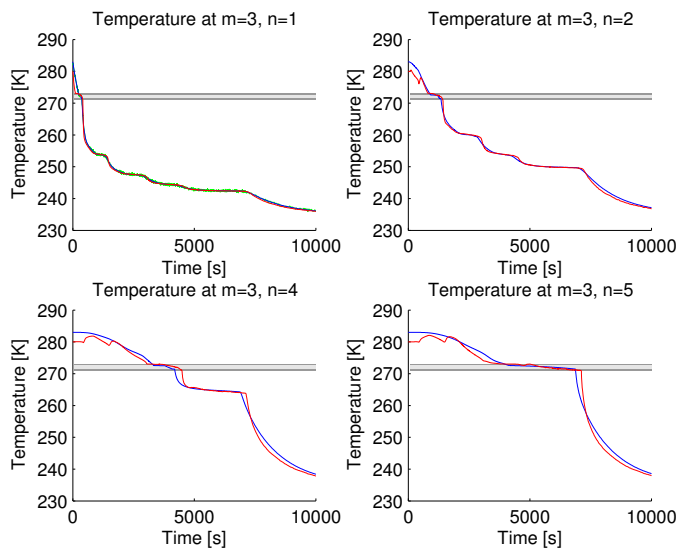


Figure 11.3: Results for the reduced model observer at $m = 3$ and different positions along the x -axis for constant Q and R

Figure F.3 shows a zoom into the latent zone at $m = 3$ and $n = 5$. Estimation is off the real state due to the fact that the latent zone for the observer is chosen to be double the size compared to the plant. However, convergence of the observer towards the real states is perceivable.

Figure 11.4 shows results at the same positions like in Figure F.1 and Figure 11.3. It can be seen that there is an estimation error present at the bottom of the domain ($m = 5$) at the respective positions along the x -axis. This is larger in the beginning and gets less over

time. The latent zone is estimated in a good manner, but an estimation error is present after crossing the latent zone. However, compared to Figure 11.2 showing the open-loop dynamics, the error is significantly smaller.

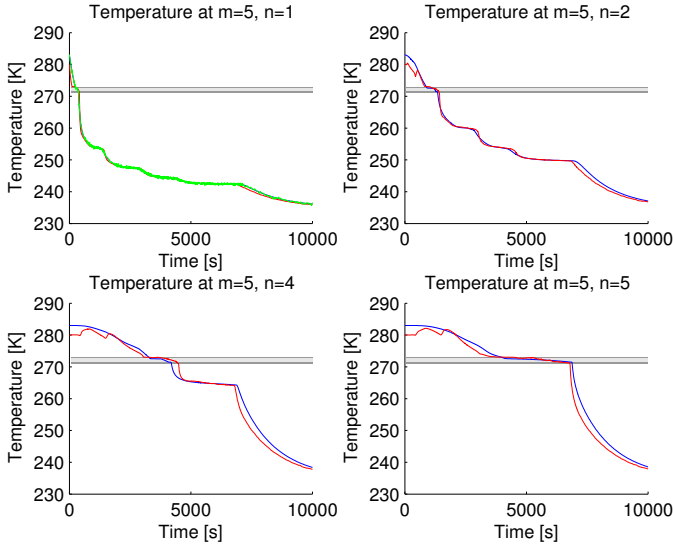


Figure 11.4: Results for the reduced model observer at $m = 5$ and different positions along the x -axis for constant Q and R

In Figure 11.5 a 3-dimensional plot of the estimation error at $m = 5$ along the whole x -domain is presented. This illustrates convergence to the real states as the error is brought back to zero in the simulation time.

11.2.2 Results for switched covariance matrices Q and R

Like presented in Section 10.4.2, the observer performance can be improved by switching the observer covariance matrices Q and R . Again, the switching from Q_1 to Q_2 and R_1 to R_2 occurs when $T_{1,5} < 271$ K. The results represent a comparative study to the results presented in Section 11.2.1 and thus only three Figures will be presented to visualize the improved estimation.

Figure 11.6 shows results at $m = 3$ and different positions along the x -axis for switched Q and R . Faster convergence is achieved, meaning that the estimation error goes to a small region around zero (due to the measurement noise) faster than for the case presented in Figure 11.3 for constant covariance matrices after crossing the latent zone.

In Figure 11.7 faster convergence can be seen after crossing the latent zone for $m = 5$ and different positions along the x -axis, when compared to Figure 11.4. The estimation error is brought back to a small region around zero in faster time. This can be seen by looking at the peaks bringing the observer states (red) to the real states (blue).

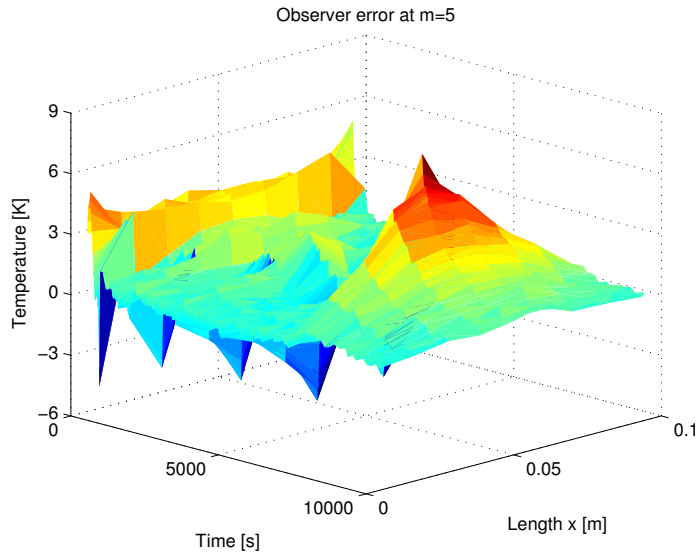


Figure 11.5: A 3-dimensional plot of the estimation error for the reduced observer at $m = 5$ for constant Q and R

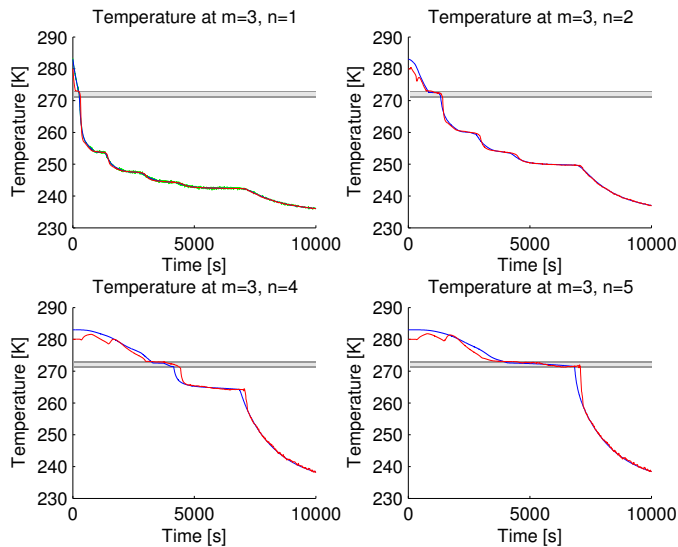


Figure 11.6: Results for the reduced model observer at $m = 3$ and different positions along the x -axis for switched Q and R

Figure 11.8 depicts the estimation error at $m = 5$ and it can be seen that the error gets close to zero faster and steadier than for the case with constant covariance matrices Q and

11. Reduced model inner-domain temperature estimation for freezing

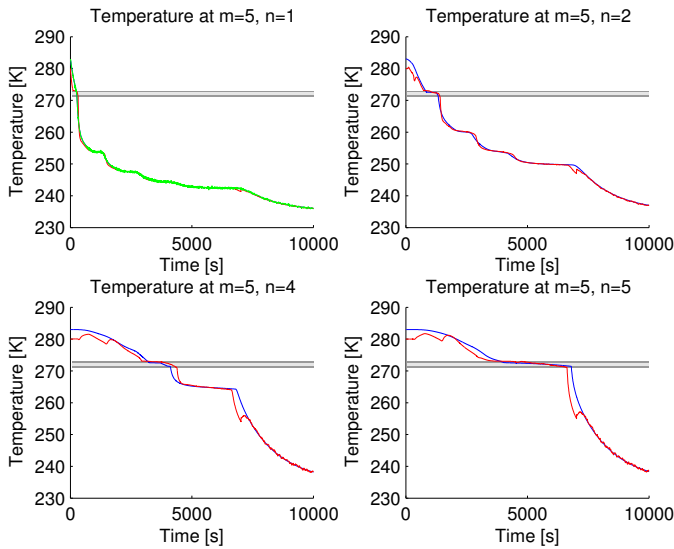


Figure 11.7: Results for the reduced model observer at $m = 5$ and different positions along the x -axis for switched Q and R

R in Figure 11.5, as can be seen by comparing the color patterns of the respective plots. However, the maximum peak in the transient phase is larger than in Figure 11.5.

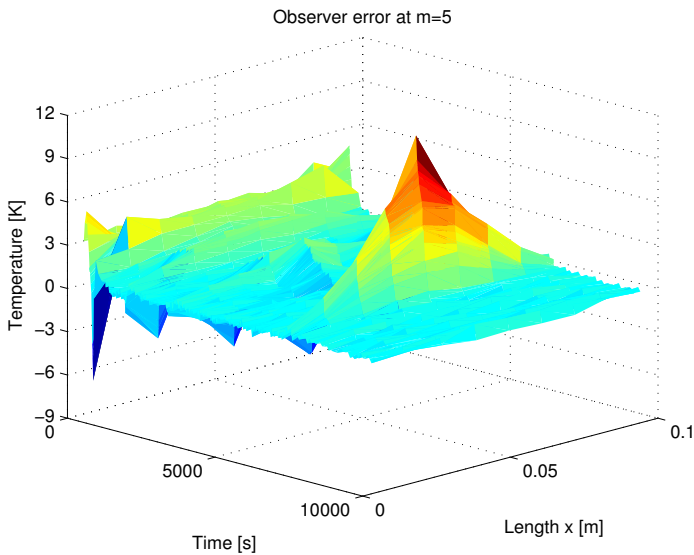


Figure 11.8: A 3-dimensional plot for the reduced model observer at $m = 5$ for switched Q and R

11.2.3 Simulations for perfect knowledge of the parameter values

As shown by comparing Figures 10.3 and 11.2 the definition of the observer dynamics in the reduced form (11.1) has a significant effect on the simulation and convergence time of the observer dynamics. Therefore, it is crucial to investigate estimation for other than the chosen parameter ratios, meaning the ratios between $k(T)$ and $\kappa(T)$ and the size of the latent zone ΔT for the plant and the observer. Particularly, in this Subsection an investigation will be presented for the observer parameters to have identical values to the plant's parameters, meaning perfect knowledge of the plant's parameters. This leads to the difference in response as shown in Figure 11.9.

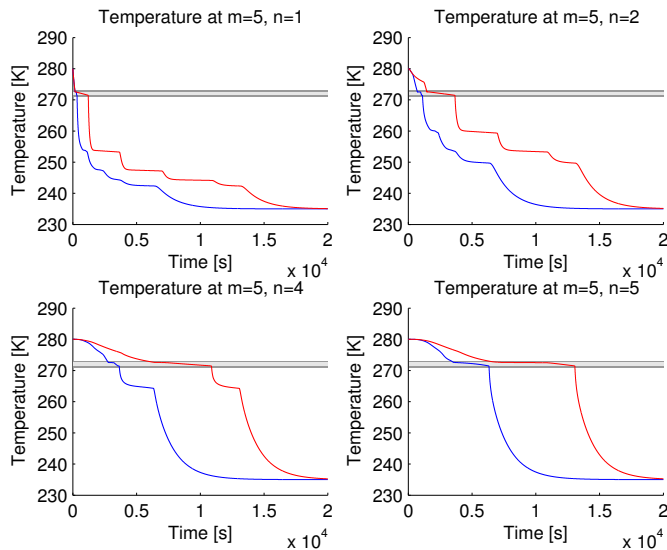


Figure 11.9: Comparison between the dynamics of the plant (blue) and those of the observer (red) at $m = 5$ and different positions along the x -axis for parameter functions with identical values

As can be seen, choosing the parameters in the described fashion, the differences between the dynamic responses of the plant and the observer are significantly larger than for differing parameter values (see Figure 11.2). Thus, the observer design must be investigated for this case as well. However, as the switching of Q and R has shown itself beneficial for performance, only this case will be presented here.

In Figure 11.10 results for $m = 3$ and different positions along the x -axis are presented. It can be seen that the temperatures are estimated quite well, compared to the differences in the dynamic behaviors of the plant and observer models shown in Figure 11.9. In particular, the estimation error is brought to a neighborhood around zero quite fast after crossing the latent zone.

The same trend that is shown in Figure 11.10 can be seen in Figure 11.11 for the bottom of the block ($m = 5$), namely that the observer converges to the real states rather fast after

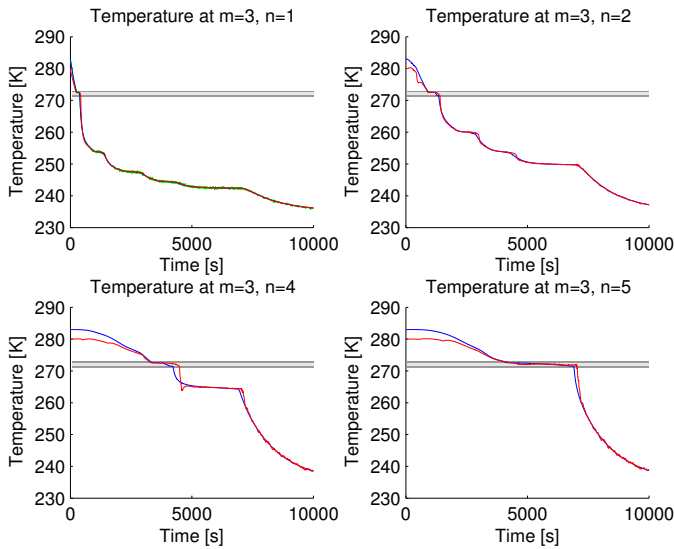


Figure 11.10: Results for the reduced model observer at $m = 3$ and different positions along the x -axis for switched Q and R and identical parameter definitions

crossing the latent zone and that the temperatures and the time in the latent zone are estimated quite well. The observer error at $m = 5$ over the spatial domain x is presented in Figure 11.12 and demonstrates the convergence of the estimated states to the plant's states. The transient peaks are fairly small compared to earlier presented cases.

11.2.4 Real-time applicable observer

Both, the full model observer as presented in Chapter 10 and the reduced model observer as presented above, are not real-time applicable. The main reason for this is that the calculations of the Riccati differential equation as well as that of the Jacobian $A_{\hat{T}_S}$ are computationally intense and have to be conducted at any time-step. For the reduced model observer as described in Section 11.1 the calculations per time step were reduced by defining the parameter functions such that $\kappa(T) = 0$. There is a second possibility of reducing the calculation effort and this is by defining the parameter functions in the form as can be seen in Figure 11.13

Defining both, $c(T)$ and $\lambda(T)$ as discontinuous step functions has the effect that now even the derivative $\frac{\partial}{\partial T}k(T)$ is zero for all T . Thus, these terms do not have to be regarded in the calculation of the Jacobian $A_{\hat{T}_S}$ and its computation effort and that of the Riccati differential equation are reduced even more. This has the effect that the observer dynamics look similar, but slightly different from the ones shown in Figure 11.9, namely as shown in Figure 11.14.

As it has shown to deliver good results, only simulations with switched covariance matrices Q and R will be presented here. Note that the matrix Q_1 is slightly retuned in or-

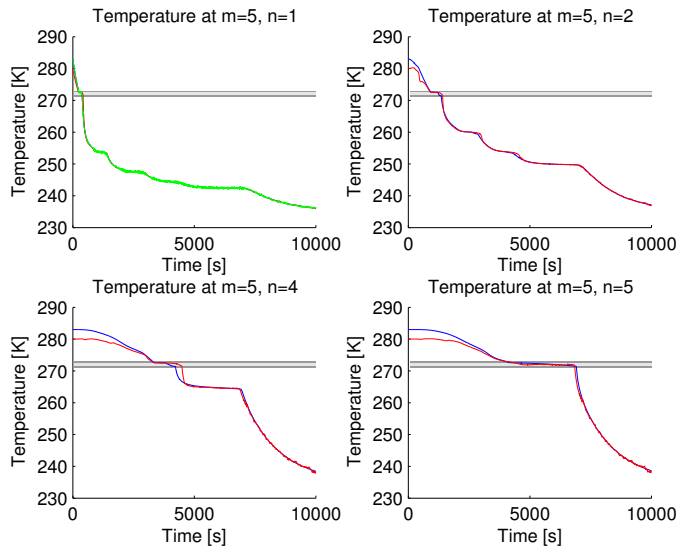


Figure 11.11: Results for the reduced model observer at $m = 5$ and different positions along the x -axis for switched Q and R and identical parameter definitions

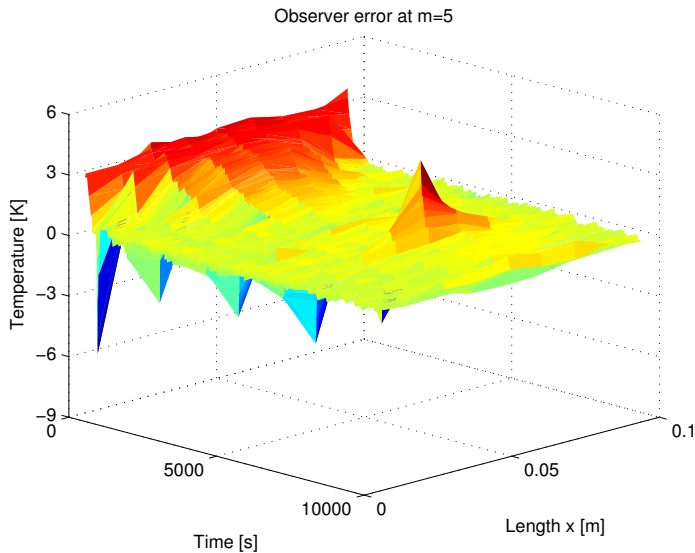


Figure 11.12: A 3-dimensional plot for the reduced model observer at $m = 5$ for switched Q and R and identical parameter definitions

der to improve performance, $\Phi_1 = \text{diag}([1 \ 10 \ 100 \ 100 \ 10 \ 100 \ 100 \ 10 \ 1])$. Also the amount of presented Figures will be limited in order to show qualitative results.

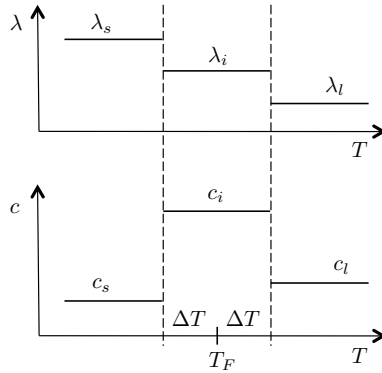


Figure 11.13: Step-wise definition of the parameter function definitions for the real-time applicable reduced observer case

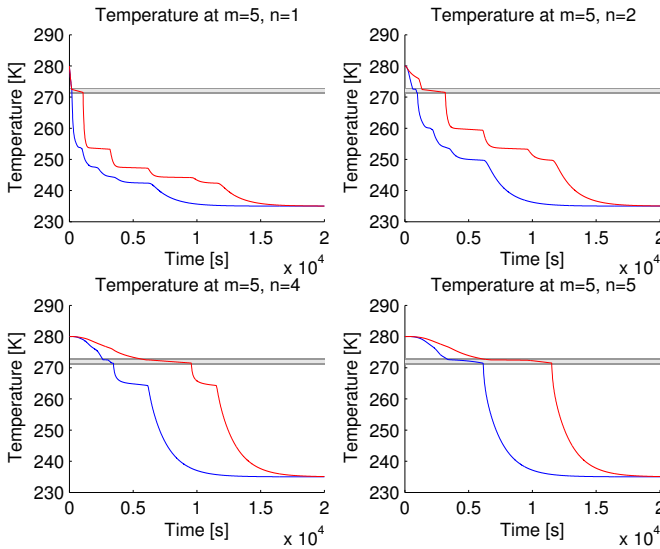


Figure 11.14: Comparison between the dynamics of the plant (blue) and those of the observer (red) at $m = 5$ and different positions along the x -axis for the parameters as defined in Figure 11.13 and identical parameter definitions

The simulations have been conducted with the fixed step solver ode8 of MATLAB[®] with a step size of 1 s. The results are illustrated in Figures 11.15, 11.16 and 11.17, where very good convergence in and after the latent zone is shown for the real-time applicable case. These results are obtained for identical parameter values for plant and observer, respectively. The estimation errors at positions $m = 3$ and $m = 5$ are very small after an initial phase with larger errors.

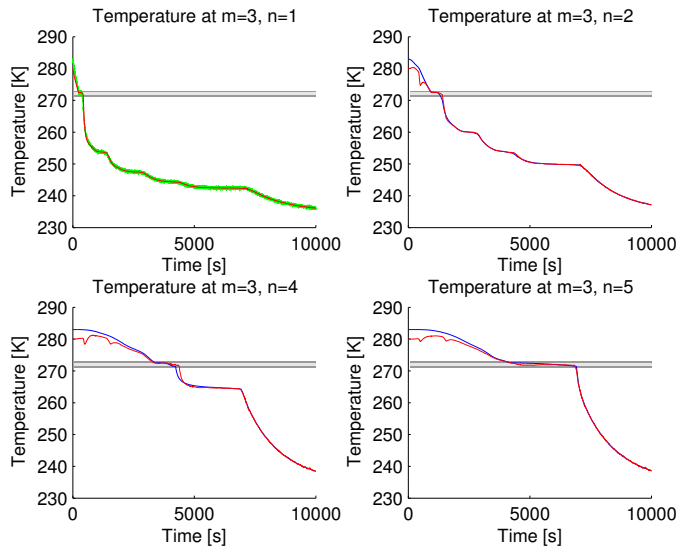


Figure 11.15: Results for the real-time applicable observer at $m = 3$ and different positions along the x -axis for switched Q and R and identical parameter definitions

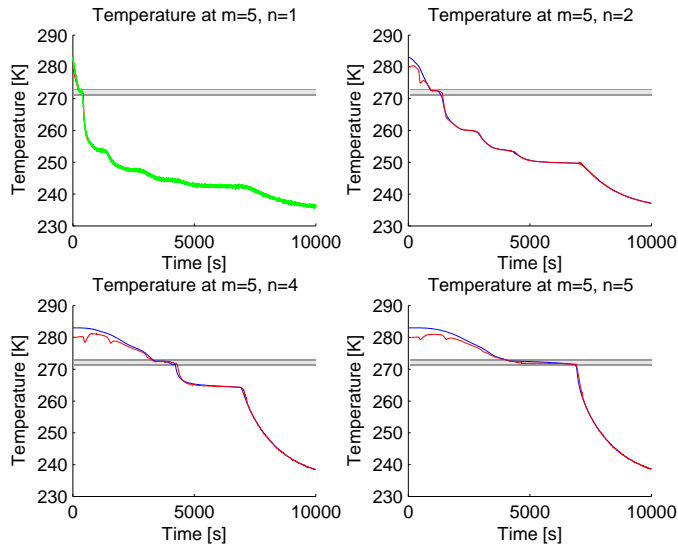


Figure 11.16: Results for the real-time applicable observer at $m = 5$ and different positions along the x -axis for switched Q and R and identical parameter definitions

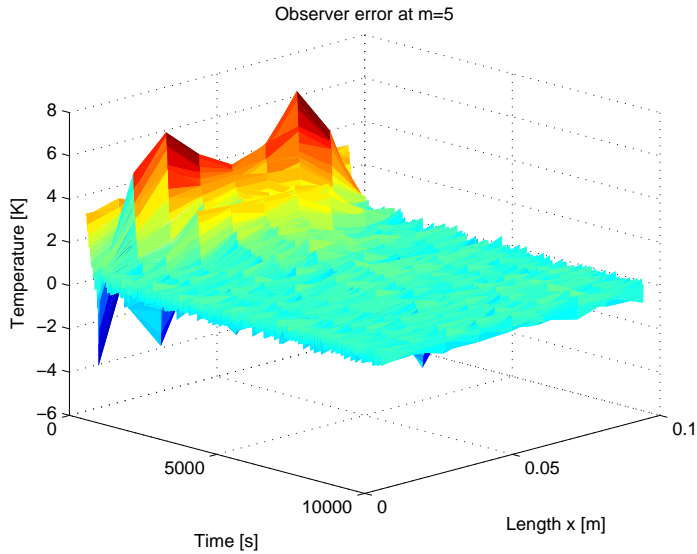


Figure 11.17: A 3-dimensional plot for the real-time applicable observer at $m = 5$ for switched Q and R and identical parameter definitions

Now the parameters $k(T)$, $\kappa(T)$ and ΔT are set back to differing values, meaning that those of the observer are again twice as large as those of the plant. The corresponding simulation results are presented in Figures 11.18, 11.19 and 11.20. These illustrate slightly worse convergence quality than for the case presented before, especially in the beginning of the simulation before entering the latent zone, where the estimation error is quite large. However, the estimation errors go back to a region around zero not only by the end of the simulation time, but also in the latent zone.

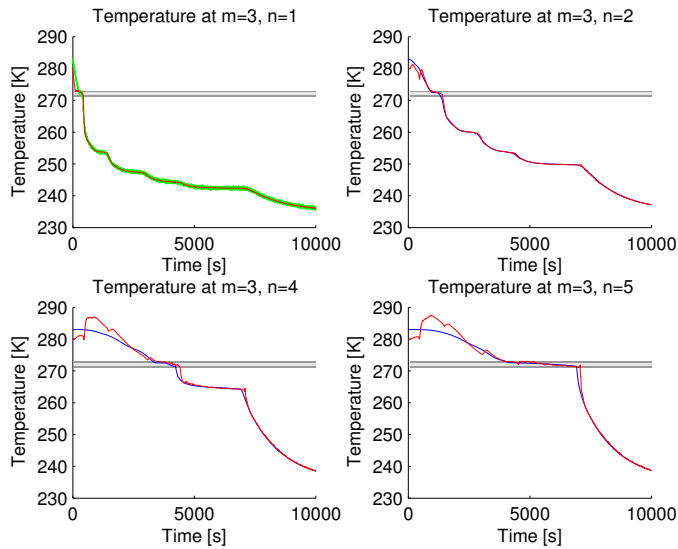


Figure 11.18: Results for the real-time applicable observer at $m = 3$ and different positions along the x -axis for switched Q and R and differing parameter definitions

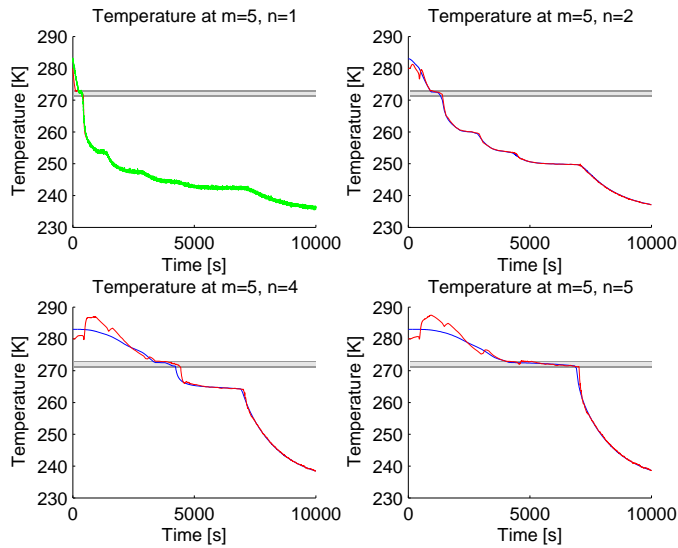


Figure 11.19: Results for the real-time applicable observer at $m = 5$ and different positions along the x -axis for switched Q and R and differing parameter definitions

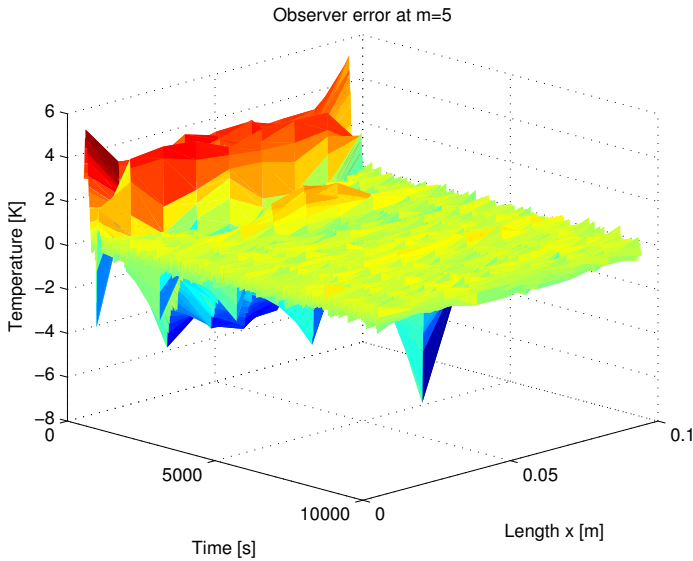


Figure 11.20: A 3-dimensional plot for the real-time applicable observer at $m = 5$ for switched Q and R and differing parameter definitions

Comments on the real-time applicable observer

The system as defined by the parameters shown in Figure 11.13 represents three interconnected linear heat equations. Each of these has a constant thermal diffusivity k in a defined temperature region. Therefore, the system can be considered to be a switched system of linear heat equations.

The question of stability of this switched system of PDEs automatically arises. It is known from the theory of switched systems with state-dependent switching that unstable behavior can occur as a consequence of switching, see Branicky [22]. This happens when the switching occurs at *disadvantageous state instances*, see also Leth et al. [74] for another example, where switching can potentially lead to unstable behavior. Showing stability for such systems in the world of ODEs is a challenging task; in the world of PDEs this task is even more challenging.

However, it is known that the heat equation has certain damping properties, in particular the damping of singularities that are likely to occur. In fact, the boundary conditions as chosen in (6.2) pose such singularities to the model (6.6) as their formulation is not consistent with the initial condition. This can be illustrated by the following example:

Define the linear heat equation

$$u_t = ku_{xx}$$

with boundary conditions

$$u(0,t) = 0, \quad u(L,t) = 0$$

and initial condition

$$u(x, 0) = f(x).$$

Now it can be seen that for the initial condition at the boundary it must hold

$$u(0, 0) = f(0) = 0, \quad u(L, 0) = f(L) = 0.$$

This, however, does not hold for the freezing and thawing cases that are the basis for this thesis. Nevertheless, defining the boundary and initial conditions in the forms presented in Chapter 6 is correct as they model the real world application of freezing and thawing.

Choosing the boundary and initial conditions for the freezing and thawing cases is not the only possible singularity for the heat equation. Changing parameters in a step-wise manner can also be counted as a singularity. In addition, adding noise in the initial conditions will count as such. All of these singularities are known to be canceled out after a while due to the aforementioned damping character.

For other PDEs, however, this damping character is not necessarily present. Adding noise to the initial condition of a wave equation will not be damped, but is likely to travel through the spatial domain and, depending on the boundary conditions, being reflected.

Chapter 12

Full model inner-domain temperature estimation for thawing

In this Chapter an observer design similar to the one presented in Chapter 10 is introduced. The same measurements are assumed to be available, however, the discretization scheme is changed to the one described in (6.13). The boundary conditions are of the same type, but of course, have different values.

In general, estimation of temperatures for thawing in the proposed setup is harder to obtain than for the freezing case. This has to do with the fact that the object's interior should only be thawed just above the freezing point, meaning that the core temperature should just be outside the latent zone. As the real values for the parameters $k(T)$, $\kappa(T)$ and ΔT are unknown and due to the fact that differences in these parameters have a big influence on the resting time in the latent zone, correct estimation is harder to achieve. The white Gaussian noise added to the output makes this task even harder.

12.1 Simulation examples

Like in the two Chapters about estimation of inner-domain temperatures for freezing processes, also for the thawing case an investigation of the dynamical responses of the plant and the observer has to be conducted. This happens for parameter functions $k(T)$, $\kappa(T)$ and ΔT , which are chosen to be double the size for the observer compared to the plant. The simulation results for this case are shown in Figure 12.1.

As can be seen the observer dynamics in red are faster than those of the plant in blue. This is due to the differing parameter values and corresponds to the results that could be seen in Figure 10.3. The simulation parameters are the same as in Chapters 10 and 11, besides the initial and boundary conditions and are displayed in Table 12.1 for completeness. However, the initial conditions have been chosen to be alike for the comparative plots.

The values for the covariance matrices Q and R were newly tuned for the thawing case and hold for this Chapter, as well as in the upcoming Chapter 13, where reduced observer

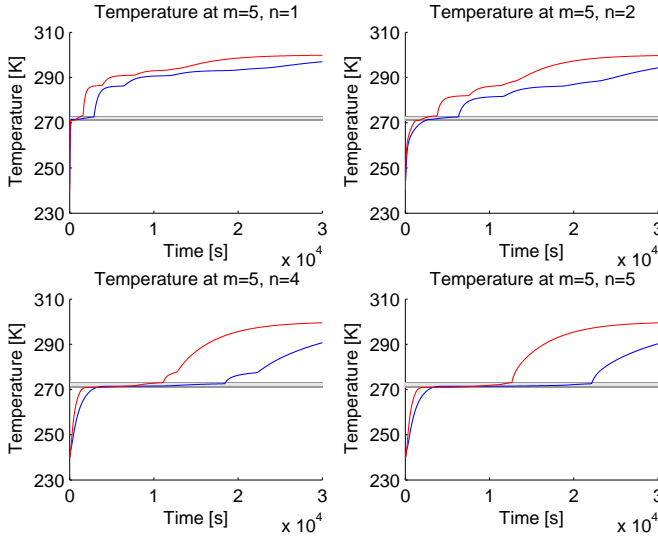


Figure 12.1: Comparison between the dynamics of the plant (blue) and those of the observer (red) at $m = 5$ and different positions along the x -axis for differing parameter definitions

designs corresponding to those of Chapter 11 are presented.

$$R_1 = 10^5 \begin{bmatrix} \Gamma & 0 & 0 & 0 & 0 \\ 0 & \Sigma & 0 & 0 & 0 \\ 0 & 0 & \Sigma & 0 & 0 \\ 0 & 0 & 0 & \Sigma & 0 \\ 0 & 0 & 0 & 0 & \Sigma \end{bmatrix}, \quad R_2 = 10^4 \begin{bmatrix} \Gamma & 0 & 0 & 0 & 0 \\ 0 & \Sigma & 0 & 0 & 0 \\ 0 & 0 & \Sigma & 0 & 0 \\ 0 & 0 & 0 & \Sigma & 0 \\ 0 & 0 & 0 & 0 & \Sigma \end{bmatrix}$$

$$Q_1 = 10^2 \begin{bmatrix} \Gamma & 0 & 0 & 0 & 0 \\ 0 & \Phi_1 & 0 & 0 & 0 \\ 0 & 0 & \Phi_1 & 0 & 0 \\ 0 & 0 & 0 & \Phi_1 & 0 \\ 0 & 0 & 0 & 0 & \Phi_1 \end{bmatrix}, \quad Q_2 = 10^1 \begin{bmatrix} \Gamma & 0 & 0 & 0 & 0 \\ 0 & \Phi_2 & 0 & 0 & 0 \\ 0 & 0 & \Phi_2 & 0 & 0 \\ 0 & 0 & 0 & \Phi_2 & 0 \\ 0 & 0 & 0 & 0 & \Phi_2 \end{bmatrix}$$

$$\Gamma = I_{(9 \times 9)}$$

$$\Sigma = \begin{bmatrix} 10 & 0 \\ 0 & 10 \end{bmatrix}$$

$$\Phi_1 = \text{diag}([1 \ 10 \ 10 \ 10 \ 10 \ 10 \ 10 \ 10 \ 1])$$

$$\Phi_2 = \text{diag}([1 \ 1 \ 10 \ 100 \ 100 \ 100 \ 10 \ 1 \ 1])$$

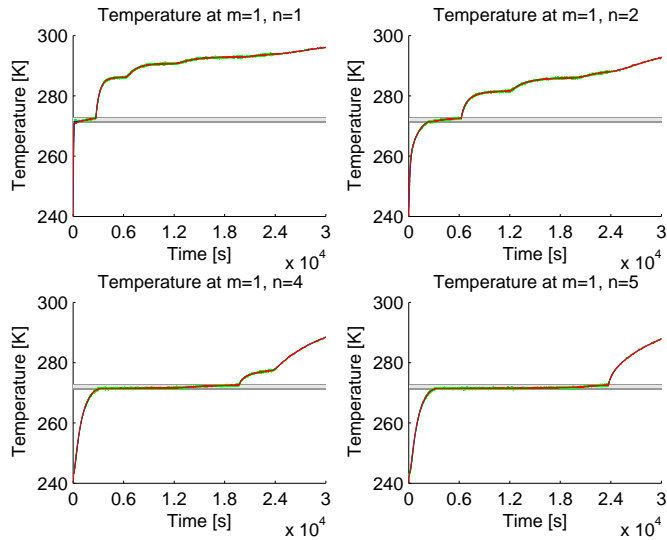
12.1.1 Results for constant covariance matrices Q and R

In this Subsection results for constant covariance matrices Q and R over the whole simulation time are presented. Figure 12.2 displays results for $m = 1$ and different positions

L	0.1	m
H	0.5	m
T_F	272	K
$T_{init,EKF}$	240	K
$T_{init,Sys}$	243	K
ΔT_{EKF}	1	K
ΔT_{Sys}	0.5	K
δT	0.1	K
$T_{Boundary}$	300	K
T_{Air}	278	K
c_s	2200	J kg ⁻¹ K ⁻¹
c_l	3800	J kg ⁻¹ K ⁻¹
c_i	283000	J kg ⁻¹ K ⁻¹
ρ	950	kg m ⁻³
λ_s	1.8	W m ⁻¹ K ⁻¹
λ_l	0.5	W m ⁻¹ K ⁻¹

Table 12.1: Simulation parameters for the observer design cases for thawing

along the x -axis. All states are estimated correctly, even in the presence of added measurement noise. This is due to the fact that all measurements are available and could be expected from the results of the observer designs for the freezing case.

Figure 12.2: Results for the full model observer at $m = 1$ and different positions along the x -axis for constant Q and R

In Figure 12.3 a zoom into the latent zone at $m = 1$ and $n = 5$ is presented. Again, the state can be estimated correctly, even for differing parameter functions. What happens if the measurements are not available can be seen in Figure 12.5.

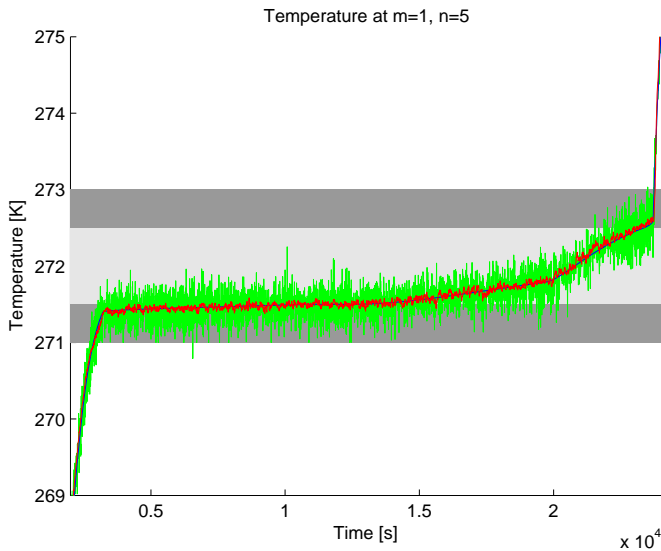


Figure 12.3: Results for the full model observer at $m = 1$ and $n = 5$ for constant Q and R , zoom into the latent zone

Figure 12.4 depicts similar plots like in Figure 12.2, but now at $m = 3$. It can be seen that at position $m = 3$ and $n = 1$ the estimation has very low error. This is again due to the fact that the measurement at this position is available. For the other positions the error becomes larger the further the specific position is away from the measurement. However, the plots clearly show convergence of the observer states towards the states of the plant.

Figure 12.5 shows a zoom into the latent zone at $m = 3$ and $n = 5$. The converging trend is obvious, however, the estimated state is off the real state due to the fact that the latent zone for the observer is chosen to be double the size compared to the plant.

In Figure 12.6 similar plots compared to those shown in Figures 12.4 and 12.2 are presented. The estimation error gets larger the further the respective positions are from the boundary, but convergence of the observer to the real states is better than for the open-loop case presented in Figure 12.1, meaning that the error is smaller. By comparing it can be seen that the latent zone is estimated quite well, but still an estimation error is present after crossing the latent zone.

Figure 12.7 depicts a 3-dimensional plot of the estimation error at $m = 5$ to illustrate convergence of the observer at this position along the whole x -axis.

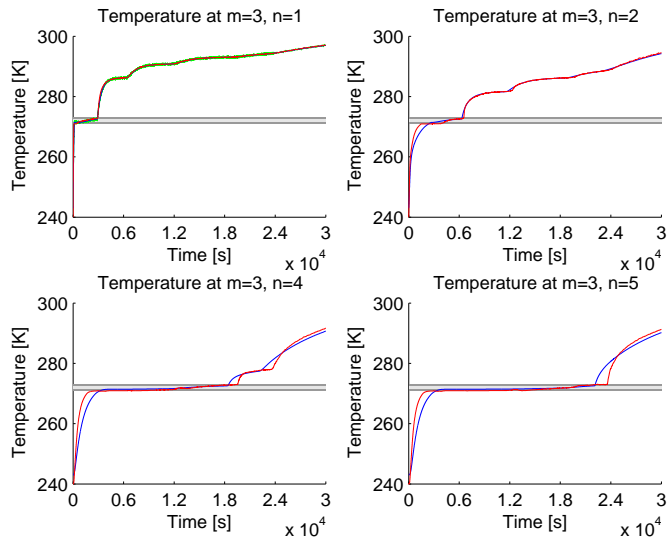


Figure 12.4: Results for the full model observer at $m = 3$ and different positions along the x -axis for constant Q and R

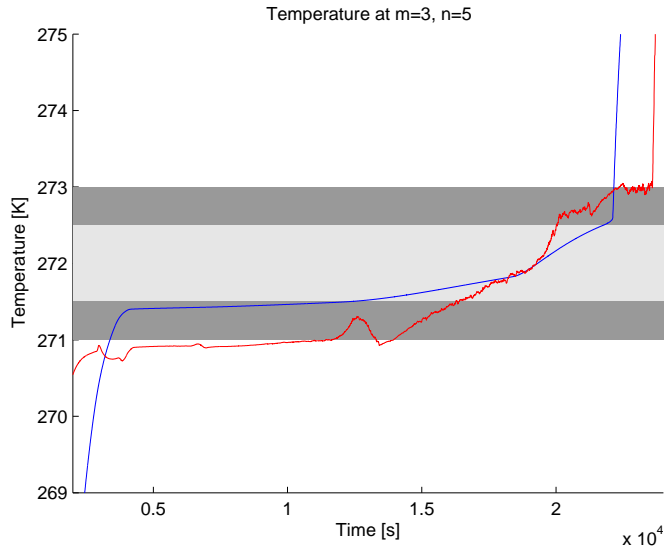


Figure 12.5: Results for the full model observer at $m = 3$ and $n = 5$ for constant Q and R , zoom into the latent zone

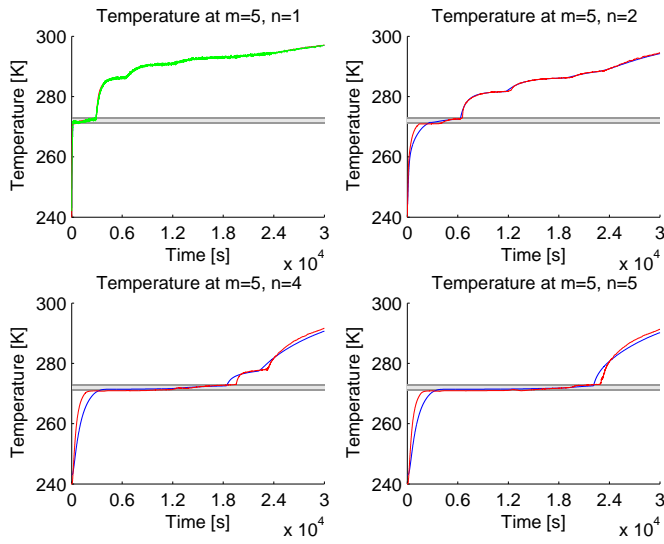


Figure 12.6: Results for the full model observer at $m = 5$ and different positions along the x -axis for constant Q and R

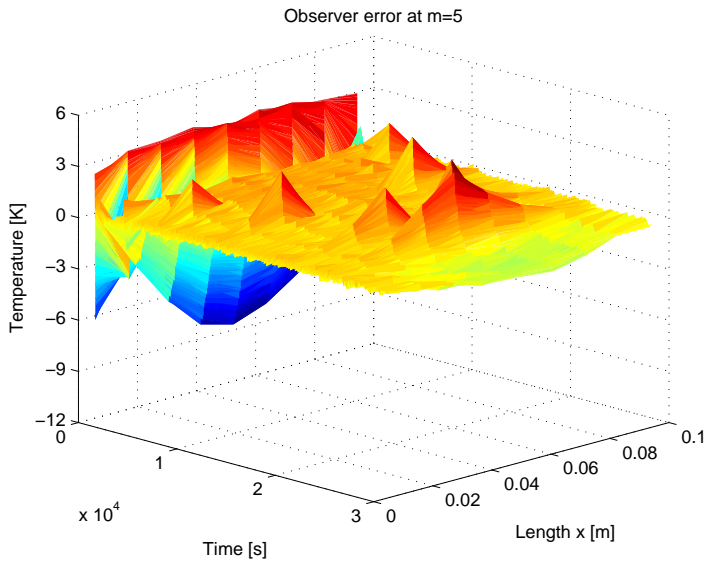


Figure 12.7: A 3-dimensional plot of the estimation error for the full observer at $m = 5$ for constant Q and R

12.1.2 Results for switched covariance matrices Q and R

Like already known from the previous Chapters about estimation of freezing processes, observer performance can be improved by switching the covariance matrices Q and R after crossing the latent zone $I_{\Delta T}$. The switching from Q_1 to Q_2 and R_1 to R_2 happens now after the measurable state $T_{1,5}$ is bigger than 273 K. Like in Section 10.4.2 only three Figures will be presented in order to illustrate the enhanced estimation after crossing the freezing point.

Figure 12.8 shows the results attained for switched covariance matrices at $m = 3$ for different positions along the x -axis. By directly comparing it to Figure 12.4, a significant improvement is not directly perceivable as the estimation errors look about the same. However, as will be seen by comparing the three-dimensional plots (Figures 12.10 and 12.7), the switching has a slight positive effect on the estimation error.

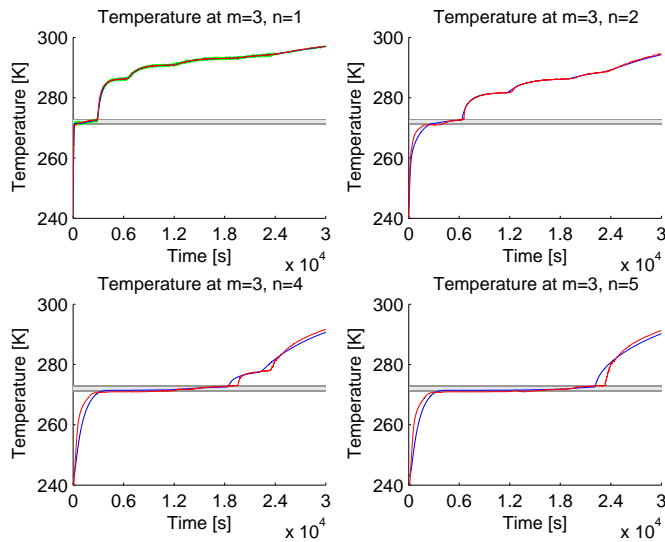


Figure 12.8: Results for the full model observer at $m = 3$ and different positions along the x -axis for switched Q and R

Figure 12.9 shows similar responses of the observer compared to Figure 12.6. Again, like in Figure 12.8 an improvement in performance is not directly noticeable. Nevertheless, the states are estimated quite accurately when compared to the open-loop simulation presented in Figure 12.1.

In Figure 12.10 a 3-dimensional plot of the estimation error at $m = 5$ along the x -axis is presented. By comparing it to Figure 12.7 with respect to the color pattern, the estimation error is slightly lower and thus an actual improvement is obtained by switching the covariance matrices Q and R .

It must be mentioned that with different tuning of the covariance matrices, better estima-

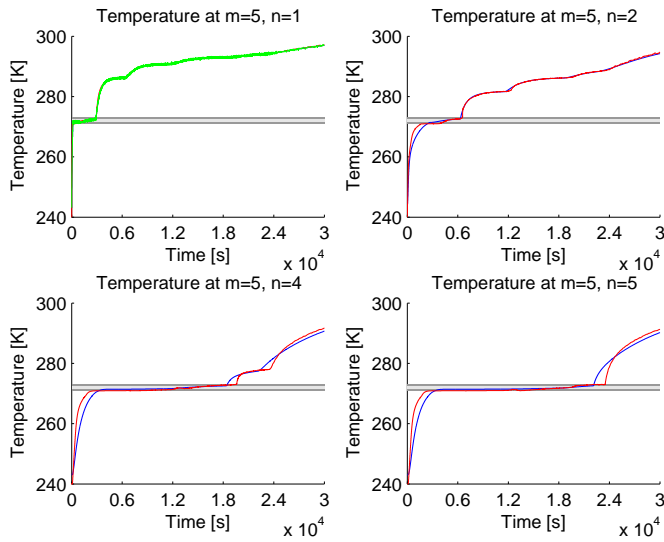


Figure 12.9: Results for the full model observer at $m = 5$ and different positions along the x -axis for switched Q and R

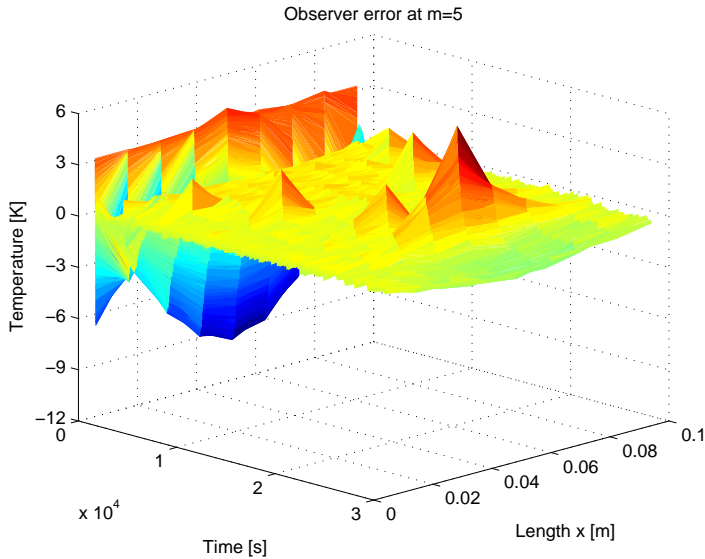


Figure 12.10: A 3-dimensional plot of the estimation error for the full observer at $m = 5$ for switched Q and R

tion and thus lower errors could be achieved. However, for reasons of comparability, only the results for covariance matrices of the same values are presented in this Chapter.

Chapter 13

Reduced model inner-domain temperature estimation for thawing

In this Chapter, an observer design similar to the one presented in Chapter 11 is introduced, namely for reduced descriptions of the observer dynamics in the case of thawing. This is again achieved by defining the observer's parameters differently compared to those of the plant, meaning that only parameter definitions have been regarded for which $\kappa(T) = 0$ such that the term $\kappa(T)T_x^2$ vanishes.

13.1 Simulation examples

As outlined in Chapter 12 the task of estimating the temperatures for the thawing case is harder compared to that for freezing. One reason for this is that the time it takes to cross the latent zone is significantly higher for the thawing case compared to the freezing case. This can be seen in Figure 13.1, where a comparative plot for differing parameter values of plant and observer is shown. The covariance matrices Q_1 , Q_2 , R_1 and R_2 in this Chapter are based on the definitions in Chapter 12

13.1.1 Results for constant covariance matrices Q and R

The simulations were conducted for constant covariance matrices $Q = Q_1$ and $R = R_1$. Figures show the same positions as already depicted in Section 12.1.1 for the full observer design case for direct comparison.

Hence, Figure F.4 presents simulation results for $m = 1$ at different x -positions. Accurate estimation is achieved due to the fact that the (noisy) measurements are available.

Figure F.5 zooms into the latent zone at $m = 1$ and $n = 5$. The green curve shows the noisy measurement signal. Still, accurate estimation is ensured as all states are assumed measurable for this position.

In Figure 13.2, results for $m = 3$ and different positions along the x -axis are presented. The estimation error is quite low, however, becomes larger the further the specific position is

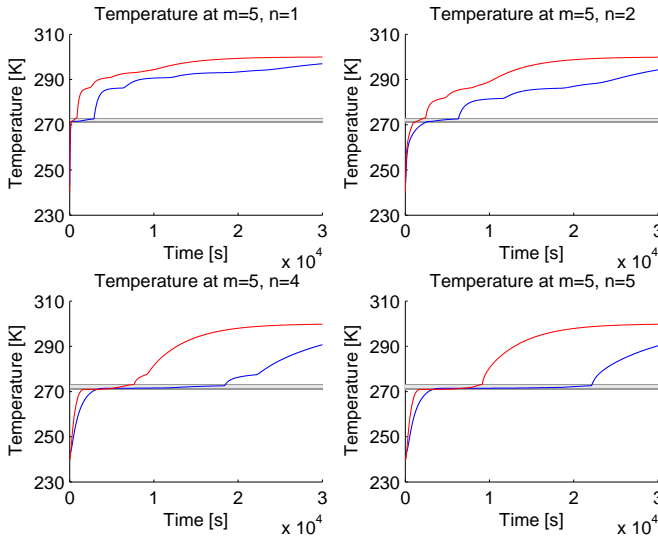


Figure 13.1: Comparison between the dynamics of the plant (blue) and those of the observer (red) at $m = 5$ and different positions along the x -axis for parameter definitions that can be found in Table 12.1

away from the boundary. However, the latent zone is captured quite well in all of the plots and the estimation error is small after crossing the latent zone.

Figure F.6 shows a zoom into the latent zone at $m = 3$ and $n = 5$. The latent zone for the observer is chosen to be double the size compared to the plant and thus an estimation error is present. Nevertheless, convergence of the observer states towards the real states can be seen.

Figure 13.3 shows results for the bottom of the domain ($m = 5$) and depicts low estimation errors and good estimation of the latent zone for the respective positions along the x -axis, especially when compared to the open-loop simulations displayed in Figure 13.1. The latent zone is captured quite well and the estimation errors after crossing the latent zone are fairly small.

In Figure 13.4 a 3-dimensional plot of the estimation error at $m = 5$ along the whole x -domain is presented. It shows that the estimation error is brought back to a region around zero during the simulation time.

13.1.2 Results for switched covariance matrices Q and R

As shown in Section 12.1.2, observer performance can be improved by switching the observer covariance matrices Q and R . The switching between Q_1 and Q_2 as well as R_1 and R_2 occurs when $T_{1,5} > 273$ K. This is done in order to obtain more accurate estimation results after crossing the latent zone. The results presented in this Subsection serve as a comparative study to the results shown in Section 13.1.1 and therefore only three Figures

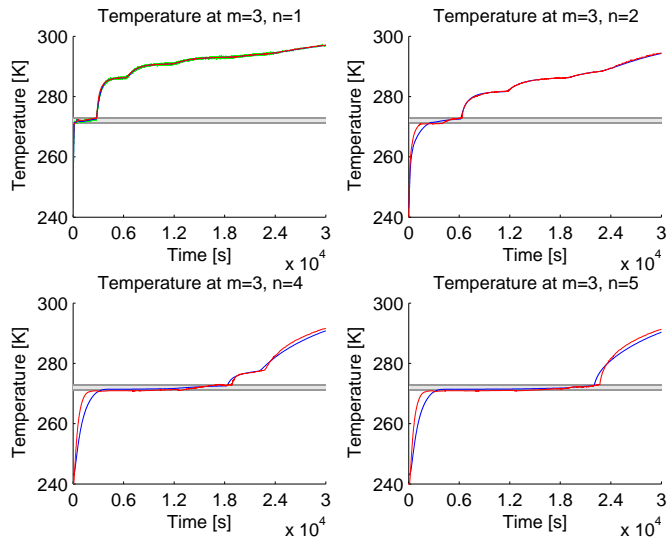


Figure 13.2: Results for the reduced model observer at $m = 3$ and different positions along the x -axis for constant Q and R

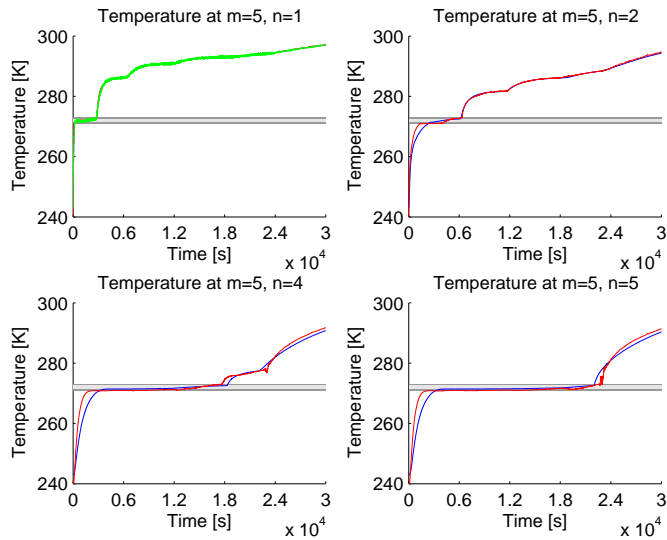


Figure 13.3: Results for the reduced model observer at $m = 5$ and different positions along the x -axis for constant Q and R

will be presented to display the slightly enhanced quality of estimation, meaning that lower estimation errors can be achieved.

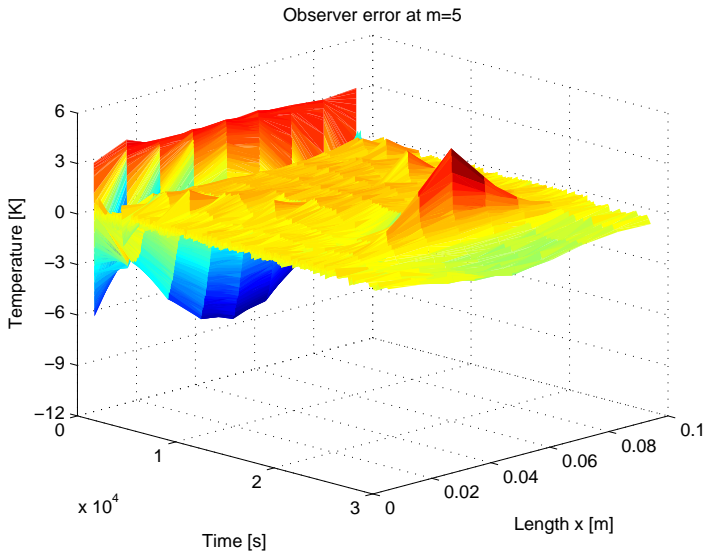


Figure 13.4: A 3-dimensional plot of the estimation error for the reduced observer at $m = 5$ for constant Q and R

In Figure 13.5, results at $m = 3$ and different positions along the x -axis for switched Q and R are presented. Slightly faster convergence and lower estimation errors are achieved, as can be seen by comparison to Figure 13.2.

Figure 13.6 shows somewhat faster convergence after crossing the latent zone for $m = 5$ and different positions along the x -axis, when compared to Figure 13.3. Furthermore, it can be seen that the estimation error is smaller and that the latent zone is estimated in the same manner.

In Figure 13.7 the estimation error at $m = 5$ is displayed. It is perceivable that the absolute values of the error are smaller than for the case with constant covariance matrices Q and R in Figure 13.4 by direct comparison.

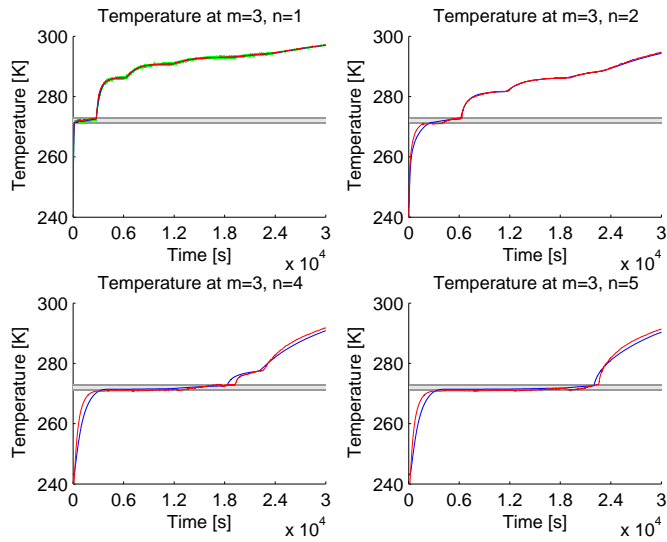


Figure 13.5: Results for the reduced model observer at $m = 3$ and different positions along the x -axis for switched Q and R

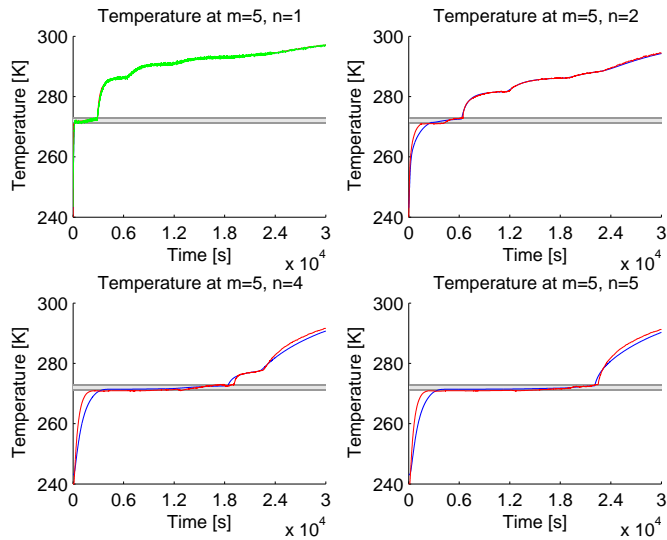


Figure 13.6: Results for the reduced model observer at $m = 5$ and different positions along the x -axis for switched Q and R

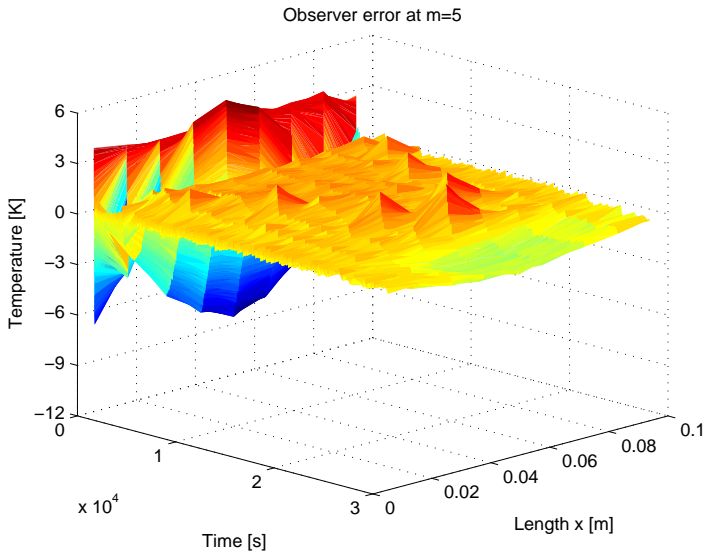


Figure 13.7: A 3-dimensional plot for the reduced model observer at $m = 5$ for switched Q and R

13.1.3 Simulations for perfect knowledge of the parameter values

Also for the thawing case an investigation for the reduced observer design and perfect knowledge of the parameter values is important. This is due to significant variances in convergence times for the reduced observer and the plant. This has been introduced for freezing in Section 11.2.3 and will be covered also here for completeness. The difference in response for identical parameters for the observer and the plant is shown in Figure 13.8.

It can be seen that the differences between the respective dynamics are significant. In the sequel only simulations for switched Q and R will be presented, as this approach has shown itself favorable with respect to performance.

Thus, Figure 13.9 depicts results for $m = 3$ at different positions along the x -axis. The estimation error is brought back to a region around zero after crossing the latent zone and the latent zone itself is estimated correctly. However, the case for $m = 3$ and $n = 4$ shows larger estimation errors than for the other presented cases. Nevertheless, these get brought back to zero by the end of the simulation time.

In Figure 13.10 results for $m = 5$ at different positions along the x -axis are depicted and better convergence than in Figure 13.9 is shown. The estimation error is small and the latent zone is estimated well.

The observer error at $m = 5$ over the spatial domain x is presented in Figure 13.11 for illustration purposes.

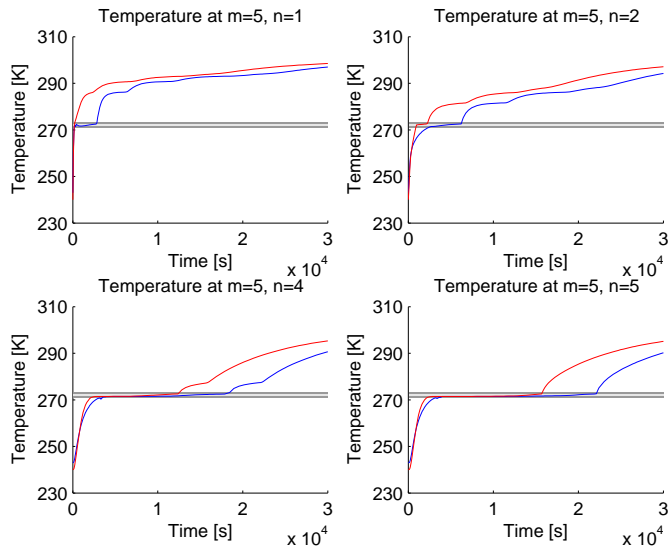


Figure 13.8: Comparison between the dynamics of the plant (blue) and those of the observer (red) at $m = 5$ and different positions along the x -axis for parameter functions with identical values

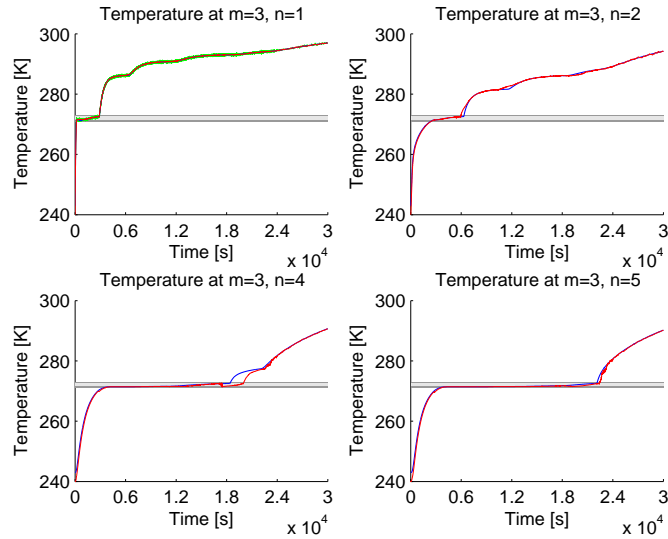


Figure 13.9: Results for the reduced model observer at $m = 3$ and different positions along the x -axis for switched Q and R and identical parameter definitions

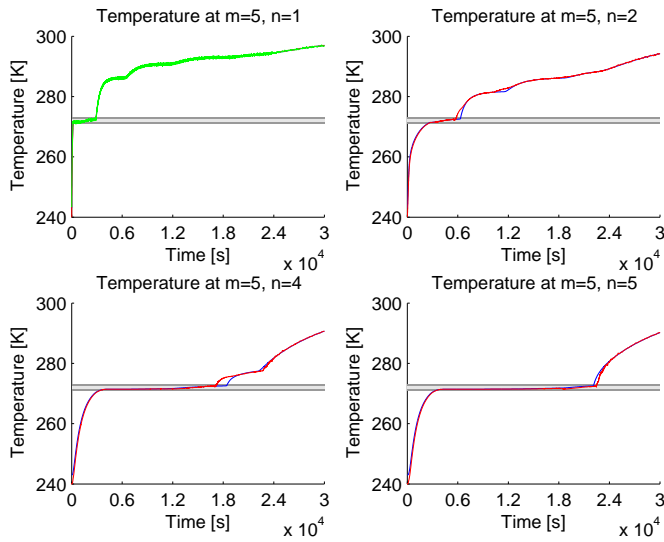


Figure 13.10: Results for the reduced model observer at $m = 5$ and different positions along the x -axis for switched Q and R and identical parameter definitions

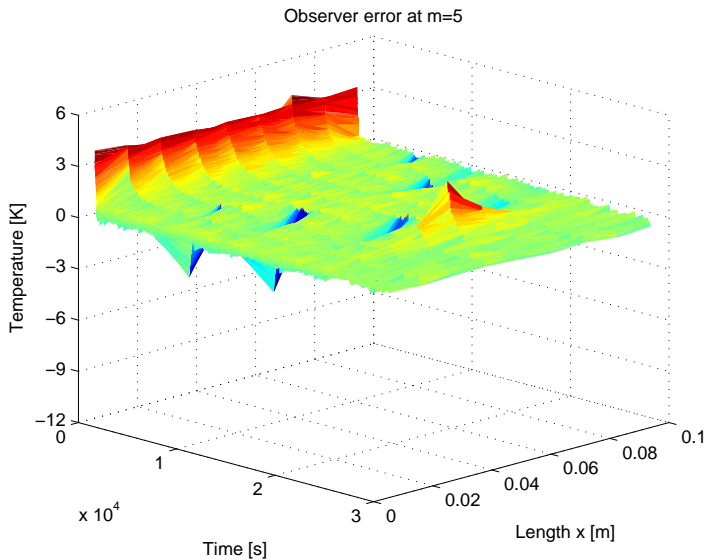


Figure 13.11: A 3-dimensional plot for the reduced model observer at $m = 5$ for switched Q and R and identical parameter definitions

13.2 Real-time applicable observer

In this Section a real-time applicable design is tested. This was introduced in Section 11.2.4 for the freezing case.

In Figures 13.12, 13.13 and 13.14 the simulation results for the case with identical parameter values for $k(T)$, $\kappa(T)$ and ΔT are presented. The estimation errors are quite small, except in the transient phase just before entering the latent zone, where the observer produces some error by predicting a wrong negative slope for all non-measurable states. Compared to the simulation time, however, this error gets evened out fairly fast.

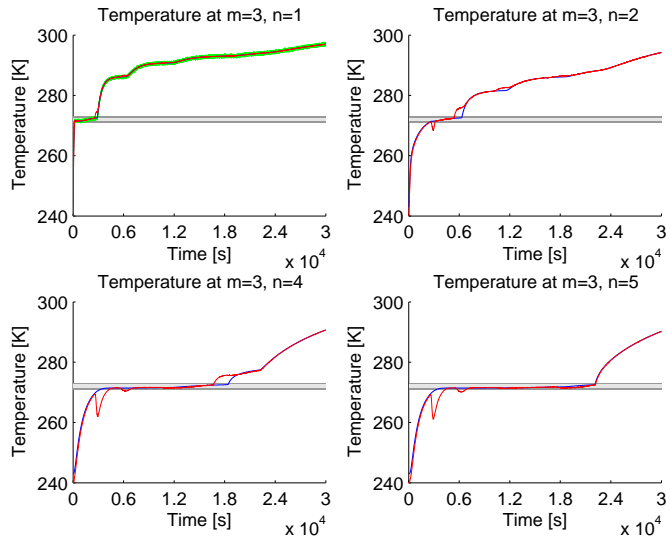


Figure 13.12: Results for the real-time applicable observer at $m = 3$ and different positions along the x -axis for switched Q and R and identical parameter definitions

If the parameters $k(T)$, $\kappa(T)$ and ΔT are set back to differing values, meaning those of the observer are chosen twice as big as those of the plant, the simulation results still look good in terms of convergence rate and accuracy. Figures 13.15, 13.16 and 13.17 depict that even for this case the real-time applicable observer offers a good and satisfying performance. Only in the transient phase before entering the latent zone a significant estimation error is present, which gets evened out fast. The latent zone is estimated quite well and only a little estimation error is present after crossing the latent zone.

The high quality of estimation for the real-time applicable observer might be due to *advantageous noise patterns* for these cases. Other noise patterns might give different results, as could be seen while conducting dozens of simulations with randomized white Gaussian noise. This might be the reason why, at least for the thawing case, the real-time applicable observer delivered these good results.

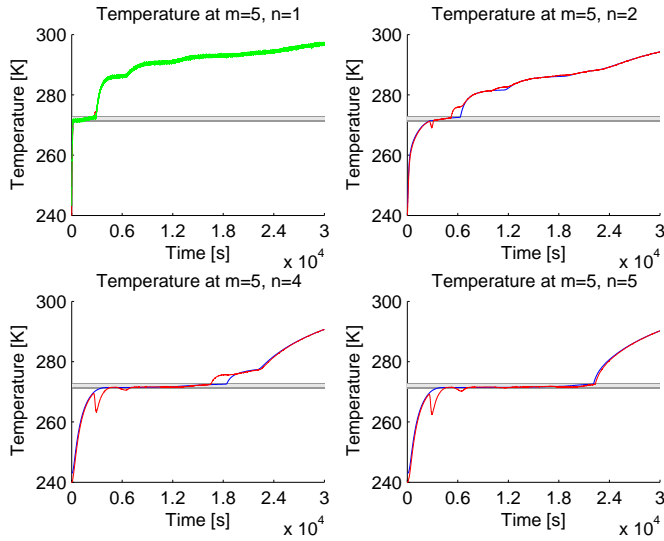


Figure 13.13: Results for the real-time applicable observer at $m = 5$ and different positions along the x -axis for switched Q and R and identical parameter definitions

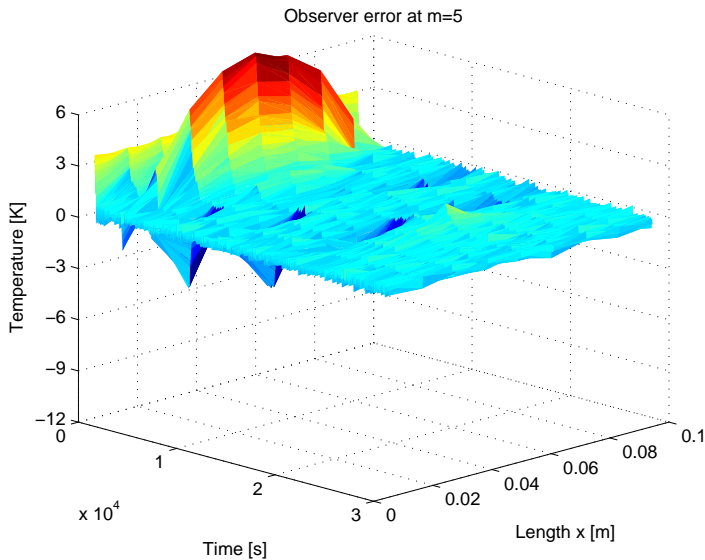


Figure 13.14: A 3-dimensional plot for the real-time applicable observer at $m = 5$ for switched Q and R and identical parameter definitions

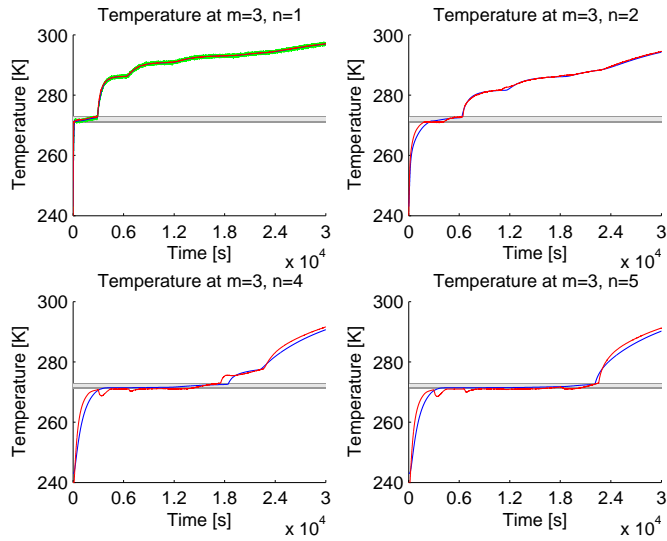


Figure 13.15: Results for the real-time applicable observer at $m = 3$ and different positions along the x -axis for switched Q and R and differing parameter definitions

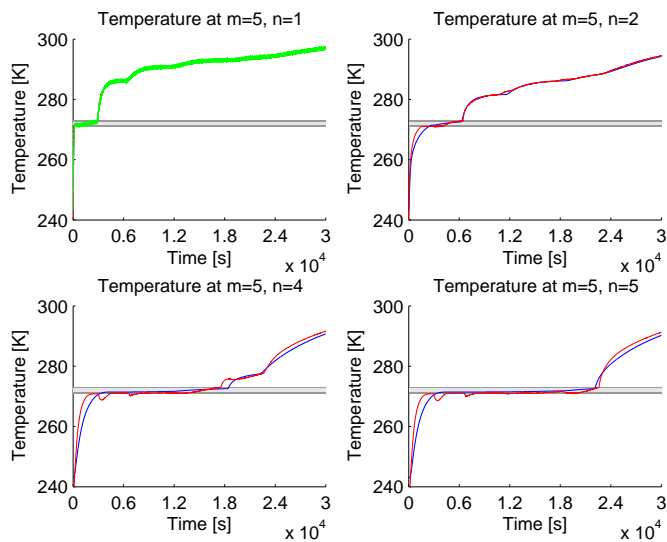


Figure 13.16: Results for the real-time applicable observer at $m = 5$ and different positions along the x -axis for switched Q and R and differing parameter definitions

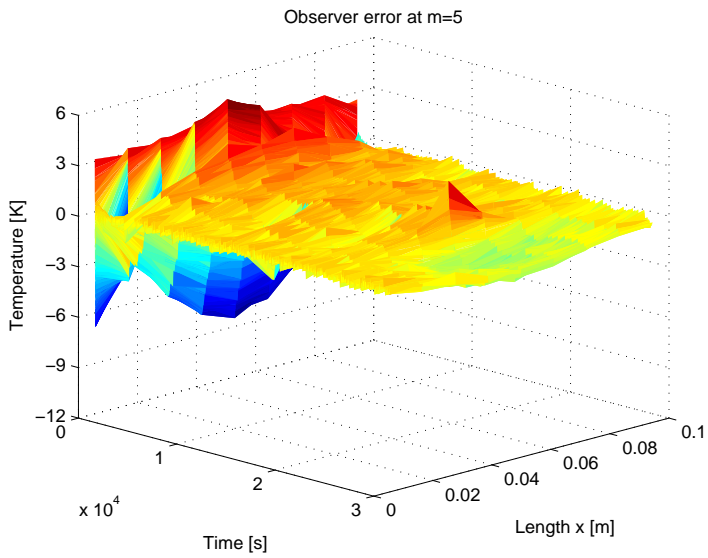


Figure 13.17: A 3-dimensional plot for the real-time applicable observer at $m = 5$ for switched Q and R and differing parameter definitions

Chapter 14

Introduction to Optimal control and problem formulation

14.1 Introduction to Optimization

Generally, optimization, or more precisely mathematical optimization (earlier *mathematical programming*), is used in order to find a best element among existing alternatives. Usually it is used to find a minimum or a maximum to some objective function with respect to an input. This is called an optimization problem, which in general can be divided into two main branches, namely discrete and continuous optimization problems. A standard form of a continuous optimization problem looks as follows:

$$\underset{s}{\text{minimize}} \quad f(s) \tag{14.1a}$$

$$\text{subject to} \quad g_i(s) \leq 0, \quad i = 1, \dots, m \tag{14.1b}$$

$$h_j(s) = 0, \quad j = 1, \dots, p, \tag{14.1c}$$

where $f(s)$ denotes the objective function, $g_i(s)$ indicates inequality constraints and $h_j(s)$ represents equality constraints.

A maximization problem for the objective $f(s)$ is simply achieved by changing its sign in the minimization problem, thus it holds

$$\underset{s}{\text{minimize}} \quad f(s) = \underset{s}{\text{maximize}} \quad -f(s).$$

The minimization problem (14.1) formulated as a maximization problem is thus simply

$$\underset{s}{\text{minimize}} \quad -f(s) \tag{14.2a}$$

$$\text{subject to} \quad g_i(s) \leq 0, \quad i = 1, \dots, m \tag{14.2b}$$

$$h_j(s) = 0, \quad j = 1, \dots, p. \tag{14.2c}$$

A broad introduction to (Numerical) Optimization is provided by Nocedal and Wright [84]. However, for completeness the most important concepts in optimization are introduced here.

Constrained and unconstrained optimization: As the names suggests, there exists both, problems that are subject to constraints and problems that are not. Most technical and engineering applications, however, are constrained. A typical constraint for engineering applications is e.g. posed by the dynamical equations of the system. In addition, environmental factors pose limitations and constraints, e.g. for the optimization variable.

Global and local optimization: Most optimization algorithms only look for a local solution, meaning that for this point the objective function is smaller than for all feasible solutions in its vicinity. Global solutions on the other hand provide the smallest value of the objective function for all feasible points.

Convexity: This property is important for optimization problems as convex problems are generally easier to solve, both in theory and practice. Convexity often holds for the objective function, however, in order to obtain a *convex programming problem*, in addition the equality constraints must be linear and the inequality constraints convex. The latter two requirements are often not the case, due to physical limitations, at least for engineering applications.

14.2 Introduction to Optimal Control

Optimal Control is a branch of optimization and uses optimization tools in order to find an optimal solution to a problem with respect to constraints. For Optimal Control Problems (OCP) these constraints often include a dynamical system; thus these problems are often called dynamic optimization. In general, Optimal Control provides an optimal input function to a dynamical system model, which minimizes a cost function over a (fixed) time horizon subject to the dynamical system. Furthermore, it can be designed to fulfill constraints arising from physical limitations of the system and / or desired limitations to the states and inputs. In the subsequent investigation the focus lies on time-continuous nonlinear Optimal Control Problems. There are several methods to solve these problems: Solving a Hamilton-Jacobi-Bellmann PDE (HJB-PDE) which tries to find a solution for all $x(t)$ and provides a state-feedback law in the form $u = k(x)$ rendering it valid for all initial conditions. Euler-Lagrange differential equations (EL-DE) deliver an explicit time-continuous solution $u(\tau)$, which is only valid for a specific initial condition. Direct methods using a finite discretization in time yield inputs in the finitely parameterized form $u_{\tau+\Delta\tau}$. They can be roughly divided into sequential and simultaneous approaches, where *single / multiple shooting* and *collocation* techniques are used in order to solve the problem. Direct methods are mostly used for solving OCPs; this also holds for this work. The advantages and disadvantages of these methods are addressed e.g. in the works of Findenstein and Allgöwer [42] and Diehl [35]. The latter provides overviews over numerical methods for both, time-continuous and time-discrete formulations.

However, Optimal Control as introduced above is an open loop technique and thus not able to include disturbances and errors affecting the system, e.g. measurement-noise or errors in the model. To take these phenomena into account, the loop has to be closed, meaning to feed back the actual measurements / estimated states to the optimizer. This is known as Model Predictive Control (MPC) or sometimes also called Receding Horizon Control (RHC). The functional principle of MPC is that an OCP with known initial conditions (measured / estimated) is solved on-line in parallel to the physical process. Also for MPC

mostly Direct methods with a finite parameterization of the input function are used to solve the OCP. The reason for this is that the computational effort for both, HJB-PDE and EL-DE, are fairly high. The HJB-PDE is calculated off-line, however, for large applications the size of the problem becomes very high (“curse of dimensionality”). After the solution to the OCP has been obtained, the first input(s) are applied to the physical system. Now the states are measured / estimated and fed back into the optimizer, where they serve as the new initial conditions. Then the OCP is solved again, and so on. It is clear that this should happen in real-time, although direct solutions provide a non-optimal input even before convergence is achieved. An introduction to nonlinear MPC is provided in Findeisen and Allgöwer [42].

The question of stability of the OOC and MPC approaches must be mentioned. For MPC for example, stability can be enforced by the introduction of terminal region constraints and / or terminal penalty terms in the objective function, as described e.g. in Findeisen and Allgöwer [42]. This holds for the system in error coordinates, meaning that the equilibrium is moved into the origin. For the case presented here, however, this does not necessarily have to be done: As shown in Chapter 8, the system is stable for constant inputs, meaning for fixed boundary conditions. In addition, as already mentioned in Section 11.2.4, the heat equation has certain damping properties with respect to arising singularities. A change in the boundary condition can be interpreted as a singularity. In fact, the system will converge to a steady state defined by the two boundary conditions and thus undesired behavior can be avoided by bounding the inputs at the boundaries.

14.3 ACADO Software Package

In the upcoming two Chapters the optimization software package ACADO (Automatic Control And Dynamic Optimization) is used in order to conduct Optimal Control and MPC for freezing processes in plate freezers and thawing processes performed by contact methods, as described in Section 4.1.4.

With ACADO, different Optimal Control Problems can be solved, such as offline dynamic optimization, parameter and state estimation as well as combined on-line estimation and MPC. In this work, ACADO’s user-friendly MATLAB[®] implementation with automatic C++ code generation is used.

The basic structure of ACADO consists of so called base classes, where lower classes inherit from their base class, as described by Houska et al. [54]. It has to be mentioned that each of the base classes can also be used stand-alone. This object-oriented design allows free choice of base classes, meaning that standard ACADO classes can be replaced by external classes. Houska et al. [54], Ariens et al. [7] and Ariens et al. [8] provide deeper insights to the structure and the principles behind ACADO, where the latter two are manuals describing how to formulate Optimization problems and OCPs in ACADO and in ACADO for MATLAB[®], respectively.

14.3.1 Solving method for the specific cases in Chapters 15 and 16

The considered problems are solved by a direct single shooting method, a sequential approach. As explained earlier, for sequential methods a time horizon τ gets divided into a

fixed time grid $0 = t_0 < t_1 < \dots < t_G = \tau$. This time grid does not necessarily have to be equidistant, however, due to convenience it is chosen as such. Nevertheless, it should be pointed out that some problems might be solved more efficiently and faster if the time grid is defined non-equidistant.

Between each of these time instances a piecewise constant input function, the optimization variable, gets chosen and implemented into the ODEs. However, piecewise constant input functions are often not practical due to their stepwise definition. Therefore, also the time-derivative of the control variable can be defined as optimization variable. This will result in smoother control variables, as the piecewise continuous optimization variable will get integrated. This approach is also chosen in the applications in Chapters 15 and 16.

Discretizing the control variable in the aforementioned fashion and implementation into the objective function and the constraints defines a Nonlinear Programming (NLP) problem. An NLP can be solved by different methods (e.g. interior point methods), however, Sequential Quadratic Programming (SQP), an iterative method, is often the most effective for shooting methods as they generate small and dense NLPs. This is done by defining quadratic (QP) optimization subproblems, which are solved by an active-set strategy relying on linearized dynamics and constraints. Here, line search algorithms are used in order to find a search direction leading to a decrease in the objective function. Thus, one SQP iteration delivers an optimal search direction, however, this may have been achieved by several iterations solving the QP.

The integration method used to solve the QP is a Runge Kutta method of order 7/8 with relative tolerance 10^{-6} . The built-in QP solver in ACADO is *qpOASES*, an open-source C++ implementation of an active set strategy. The Hessian is chosen to be an approximation of Gauss-Newton type and the tolerance level for the *Karush-Kuhn-Tucker* conditions is set to 10^{-6} .

The method briefly explained above only represents one possibility to solve NLPs. For more details, also about terminology and deeper understanding, please consult e.g. Nocedal and Wright [84] and Diehl [35].

14.4 Parameters

The parameters $c(T)$ and $\lambda(T)$ are still based on the parameter description introduced in Section 6.2. However, the definition of these functions in the introduced form cannot be used in ACADO for MATLAB[®] as they are required to be formulated in a continuous form. In particular, case-defined statements as for (6.10) and (6.11) cannot be used, this might also hold for other optimization software. Therefore, other formulations for the functions have to be imposed.

A good approach to express functions with large gradients in a continuous way is to use arctan-functions. Therefore, the two parameters $c(T)$ and $\lambda(T)$ are reformulated after curve fitting with manual coefficient determination as the following expressions:

$$\begin{aligned}
 c(T) = & -1.4028 \cdot 10^5 + 9.12 \cdot 10^4 \left[\arctan \left(\left(\frac{T}{T_F - \Delta T - 0.5\delta T} - 1 \right) 50000\pi \right) + \frac{\pi}{2} \right] \\
 & + 9.07 \cdot 10^4 \left[-\arctan \left(\left(\frac{T}{T_F + \Delta T + 0.5\delta T} - 1 \right) 50000\pi \right) \right],
 \end{aligned} \tag{14.3}$$

whose plot can be seen in Figure 14.1 compared to the definition in (6.11)

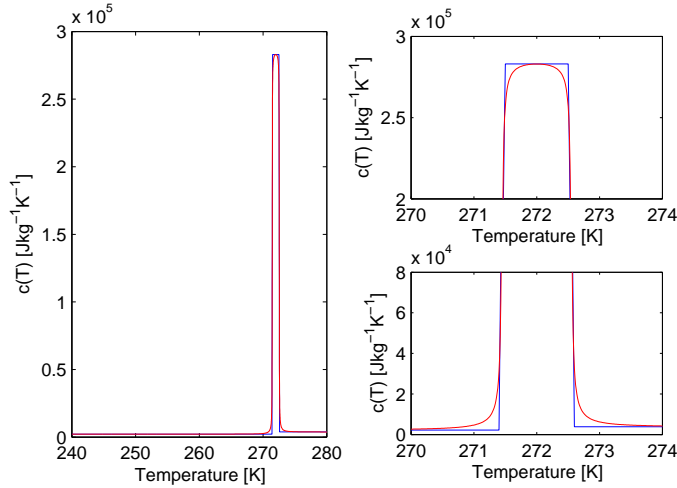


Figure 14.1: Parameter $c(T)$ as defined in (6.11) (blue) compared to the approximation defined in (14.3) (red)

as well as

$$\lambda(T) = 0.49 + 0.42 \left[-\arctan \left(\left(\frac{T}{T_F} - 1 \right) 400\pi \right) + \frac{\pi}{2} \right], \tag{14.4}$$

whose plot can be seen in Figure 14.2, also compared to original definition, namely in (6.10).

In addition, the derivative of $\lambda(T)$ with respect to temperature T has to be evaluated. Hence, differentiating (14.4) with respect to T yields

$$\lambda_T(T) = -\frac{168\pi}{T_F \left[160000\pi^2 \left(\frac{T}{T_F} - 1 \right)^2 + 1 \right]}, \tag{14.5}$$

where the plot of (14.5) can be seen in Figure 14.3.

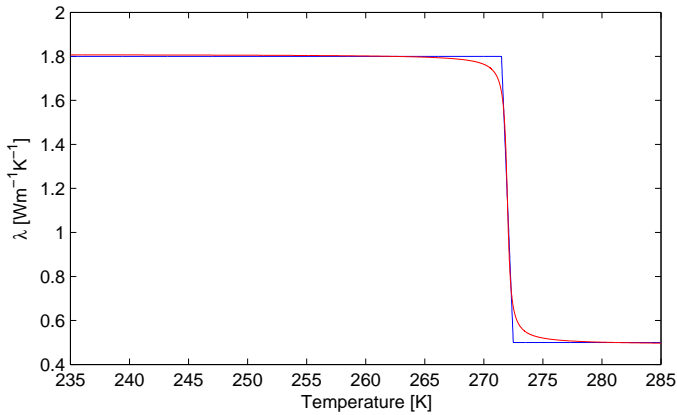


Figure 14.2: Parameter $\lambda(T)$ as defined in (6.10) (blue) compared to the approximation defined in (14.4) (red)

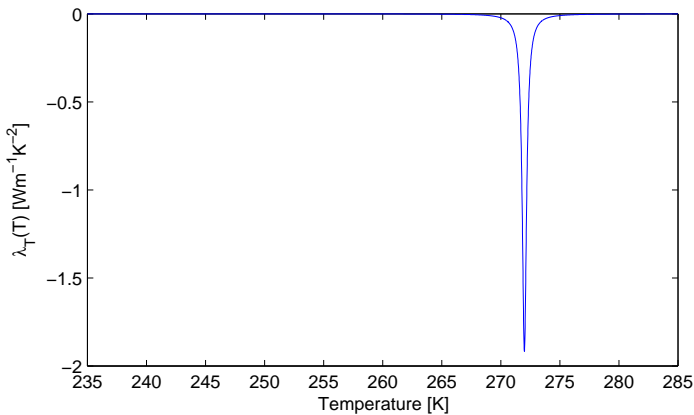


Figure 14.3: Parameter $\lambda_T(T)$ as defined in (14.5)

Now the two approximations of the parameters $k(T)$ and $\kappa(T)$ can be calculated by putting the expressions (14.3), (14.4), (14.5) and $\rho(T) = \rho = 950 \text{ kg m}^{-3}$ into (6.4) and (6.5). This gives the function shapes as shown in Figure 14.4 and Figure 14.5.

As can be seen, defining the approximations of $k(T)$ and $\kappa(T)$ using the approximations of $c(T)$ and $\lambda(T)$ leads to results, which are quite far off the functions defined in (6.10) and (6.11). Therefore, it makes sense to define the functions $k(T)$ and $\kappa(T)$ directly by approximative functions. These were also found by curve fitting with manual coefficient

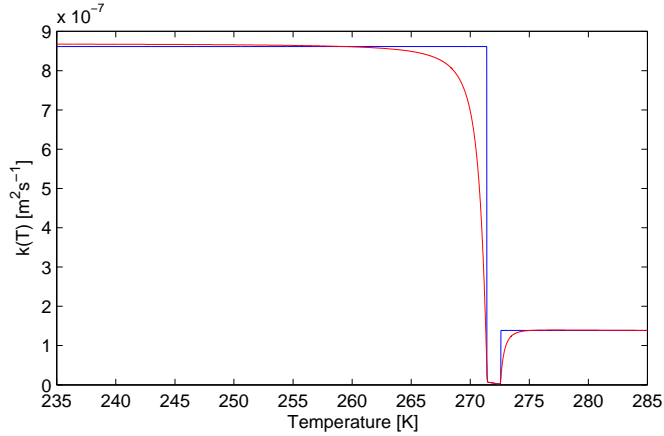


Figure 14.4: Parameter $k(T)$ as defined with (6.10) and (6.11) (blue) compared to the approximation calculated with (14.3) and (14.4) (red)

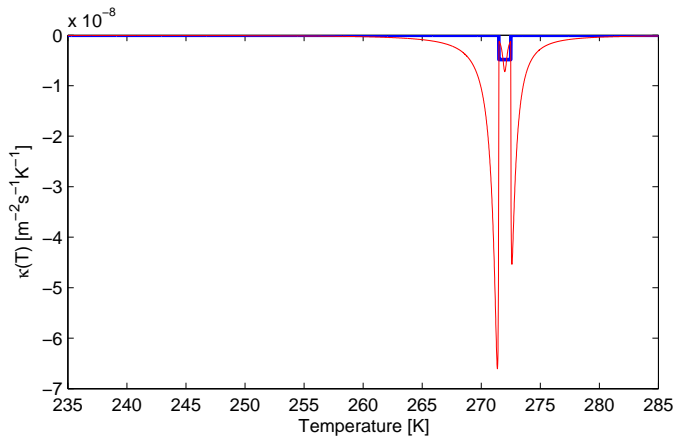


Figure 14.5: Parameter $\kappa(T)$ as defined with (6.10) and (6.11) (blue) compared to the approximation calculated with (14.3) and (14.5) (red)

determination and result in the following expressions

$$k(T) = 7 \cdot 10^{-8} + 2.737 \cdot 10^{-7} \left[-\arctan \left(\left(\frac{T}{T_F - \Delta T - 1.1\delta T} - 1 \right) 20000\pi \right) + \frac{\pi}{2} \right] \\ + 4.35 \cdot 10^{-8} \left[\arctan \left(\left(\frac{T}{T_F + \Delta T + 1.1\delta T} - 1 \right) 50000\pi \right) \right], \quad (14.6)$$

$$\kappa(T) = 1.543 \cdot 10^{-9} \left[-\arctan \left(\left(\frac{T}{T_F - \Delta T} - 1 \right) 50000\pi \right) \right] \\ + 1.543 \cdot 10^{-9} \left[\arctan \left(\left(\frac{T}{T_F + \Delta T} - 1 \right) 50000\pi \right) \right], \quad (14.7)$$

whose plots can be seen in Figure 14.6 and Figure 14.7 compared to the definitions of $k(T)$ and $\kappa(T)$ using (6.10) and (6.11), respectively.

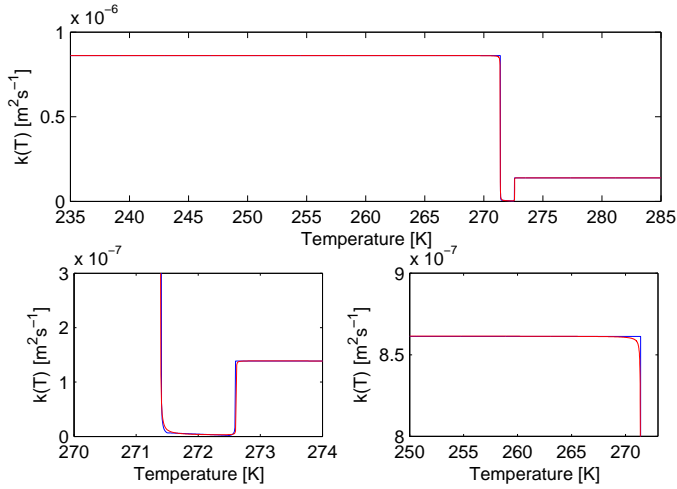


Figure 14.6: Parameter $k(T)$ as defined with (6.10) and (6.11) (blue) compared to the approximation defined in (14.6) (red)

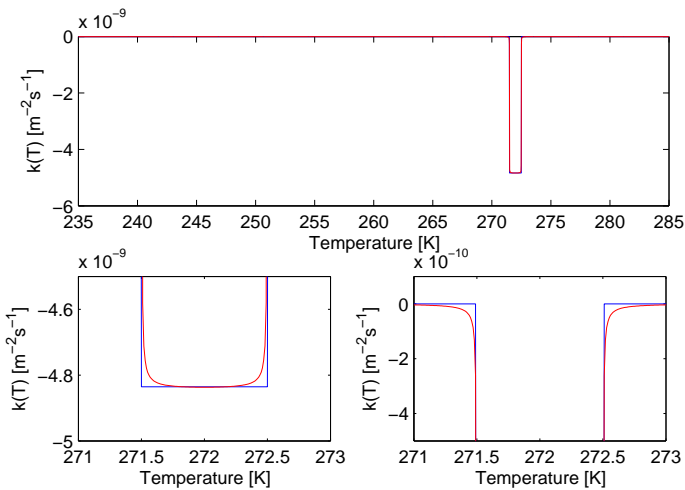


Figure 14.7: Parameter $\kappa(T)$ as defined with (6.10) and (6.11) (blue) compared to the approximation defined in (14.7) (red)

Note that for all plots of the approximated parameters the values $T_F = 272$ K, $\Delta T = 0.5$ K

and $\delta T = 0.1$ K are used. Due to the fact that

$$\frac{d}{dT} \arctan(aT + b) = \frac{a}{1 + (aT + b)^2} \quad (14.8)$$

exists and is at least twice continuously differentiable for all T , it can be concluded that the arctan-approximations of the parameters do not impose problems to the numerical solvers underlying the optimization algorithm.

14.5 Assumptions and comments on the OOC and MPC simulations and the controller performances

The performance goal of the controller for the open loop Optimal Control (OOC) problems is to either freeze or thaw a block of foodstuff in a given time-window using as high or as low temperatures as possible. It is assumed that high temperatures for freezing as well as low temperatures for thawing are beneficial with respect to saving energy. Another constraint on the boundary temperature is the use of high temperatures for the thawing process, which can lead to (partial) cooking and thus to quality degradation. For freezing such a constraint does not exist, except for the case when the temperature of the frozen storage room, where the blocks are stored after initial freezing, is taken into account. This storage room should not do any further freezing, but only keep a constant and steady temperature, meaning that the final temperature after freezing should not be significantly higher than the storage room temperature.

As there has not been any quantitative analysis of the energy saving during freezing and thawing, it is unknown if actual energy has been saved compared to the case when freezing and thawing temperatures are held constant. In fact, the energy required to cool down or heat up a block of foodstuff from one temperature to another is constant. What can be regarded, and in fact can be seen in the simulation results, is that it is beneficial to use full freezing or thawing capacity in the beginning and then gradually switch to lower capacities (meaning higher or lower temperatures, respectively). A next step can be to simply turn off the freezing or thawing process at some point and let the fish block even out its temperature in the storage room. This, however, is not part of the investigation.

A quantitative analysis is aggravated by the fact that the OCP is quite sensitive to changes in e.g. weighting matrices or constraints. Therefore, the presented results only cover a small fraction of possible cases and thus a quantitative analysis can only hold for these particular cases.

The system will converge to states that are not the equilibrium. This does not impose problems in practice as the block will even out its temperature when brought to the storage freezer after freezing or to a chilled storage room after thawing. It should be ensured that for the freezing case the outer layers are colder than the interior in order to have a temperature margin while the block is transported to the storage freezer. For the thawing case the outer layers are typically warmer than the interior as the interior's temperature is just above the freezing point (outside the latent zone).

Chapter 15

Optimal boundary control for freezing

In this Chapter, approaches to optimally control the model (6.6) for freezing applications are derived. There are many publications concerning the optimal control of PDEs or processes that are governed by PDEs. Dubljevic et al. [37] present results for predictive control of parabolic PDEs by defining operators for spatial derivatives. Dubljevic and Christofides [36] report about predictive control of parabolic PDEs with state and control constraints, using modal decomposition techniques to obtain a finite-dimensional system. Hinze et al. [52] give a broad overview over optimization with PDE constraints. In order to find solutions to optimal control problems for the system (6.6), a reduction of the infinite-dimensional PDE into a finite-dimensional system is required. This will be done in the same fashion like in the Chapters before, namely by spatial discretization, see Section 10.1.2.

15.1 Introduction

Two different ways of optimally controlling the freezing process will be investigated, namely by means of open loop Optimal Control (OOC) and closed loop Model Predictive Control (MPC). For perfect knowledge of the system dynamics and without disturbances acting on the system, OOC delivers an optimal input function satisfying defined constraints on the system. However, as there exist no perfect models and processes without disturbances, applying a control input obtained by OOC to a real process will deliver different results than predicted. Therefore, it is essential to feed back updated state information into the optimizer and calculate a new, updated control law. Nevertheless, a solution provided by OOC can deliver a qualitative solution to which the solution obtained by MPC should converge for small disturbances and good knowledge of the system dynamics, meaning that the OOC can serve as a benchmark.

For both, OOC and MPC, suitable objective functions will be defined in order to make each of them feasible. They are defined as least squares (LSQ) tracking terms with constant reference values for the states T_{ref} , the input a_{ref} and the input derivative b_{ref} , which represents the optimization variable. Furthermore, constraints such as lower bounds for the states, \underline{T} , and upper and lower bounds for the input, \bar{a} and \underline{a} , as well as the input derivative, \bar{b} and \underline{b} , are introduced.

Controlling the temperature at the boundaries in the manner that is proposed in this Chapter is not standard procedure for the refrigeration system shown in Figure 3.1. This is due to the fact that the pressure might have to be adapted and controlled constantly in order to follow up the desired temperature of the refrigerant. In Figure 15.1 the temperature of the respective refrigerants ammonia (NH_3) and carbon dioxide (CO_2) are displayed over the pressure. It can be seen that for NH_3 small differences in pressure cause relatively

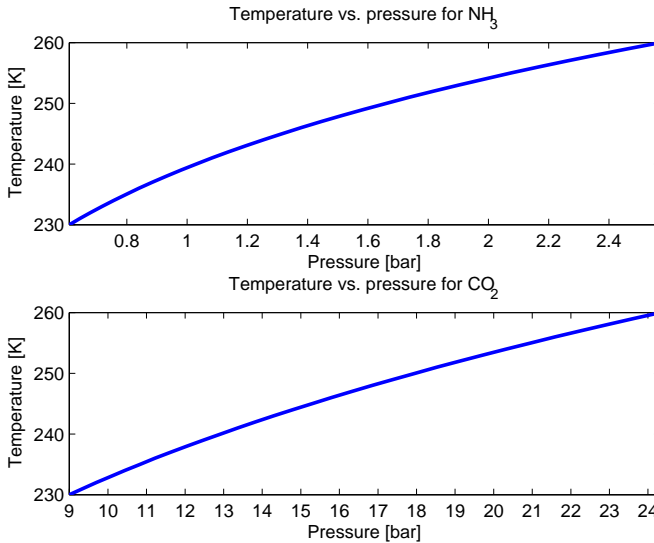


Figure 15.1: Temperature vs. pressure for the refrigerants NH_3 and CO_2

large changes in temperature, when compared to CO_2 . In addition, to obtain refrigerant temperatures below $240 \text{ K} \approx -33 \text{ }^\circ\text{C}$ for NH_3 , a pressure lower than ambient pressure has to be generated. This can be of consequence if there is any leakage in the refrigeration system, as outside air is drawn into the system.

The standard operation of the process in Figure 3.1 is such that the compressor works against a rising pressure in the separator unit and tries to hold this pressure as low as possible, as this ensures low refrigerant temperatures. Naturally, the pressure will rise in the separator due to an increased fraction of the vapor phase caused by the evaporation in the plate freezers and the expansion in the expansion valve. However, with large enough compressor power, these variances can be kept to a minimum and at the same time a pressure control can be achieved to ensure the proposed optimal control strategies.

On board fishing vessels it is mostly NH_3 that is taken as refrigerant due to its high sensory detectability in the ppm^1 -range; at these low concentrations it is not hazardous or life-threatening. In the contrary to CO_2 , NH_3 has no negative effects on the climate as it is not considered to be a greenhouse gas. However, in order to control the pressure to obtain the desired temperature of the refrigerant, CO_2 seems to be the better choice.

¹parts per million

15.2 Open loop Optimal Control

In addition to the previously described objective function and constraints, a least squares end term is defined in order to penalize deviations from state reference values at the end of the time horizon. Furthermore, the optimization is conducted over a variable time horizon, Z , which is defined as a free parameter and bounded by upper and lower bounds, \bar{Z} and \underline{Z} , respectively. Deviations from its reference value Z_{ref} will be penalized in the objective function. In addition, a terminal constraint in the form of a terminal region will be imposed.

Thus, the formulation of the OCP for OOC looks as follows

$$\min_{b,Z} J = \int_0^Z (T - T_{ref})^T E (T - T_{ref}) + F(a - a_{ref})^2 + G(b - b_{ref})^2 + U(Z - Z_{ref})^2 dt + (T(Z) - T_{ref})^T W (T(Z) - T_{ref}) \quad (15.1a)$$

$$\text{subject to } \dot{T} - f(T, a) = 0 \quad (15.1b)$$

$$b = \dot{a} \quad (15.1c)$$

$$T(0) = T_{init} \quad (15.1d)$$

$$a(0) = a_{init} \quad (15.1e)$$

$$\underline{T} \leq T \quad (15.1f)$$

$$\underline{a} \leq a \leq \bar{a} \quad (15.1g)$$

$$\underline{b} \leq b \leq \bar{b} \quad (15.1h)$$

$$\underline{Z} \leq Z \leq \bar{Z} \quad (15.1i)$$

$$\underline{T}(Z) \leq T(Z) \leq \bar{T}(Z) \quad (15.1j)$$

where $\dot{T} - f(T, a) = 0$ is the discretized version of (6.6) according to Section 10.1.2, but in the one-dimensional case for $M = 1$. Furthermore, $b = \dot{a}$ denotes the relation between optimization variable b and input a . Discretization is chosen to $N = 25$, which is a compromise between accuracy of the solution and computational effort. In addition, E and W are positive definite diagonal matrices that suit the dimension of $(T - T_{ref})$ containing weights on state deviations over the whole time horizon and the end of the time horizon, respectively. F , G and U are scalars representing the weights on deviations of the input, its derivative and the time horizon length, respectively. T_{init} and a_{init} indicate initial values for temperatures and input.

15.2.1 Simulation results for the OOC case

Simulations have been conducted for the parameters, which can be seen in Table 15.1. The matrices E , F , G , U and W are chosen in order to prioritize tracking of the state-reference T_{ref} followed by the optimization variable b_{ref} and the input a_{ref} over tracking the time horizon parameter Z_{ref} . In the LSQ end term only deviations of the states from T_{ref} at the end of the horizon are penalized; in the same fashion like the tracking over the whole time horizon. The variable time horizon Z is divided into a grid of 150 equidistant steps. \underline{T} is chosen as 245 K in order to avoid too large temperature gradients in the frozen state as the boundary layers of the object to be frozen will converge to the boundary temperature

T_{ref}	[251 251 251 251.5 251.5 251.5 252 252 252 252.5 252.5 252.5 253 252.5 252.5 252.5 252 252 252 251.5 251.5 251.5 251 251 251] K
$\underline{T}(Z)$	[250 250 250 250.5 250.5 250.5 251 251 251 251.5 251.5 251.5 252 251.5 251.5 251.5 251 251 251 250.5 250.5 250.5 250 250 250] K
$\overline{T}(Z)$	[252 252 252 252.5 252.5 252.5 253 253 253 253.5 253.5 253.5 254 253.5 253.5 253.5 253 253 253 252.5 252.5 252.5 252 252 252] K
T_{init}	280 K
\underline{T}	245 K
\underline{a}	240 K
\bar{a}	255 K
a_{init}	240 K
a_{ref}	255 K
\underline{b}	-0.01 K s^{-1}
\bar{b}	0.01 K s^{-1}
b_{ref}	0 K s^{-1}
\underline{Z}	8000 s
\overline{Z}	9000 s
Z_{ref}	8000 s
E	$10^2 \cdot \mathbf{I}_{(25 \times 25)}$
F	10^1
G	10^1
U	10^{-1}
W	$10^2 \cdot \mathbf{I}_{(25 \times 25)}$

Table 15.1: Simulation parameters for the OOC freezing case

fairly fast. This constraint might have to be adapted, depending on what is the desired final temperature distribution. The bounds on a are defined based on physical limitations: \underline{a} limits the lower pressure of NH_3 to approximately 1 bar for ammonia, see Figure 15.1, and \bar{a} is set to the same value as the reference $a_{ref} = 255 \text{ K}$ in order to keep the energy-consumption of the compressor low. The dynamics of temperature change \underline{b} and \bar{b} are limited to -0.01 K s^{-1} and 0.01 K s^{-1} , respectively, in order to model for the dynamics of the *regeneration loop*, introduced in Chapter 3. The reference b_{ref} is 0 K s^{-1} to avoid excessive temperature change.

In Figure 15.2 the states T_1 to T_{13} are shown, where T_1 is to be found at the outer layer of the block, whereas T_{13} stands for the block's central layer. It has to be mentioned that due to symmetry and the absence of noise, T_1 is the same like T_{25} , T_2 corresponds to T_{24} , etc. The plot shows that especially the lower bound on the temperatures $\underline{T} = 245 \text{ K}$ as well as other constraints are fulfilled. The region $I_{\Delta T}$ around the freezing point is visualized in grey.

Figure 15.3 displays the derivative of the input b as well as the input a . Also here the

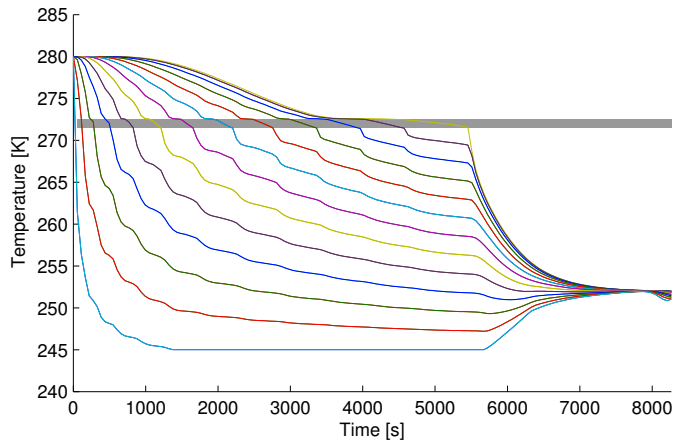


Figure 15.2: State evolution over time - OOC case

constraints on the optimization variable and the input are satisfied. These are indicated by the red lines.

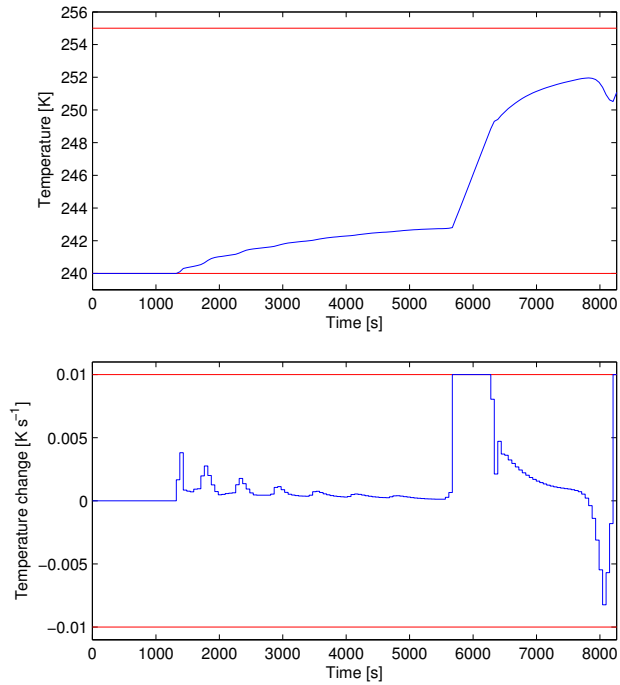


Figure 15.3: Boundary temperature (top) and its rate of change over time (bottom) - OOC case

Figure 15.4 shows the states T_1 to T_{25} at the end of the time horizon. The reference temperature T_{ref} is shown in black, whereas the bounds for the terminal constraint, $\underline{T}(Z)$ and $\overline{T}(Z)$, are marked in red. Hence it can be seen that the terminal constraints are fulfilled and that the final temperature is close to the reference.

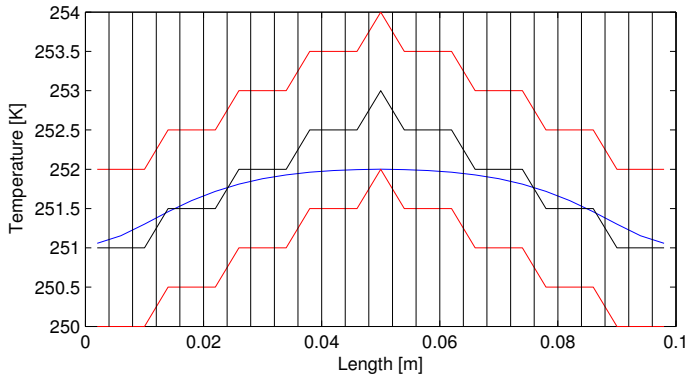


Figure 15.4: States T_1 to T_{25} at the end of the time horizon - OOC case

In Figure 15.5 an illustrative 3-dimensional plot visualizes the solution.

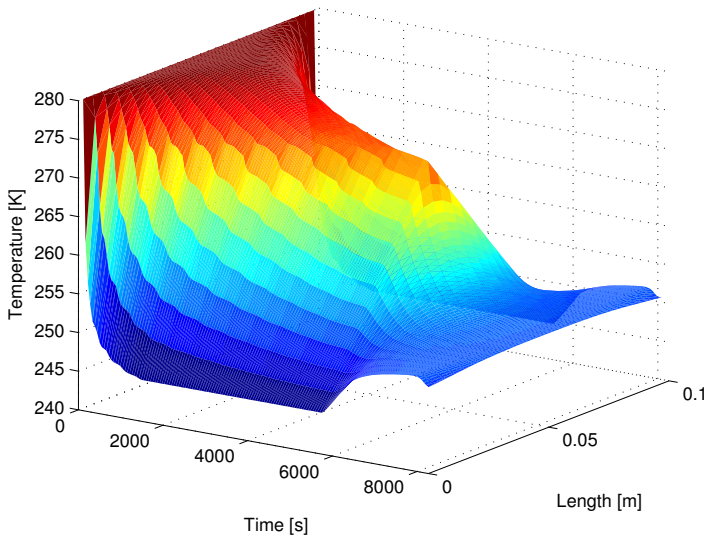


Figure 15.5: A 3-dimensional plot of the temperatures - OOC case

15.3 Model Predictive Control

In this Section an MPC strategy for the freezing process is proposed. A disturbance in the form of white Gaussian noise is added to the states after every MPC iteration. This models for uncertainties in the model compared to the plant and errors in the measurement / estimation at the same time. The OCP underlying the MPC approach is defined in the same manner like in the OOC approach before. However, the terminal region constraint and the bounds on Z can be removed. Furthermore, the term penalizing deviations from Z_{ref} as well as the terminal penalty term in the objective function can be removed as well. The reason for this is that they would render the OCP infeasible due to the constant and relatively short time horizon. The time horizon is set to $\tau = 500$ s and is divided into 10 equidistant time instances. After having obtained the solution to the OCP, the input of the first 50 s (corresponding to one time instance) is applied to a simulation of the real process. Then the temperatures after 50 s of simulation with added white Gaussian noise are fed back to the OCP as the new initial condition for the states. This is continued until all temperatures are below 251 K. The OCP for the MPC approach is formulated as follows

$$\min_b J = \int_0^{\tau} (T - T_{ref})^T E (T - T_{ref}) + F(a - a_{ref})^2 + G(b - b_{ref})^2 dt \quad (15.2a)$$

$$\text{subject to } \dot{T} - f(T, a) = 0 \quad (15.2b)$$

$$b = \dot{a} \quad (15.2c)$$

$$T(0) = T_{init} \quad (15.2d)$$

$$a(0) = a_{init} \quad (15.2e)$$

$$\underline{T} \leq T \quad (15.2f)$$

$$\underline{a} \leq a \leq \bar{a} \quad (15.2g)$$

$$\underline{b} \leq b \leq \bar{b}, \quad (15.2h)$$

where the notation is the same as for the OOC case presented in (15.1).

15.3.1 Simulation results for the MPC case

It must be pointed out that the number of states is reduced to $N = 9$ in order to reduce the computational effort. The parameters chosen for the MPC approach are chosen to be slightly different from those of the OOC. They can be seen in Table 15.2

State tracking is prioritized somewhat higher than for the OOC case, compare E for both cases. The temperature reference is chosen to be lower than for the OOC simulations, which can be seen by comparing T_{ref} in Tables 15.1 and 15.2. This is done in order to account for the present disturbances and to obtain some temperature-margin when the goals of the MPC are achieved.

Figure 15.6 displays the states T_1 to T_9 . It must be pointed out that now, in contrary to the OOC simulation case in Figure 15.2, the states in the presence of noise are not symmetrical. This can be clearly seen by comparing the red and black as well as the green and magenta colored curves (solid and dashed, respectively). Furthermore, it can be noticed that the constraints are fulfilled, especially the lower bound on the temperature $\underline{T} = 245$ K

T_{ref}	[249 249.5 250 250.5 251 250.5 250 249.5 249] K
T_{init}	280 K
\underline{T}	245 K
\underline{a}	240 K
\bar{a}	255 K
a_{init}	240 K
a_{ref}	255 K
\underline{b}	-0.01 K s ⁻¹
\bar{b}	0.01 K s ⁻¹
b_{ref}	0 K s ⁻¹
E	$10^3 \cdot I_{(9 \times 9)}$
F	10^1
G	10^1

Table 15.2: Simulation parameters for the MPC freezing case

visualized in grey. The region around the freezing point $I_{\Delta T}$ is displayed in grey as well.

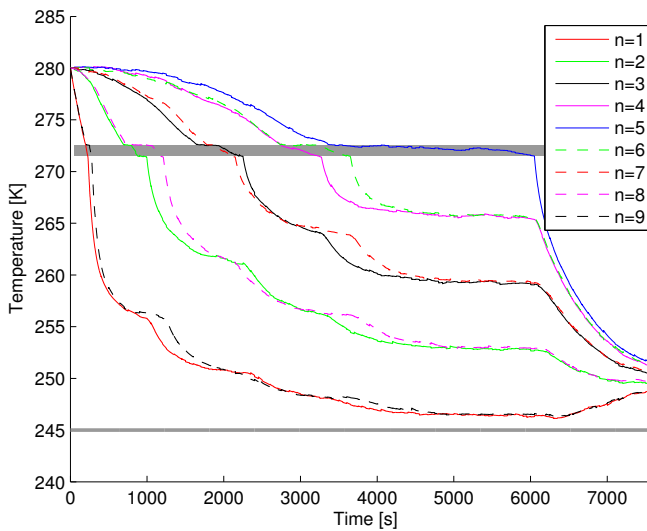


Figure 15.6: State evolution over time - MPC case

In Figure 15.7 the derivative of the input b and the input a itself are shown. The difference to the OOC case in actuation is obvious due to the fact that the matrix E is chosen larger in the MPC case and thus tracking of states is prioritized higher. The constraints marked in red are satisfied for both, the rate of change of the input and the input itself.

Figure 15.8 depicts an illustrative 3-dimensional plot to show the converging character over time and space.

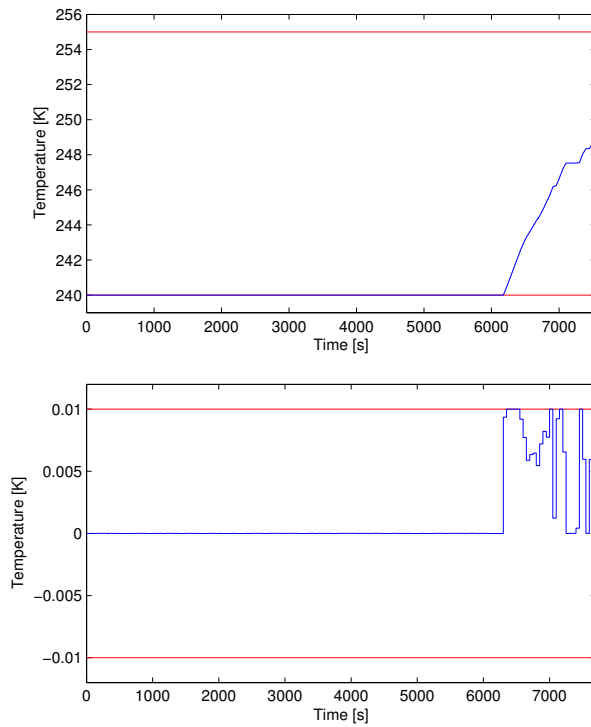


Figure 15.7: Boundary temperature (top) and its rate of change over time (bottom) - MPC case

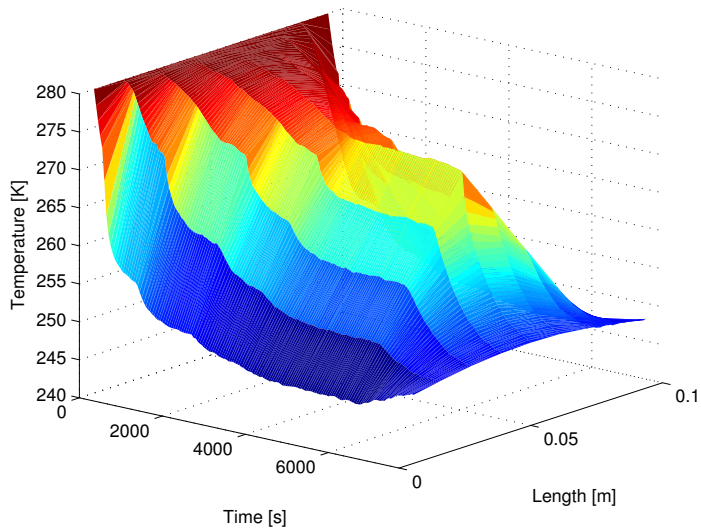


Figure 15.8: A 3-dimensional plot of the temperatures - MPC case

Chapter 16

Optimal boundary control for thawing

In Chapter 15 optimal control strategies for freezing applications in plate freezers are presented. Now the focus lies on optimally controlling the reversed freezing process, namely thawing. The principle behind the considered thawing process is described in Section 4.1.4, namely contact thawing. It is demonstrated how this method can be controlled optimally using open loop Optimal Control and Model Predictive Control.

16.1 Introduction

There are basically two different methods for contact thawing. One method heats up the walls of the thawer electrically, for example with electrical sheet heaters. This is described in the work of Haugland [47]. Another method is based on thawing in a rebuilt plate freezer, a plate thawer, which is not necessarily operated with the refrigerant, but with another thawing medium, e.g. water or mixtures of water and ethylene glycol ($C_2H_6O_2$).

The temperature ranges for both processes are limited by two bounds, the freezing point of water and the maximal acceptable temperature of the good during thawing, respectively. However, both methods have their own limitations when it comes to the lowest possible temperature. The lowest value for electrical heating is taken from Haugland [47] and defined to $278\text{ K} \approx 5\text{ }^\circ\text{C}$. The experiments in the aforementioned publication, however, were conducted in a cold store room at 273 K and thus the temperature of 278 K at the boundaries could be achieved.

The actuation speeds for both methods differ. Contact thawing with electrical sheet heaters offers larger gradients, whereas plate thawers work with lower rates of temperature change. This is due to the fact that plate thawers can be operated with two feeding lines, one with a cooled medium and another with a heated medium, which are fed from respective storage tanks. The controller then controls the mixture of these two media for example with a three-way control valve in order to obtain the desired temperature. In the sequel the lower bound on the temperature of the thawing medium will be defined to 283 K as this seems to be practical and to reflect reality.

In Figure 16.1 a simplified structure representing the proposed thawing process is shown. The optimal control algorithm controls the unit marked with dashed lines consisting of two pumps and a valve. Thereby the dynamics of this unit are implemented as a constraint to the optimization problem, namely the rate of change of the boundary temperature. The mentioned unit mixes hot water from a buffer tank with cold water either from tap or from another buffer tank. Then this mixed water is pumped through the thawer, where it provides heat to the thawing good and thus cools down. A fraction of the cooled water is then fed back to the buffer tank for reheating, whereas the other fraction is used either disposed or can be used for other purposes. Fractions of this disposable, used water can also be fed back together with the cold water feed. A closed water system seems also possible with a constant amount of water in the whole system. An investigation of such designs, however, was not part of this thesis. In the following it will be assumed that the calculated, optimal boundary temperature can be provided by the feeding system.

The thawer is a modified plate freezer (both, vertical and horizontal constructions seem to be possible). However, due to better contact between the block and the thawer walls, a vertical form should be preferred. For horizontal constructions the space between the plates must be adjusted in order to keep the contact between the plates and the thawing object. In the present work only the temperature dynamics of the thawer will be considered. The process relies on tap water as thawing medium and therefore the lower bound for temperature is defined by the temperature of the tap water (cold water feed) itself.

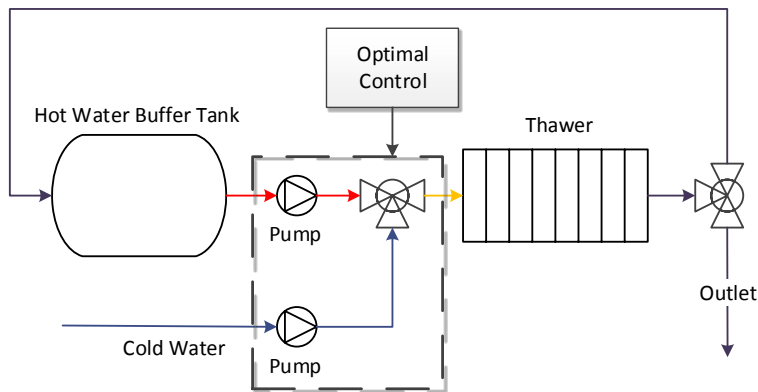


Figure 16.1: Functional principle

16.2 Open loop Optimal Control

The OOC case for thawing is almost the same like for the corresponding freezing case stated in Section 15.2. The difference lies in the fact that the terminal constraint is reduced to the very center of the block, meaning that only the temperature T_{13} will be regarded. This is now required to be in between the range $272.5 - 273$ K, just outside the region $I_{\Delta T}$. This is valid due to the fact that the temperature margin for the boundary temperature is

limited to the range 283 – 293 K as well as that all temperatures should not violate the constraint $\bar{T} = 285$ K. The latter is imposed to avoid high temperatures, which can cause protein denaturation and increased drip loss and thus a degradation in quality. Furthermore, a variable time horizon Z is defined as an optimization variable, which is split into 300 equidistant time instances. This is chosen as such due to the fact that the thawing process is considered to be harder to solve than the freezing process and thus more accurate actuation might be needed.

$$\min_{b,Z} J = \int_0^Z (T - T_{ref})^T E (T - T_{ref}) + F(a - a_{ref})^2 + G(b - b_{ref})^2 + U(Z - Z_{ref})^2 dt + (T(Z) - T_{ref})^T W (T(Z) - T_{ref}) \quad (16.1a)$$

$$\text{subject to } \dot{T} - f(T, a) = 0 \quad (16.1b)$$

$$b = \dot{a} \quad (16.1c)$$

$$T(0) = T_{init} \quad (16.1d)$$

$$a(0) = a_{init} \quad (16.1e)$$

$$\underline{T} \leq T \quad (16.1f)$$

$$\underline{a} \leq a \leq \bar{a} \quad (16.1g)$$

$$\underline{b} \leq b \leq \bar{b} \quad (16.1h)$$

$$\underline{Z} \leq Z \leq \bar{Z} \quad (16.1i)$$

$$\underline{T}_{13}(Z) \leq T_{13}(Z) \leq \bar{T}_{13}(Z) \quad (16.1j)$$

where $\dot{T} - f(T, a) = 0$ and $b = \dot{a}$ are described in (15.1), respectively.

16.2.1 Simulation results for the OOC case

The simulations are conducted in the same fashion like in Chapter 15 and the simulation parameters are displayed in Table 16.1.

It must be mentioned that the bounds on the rate of change for the boundary temperature, \underline{b} and \bar{b} , are set to two different values, see Table 16.1. This is done in order to model for both systems, plate thawer operated with water / water-glycol with a lower rate of temperature change and the contact thawer based on electric sheet heating with a higher rate of temperature change.

Figure 16.2 displays the rate of change of the boundary temperature as well as the input itself. The upper and lower bounds on the input rate of change and the input are visualized by constant red lines in both plots and one can see that these constraints are fulfilled. The resulting state evolution is shown in Figure 16.3. In the same Figure also the temperature distribution at the end of the time horizon $Z = 35083$ s in blue and the reference T_{ref} in red are demonstrated. Also here the constraints are satisfied, especially the upper bound for the temperatures $\bar{T} = 285$ K. Again, the region around the freezing point $I_{\Delta T}$ is displayed in the upper plot in grey.

In Figure 16.4 the rate of change of the input and the input itself are displayed. In this example, simulations are conducted for $\underline{b} = -0.01$ K s⁻¹ and $\bar{b} = 0.01$ K s⁻¹, while all other

T_{ref}	[278.5 278 277.5 277 276.5 276 275.5 25 274.5 274 273.5 273 272.5 273 273.5 274 274.5 275 275.5 276 276.5 277 277.5 278 278.5] K
$\underline{T}_{13}(Z)$	272.5 K
$\overline{T}_{13}(Z)$	273 K
T_{init}	235 K
\overline{T}	285 K
\underline{a}	283 K
\overline{a}	293 K
a_{init}	283 K
a_{ref}	283 K
\underline{b}	$-0.01 \text{ K s}^{-1} / -0.1 \text{ K s}^{-1}$
\overline{b}	$0.01 \text{ K s}^{-1} / 0.1 \text{ K s}^{-1}$
b_{ref}	0 K s^{-1}
\underline{Z}	33000 s
\overline{Z}	37000 s
Z_{ref}	35000 s
E	$10^2 \cdot I_{(25 \times 25)}$
F	10^1
G	10^1
U	10^{-1}
W	$10^2 \cdot I_{(25 \times 25)}$

Table 16.1: Simulation parameters for the OOC thawing case

parameters and values are not changed. Figure 16.5 shows the state evolution as well as the temperatures at the end of the time horizon $Z = 35083$ s, in the same fashion like already presented in Figure 16.3.

It is remarkable that for both simulation examples nearly identical results at the end of optimization and simulation are obtained. This gets clear when comparing both plots showing the temperatures at the end of the time horizon in Figures 16.3 and 16.5. Furthermore, the simulation times are identical for the two cases, namely $Z = 35083$ s. This is probably due to the fact that the chosen bounds and reference value for the time horizon parameter are not changed.

16.3 Model Predictive Control

For the MPC a terminal constraint for the temperatures is not defined as this would make the OCP infeasible for short time horizons. Furthermore, it seems impractical to choose a variable time horizon. Therefore the two last constraints in (16.1) will not be regarded.

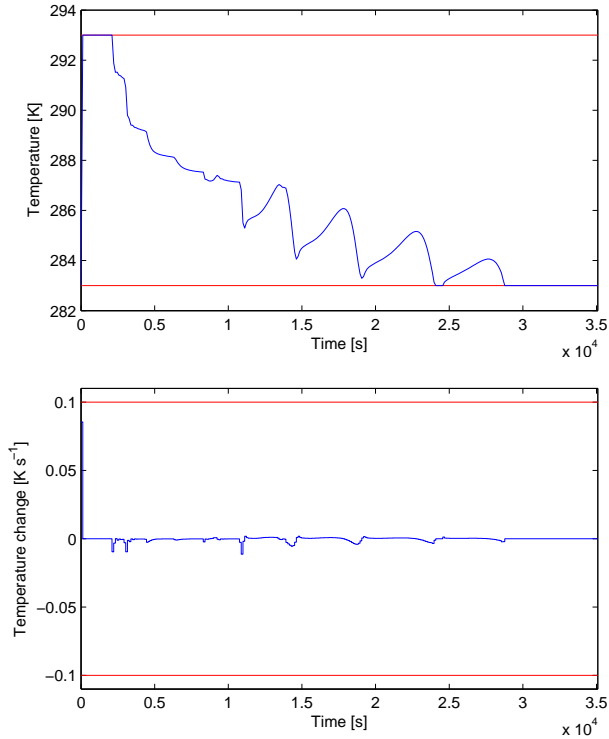


Figure 16.2: Boundary temperature (top) and its rate of change over time (bottom) - OOC case for large rates of change

Furthermore, the LSQ end term is left out as well and thus the OCP looks as follows:

$$\min_b J = \int_0^{\tau} (T - T_{ref})^T E (T - T_{ref}) + F(a - a_{ref})^2 + G(b - b_{ref})^2 dt \quad (16.2a)$$

$$\text{subject to } \dot{T} - f(T, a) = 0 \quad (16.2b)$$

$$b = \dot{a} \quad (16.2c)$$

$$T(0) = T_{init} \quad (16.2d)$$

$$a(0) = a_{init} \quad (16.2e)$$

$$\underline{T} \leq T \quad (16.2f)$$

$$\underline{a} \leq a \leq \bar{a} \quad (16.2g)$$

$$\underline{b} \leq b \leq \bar{b} \quad (16.2h)$$

$$(16.2i)$$

where $\dot{T} - f(T, a) = 0$ and $b = \dot{a}$ are the the same as described in (15.1). The setup is the same like in the MPC simulation case for freezing applications in Section 15.3.1, except that the fixed time horizon of $\tau = 500$ s is now divided into 5 equidistant time

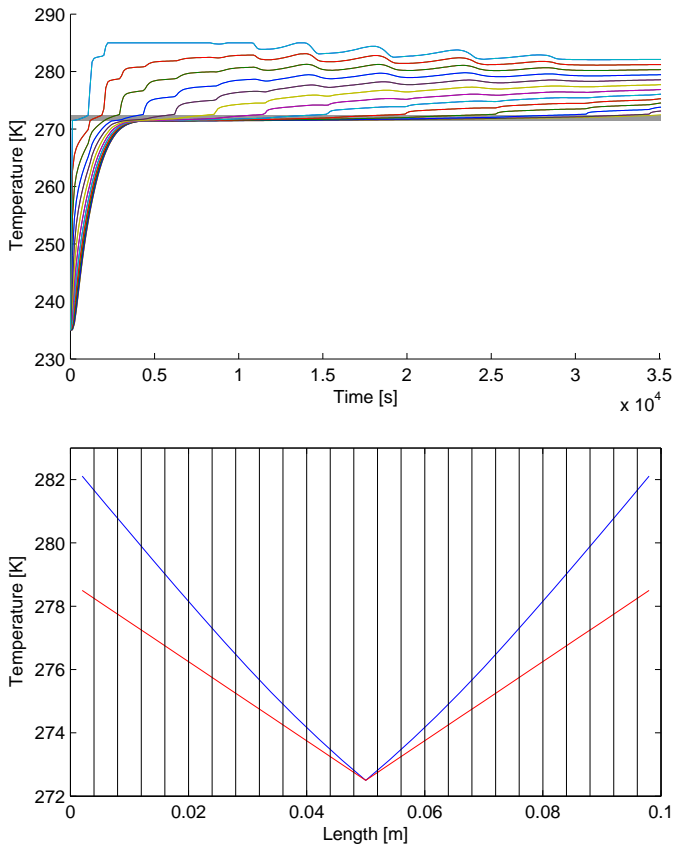


Figure 16.3: State evolution over time (top) and temperatures at the end of the time horizon (bottom) - OOC case for large rates of change

instances, where the first time instance of 100 s is fed into the simulator. Again, after 100 s of simulation, the states are fed back to the optimizer perturbed by white Gaussian noise before another MPC iteration starts.

16.3.1 Simulation examples

The simulation parameters are displayed in Table 16.2, where again two different rates of change for the boundary temperature are defined, just like for the OOC case presented in Section 16.2. Just like in Section 15.3, the discretization is cut down to $N = 9$ in order to reduce the calculation effort. Optimization and simulation are stopped when $T_i \geq 272.5$ K for all i .

In Figure 16.6 the input rate of change as well as the input itself are displayed for the case with large rates of change, ± 0.1 K s⁻¹. As can be seen the constraints, which are marked in red, are satisfied.

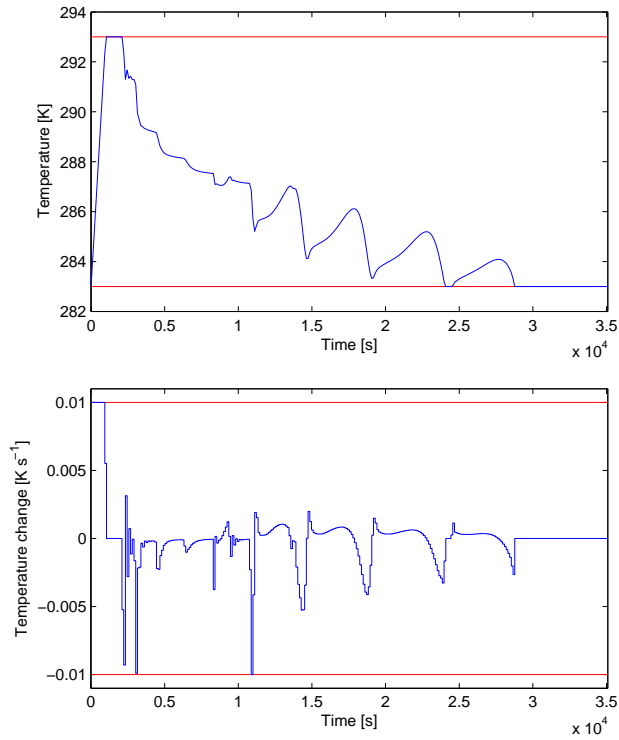


Figure 16.4: Boundary temperature (top) and its rate of change over time (bottom) - OOC case for small rates of change

Figure 16.7 shows both, the 3-dimensional evolution of the temperatures over time and space and the temperatures at the end of the optimization and simulation time. In the bottom plot, T_{ref} is displayed in red in addition to the states in blue.

The temperatures resulting from the input shown in Figure 16.6 can be seen in Figure 16.8. The added white Gaussian noise becomes obvious when comparing curves at identical positions with respect to the boundaries. The upper bound on the temperatures $\bar{T} = 285$ K is satisfied.

In Figure 16.9 the rate of change of the input and the temperature at the boundaries are demonstrated for small permissible rates of change, namely ± 0.01 K s⁻¹. Again, the constraints are fulfilled as can be seen. Figure 16.10 shows the 3-dimensional plot of the states and the states at the end of the simulation time (blue) together with T_{ref} (red). Compared to Figure 16.7, the results show no significant differences, except that for state T_6 , which is likely to be caused by the added white Gaussian noise.

The temperatures over time are visualized in Figure 16.11. The simulation time for this case is longer than for that presented in Figure 16.8. *Disadvantageous noise patterns* might lead to the longer simulation time. These noise patterns will most likely not have a large effect when the MPC control structure is combined with an observer; for example an Ex-

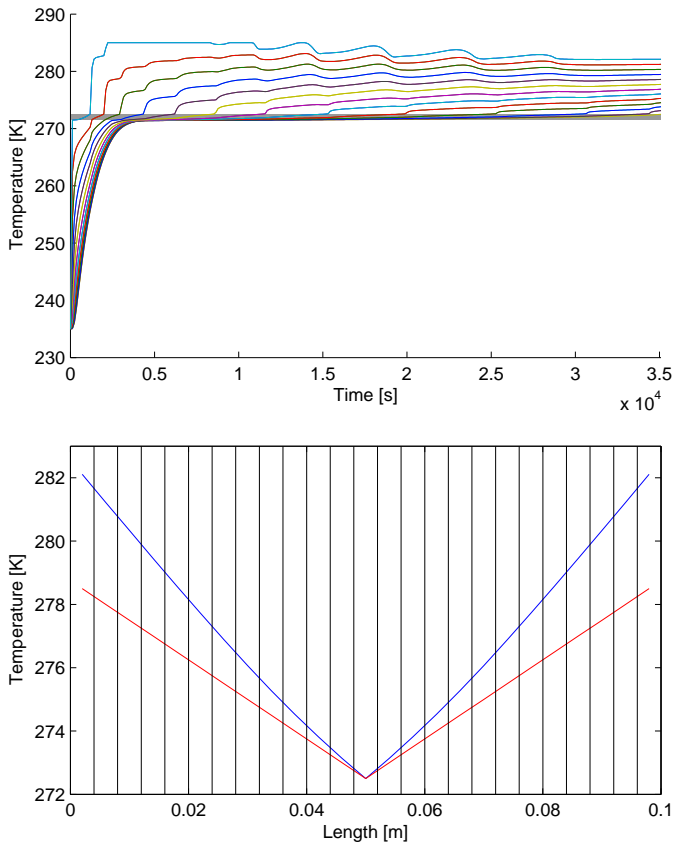


Figure 16.5: State evolution over time (top) and temperatures at the end of the time horizon (bottom) - OOC case for small rates of change

tended Kalman Filter (EKF) as described earlier in this Thesis. A reason for this is that the EKF has a damping property on the noise pattern introduced to the measurement signals, as could be seen in the simulation results for the EKF.

T_{ref}	[276.5 275.5 274.5 273.5 272.5 273.5 274.5 275.5 276.5] K
T_{init}	235 K
\bar{T}	285 K
\underline{T}	285 K
\underline{a}	283 K
\bar{a}	293 K
a_{init}	285 K
a_{ref}	283 K
\underline{b}	$-0.01 \text{ K s}^{-1} / -0.1 \text{ K s}^{-1}$
\bar{b}	$0.01 \text{ K s}^{-1} / 0.1 \text{ K s}^{-1}$
b_{ref}	0 K s^{-1}
E	$10^3 \cdot I_{(25 \times 25)}$
F	10^1
G	10^1

Table 16.2: Simulation parameters for the MPC thawing case

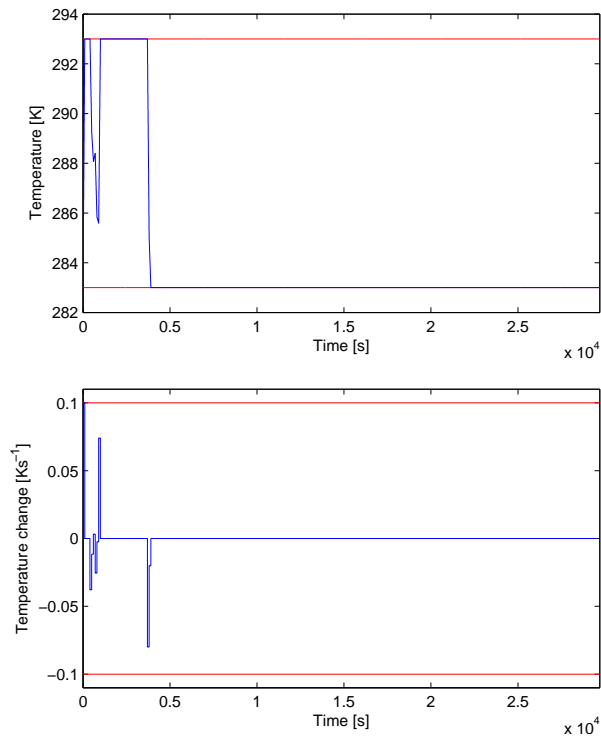


Figure 16.6: Boundary temperature (top) and its rate of change over time (bottom) - MPC case for large rates of change

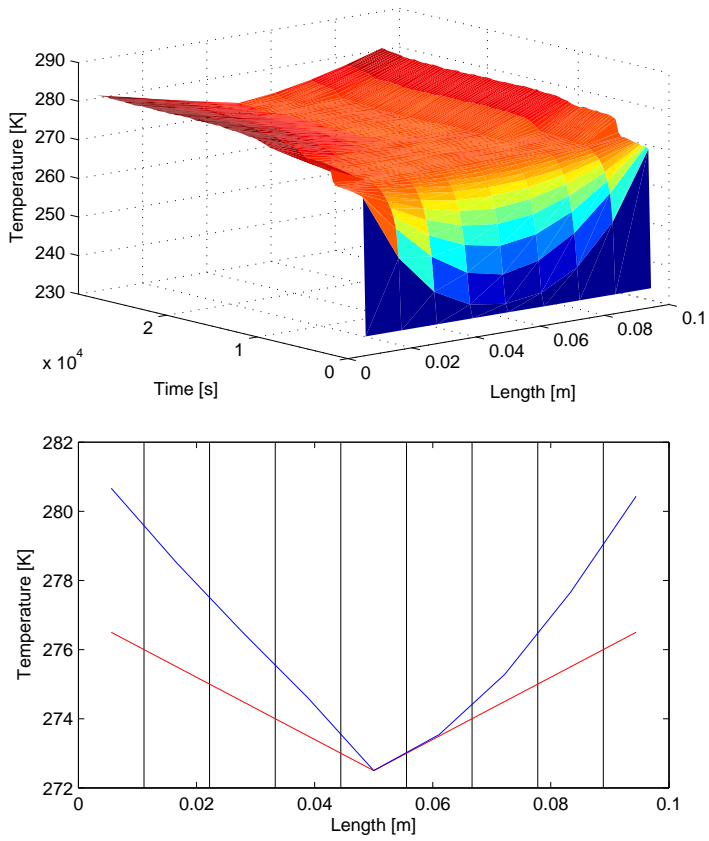


Figure 16.7: A 3-dimensional plot of the temperatures (top) and temperatures at the end of the time horizon (bottom) - MPC case for large rates of change

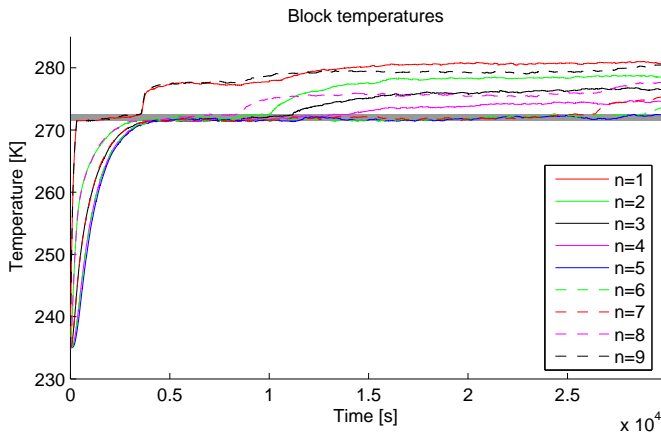


Figure 16.8: State evolution over time - MPC case for large rates of change

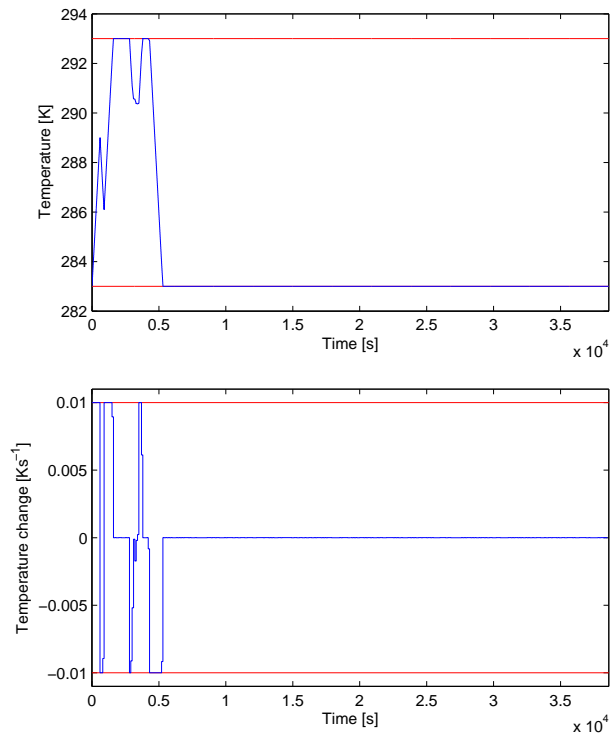


Figure 16.9: Boundary temperature (top) and its rate of change over time (bottom) - MPC case for small rates of change

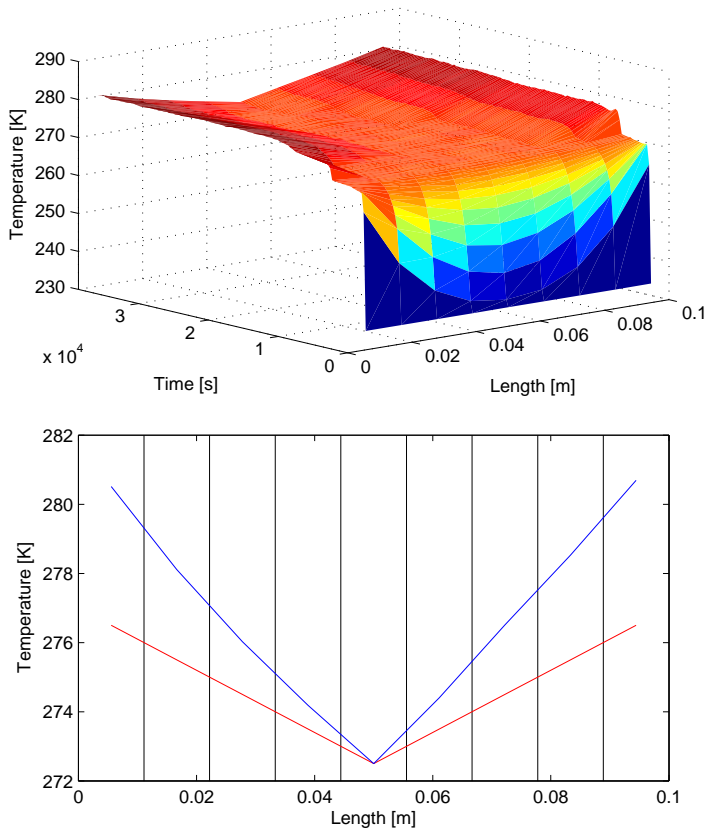


Figure 16.10: State evolution over time and space (top) and temperatures at the end of the time horizon (bottom) - MPC case for small rates of change

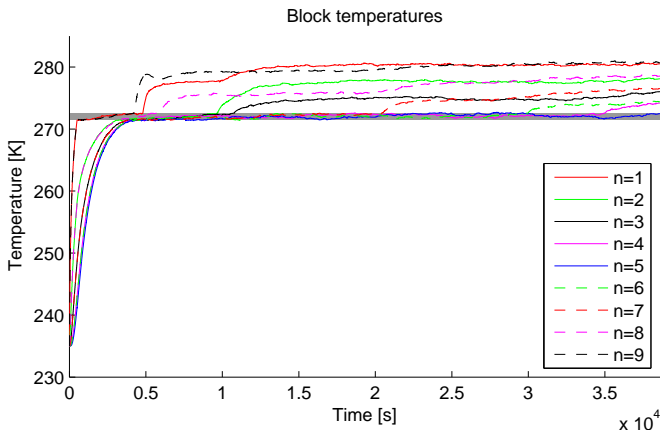


Figure 16.11: State evolution over time - MPC case for small rates of change

No matter how many times the results of experiments agree with some theory, you can never be sure that the next time the result will not contradict the theory.

Stephen Hawking

Part IV

Experiments

Chapter 17

Freezing

In order to validate the model introduced in Chapter 6, simulation results attained with these models have to be compared to measured data obtained from a real process. By comparing freezing curves from literature (e.g. in Johnston et al. [58]) to the results obtained by simulation of the model for freezing, a qualitative trend can be seen, which verifies the model. However, for completeness, experimental results for a freezing process as well as a comparative study will be presented in this Chapter. These experiments have been conducted at Matís Food Research in Reykjavík, Iceland. The equipment used was a horizontal plate freezer of Jackstone Freezing Systems Ltd., Norfolk, UK, which can be seen in Figure 17.1. For the experiments a tray made of aluminum was filled with tap water and placed in between two plates of the plate freezer. The distance between the plates was roughly 4.5 cm as this was the size of the tray.



Figure 17.1: The horizontal plate freezer used for the experiments

The temperatures were logged using button temperature loggers with a time resolution of 60 s. The positions of the logger inside the tray can be seen in Figure 17.2. The logger denoted 1 was situated on the bottom of the pan. The same holds for logger 2. Logger 3

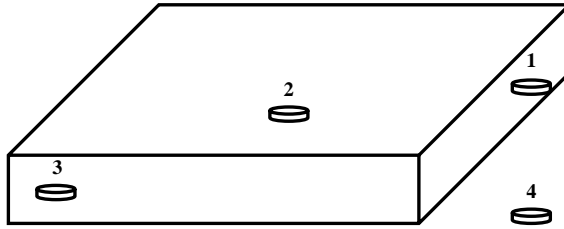


Figure 17.2: The positions of the loggers

was located halfway between the plates, whereas logger 4 was put directly on the plate of the freezer in order to monitor the refrigerant temperature.

Figure 17.3 shows the measured curves at the respective logger positions over time. As can be seen the time it takes to reach the latent zone for loggers 1 – 3 is unusually short. These large gradients are demonstrated in Figure 17.4 to visualize the differences between single curves. For loggers 1 and 2 the slope is almost the same, which corresponds with expected results, as both are located at the bottom of the tray. The slope of logger 3 is not that steep, which also corresponds with reality. In addition, the temperature of logger 3 remains in the latent zone for a long time. The same holds for logger 2, which should look more like logger 1. A reason for this delay in logger 2 might be bad contact between the tray and the freezer plate.

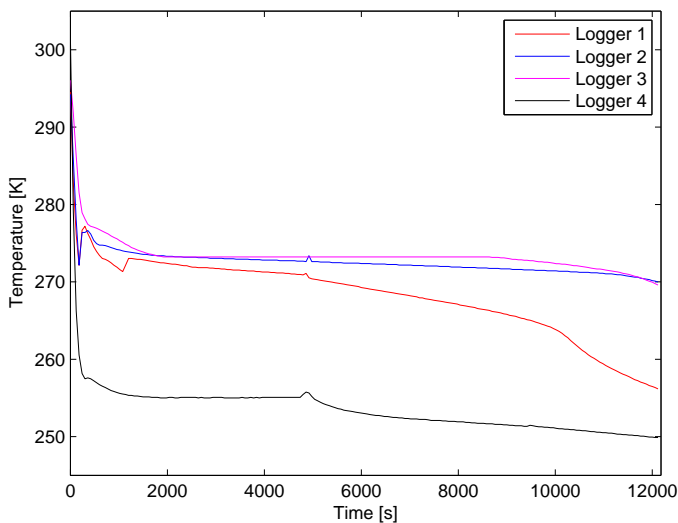


Figure 17.3: The measured freezing curves

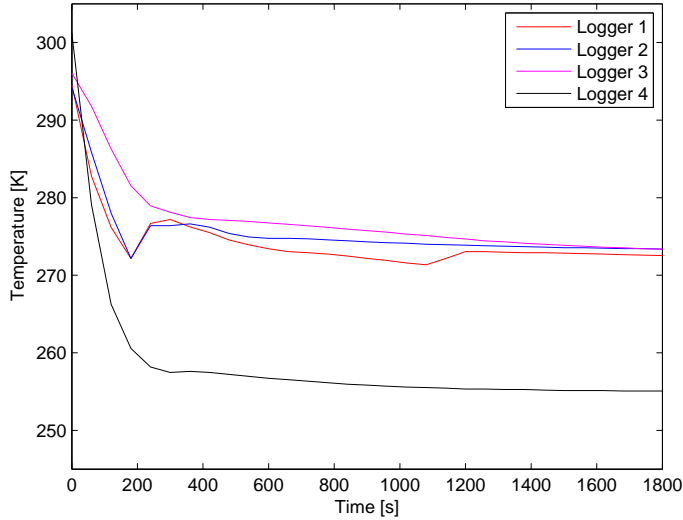


Figure 17.4: The measured freezing curves - the first 1800 s

Simulations of the freezing process for water have been conducted in the same way as already introduced in Chapter 6. Thereby the parameters were changed to those of water as can be seen in Table 17.1. The discretization grid was chosen to be $N = 99$ and the solver was chosen as ode45 of MATLAB[®]. The measurement of logger 4 was used as an input for the simulation.

T_F	273.2	K
ΔT	0.5	K
δT	0.1	K
LH	334000	$\text{J kg}^{-1} \text{K}^{-1}$
c_s	2000	$\text{J kg}^{-1} \text{K}^{-1}$
c_i	337100	$\text{J kg}^{-1} \text{K}^{-1}$
c_l	4200	$\text{J kg}^{-1} \text{K}^{-1}$
ρ	950	kg m^{-3}
λ_s	2.3	$\text{W m}^{-1} \text{K}^{-1}$
λ_l	0.55	$\text{W m}^{-1} \text{K}^{-1}$

Table 17.1: Simulation parameters for the freezing experiment

In Figure 17.5 a comparison between simulated results and the measured curves shown in Figure 17.3 is demonstrated. The dashed simulation curves correspond roughly to the positions of the loggers with the same colors. As can be seen, the simulation results are quite off the measurements. This is most likely due to the fact that heat transfer between the

plates and the water in the tray is lower than accounted for in the model. In fact the tray's bottom did not fit perfectly on the bottom plate of the freezer such that air between them caused reduced heat transfer. Furthermore it was not possible to fill the tray completely with water resulting in the top plate not having direct contact with the water, which led to reduced heat transfer at this boundary as well.

The initial steep transients are probably based on the fact that the loggers were put into the initially $7\text{ }^{\circ}\text{C}$ cold water and cooled down from room temperature very fast. Therefore, the initial condition of the simulations was chosen as $280\text{K} \approx 7\text{ }^{\circ}\text{C}$.

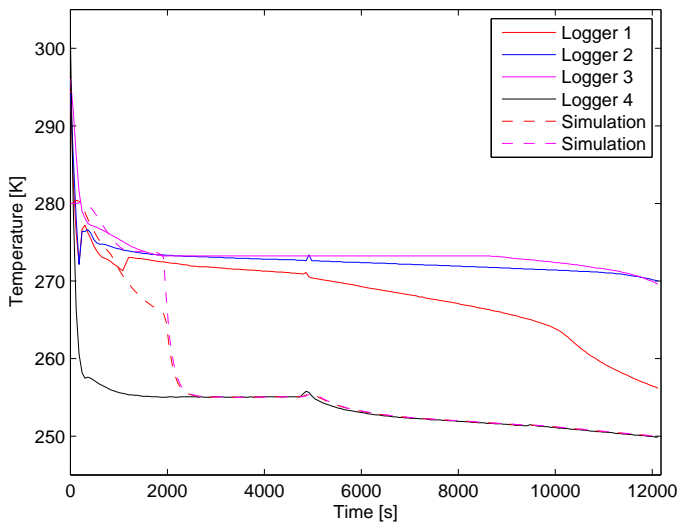


Figure 17.5: The measured freezing curves compared with the simulation results

In order to model for the reduced heat transfer at the boundaries during the experiment, the simulation was adapted to model for this case. This was achieved in the same manner as explained in Section 6.4. The simulation results are presented in Figure 17.6 and show better convergence than for the case presented in Figure 17.5. Thereby the top plot in Figure 17.6 has larger heat transfer than the bottom one, as can be seen by direct comparison.

All in all, the experiments do not show perfect results when comparing the real process to the simulations. However, by comparing the simulation results to typical freezing curves of foodstuff, one can see that the model delivers qualitative results, see e.g. Anonymous [3] or the aforementioned work of Johnston et al. [58].

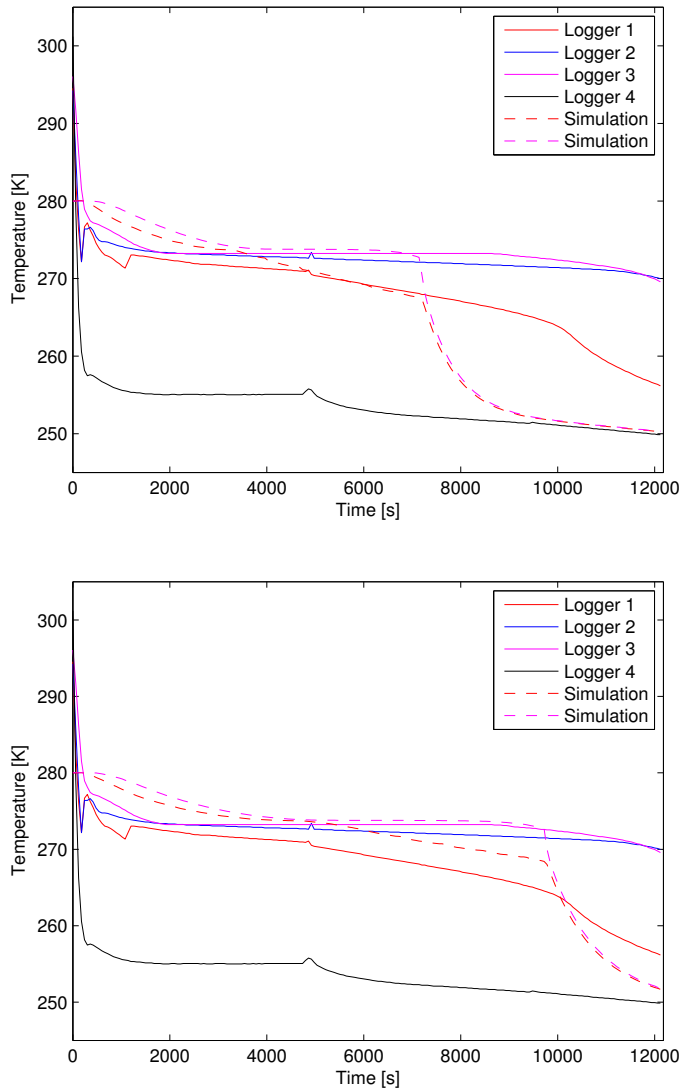


Figure 17.6: The measured freezing curves compared with the simulation results for reduced heat transfers at the boundaries

Chapter 18

Thawing

Just like for the freezing case in Chapter 17, also simulation results for the thawing case are compared to real measurement data obtained from a thawing process in a horizontal plate freezer (“plate thawer”). This is done in order to validate the model for thawing. The experiments for thawing have also been conducted at Matís Food Research in Reykjavík, Iceland. The thawing equipment was a rebuilt plate freezer, which was operated with water as the thawing medium pumped through the plate freezer walls. The plate freezer is shown in Figure 17.1 in Chapter 17. The frozen blocks of H/G cod in the tray are presented in Figure 18.1, whereas the tray together with the fish blocks inside the plate freezer can be seen in Figure 18.2. The distance between the plates was roughly 7 cm.



Figure 18.1: Two frozen fish blocks on the aluminum tray

The loggers were placed on the plate of the thawer and in three different locations inside the fish block. One just underneath the surface, the second half way to the center of the block and the third one at the center of the spatial domain. However, mounting these loggers inside the fish block at the correct and desired positions is hard to achieve and therefore the measurements are more of qualitative than of quantitative nature.



Figure 18.2: The aluminum tray with the fish blocks in between the plate thawer walls

In Figure 18.3 the temperatures of the four loggers are displayed. Logger 4 thereby denotes the temperature at the plate and thus the temperature of the thawing medium. As can be seen the control of the boundary temperature is not very sophisticated. Logger 1 is the one that was obviously closest to the center of the spatial domain, followed by logger 3 and then logger 2, which was located closest to the surface. For all the logged temperatures it seems like the latent zone is bigger than assumed in the models.

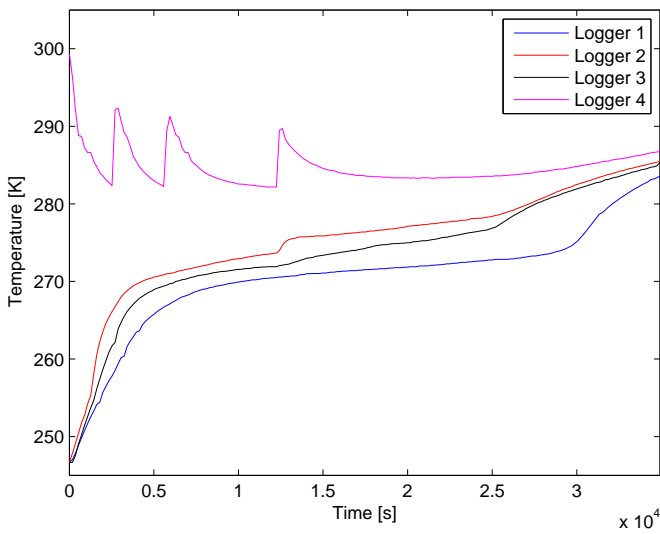


Figure 18.3: The measured thawing curves

Figure 18.4 shows a comparative plot between the measurements (solid lines) and the simulation results (dashed lines). The simulation parameters are the same as introduced in Table 6.1. Again, the discretization grid was set to $N = 99$ and `ode45` of MATLAB[®] was chosen as solver. The measurement of logger 4 was used as an input for the simulation. As can be seen the initial response of the simulated temperatures is much faster than that of the measurements. This is expected as the heat transfer in the real process is lower than for the simulations due to poorer contact between fish block and plate as well as tray and plate, respectively. The shorter time in the latent zone for the simulations is due to the fact that the fish blocks are considered to be a homogeneous mass. This is not the case in a real application, as entrapped air gives poorer heat exchange.

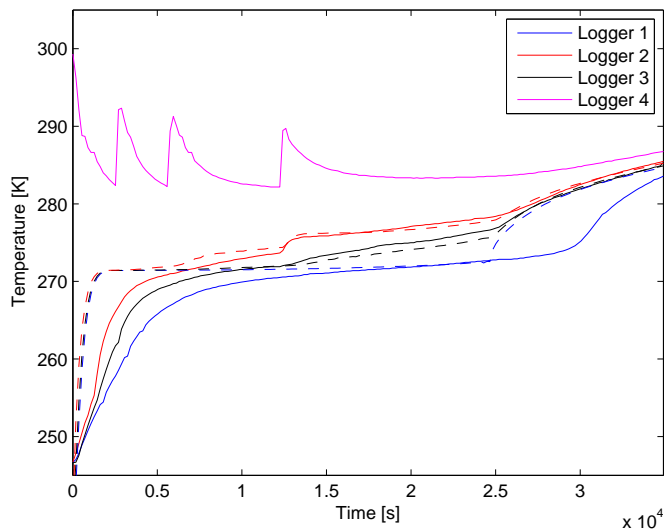


Figure 18.4: The measured thawing curves compared with the simulation results

Nevertheless, the simulated results fit the measured temperatures quite well. In fact the results obtained for thawing are better than those for freezing in Chapter 17.

It's more fun to arrive a conclusion
than to justify it.

Malcolm Forbes

Part V

Closing Remarks

Chapter 19

Conclusion

The main goal of the PhD project was the development of a mathematical model for freezing and thawing processes. This model was used in order to simulate the temperature distribution inside foodstuff during phase change processes. Furthermore, the model was used to estimate the temperature field inside the non-accessible inner-domain of the foodstuff. Another application was the development of optimal control strategies to either freeze or thaw blocks of foodstuff in an optimal way.

There have been four major contributions in the thesis, two on modeling and analysis and two on applications.

19.1 Contributions in the field of modeling and analysis

The model, which has been derived in Chapter 6, is based on the diffusion equation with state-dependent parameters; thus it is a parabolic partial differential equation (PDE). As phase change is a dominant phenomenon in the processes to be modeled, state-dependency of the parameters is inevitable. This is also due to the fact that the method used in order to model for *thermal arrest* induced by the presence of *latent heat of fusion* is the *apparent heat capacity* method, which overestimates the specific heat capacity $c(T)$ in a region around the freezing point. The resulting model could be denoted nonlinear heat equation. Strictly speaking, the model is a quasi-linear PDE as the highest order term T_{xx} is added linearly to the PDE. However, as both, the nonlinear term T_x^2 and the linear term T_{xx} are multiplied by parameters that are functions of the state-variable T itself, denoting it as a nonlinear PDE could make sense. The model showed itself suitable for freezing and thawing applications. Relevant discretization schemes were chosen for the freezing and thawing cases, respectively, and tested against the solutions of the commercial MATLAB[®] solver `pdepe` in order to validate them.

The contribution in terms of analysis lies in showing similarities of the derived model with other classes of PDEs, in particular the Burgers' equation and its potential form. However, existing transformations to rewrite the derived model into another form for which certain stability properties are known to hold, could not be applied. Therefore, a stability investigation for the model was conducted. This stability analysis, however, only holds for distinct parameter functions, which are actually valid for the freezing and thawing cases.

The stability analysis was conducted by means of Lyapunov theory by defining positive definite Lyapunov candidates for the model rewritten in error coordinates consisting of a stationary and a transient part. The stability investigation was conducted in both, L^2 and H^1 functional spaces, respectively. Therefore, the Lyapunov candidates were defined as kind of norms in the respective functional spaces. The reason for conducting the analysis in both norms is that it is not sufficient to show that the function decreases in the L^2 -norm only, as this norm can not take peaks in the spatial domain into account. Therefore, a higher order norm, like e.g. the H^1 -norm has to be included as it contains the first spatial derivative of the function to be investigated.

19.2 Contributions in the field of applications

There were two major contributions in the field of applications for the models derived in this thesis. One is the development of an observer to estimate inner-domain temperatures during freezing and thawing processes, mainly in plate freezers or contact thawing devices, like e.g. plate thawers or electrically heated plates. The observer design was chosen to be based on the widely established Extended Kalman Filter (EKF). Therefore, the PDE had to be discretized in the spatial domain, which yielded a set of nonlinear ordinary differential equations (or more general a differential algebraic equation (DAE) system). The main reason for choosing this approach is the presence of state-dependent parameter functions, which make the application of other observers (finite- and infinite-dimensional) challenging, if not impossible. There are already established methods to design observers for PDEs. These, however, hold for constant parameter functions and are limited to specific classes of PDEs. There were three different observer designs presented, namely a full model observer, a reduced model observer and a real-time applicable observer. The difference between these types was the definition of the parameter functions $k(T)$ and $\kappa(T)$. Reducing the complexity of these parameter functions reduced the complexity of the observers, mainly with respect to calculation, but not necessarily with regards to performance. Another feature was the introduction of state-dependent switching of the covariance matrices to enhance the quality of estimation.

The second major contribution in application is the design of optimal control structures for open loop and closed loop control of freezing and thawing processes in plate freezers and contact thawers, respectively. For these numerical optimization problems, the PDE was discretized in the spatial domain in the same way like the aforementioned observer designs. The optimization variable was the temperature rate of change at the boundaries, while the boundary temperature itself was the input to the system. The control objective was thereby to track a temperature reference in a variable time horizon for the open loop Optimal Control case for both, freezing and thawing. The objective function was defined as a least squares (LSQ) tracking term penalizing deviations from state-, input- and time-horizon-references. Several constraints have been imposed to the optimization problem, such as the dynamical system itself and bounds on the states, the input as well as on the optimization variable. Furthermore, a terminal region constraint was defined as well as an LSQ end term penalizing temperature-deviations from a reference at the end of the time horizon. For the closed loop MPC cases for freezing and thawing, the objective function was still an LSQ for state- and input-tracking. In addition, bounds on the states, the input and the optimization variable constrained the Optimal Control Problem together with the

dynamical system. However, for the MPC approach no terminal region constraint as well as no LSQ end term were defined. This is reasoned by feasibility issues that might arise for the relatively short time horizons used in MPC approaches. In addition, white Gaussian noise was added to the state vector after applying the first calculated input of the MPC to a simulation of the plant. This noisy state vector was then fed back as the new initial condition for the new MPC iteration. This procedure continued until all temperatures were smaller or bigger than a certain temperature, depending on the application (freezing or thawing, respectively).

Chapter 20

Future Work

In this Chapter several issues concerning future work and other fields of application are covered. Firstly, some further comments on future work regarding the modeling and the analysis of the models are given. Thereafter, topics concerning future work regarding the applications are presented. In the end some general comments on freezing, thawing and other possible applications are mentioned.

20.1 Future work regarding modeling and model analysis

The model introduced in Chapter 6 is stable. This is shown by the various simulations presented in this thesis. However, stability analysis has only been conducted for special cases of the parameter functions $k(T)$ and $\kappa(T)$. Topics for future work can therefore include stability analyses for the model with respect to more general classes of parameter functions.

The stability investigation presented is based on boundary conditions of Dirichlet type. Further investigations could approach stability for Neumann boundary conditions as well.

Showing existence and uniqueness of solutions for the model in Chapter 6 is another potential subject, as it hasn't been regarded in this thesis.

With the design of the real-time applicable observers presented in Sections 11.2.4 and 13.2 new questions arise in the field of stability of interconnected, switched linear PDEs (linear heat equations). Simulations indicate stability for such systems, which can be reasoned with certain damping properties of the heat equation with respect to singularities. Nevertheless, investigation of stability for these kinds of systems can be another topic for future work.

20.2 Future work regarding the observer designs

In the field of observer design, the main issue was the fact that the parameter functions were state-dependent. Therefore, an established design, the Extended Kalman Filter, was chosen, also due to its known robustness properties. In future work other observer designs could be investigated, e.g. observers formulated as partial differential equations (PDEs). There exist PDE-observers for the linear heat equation based upon a backstepping design

as introduced by Krstić and Smyshlyaev [69]. This design could potentially be used in the same fashion like the real-time applicable observers presented in Subsections 11.2.4 and 13.2, namely as an observer based on switched linear PDEs.

Furthermore, nonlinear observer designs as known from the world of ordinary differential equations (ODEs), able to deal with state-dependent parameters could be investigated and applied as spatially discretized observers for the PDEs.

Another aspect of more practical nature lies in the availability of measurements for the observers proposed in Chapters 10–13. An investigation for a reduced set of measurements can make sense. In addition, observability verification for time-varying system-matrices are a topic, which has not been approached in this work. As the structures of the linearized, sparse system matrices are known and don't change their shape, general rules could possibly be derived for bounded elements in these matrices.

Also for the observer designs, the possibility for application of Neumann boundary conditions could be investigated. However, the calculation of the heat transfer by Neumann boundary conditions will be based upon temperature and pressure measurements of the refrigerants and thawing media, respectively. Therefore, the measurements will be the same like for Dirichlet boundary conditions, but the implementation of these measurements into the equations will differ.

An implementation of the developed real-time observers in a real freezing or thawing process should also be conducted in order to validate the design and see if the same performance can be achieved as already obtained in simulations.

20.3 Future work regarding the optimal control designs

For the conducted studies on optimal control of the freezing and thawing processes, the implementation of Neumann boundary conditions can also be done here. This has to be performed in the same manner as already described for the observer designs.

Another aspect is the simulation of the optimal control strategies, in particular Model Predictive Control (MPC), together with an observer estimating the inner domain temperatures. Therefore, the optimal control applications will have to be extended into two-dimensional descriptions. Coupling the MPC with an estimator is crucial, as the added white Gaussian noise can only model for errors in the model and measurements to a limited degree. If this merging of the observer with the MPC structure is successful in simulations, application of the overall design into real freezing and thawing processes can be tried. However, a potential success is mainly based on how good the observer works in a real world application. The developed real-time applicable observers represent a promising step towards this.

20.4 Further comments on freezing, thawing and other applications

Further comments are mainly based upon other ideas concerning freezing and thawing processes, as well as other fields of application, where the developed models and designs can potentially be implemented. The model developed in Chapter 6 could be applied to other applications in the area of freezing and thawing. This holds for example for water-

and air-based freezing and thawing methods, especially for regular shaped objects, like blocks in rectangular form. Furthermore, other processes subject to phase change can be of interest, like for example latent heat thermal energy storage systems. Another example could be the estimation of the temperatures throughout a steel slab in an iron mill. This is not particularly a phase change process, however, due to the large temperature range the parameters might have to be modeled temperature-dependent.

Regarding measurements for the initial freezing and thawing problems of foodstuff, one could think about applying other techniques for detecting frozen and thawed states in the blocks. Especially ultrasound methods could detect when water is not in frozen but in liquid state. However, for freezing, this seems not to be applicable as accurate temperature measurements can not be obtained by ultrasound, but a phase change can be detected and thus it could be applicable for thawing.

Somewhere, something incredible is
waiting to be known.

Carl Sagan

Appendices

Appendix A

Comparative plots for the chosen discretization schemes

In the plots presented in this Chapter green lines represent the block's center position and blue lines indicate the outermost position at the left boundary. The dashed lines in the bottom left plots show results for the discretization scheme used in the thesis while the solid lines show results obtained by the solver pdepe of MATLAB[®] at the respective positions.

A.1 Freezing

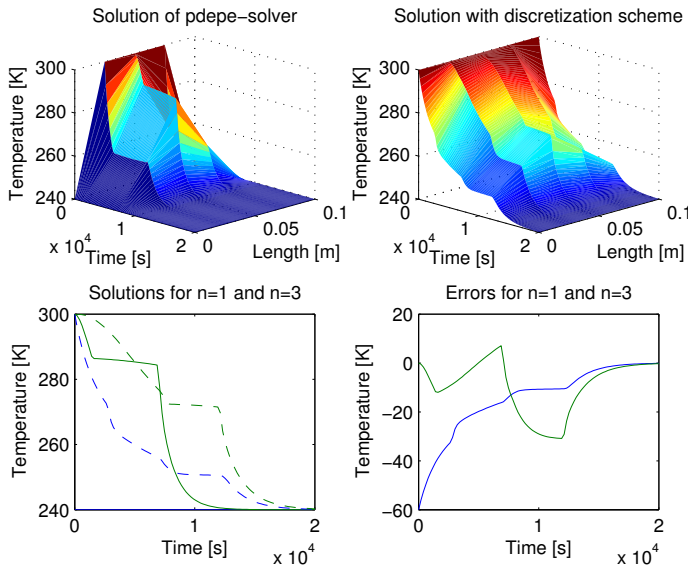


Figure A.1: N=5 discretization steps

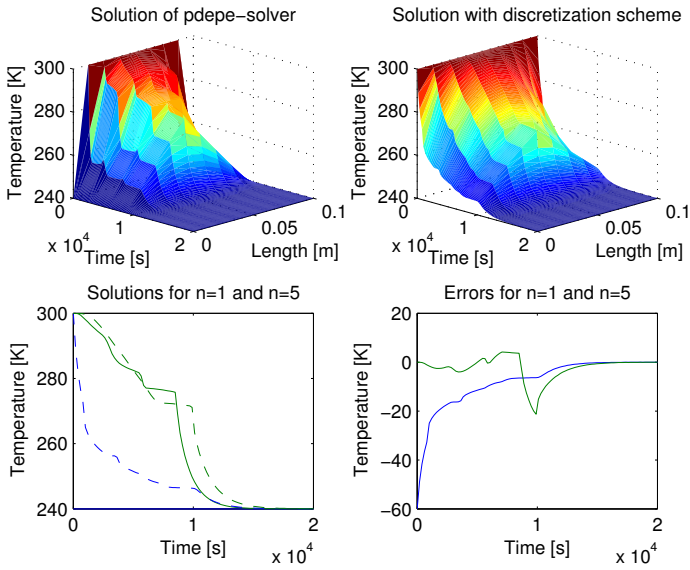


Figure A.2: N=9 discretization steps

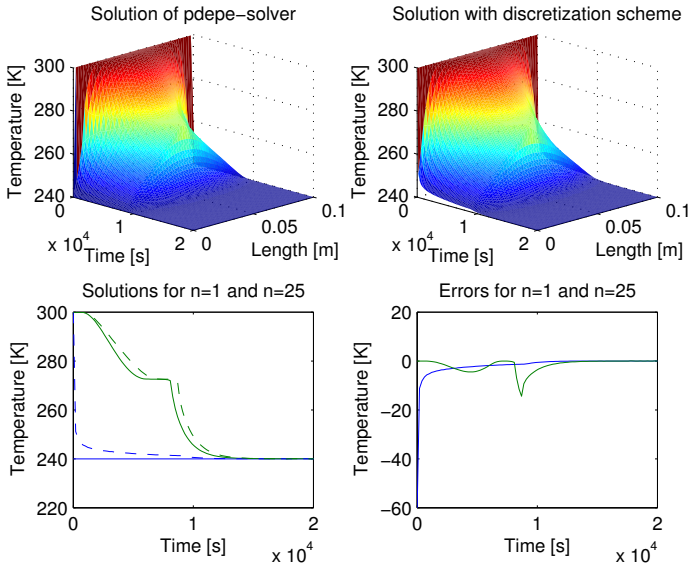
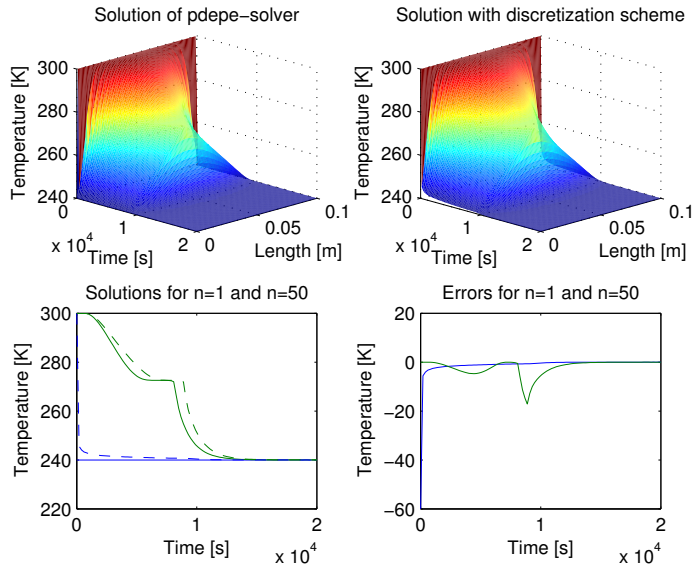
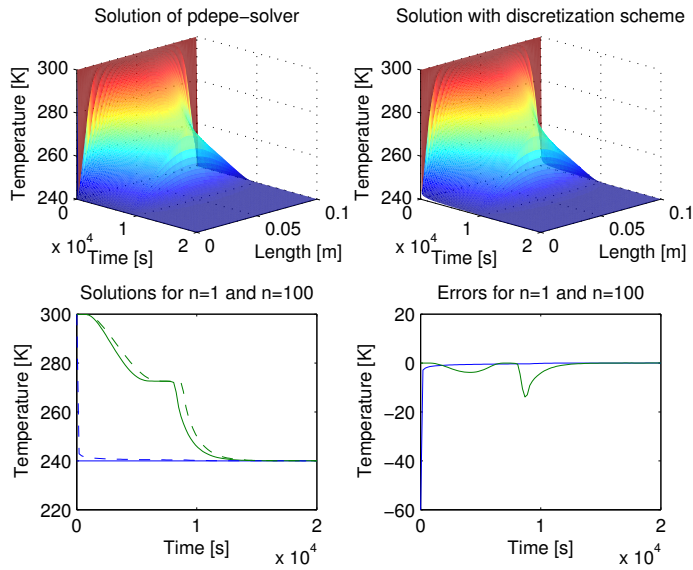


Figure A.3: N=49 discretization steps

Figure A.4: $N=99$ discretization stepsFigure A.5: $N=199$ discretization steps

A.2 Thawing

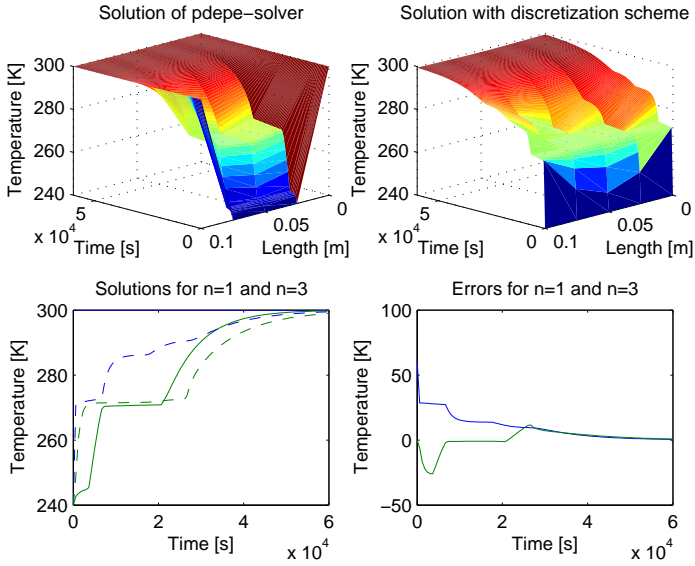


Figure A.6: $N=5$ discretization steps

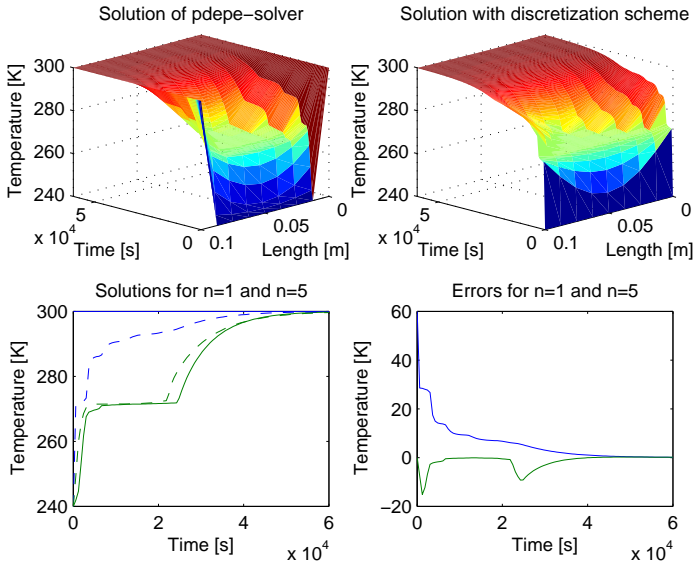
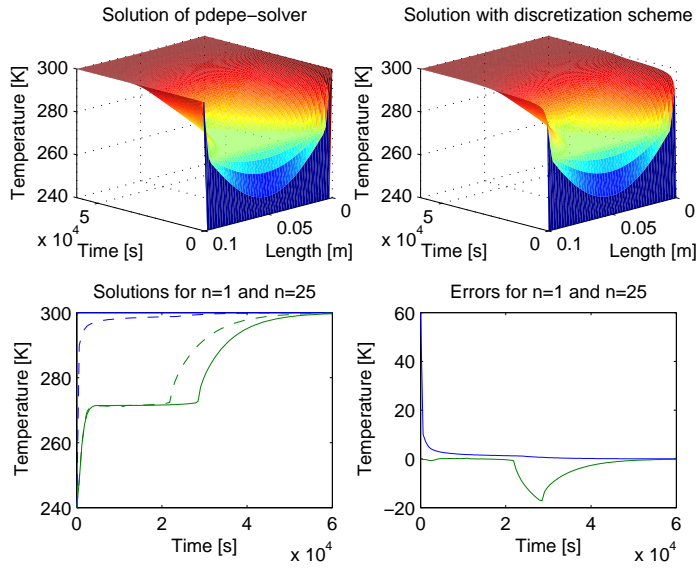
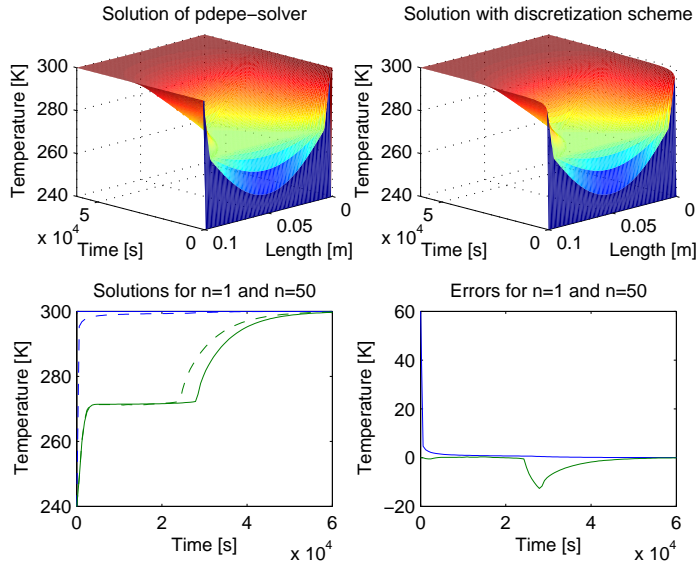


Figure A.7: $N=9$ discretization steps

Figure A.8: $N=49$ discretization stepsFigure A.9: $N=99$ discretization steps

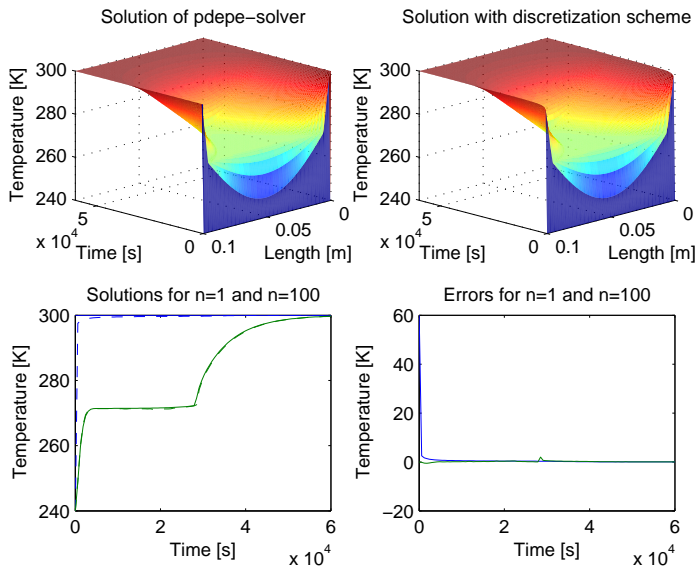


Figure A.10: N=199 discretization steps

Appendix B

Proof of Lemma 8.1

Proof. Define the Lyapunov candidate V by

$$V = \int_0^1 \frac{1}{k} w^2 dx \quad (\text{B.1})$$

and note that V is lower bounded by the L^2 -norm

$$V \geq \frac{1}{\beta} \|w(t)\|^2 \quad (\text{B.2})$$

since $k \leq \beta$ by assumption.

Differentiating (B.1) with respect to time leads to

$$\begin{aligned} \dot{V} &= \int_0^1 \left(\frac{2}{k} w w_t - \frac{k_u}{k^2} w^2 w_t \right) dx \\ &= \frac{1}{L^2} \int_0^1 \left(\frac{2\kappa}{k} w w_x^2 + \frac{2\kappa}{k} w S^2 + \frac{4\kappa}{k} w S w_x + 2 w w_{xx} \right. \\ &\quad \left. - \frac{\kappa k_u}{k^2} w^2 w_x^2 - \frac{\kappa k_u}{k^2} w^2 S^2 - \frac{2\kappa k_u}{k^2} w^2 S w_x - \frac{k_u}{k} w^2 w_{xx} \right) dx. \end{aligned} \quad (\text{B.3})$$

Integrating the term $w w_{xx}$ by parts yields

$$\int_0^1 w w_{xx} dx = \left[w w_x \right]_0^1 - \int_0^1 w_x^2 dx \quad (\text{B.4})$$

with $\left[w w_x \right]_0^1 = 0$ due to (8.10b).

Furthermore, integrating $\frac{k_u}{k} w^2 w_{xx}$ by parts as well leads to

$$\int_0^1 \frac{k_u}{k} w^2 w_{xx} dx = \left[\frac{k_u}{k} w^2 w_x \right]_0^1 - 2 \int_0^1 \frac{k_u}{k} w w_x^2 dx - \int_0^1 \frac{k_{uu} k - k_u^2}{k^2} w^2 w_x^2 dx \quad (\text{B.5})$$

with $\left[\frac{k_u}{k} w^2 w_x\right]_0^1 = 0$ due to (8.10b).

Then, after inserting (B.4) and (B.5) into (B.3) and collecting terms the following expression is obtained

$$\dot{V} = \frac{1}{L^2} \int_0^1 \frac{1}{k} \left[A w_x^2 + B w_x + C \right] dx \quad (\text{B.6})$$

with the shorthand

$$A = -w^2 \frac{1}{k} (\kappa k_u - k_{uu} k + k_u^2) + w(2\kappa + 2k_u) - 2k, \quad (\text{B.7a})$$

$$B = w^2 \frac{1}{k} (-2\kappa k_u S) + w(4\kappa S), \quad (\text{B.7b})$$

$$C = w^2 \frac{1}{k} (-\kappa k_u S^2) + w(2\kappa S^2). \quad (\text{B.7c})$$

Note that $A < 0$, since the coefficients

$$a = -\frac{1}{k} (\kappa k_u - k_{uu} k + k_u^2), \quad (\text{B.8a})$$

$$b = 2\kappa + 2k_u, \quad (\text{B.8b})$$

$$c = -2k \quad (\text{B.8c})$$

of the parabola $aw^2 + bw + c$ defined in (B.7a) fulfill $a < 0$ and $b^2 - 4ac < 0$, by assumptions (8.11d)-(8.11g).

The rest of the proof consists of the following two observations outside and inside $I_{\Delta u}$, respectively.

Firstly, by (8.11g) it can be inferred that outside $I_{\Delta u}$ both $B = 0$ and $C = 0$. Hence, for this case, (B.6) can be bounded using that $\frac{1}{\beta} \leq \frac{1}{k}$ followed by applying Lemma 2.1 (*Poincaré's Inequality*), leading to

$$\dot{V} \leq \frac{K_1}{L^2 \beta} \|w_x\|^2 \leq \frac{K_1}{4L^2 \beta} \|w\|^2 \quad (\text{B.9})$$

with $K_1 = \max(A) < 0$.

Secondly, the inequality $B^2 - 4AC < 0$ holds true inside $I_{\Delta u}$, as can be seen as follows. Using (B.7), the inequality $B^2 - 4AC < 0$ is equivalent to the following quartic inequality

$$\frac{w^4}{k^4} (4\kappa k_u S^2 (k_{uu} k - k_u^2)) + \frac{w^3}{k^3} (-8\kappa S^2 (k_{uu} k - 2k_u^2)) + \frac{w^2}{k^2} (-24\kappa k_u S^2) + \frac{w}{k} (16\kappa S^2) < 0. \quad (\text{B.10})$$

Let

$$\psi(w) = a_4 w^4 + a_3 w^3 + a_2 w^2 + a_1 w$$

denote the fourth order polynomial defined by the left hand side of (B.10) and note that $a_i < 0$, $i = 1, 2, 3, 4$ inside $I_{\Delta u}$ by the assumptions (8.11d)-(8.11f). Let $\phi(w)$ denote the

third order polynomial defined by $\psi(w) = w\phi(w)$. Then (B.10) holds true inside $I_{\Delta u}$ iff $\phi(w) < 0$ for $w > 0$. Since both, $a_4 < 0$ and $a_1 < 0$ inside $I_{\Delta u}$, it is enough to show that the roots of $\phi(w)$ all are negative or complex, which follows from the fact that inside $I_{\Delta u}$ the following relations hold: $a_4 < 0$, $\phi_w(0) = a_2 < 0$ and $\phi_{ww}(0) = a_3 < 0$. Hence, when inside $I_{\Delta u}$, there exists a constant $K_2 < 0$ such that

$$\dot{V} \leq \frac{K_2}{L^2\beta} \|w_x\|^2 \leq \frac{K_2}{4L^2\beta} \|w\|^2 \quad (\text{B.11})$$

By letting $\bar{K} = \max\{K_1, K_2\}$, both inequalities (B.9) and (B.11) now yield

$$\dot{V} \leq \frac{\bar{K}}{4L^2\beta} \|w\|^2, \quad (\text{B.12})$$

which together with (B.1) and Henry [48, Theorem 4.1.4] proves the lemma. \square

Appendix C

Proof of Lemma 8.2

Proof. Define the Lyapunov candidate Λ by

$$\Lambda = V_1 + V = \frac{1}{2} \int_0^1 w_x^2 dx + V, \quad (\text{C.1})$$

where V denotes the Lyapunov function defined by (B.1).

The time derivative of V_1 is

$$\dot{V}_1 = \int_0^1 w_x w_{tx} dx. \quad (\text{C.2})$$

To obtain an expression for w_{tx} in terms of spatial derivatives of w only, the derivative of (8.10) with respect to x is calculated and one obtains

$$w_{tx} = \frac{1}{L^2} \left(\kappa_u w_x^3 + 2\kappa_u S w_x^2 + \kappa_u S^2 w_x + 2\kappa w_x w_{xx} + 2\kappa S w_{xx} + k_u w_x w_{xx} + k w_{xxx} \right). \quad (\text{C.3})$$

Combining (C.3) and (C.2) and collecting terms gives

$$\dot{V}_1 = \frac{1}{L^2} \int_0^1 \left(\kappa_u w_x^4 + 2\kappa_u S w_x^3 + \kappa_u S^2 w_x^2 + 2\kappa w_x^2 w_{xx} + 2\kappa S w_x w_{xx} + k_u w_x^2 w_{xx} + k w_x w_{xxx} \right) dx. \quad (\text{C.4})$$

Integrating the terms $k w_x w_{xxx}$ and $\kappa w_x w_{xx}$ by parts yields

$$\int_0^1 k w_x w_{xxx} dx = \left[k w_x w_{xx} \right]_0^1 - \int_0^1 k w_{xx}^2 dx - \int_0^1 k_u w_x^2 w_{xx} dx \quad (\text{C.5})$$

$$\begin{aligned} \int_0^1 \kappa w_x w_{xx} dx &= \left[\kappa w_x^2 \right]_0^1 - \int_0^1 \kappa w_x w_{xx} dx - \int_0^1 \kappa_u w_x^3 dx \\ &= \left[\frac{\kappa}{2} w_x^2 \right]_0^1 - \int_0^1 \frac{\kappa_u}{2} w_x^3 dx. \end{aligned} \quad (\text{C.6})$$

Putting (C.5) and (C.6) into (C.4) one obtains

$$\dot{V}_1 = \frac{1}{L^2} \int_0^1 \left(\kappa_u w_x^4 + \kappa_u S w_x^3 + \kappa_u S^2 w_x^2 + 2\kappa w_x^2 w_{xx} - k w_{xx}^2 \right) dx + \frac{1}{L^2} \left[k w_x w_{xx} + \kappa S w_x^2 \right]_0^1. \quad (\text{C.7})$$

Furthermore, integrating the expression $\kappa w_x^2 w_{xx}$ by parts gives

$$\begin{aligned} \int_0^1 \kappa w_x^2 w_{xx} dx &= \left[\kappa w_x^3 \right]_0^1 - \int_0^1 2\kappa w_x^2 w_{xx} dx - \int_0^1 \kappa_u w_x^4 dx \\ &= \left[\frac{1}{3} \kappa w_x^3 \right]_0^1 - \int_0^1 \frac{1}{3} \kappa_u w_x^4 dx. \end{aligned} \quad (\text{C.8})$$

Substituting (C.8) into (C.7) yields

$$\dot{V}_1 = \frac{1}{L^2} \int_0^1 \left(\frac{\kappa_u}{3} w_x^4 + \kappa_u S w_x^3 + \kappa_u S^2 w_x^2 - k w_{xx}^2 \right) dx + \frac{1}{L^2} \left[k w_x w_{xx} + \kappa S w_x^2 + \frac{2\kappa}{3} w_x^3 \right]_0^1. \quad (\text{C.9})$$

Now the quartic equation $\theta(w_x) = d w_x^4 + e w_x^3 + f w_x^2$ with the shorthand

$$d = \frac{\kappa_u}{3}, \quad e = \kappa_u S, \quad f = \kappa_u S^2,$$

needs a further investigation. The quartic equation $\theta(w_x)$ can be rewritten as $w_x^2 \gamma(w_x)$. For the quadratic equation $\gamma(w_x)$ it must be imposed that it is less than zero for all w_x and thus $d < 0$ and $e^2 - 4df \leq 0$ have to hold. If now (8.12a) holds, it gets clear that $\gamma(w_x) \leq 0$ for all w_x and therefore $\theta(w_x) \leq 0$. If furthermore (8.12b)–(8.12d) hold, one can infer that

$$\dot{V}_1 \leq -\frac{1}{L^2} \int_0^1 k w_{xx}^2 dx \leq -\frac{\alpha}{L^2} \int_0^1 w_{xx}^2 dx. \quad (\text{C.10})$$

Thus by putting (B.12) in its integral form and (C.10) into the time-derivative of (C.1), using Lemma 2.1 (*Poincaré's Inequality*) and recalling that $\bar{K} < 0$, the following expression

is received

$$\begin{aligned}\dot{\Lambda} &\leq \frac{\bar{K}}{L^2\beta} \int_0^1 w_x^2 dx - \frac{\alpha}{L^2} \int_0^1 w_{xx}^2 dx \\ &\leq \frac{\bar{K}}{L^2\beta} \int_0^1 w_x^2 dx \\ &\leq \frac{\bar{K}}{2L^2\beta} \int_0^1 w_x^2 dx + \frac{\bar{K}}{2L^2\beta} w_x^2 dx \\ &\leq \frac{\bar{K}}{8L^2\beta} \int_0^1 w^2 dx + \frac{\bar{K}}{2L^2\beta} w_x^2 dx \\ &\leq \frac{\bar{K}}{8L^2\beta} \|w(t)\|_{H^1},\end{aligned}\tag{C.11}$$

which, together with (C.1) and [48, Theorem 4.1.4] proves the lemma. \square

Appendix D

Illustration of the full model observer design case

Consider a discretization of the spatial domain using a rather large grid of $N = 3$ and $M = 3$, respectively. This leads to 9 coupled ODEs in the form

$$\begin{aligned} \dot{T}_{1,1} = & \kappa(T_{1,1}) \left[\left(\frac{T_{1,1} - T_{Boundary}}{\Delta x} \right)^2 + \left(\frac{T_{1,1} - T_{Air}}{\Delta y} \right)^2 \right] \\ & + k(T_{1,1}) \left[\frac{T_{1,2} - 2T_{1,1} + T_{Boundary}}{\Delta x^2} + \frac{T_{2,1} - 2T_{1,1} + T_{Air}}{\Delta y^2} \right] + v_{1,1}, \end{aligned} \quad (D.1)$$

$$\begin{aligned} \dot{T}_{1,2} = & \kappa(T_{1,2}) \left[\left(\frac{T_{1,3} - T_{1,1}}{2\Delta x} \right)^2 + \left(\frac{T_{1,2} - T_{Air}}{\Delta y} \right)^2 \right] \\ & + k(T_{1,2}) \left[\frac{T_{1,3} - 2T_{1,2} + T_{1,1}}{\Delta x^2} + \frac{T_{2,2} - 2T_{1,2} + T_{Air}}{\Delta y^2} \right] + v_{1,2}, \end{aligned} \quad (D.2)$$

$$\begin{aligned} \dot{T}_{1,3} = & \kappa(T_{1,3}) \left[\left(\frac{T_{Boundary} - T_{1,3}}{\Delta x} \right)^2 + \left(\frac{T_{1,3} - T_{Air}}{\Delta y} \right)^2 \right] \\ & + k(T_{1,3}) \left[\frac{T_{Boundary} - 2T_{1,3} + T_{1,2}}{\Delta x^2} + \frac{T_{2,3} - 2T_{1,3} + T_{Air}}{\Delta y^2} \right] + v_{1,3}, \end{aligned} \quad (D.3)$$

$$\begin{aligned} \dot{T}_{2,1} = & \kappa(T_{2,1}) \left[\left(\frac{T_{2,1} - T_{Boundary}}{\Delta x} \right)^2 + \left(\frac{T_{3,1} - T_{1,1}}{2\Delta y} \right)^2 \right] \\ & + k(T_{2,1}) \left[\frac{T_{2,2} - 2T_{2,1} + T_{Boundary}}{\Delta x^2} + \frac{T_{3,1} - 2T_{2,1} + T_{1,1}}{\Delta y^2} \right] + v_{2,1}, \end{aligned} \quad (D.4)$$

$$\begin{aligned} \dot{T}_{2,2} = & \kappa(T_{2,2}) \left[\left(\frac{T_{2,3} - T_{2,1}}{2\Delta x} \right)^2 + \left(\frac{T_{3,2} - T_{1,2}}{2\Delta y} \right)^2 \right] \\ & + k(T_{2,2}) \left[\frac{T_{2,3} - 2T_{2,2} + T_{2,1}}{\Delta x^2} + \frac{T_{3,2} - 2T_{2,2} + T_{1,2}}{\Delta y^2} \right] + v_{2,2}, \end{aligned} \quad (D.5)$$

$$\begin{aligned} \dot{T}_{2,3} = & \kappa(T_{2,3}) \left[\left(\frac{T_{Boundary} - T_{2,3}}{\Delta x} \right)^2 + \left(\frac{T_{3,3} - T_{1,3}}{2\Delta y} \right)^2 \right] \\ & + k(T_{2,3}) \left[\frac{T_{Boundary} - 2T_{2,3} + T_{2,2}}{\Delta x^2} + \frac{T_{3,3} - 2T_{2,3} + T_{1,3}}{\Delta y^2} \right] + v_{2,3}, \end{aligned} \quad (D.6)$$

$$\dot{T}_{3,1} = \kappa(T_{3,1}) \left(\frac{T_{3,1} - T_{Boundary}}{\Delta x} \right)^2 + k(T_{3,1}) \left[\frac{T_{3,2} - 2T_{3,1} + T_{Boundary}}{\Delta x^2} + \frac{-T_{3,1} + T_{2,1}}{\Delta y^2} \right] + v_{3,1}, \quad (D.7)$$

$$\dot{T}_{3,2} = \kappa(T_{3,2}) \left(\frac{T_{3,3} - T_{3,1}}{2\Delta x} \right)^2 + k(T_{3,2}) \left[\frac{T_{3,3} - 2T_{3,2} + T_{3,1}}{\Delta x^2} + \frac{-T_{3,2} + T_{2,2}}{\Delta y^2} \right] + v_{3,2}, \quad (D.8)$$

$$\dot{T}_{3,3} = \kappa(T_{3,3}) \left(\frac{T_{Boundary} - T_{3,3}}{\Delta x} \right)^2 + k(T_{3,3}) \left[\frac{T_{Boundary} - 2T_{3,3} + T_{3,2}}{\Delta x^2} + \frac{-T_{3,3} + T_{2,3}}{\Delta y^2} \right] + v_{3,3} \quad (D.9)$$

with the state vector

$$T = [T_{1,1} \quad T_{1,2} \quad T_{1,3} \quad T_{2,1} \quad T_{2,2} \quad T_{2,3} \quad T_{3,1} \quad T_{3,2} \quad T_{3,3}] \quad (D.10)$$

and the output being defined as follows

$$y = CT + v = [T_{1,1} \quad T_{1,2} \quad T_{1,3} \quad T_{2,1} \quad T_{2,3} \quad T_{3,1} \quad T_{3,3}]^T + z_{(7 \times 1)} \quad (D.11)$$

$$\text{with } C_{(7 \times 9)} = \begin{bmatrix} 1 & 0 & 0 & 0 & 0 & 0 & 0 & 0 & 0 \\ 0 & 1 & 0 & 0 & 0 & 0 & 0 & 0 & 0 \\ 0 & 0 & 1 & 0 & 0 & 0 & 0 & 0 & 0 \\ 0 & 0 & 0 & 1 & 0 & 0 & 0 & 0 & 0 \\ 0 & 0 & 0 & 0 & 0 & 1 & 0 & 0 & 0 \\ 0 & 0 & 0 & 0 & 0 & 0 & 1 & 0 & 0 \\ 0 & 0 & 0 & 0 & 0 & 0 & 0 & 0 & 1 \end{bmatrix}.$$

In (D.1)–(D.9) $v \sim \mathcal{N}(0, Q)$ represents errors in the model and $z \sim \mathcal{N}(0, R)$ in (D.11) indicates measurement noise. Both, v and z are defined as white Gaussian noise with zero mean and the covariance matrices $Q_{(9 \times 9)}$ (positive definite) and $R_{(7 \times 7)}$ (positive semi-definite), respectively.

The system dynamics (D.1)–(D.9) can be rewritten as

$$\dot{T} = f_1(T) + v,$$

and thus, the observer dynamics can be formulated in the form

$$\hat{\dot{T}} = f_2(\hat{T}) + KC(T - \hat{T}), \quad (D.12)$$

where $f_2(\cdot) = f_1(\cdot) - v$ and the respective states $T_{m,n}$ being replaced by $\hat{T}_{m,n}$.

Thus the observer dynamics can be described by the following equations

$$\begin{aligned} \dot{\hat{T}}_{1,1} = & \kappa(\hat{T}_{1,1}) \left[\left(\frac{T_{1,1} - \hat{T}_{Boundary}}{\Delta x} \right)^2 + \left(\frac{T_{1,1} - \hat{T}_{Air}}{\Delta y} \right)^2 \right] \\ & + k(\hat{T}_{1,1}) \left[\frac{\hat{T}_{1,2} - 2\hat{T}_{1,1} + T_{Boundary}}{\Delta x^2} + \frac{\hat{T}_{2,1} - 2\hat{T}_{1,1} + T_{Air}}{\Delta y^2} \right] + KC(T - \hat{T}), \end{aligned} \quad (D.13)$$

$$\begin{aligned} \dot{\hat{T}}_{1,2} = & \kappa(\hat{T}_{1,2}) \left[\left(\frac{\hat{T}_{1,3} - \hat{T}_{1,1}}{2\Delta x} \right)^2 + \left(\frac{T_{1,2} - \hat{T}_{Air}}{\Delta y} \right)^2 \right] \\ & + k(\hat{T}_{1,2}) \left[\frac{\hat{T}_{1,3} - 2\hat{T}_{1,2} + \hat{T}_{1,1}}{\Delta x^2} + \frac{\hat{T}_{2,2} - 2\hat{T}_{1,2} + T_{Air}}{\Delta y^2} \right] + KC(T - \hat{T}), \end{aligned} \quad (D.14)$$

$$\begin{aligned} \dot{\hat{T}}_{1,3} = & \kappa(\hat{T}_{1,3}) \left[\left(\frac{T_{Boundary} - \hat{T}_{1,3}}{\Delta x} \right)^2 + \left(\frac{T_{1,3} - \hat{T}_{Air}}{\Delta y} \right)^2 \right] \\ & + k(\hat{T}_{1,3}) \left[\frac{T_{Boundary} - 2\hat{T}_{1,3} + \hat{T}_{1,2}}{\Delta x^2} + \frac{\hat{T}_{2,3} - 2\hat{T}_{1,3} + T_{Air}}{\Delta y^2} \right] + KC(T - \hat{T}), \end{aligned} \quad (D.15)$$

$$\begin{aligned} \dot{\hat{T}}_{2,1} = & \kappa(\hat{T}_{2,1}) \left[\left(\frac{T_{2,1} - \hat{T}_{Boundary}}{\Delta x} \right)^2 + \left(\frac{\hat{T}_{3,1} - \hat{T}_{1,1}}{2\Delta y} \right)^2 \right] \\ & + k(\hat{T}_{2,1}) \left[\frac{\hat{T}_{2,2} - 2\hat{T}_{2,1} + T_{Boundary}}{\Delta x^2} + \frac{\hat{T}_{3,1} - 2\hat{T}_{2,1} + \hat{T}_{1,1}}{\Delta y^2} \right] + KC(T - \hat{T}), \end{aligned} \quad (D.16)$$

$$\begin{aligned} \dot{\hat{T}}_{2,2} = & \kappa(\hat{T}_{2,2}) \left[\left(\frac{\hat{T}_{2,3} - \hat{T}_{2,1}}{2\Delta x} \right)^2 + \left(\frac{\hat{T}_{3,2} - \hat{T}_{1,2}}{2\Delta y} \right)^2 \right] \\ & + k(\hat{T}_{2,2}) \left[\frac{\hat{T}_{2,3} - 2\hat{T}_{2,2} + \hat{T}_{2,1}}{\Delta x^2} + \frac{\hat{T}_{3,2} - 2\hat{T}_{2,2} + \hat{T}_{1,2}}{\Delta y^2} \right] + KC(T - \hat{T}), \end{aligned} \quad (D.17)$$

$$\begin{aligned} \dot{\hat{T}}_{2,3} = & \kappa(\hat{T}_{2,3}) \left[\left(\frac{T_{Boundary} - \hat{T}_{2,3}}{\Delta x} \right)^2 + \left(\frac{\hat{T}_{3,3} - \hat{T}_{1,3}}{2\Delta y} \right)^2 \right] \\ & + k(\hat{T}_{2,3}) \left[\frac{T_{Boundary} - 2\hat{T}_{2,3} + \hat{T}_{2,2}}{\Delta x^2} + \frac{\hat{T}_{3,3} - 2\hat{T}_{2,3} + \hat{T}_{1,3}}{\Delta y^2} \right] + KC(T - \hat{T}), \end{aligned} \quad (D.18)$$

$$\begin{aligned} \dot{\hat{T}}_{3,1} = & \kappa(\hat{T}_{3,1}) \left(\frac{T_{3,1} - \hat{T}_{Boundary}}{\Delta x} \right)^2 + k(\hat{T}_{3,1}) \left[\frac{\hat{T}_{3,2} - 2\hat{T}_{3,1} + T_{Boundary}}{\Delta x^2} + \frac{-\hat{T}_{3,1} + \hat{T}_{2,1}}{\Delta y^2} \right] \\ & + KC(T - \hat{T}), \end{aligned} \quad (D.19)$$

$$\begin{aligned} \dot{\hat{T}}_{3,2} = & \kappa(\hat{T}_{3,2}) \left(\frac{\hat{T}_{3,3} - \hat{T}_{3,1}}{2\Delta x} \right)^2 + k(\hat{T}_{3,2}) \left[\frac{\hat{T}_{3,3} - 2\hat{T}_{3,2} + \hat{T}_{3,1}}{\Delta x^2} + \frac{-\hat{T}_{3,2} + \hat{T}_{2,2}}{\Delta y^2} \right] \\ & + KC(T - \hat{T}), \end{aligned} \quad (D.20)$$

$$\begin{aligned} \dot{\hat{T}}_{3,3} = & \kappa(\hat{T}_{3,3}) \left(\frac{T_{Boundary} - \hat{T}_{3,3}}{\Delta x} \right)^2 + k(\hat{T}_{3,3}) \left[\frac{T_{Boundary} - 2\hat{T}_{3,3} + \hat{T}_{3,2}}{\Delta x^2} + \frac{-\hat{T}_{3,3} + \hat{T}_{2,3}}{\Delta y^2} \right] \\ & + KC(T - \hat{T}). \end{aligned} \quad (D.21)$$

K in (D.12)–(D.21) is calculated via the Riccati differential equation

$$\dot{P} = A(\hat{T})P + PA^T(\hat{T}) - PC^T R^{-1} CP + Q, \quad (\text{D.22})$$

with $A_{(9 \times 9)}(\hat{T})$ being a sparse matrix obtained by calculating the Jacobian $\frac{\partial f_2(\hat{T})}{\partial \hat{T}}$

$$A(\hat{T}) = \begin{bmatrix} * & * & 0 & * & 0 & 0 & 0 & 0 & 0 \\ * & * & * & 0 & * & 0 & 0 & 0 & 0 \\ 0 & * & * & 0 & 0 & * & 0 & 0 & 0 \\ * & 0 & 0 & * & * & 0 & * & 0 & 0 \\ 0 & * & 0 & * & * & * & 0 & * & 0 \\ 0 & 0 & * & 0 & * & * & 0 & 0 & * \\ 0 & 0 & 0 & * & 0 & 0 & * & * & 0 \\ 0 & 0 & 0 & 0 & * & 0 & * & * & * \\ 0 & 0 & 0 & 0 & 0 & * & 0 & * & * \end{bmatrix} \quad (\text{D.23})$$

and thus the observer feedback gain $K_{(9 \times 7)}$ is calculated via

$$K = PC^T R^{-1}. \quad (\text{D.24})$$

Appendix E

Illustration of the reduced model observer design case

The case for the reduced observer design relies on the same model like the full design case in Appendix D, namely (D.1)–(D.9). However, the parameters of the observer get chosen differently compared to the system such that $\kappa(T) = 0$ for all T . The outputs are also identical to those defined in (D.11).

Now the observer dynamics can be written in the following form:

$$\dot{\hat{T}}_{1,1} = k(\hat{T}_{1,1}) \left[\frac{\hat{T}_{1,2} - 2\hat{T}_{1,1} + T_{Boundary}}{\Delta x^2} + \frac{\hat{T}_{2,1} - 2\hat{T}_{1,1} + T_{Air}}{\Delta y^2} \right] + KC(T - \hat{T}), \quad (E.1)$$

$$\dot{\hat{T}}_{1,2} = k(\hat{T}_{1,2}) \left[\frac{\hat{T}_{1,3} - 2\hat{T}_{1,2} + \hat{T}_{1,1}}{\Delta x^2} + \frac{\hat{T}_{2,2} - 2\hat{T}_{1,2} + T_{Air}}{\Delta y^2} \right] + KC(T - \hat{T}), \quad (E.2)$$

$$\dot{\hat{T}}_{1,3} = k(\hat{T}_{1,3}) \left[\frac{T_{Boundary} - 2\hat{T}_{1,3} + \hat{T}_{1,2}}{\Delta x^2} + \frac{\hat{T}_{2,3} - 2\hat{T}_{1,3} + T_{Air}}{\Delta y^2} \right] + KC(T - \hat{T}), \quad (E.3)$$

$$\dot{\hat{T}}_{2,1} = k(\hat{T}_{2,1}) \left[\frac{\hat{T}_{2,2} - 2\hat{T}_{2,1} + T_{Boundary}}{\Delta x^2} + \frac{\hat{T}_{3,1} - 2\hat{T}_{2,1} + \hat{T}_{1,1}}{\Delta y^2} \right] + KC(T - \hat{T}), \quad (E.4)$$

$$\dot{\hat{T}}_{2,2} = k(\hat{T}_{2,2}) \left[\frac{\hat{T}_{2,3} - 2\hat{T}_{2,2} + \hat{T}_{2,1}}{\Delta x^2} + \frac{\hat{T}_{3,2} - 2\hat{T}_{2,2} + \hat{T}_{1,2}}{\Delta y^2} \right] + KC(T - \hat{T}), \quad (E.5)$$

$$\dot{\hat{T}}_{2,3} = k(\hat{T}_{2,3}) \left[\frac{T_{Boundary} - 2\hat{T}_{2,3} + \hat{T}_{2,2}}{\Delta x^2} + \frac{\hat{T}_{3,3} - 2\hat{T}_{2,3} + \hat{T}_{1,3}}{\Delta y^2} \right] + KC(T - \hat{T}), \quad (E.6)$$

$$\dot{\hat{T}}_{3,1} = k(\hat{T}_{3,1}) \left[\frac{\hat{T}_{3,2} - 2\hat{T}_{3,1} + T_{Boundary}}{\Delta x^2} + \frac{-\hat{T}_{3,1} + \hat{T}_{2,1}}{\Delta y^2} \right] + KC(T - \hat{T}), \quad (E.7)$$

$$\dot{\hat{T}}_{3,2} = k(\hat{T}_{3,2}) \left[\frac{\hat{T}_{3,3} - 2\hat{T}_{3,2} + \hat{T}_{3,1}}{\Delta x^2} + \frac{-\hat{T}_{3,2} + \hat{T}_{2,2}}{\Delta y^2} \right] + KC(T - \hat{T}), \quad (E.8)$$

$$\dot{\hat{T}}_{3,3} = k(\hat{T}_{3,3}) \left[\frac{T_{Boundary} - 2\hat{T}_{3,3} + \hat{T}_{3,2}}{\Delta x^2} + \frac{-\hat{T}_{3,3} + \hat{T}_{2,3}}{\Delta y^2} \right] + KC(T - \hat{T}). \quad (E.9)$$

with K calculated via the same Riccati differential equation as defined in (D.22) and (D.24), respectively. In order to solve (D.22) and (D.24) the Jacobian $A(\hat{T})$ of the ob-

server dynamics (E.1)–(E.9) has to be calculated, which gives

$$A_{(9 \times 9)}(\hat{T}) = \begin{bmatrix} * & * & 0 & * & 0 & 0 & 0 & 0 & 0 \\ * & * & * & 0 & * & 0 & 0 & 0 & 0 \\ 0 & * & * & 0 & 0 & * & 0 & 0 & 0 \\ * & 0 & 0 & * & * & 0 & * & 0 & 0 \\ 0 & * & 0 & * & * & * & 0 & * & 0 \\ 0 & 0 & * & 0 & * & * & 0 & 0 & * \\ 0 & 0 & 0 & * & 0 & 0 & * & * & 0 \\ 0 & 0 & 0 & 0 & * & 0 & * & * & * \\ 0 & 0 & 0 & 0 & 0 & * & 0 & * & * \end{bmatrix}. \quad (\text{E.10})$$

Note that the shape of $A(\hat{T})$ in the present case is identical to that in Appendix D for the full case design. This means that the nonzero entries in (E.10) are found to be at the same positions like in (D.23). However, these are not identical, which is denoted by changing symbols from \star to $*$.

Appendix F

Further simulation results for the observer design cases

F.1 Reduced observers for freezing

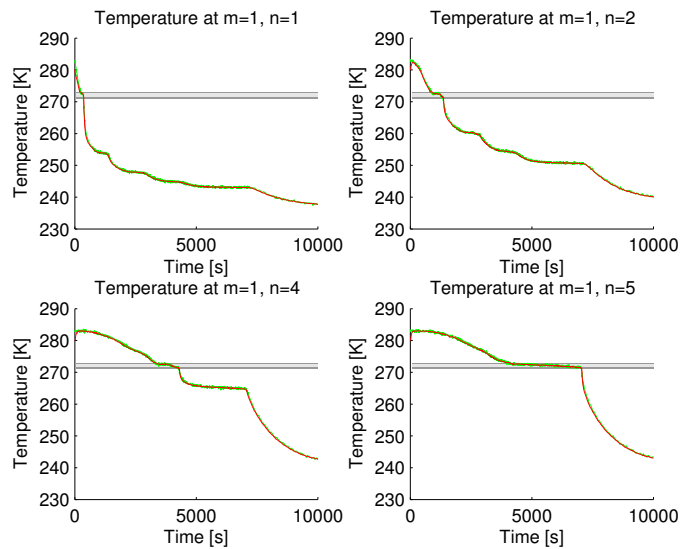


Figure F.1: Results for the reduced model observer at $m = 1$ and different positions along the x -axis for constant Q and R

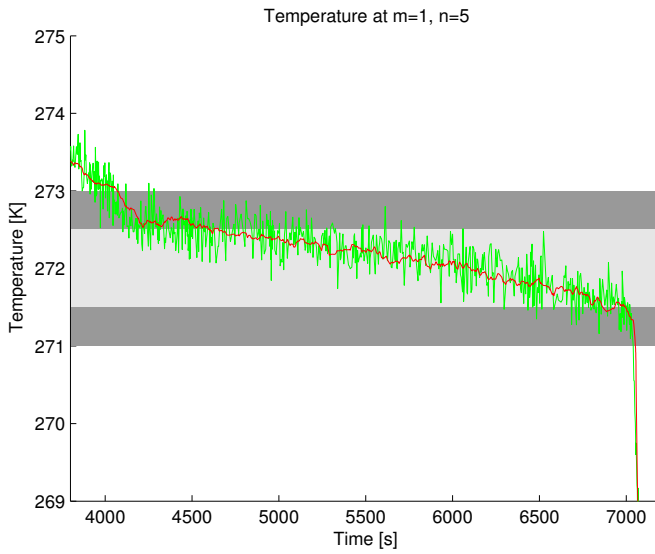


Figure F.2: Results for the reduced model observer at $m = 1$ and $n = 5$ for constant Q and R , zoom into the latent zone

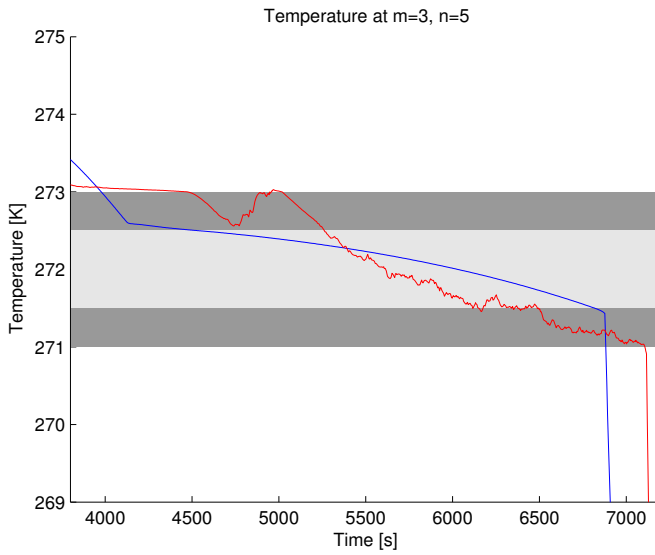


Figure F.3: Results for the reduced model observer at $m = 3$ and $n = 5$ for constant Q and R , zoom into the latent zone

F.2 Reduced observers for thawing

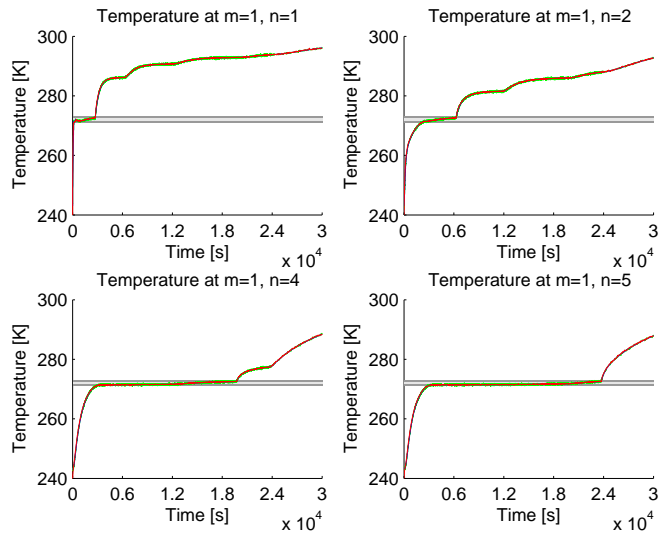


Figure F.4: Results for the reduced model observer at $m = 1$ and different positions along the x -axis for constant Q and R

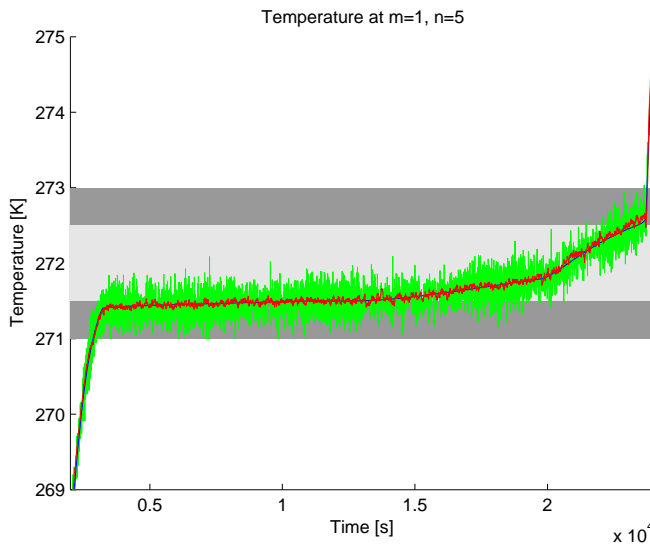


Figure F.5: Results for the reduced model observer at $m = 1$ and $n = 5$ for constant Q and R , zoom into the latent zone

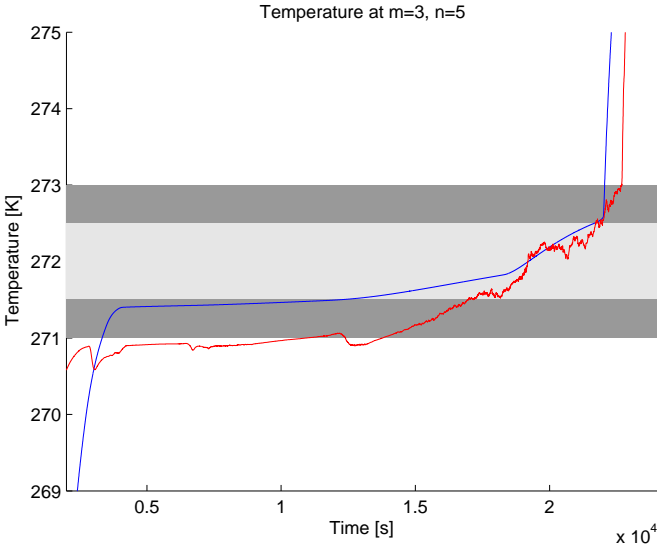


Figure F.6: Results for the reduced model observer at $m = 3$ and $n = 5$ for constant Q and R , zoom into the latent zone

Appendix G

Design of a 1-dimensional observer

Consider a discretization of the spatial domain using a grid of $N = 9$ and $M = 1$, respectively. This could for example correspond to the bottom of the block shown in Figure 10.1 leading to 9 coupled ODEs in the form

$$\dot{T}_1 = \kappa(T_1) \left(\frac{T_1 - T_{Boundary}}{\Delta x} \right)^2 + k(T_1) \left(\frac{T_2 - 2T_1 + T_{Boundary}}{\Delta x^2} \right) + v_1, \quad (G.1)$$

$$\dot{T}_2 = \kappa(T_2) \left(\frac{T_2 - T_1}{\Delta x} \right)^2 + k(T_2) \left(\frac{T_3 - 2T_2 + T_1}{\Delta x^2} \right) + v_2, \quad (G.2)$$

$$\dot{T}_3 = \kappa(T_3) \left(\frac{T_3 - T_2}{\Delta x} \right)^2 + k(T_3) \left(\frac{T_4 - 2T_3 + T_2}{\Delta x^2} \right) + v_3, \quad (G.3)$$

$$\dot{T}_4 = \kappa(T_4) \left(\frac{T_4 - T_3}{\Delta x} \right)^2 + k(T_4) \left(\frac{T_5 - 2T_4 + T_3}{\Delta x^2} \right) + v_4, \quad (G.4)$$

$$\dot{T}_5 = \kappa(T_5) \left(\frac{T_6 - T_4}{2\Delta x} \right)^2 + k(T_5) \left(\frac{T_6 - 2T_5 + T_4}{\Delta x^2} \right) + v_5, \quad (G.5)$$

$$\dot{T}_6 = \kappa(T_6) \left(\frac{T_7 - T_6}{\Delta x} \right)^2 + k(T_6) \left(\frac{T_7 - 2T_6 + T_5}{\Delta x^2} \right) + v_6, \quad (G.6)$$

$$\dot{T}_7 = \kappa(T_7) \left(\frac{T_8 - T_7}{\Delta x} \right)^2 + k(T_7) \left(\frac{T_8 - 2T_7 + T_6}{\Delta x^2} \right) + v_7, \quad (G.7)$$

$$\dot{T}_8 = \kappa(T_8) \left(\frac{T_9 - T_8}{\Delta x} \right)^2 + k(T_8) \left(\frac{T_9 - 2T_8 + T_7}{\Delta x^2} \right) + v_8, \quad (G.8)$$

$$\dot{T}_9 = \kappa(T_9) \left(\frac{T_{Boundary} - T_9}{\Delta x} \right)^2 + k(T_9) \left(\frac{T_{Boundary} - 2T_9 + T_8}{\Delta x^2} \right) + v_9. \quad (G.9)$$

The output is defined as

$$y = CT + v = [T_1 \quad T_9]^T + z_{(2 \times 1)} \quad (G.10)$$

$$\text{with } C_{(2 \times 9)} = \begin{bmatrix} 1 & 0 & 0 & 0 & 0 & 0 & 0 & 0 & 0 \\ 0 & 0 & 0 & 0 & 0 & 0 & 0 & 0 & 1 \end{bmatrix}.$$

Again, in (G.1)–(G.9) $v \sim \mathcal{N}(0, Q)$ indicates errors in the model and $z \sim \mathcal{N}(0, R)$ in (G.10) represents measurement noise. Both, v and z are defined as white Gaussian noise with zero mean and the covariance matrices $Q_{(9 \times 9)}$ (positive definite) and $R_{(2 \times 2)}$ (positive semi-definite), respectively.

The observer dynamics are thus represented by the following equations

$$\dot{\hat{T}}_1 = \kappa(\hat{T}_1) \left(\frac{T_1 - \hat{T}_{Boundary}}{\Delta x} \right)^2 + k(\hat{T}_1) \left(\frac{\hat{T}_2 - 2\hat{T}_1 + T_{Boundary}}{\Delta x^2} \right) + KC(T - \hat{T}), \quad (G.11)$$

$$\dot{\hat{T}}_2 = \kappa(\hat{T}_2) \left(\frac{\hat{T}_1 - \hat{T}_2}{\Delta x} \right)^2 + k(\hat{T}_2) \left(\frac{\hat{T}_3 - 2\hat{T}_2 + \hat{T}_1}{\Delta x^2} \right) + KC(T - \hat{T}), \quad (G.12)$$

$$\dot{\hat{T}}_3 = \kappa(\hat{T}_3) \left(\frac{\hat{T}_2 - \hat{T}_3}{\Delta x} \right)^2 + k(\hat{T}_3) \left(\frac{\hat{T}_4 - 2\hat{T}_3 + \hat{T}_2}{\Delta x^2} \right) + KC(T - \hat{T}), \quad (G.13)$$

$$\dot{\hat{T}}_4 = \kappa(\hat{T}_4) \left(\frac{\hat{T}_3 - \hat{T}_4}{\Delta x} \right)^2 + k(\hat{T}_4) \left(\frac{\hat{T}_5 - 2\hat{T}_4 + \hat{T}_3}{\Delta x^2} \right) + KC(T - \hat{T}), \quad (G.14)$$

$$\dot{\hat{T}}_5 = \kappa(\hat{T}_5) \left(\frac{\hat{T}_4 - \hat{T}_5}{2\Delta x} \right)^2 + k(\hat{T}_5) \left(\frac{\hat{T}_6 - 2\hat{T}_5 + \hat{T}_4}{\Delta x^2} \right) + KC(T - \hat{T}), \quad (G.15)$$

$$\dot{\hat{T}}_6 = \kappa(\hat{T}_6) \left(\frac{\hat{T}_5 - \hat{T}_6}{\Delta x} \right)^2 + k(\hat{T}_6) \left(\frac{\hat{T}_7 - 2\hat{T}_6 + \hat{T}_5}{\Delta x^2} \right) + KC(T - \hat{T}), \quad (G.16)$$

$$\dot{\hat{T}}_7 = \kappa(\hat{T}_7) \left(\frac{\hat{T}_6 - \hat{T}_7}{\Delta x} \right)^2 + k(\hat{T}_7) \left(\frac{\hat{T}_8 - 2\hat{T}_7 + \hat{T}_6}{\Delta x^2} \right) + KC(T - \hat{T}), \quad (G.17)$$

$$\dot{\hat{T}}_8 = \kappa(\hat{T}_8) \left(\frac{\hat{T}_7 - \hat{T}_8}{\Delta x} \right)^2 + k(\hat{T}_8) \left(\frac{\hat{T}_9 - 2\hat{T}_8 + \hat{T}_7}{\Delta x^2} \right) + KC(T - \hat{T}), \quad (G.18)$$

$$\dot{\hat{T}}_9 = \kappa(\hat{T}_9) \left(\frac{T_{Boundary} - \hat{T}_9}{\Delta x} \right)^2 + k(\hat{T}_9) \left(\frac{T_{Boundary} - 2\hat{T}_9 + \hat{T}_8}{\Delta x^2} \right) + KC(T - \hat{T}), \quad (G.19)$$

where K in (G.11)–(G.19) is again calculated via the already introduced Riccati differential equation

$$\dot{P} = A(\hat{T})P + PA^T(\hat{T}) - PC^TR^{-1}CP + Q, \quad (G.20)$$

where $A_{(9 \times 9)}(\hat{T})$ is a tridiagonal matrix obtained by calculating the Jacobian of the observer dynamics (G.11)–(G.19)

$$A(\hat{T}) = \begin{bmatrix} \bullet & \bullet & 0 & 0 & 0 & 0 & 0 & 0 & 0 \\ \bullet & \bullet & \bullet & 0 & 0 & 0 & 0 & 0 & 0 \\ 0 & \bullet & \bullet & \bullet & 0 & 0 & 0 & 0 & 0 \\ 0 & 0 & \bullet & \bullet & \bullet & 0 & 0 & 0 & 0 \\ 0 & 0 & 0 & \bullet & \bullet & \bullet & 0 & 0 & 0 \\ 0 & 0 & 0 & 0 & \bullet & \bullet & \bullet & 0 & 0 \\ 0 & 0 & 0 & 0 & 0 & \bullet & \bullet & \bullet & 0 \\ 0 & 0 & 0 & 0 & 0 & 0 & \bullet & \bullet & \bullet \\ 0 & 0 & 0 & 0 & 0 & 0 & 0 & \bullet & \bullet \end{bmatrix} \quad (G.21)$$

and thus the observer feedback gain $K_{(9 \times 2)}$ is calculated via the already introduced expression

$$K = PC^TR^{-1}. \quad (G.22)$$

G.1 Simulation results

Simulation results for the 1-dimensional observer are conducted for the real-time applicable design with both, perfect knowledge of the plant's parameters as well as differing

parameter definitions, exclusively for freezing. The simulation parameters are the same like for Chapters 10–13. Due to the lack of some measurement, which are available for the 2-dimensional case, the covariance matrices Q and R could not be designed for switching. They are chosen as follows

$$R = 10^4 \begin{bmatrix} 1 & 0 \\ 0 & 1 \end{bmatrix}, \quad Q = 10^1 \begin{bmatrix} 1 & 0 & 0 & 0 & 0 & 0 & 0 & 0 & 0 \\ 0 & 10 & 0 & 0 & 0 & 0 & 0 & 0 & 0 \\ 0 & 0 & 100 & 0 & 0 & 0 & 0 & 0 & 0 \\ 0 & 0 & 0 & 100 & 0 & 0 & 0 & 0 & 0 \\ 0 & 0 & 0 & 0 & 10 & 0 & 0 & 0 & 0 \\ 0 & 0 & 0 & 0 & 0 & 100 & 0 & 0 & 0 \\ 0 & 0 & 0 & 0 & 0 & 0 & 100 & 0 & 0 \\ 0 & 0 & 0 & 0 & 0 & 0 & 0 & 10 & 0 \\ 0 & 0 & 0 & 0 & 0 & 0 & 0 & 0 & 1 \end{bmatrix}.$$

Figures G.1 and G.2 display the states at positions $n = 1$, $n = 2$, $n = 4$ and $n = 5$ as well as the error plot over the whole spatial domain for identical parameter values. As can be seen, estimation is sufficiently well in the inner domain.

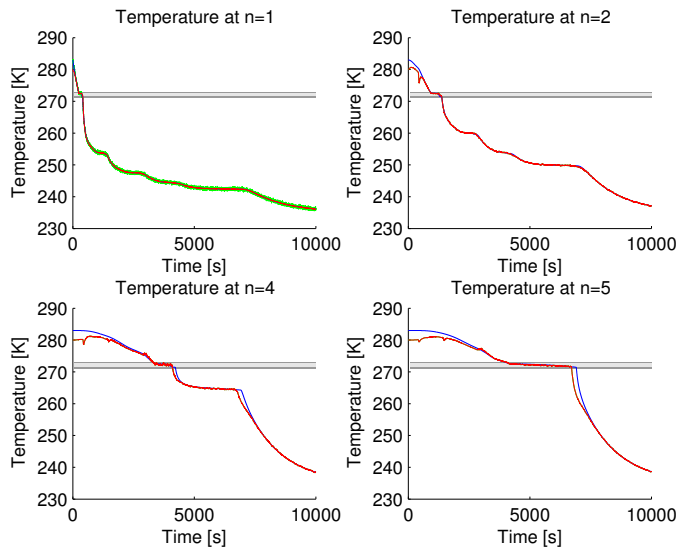


Figure G.1: States for the 1-dimensional real-time applicable observer for identical parameter definitions

In Figures G.3 and G.4 the same plots like before are shown, this time, however, for differing parameter values. Also here the quality of estimation in the inner domain is quite well.

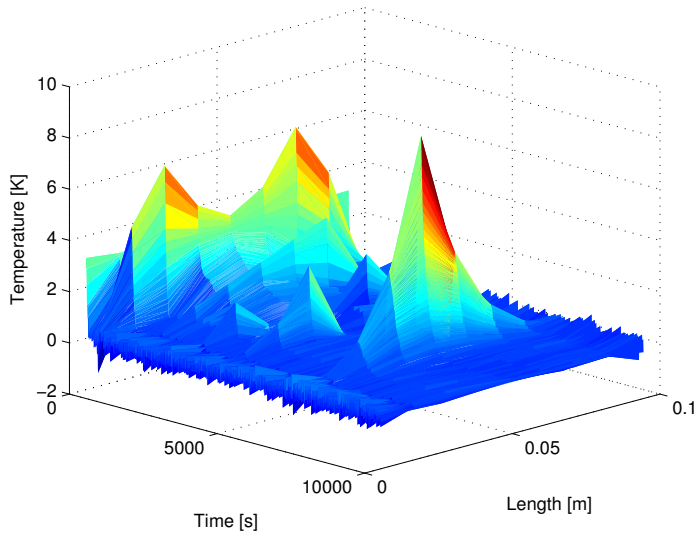


Figure G.2: Error plot for the 1-dimensional real-time applicable observer for identical parameter definitions

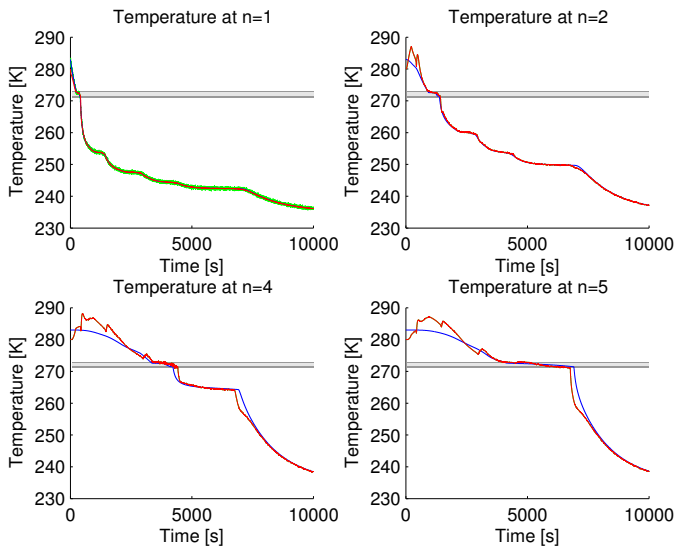


Figure G.3: States for the 1-dimensional real-time applicable observer for differing parameter definitions

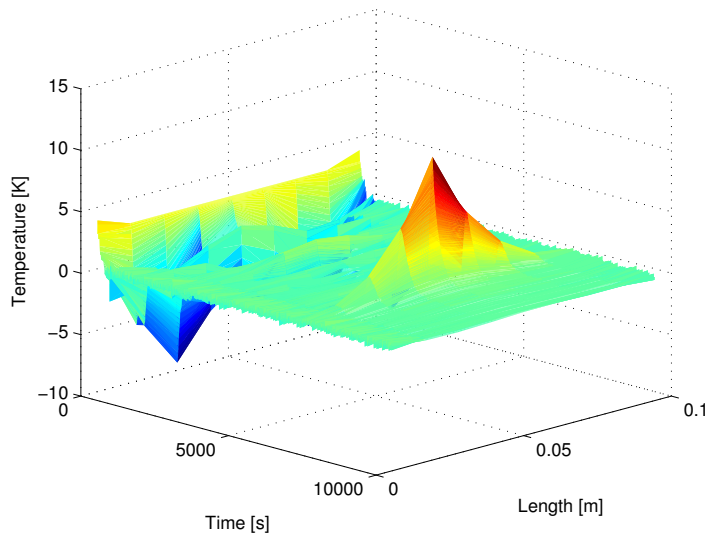


Figure G.4: Error plot for the 1-dimensional real-time applicable observer for differing parameter definitions

The Figures above indicate that a 1-dimensional observer design is also possible. Again, like already described in Section 10.2.5, an *a priori* determination of observability is hard to achieve. Nevertheless, an *a posteriori* investigation was conducted, which indicated full observability for the linearized system matrix.

References

- [1] A. Aberoumand and H. Jooyandeh. Storage quality and chemical and structural changes of fresh and frozen-thawed fish. *World Journal of Fish and Marine Sciences*, 2(3):251–253, 2010.
- [2] E. Alizadeh, N. Chapleau, M. de Lamballerie, and A. LeBail. Effects of freezing and thawing processes on the quality of Atlantic salmon (*Salmo salar*) fillets. *Journal of Food Science*, 72(5):279–284, 2007.
- [3] Anonymous. *Temperature Measurement in the Fish Industry*. Torry Advisory Note No. 94. Ministry of Technology, Torry Research Station, 1989.
- [4] M. Arcak and P. Kokotovic. Nonlinear observers: a circle criterion design and robustness analysis. *Automatica*, 37:1923–1930, 2001.
- [5] M. Archer, M. Edmonds, and M. George. Seafood thawing. Technical report, Seafish Research & Development, 2008.
- [6] F. B. Argomedeo, E. Witrant, and C. Prieur. D1-input-to-state stability of a time-varying nonhomogeneous diffusive equation subject to boundary disturbances. In *Proceedings of the American Control Conference*, pages 2978–2983, Montreal, Canada, 2012.
- [7] D. Ariens, H. J. Ferreau, B. Houska, and F. Logist. *ACADO for Matlab User's Manual*. Optimization in Engineering Center (OPTEC) and Department of Electrical Engineering, K. U. Leuven, Leuven, Belgium, version 1.0beta - v2022 edition, June 2010.
- [8] D. Ariens, M. Diehl, H. J. Ferreau, B. Houska, F. Logist, and M. Vukov. *ACADO Toolkit User's Manual*. Optimization in Engineering Center (OPTEC) and Department of Electrical Engineering, K. U. Leuven, version 1.0.2613beta edition, June 2011.
- [9] C. J. Backi. Methods for (industrial) thawing of fish blocks - a review. *Submitted to the Journal of Food Engineering*, 2015.
- [10] C. J. Backi and J. T. Graydahl. Modeling of the freezing process for fish in vertical plate freezers. In *Proceedings of the 17th Nordic Process Control Workshop*, Copenhagen, Denmark, 2012.

- [11] C. J. Backi and J. T. Gravdahl. Optimal boundary control for the heat equation with application to freezing with phase change. In *Proceedings of the 3rd Australian Control Conference*, Perth, Australia, 2013.
- [12] C. J. Backi and J. T. Gravdahl. A reduced observer design for a freezing process in plate freezers. In *Proceedings of the 19th Nordic Process Control Workshop*, Trondheim–Bodø, Norway, 2015.
- [13] C. J. Backi and J. T. Gravdahl. Optimal neumann boundary control for a freezing process with phase change. *Presented at the 18th Nordic Process Control Workshop*, Oulu, Finland, 2013.
- [14] C. J. Backi, J. T. Gravdahl, and E. I. Grøtli. Nonlinear observer design for a greitzer compressor model. In *Proceedings of the 21st Mediterranean Conference on Control and Automation*, Chania, Crete, Greece, 2013.
- [15] C. J. Backi, J. D. Bendtsen, J. Leth, and J. T. Gravdahl. The nonlinear heat equation with state-dependent parameters and its connection to the burgers’ and the potential burgers’ equation. In *Proceedings of the 19th IFAC World Congress*, Cape Town, South Africa, 2014.
- [16] C. J. Backi, J. D. Bendtsen, J. Leth, and J. T. Gravdahl. Estimation of inner-domain temperatures for a freezing process. In *Proceedings of the 2014 IEEE Multi-Conference on Systems and Control*, Antibes, France, 2014.
- [17] C. J. Backi, J. D. Bendtsen, J. Leth, and J. T. Gravdahl. Stability properties of a heat equation with state-dependent parameters and asymmetric boundary conditions. In *Proceedings of the 1st Conference on Modelling, Identification and Control of Non-linear Systems*, Saint Petersburg, Russia, 2015.
- [18] C. J. Backi, J. D. Bendtsen, J. Leth, and J. T. Gravdahl. A heat equation for freezing processes with phase change: stability analysis and applications. *International Journal of Control*, 2015. doi: 10.1080/00207179.2015.1102327.
- [19] C. J. Backi, J. Leth, and J. T. Gravdahl. Optimal boundary control of a contact thawing process for foodstuff. *Submitted to the 11th IFAC Symposium on Dynamics and Control of Process Systems, including Biosystems (DYCOPS-CAB 2016)*, Trondheim, Norway, 2016.
- [20] A. Balogh and M. Krstić. Burgers’ equation with nonlinear boundary feedback: H1 stability, well-posedness and simulation. *Mathematical Problems in Engineering*, 6:189–200, 2000.
- [21] J. Barros-Velázquez, J. M. Gallardo, P. Calo, and S. P. Aubourg. Enhanced quality and safety during on-board chilled storage of fish species captured in the grand sole north atlantic fishing bank. *Food Chemistry*, 106:493–500, 2008.
- [22] M. S. Branicky. Stability of switched and hybrid systems. In *Proceedings of the 33rd IEEE Conference on Decision and Control*, pages 3498–3503, Lake Buena Vista, FL, USA, 2010.

-
- [23] Y. A. Çengel and M. A. Boles. *Thermodynamics - An Engineering Approach*. McGraw-Hill Science/Engineering/Math, 5th edition, 2004.
- [24] J. C. Cheftel, J. Levy, and E. Dumay. Pressure-assisted freezing and thawing: Principles and potential applications. *Food Reviews International*, 16(4):453–483, 2000.
- [25] A. C. Cleland and R. L. Earle. The third kind of boundary conditions in numerical freezing calculations. *International Journal of Heat and Mass Transfer*, 20(10): 1029–1034, October 1977.
- [26] D. J. Cleland, A. C. Cleland, and R. L. Earle. Prediction of freezing and thawing times for multi-dimensional shapes by numerical methods. *International Journal of Refrigeration*, 10:32–39, 1987.
- [27] D. J. Cleland, A. C. Cleland, and R. L. Earle. Prediction of freezing and thawing times for multi-dimensional shapes by simple formulae. Part 1: regular shapes. *International Journal of Refrigeration*, 10:156–164, 1987.
- [28] D. J. Cleland, A. C. Cleland, and R. L. Earle. Prediction of freezing and thawing times for multi-dimensional shapes by simple formulae. Part 2: irregular shapes. *International Journal of Refrigeration*, 10:234–240, 1987.
- [29] D. J. Cleland, A. C. Cleland, R. L. Earle, and S. J. Byrne. Experimental data for freezing and thawing of multi-dimensional objects. *International Journal of Refrigeration*, 10:22–31, January 1987.
- [30] J. D. Cole. On a quasi-linear parabolic equation occurring in aerodynamics. *Quarterly of Applied Mathematics*, 9:225–236, 1951.
- [31] M. Costa, D. Buddhi, and A. Oliva. Numerical simulation of a latent heat thermal energy storage system with enhanced heat conduction. *Energy Conversion and Management*, 39(3/4):319–330, 1997.
- [32] A. A. Dawood, R. N. Roy, and C. S. Williams. Effect of delayed icing on the storage life of rainbow trout. *Journal of Food Technology*, 21:159–166, 1986.
- [33] A. A. P. de Alwis and P. J. Fryer. The use of direct resistance heating in the food industry. *Journal of Food Engineering*, 11:3–27, 1990.
- [34] A. E. Delgado and D.-W. Sun. Heat and mass transfer models for predicting freezing processes – a review. *Journal of Food Engineering*, 47:157–174, 2001.
- [35] M. Diehl. *Script-Draft: Numerical Optimal Control*. June 2011.
- [36] S. Dubljevic and P. D. Christofides. Predictive control of parabolic PDEs with boundary control actuation. *Chemical Engineering Science*, 61:6239–6248, 2006.
- [37] S. Dubljevic, N. El-Farra, P. Mhaskar, and P. D. Christofides. Predictive control of parabolic PDEs with state and control constraints. *International Journal of Robust and Nonlinear Control*, 16:749–772, 2006.

- [38] O. Einen, T. Guerin, S. O. Fjæra, and P. O. Skjervold. Freezing of pre-rigor fillets of Atlantic salmon. *Aquaculture*, 212:129–140, 2002.
- [39] U. G. Erikson, E. Kjørsvik, T. Bardal, H. Digre, M. Schei, T. S. Søreide, and I. G. Aursand. Comparison of flesh characteristics of Atlantic cod frozen in the cell alive system, air-blast or static cold storage freezers. *Journal of Aquatic Food Product Technology*, 2015.
- [40] P. Failler. Future prospects for fish and fishery products. 4. Fish consumption in the European Union in 2015 and 2030. Part 1: European overview., 2007.
- [41] P. P. Fernández, L. Otero, B. Guignon, and P. D. Sanz. High-pressure shift freezing versus high-pressure assisted freezing: Effects on the microstructure of a food model. *Food Hydrocolloids*, (20):510–522, 2006.
- [42] R. Findeisen and F. Allgöwer. An introduction to nonlinear model predictive control. In *Proceedings of the 21st Benelux Meeting on Systems and Control*, pages 119–141, Veldhoven, The Netherlands, 2002.
- [43] R. J. Footit and A. S. Lewis. *The canning of fish and meat*. Springer, 1995.
- [44] L. Gram and P. Dalgaard. Fish spoilage bacteria – problems and solutions. *Current Opinion in Biotechnology*, (13):262–266, 2002.
- [45] V. Harðarson. *Matvarens termofysiske egenskaper og deres betydning ved dimensjonering av frysetunneler*. PhD thesis, Universitetet i Trondheim – Norges Tekniske Høgskole, March 1996.
- [46] A. Hasan, S. Sagatun, and B. Foss. Well rate control design for gas coning problems. In *Proceedings of the 49th IEEE Conference on Decision and Control*, pages 5845–5850, Atlanta, GA, USA, 2010.
- [47] A. Haugland. *Industrial Thawing of Fish - to improve quality, yield and capacity*. PhD thesis, Norwegian University of Science and Technology Trondheim, 2002.
- [48] D. Henry. *Geometric theory of semilinear parabolic equations*, volume 840 of *Lecture Notes in Mathematics*. Springer-Verlag, Berlin, 1981. ISBN 3-540-10557-3.
- [49] R. H. Heredero, D. Levi, and P. Winternitz. Symmetries of the discrete Burgers’ equation. *Journal of Physics A: Mathematical and General*, 32(14):2685–2695, 1999.
- [50] Z. Hidayat, R. Babuska, B. D. Schutter, and A. Nunez. Observers for linear distributed-parameter systems: a review. In *Proceedings of the 2011 IEEE International Symposium on Robotic and Sensors Environment (ROSE)*, Montreal, Canada, 2011.
- [51] R. G. Hills. Model validation: Model parameter and measurement uncertainty. *Journal of Heat Transfer*, 128(4):339–351, 2006.

- [52] M. Hinze, R. Pinnau, M. Ulbrich, and S. Ulbrich. *Optimization with PDE Constraints (Mathematical Modelling: Theory and Applications)*, volume 23. Springer Netherlands, 2009.
- [53] E. Hopf. The partial differential equation $ut + uux = \mu ux$. *Communications on Pure and Applied Mathematics*, 3(3):201–230, September 1950.
- [54] B. Houska, H. J. Ferreau, and M. Diehl. Acado toolkit - an open-source framework for automatic control and dynamic optimization. *Optimal Control Applications and Methods*, 32:298–312, 2011.
- [55] H. H. Huss. Quality and quality changes in fresh fish. Technical Report 348, FAO Fisheries, 1995.
- [56] J. Iannelli. *Characteristics Finite Element Methods in Computational Fluid Dynamics*. Computational Fluid and Solid Mechanics. Springer-Verlag Berlin Heidelberg, 1st edition, 2006.
- [57] A. C. Jason. *Thawing Frozen Fish*. Torry Advisory Note. Ministry of Agriculture, Fisheries and Food, Torry Research Station, 1974.
- [58] W. A. Johnston, F. J. Nicholson, A. Roger, and G. D. Stroud. Freezing and refrigerated storage in fisheries. Technical Report 340, FAO Fisheries, 1994.
- [59] L. D. Kaale and T. M. Eikevik. A histological study of the microstructure sizes of the red and white muscles of Atlantic salmon (*Salmo salar*) fillets during superchilling process and storage. *Journal of Food Engineering*, (114):242–248, 2013.
- [60] L. D. Kaale, T. M. Eikevik, T. Bardal, and E. Kjørsvik. A study of the ice crystals in vacuum-packed salmon fillets (*Salmo salar*) during superchilling process and following storage. *Journal of Food Engineering*, (115):20–25, 2013.
- [61] L. D. Kaale, T. M. Eikevik, T. Bardal, E. Kjørsvik, and T. S. Nordtvedt. The effect of cooling rates on the ice crystal growth in air-packed salmon fillets during superchilling and superchilled storage. *International Journal of Refrigeration*, (36):110–119, 2013.
- [62] L. D. Kaale, T. M. Eikevik, T. Rustad, T. S. Nordtvedt, T. Bardal, and E. Kjørsvik. Ice crystal development in pre-rigor Atlantic salmon fillets during superchilling process and following storage. *Food Control*, (31):491–498, 2013.
- [63] H. Khalil. *Nonlinear Systems*. Prentice Hall, 3rd edition, 2002.
- [64] T. Kobayashi and S. Hitotsuya. Observers and parameter determination for distributed parameter systems. *International Journal of Control*, 33(1):31–50, 1981.
- [65] E. Kolbe and D. Kramer. *Planning for Seafood Freezing*. 2007.
- [66] A. A. Korshunova and O. S. Rozanova. The Riemann problem for the stochastically perturbed non-viscous Burgers' equation and the pressureless gas dynamics model equation and the pressureless gas dynamics model. In *Proceedings of the International Conference Days on Diffraction, DD 2009*, pages 108–113, St. Petersburg, Russia, 2009.

- [67] G. Kreiss and H.-O. Kreiss. Convergence to steady state of solutions of Burgers' equation. *Applied Numerical Mathematics*, 2(3–5):161–179, 1986.
- [68] M. Krstić. On global stabilization of Burgers' equation by boundary control. *Systems & Control Letters*, (37):123–141, 1999.
- [69] M. Krstić and A. Smyshlyaev. *Boundary Control of PDEs - A Course on Backstepping Design*. Advances in Design and Control. Society for Industrial and Applied Mathematics, 2008.
- [70] M. Krstić, I. Kenallakopoulos, and P. Kokotović. *Nonlinear and Adaptive Control Design*. John Wiley & Sons, Inc., 1995.
- [71] M. Krstić, L. Magnis, and R. Vazquez. Nonlinear stabilization of shock-like unstable equilibria in the viscous Burgers' PDE. *IEEE Transactions on Automatic Control*, 53(7):1678–1683, August 2008.
- [72] M. Krstić, L. Magnis, and R. Vazquez. Nonlinear control of the viscous Burgers' equation: Trajectory generation, tracking and observer design. *Journal of Dynamic Systems, Measurement and Control*, 131, March 2009.
- [73] A. LeBail, D. Chevalier, D. M. Mussa, and M. Ghoul. High pressure freezing and thawing of foods: a review. *International Journal of Refrigeration*, 25:504–513, 2002.
- [74] J. Leth, J. G. Rasmussen, H. Schiøler, and R. Wisniewski. A class of stochastic hybrid systems with state-dependent switching noise. In *Proceedings of the 51st IEEE Conference on Decision and Control*, pages 4737–4744, Maui, HI, USA, 2012.
- [75] B. Li and D.-W. Sun. Novel methods for rapid freezing and thawing of foods – a review. *Journal of Food Engineering*, 54:175–182, 2002.
- [76] W.-J. Liu and M. Krstić. Adaptive control of Burgers' equation with unknown viscosity. *International Journal of Adaptive Control and Signal Processing*, 15: 745–766, 2001.
- [77] M. Lopez-Leiva and B. Hallström. The original Plank equation and its use in the development of food freezing rate predictions. *Journal of Food Engineering*, 58: 267–275, 2003.
- [78] R. Marino and P. Tomei. *Nonlinear Control Design: Geometric, Adaptive and Robust*. Prentice Hall Information and System Sciences Series. Prentice Hall Europe, Hertfordshire, 1995.
- [79] T. Mørkøre, P. I. Mazo, V. Tahirovic, and O. Einen. Impact of starvation and handling stress on rigor development and quality of Atlantic salmon (*Salmo salar* L). *Aquaculture*, 277:231–238, 2008.
- [80] M. Muhieddine, É. Canot, and R. March. Various approaches for solving problems in heat conduction with phase change. *International Journal on Finite Volumes*, 6 (1), 2008.

- [81] H. Nijmeijer and T. I. Fossen, editors. *New Directions in Nonlinear Observer Design*. Springer, London, 1999.
- [82] H. Nijmeijer and A. van der Schaft. *Nonlinear Dynamical Control Systems*. Springer, New York, 1995.
- [83] K. Nilsson. *Quality of Frozen Rainbow Trout - Effects of Different Freezing and Thawing Treatments*. PhD thesis, Chalmers University of Technology, Göteborg, Sweden, 1994.
- [84] J. Nocedal and S. J. Wright. *Numerical Optimization*. Springer Series in Operations Research, second edition, 2006.
- [85] T. Norton and D.-W. Sun. Recent advances in the use of high pressure as an effective processing technique in the food industry. *Food and Bioprocess Technology*, (1): 2–34, 2008.
- [86] G. Ólafsdóttir, E. Martinsdóttir, J. Oehlenschläger, P. Dalgaard, B. Jensen, I. Undeland, I. M. Mackie, G. Henahan, J. Nielsen, and H. Nilsen. Methods to evaluate fish freshness in research and industry. *Trends in Food Science and Technology*, 8: 258–265, August 1997.
- [87] G. Ólafsdóttir, P. Nesvadba, C. D. Natale, M. Careche, J. Oehlenschläger, S. V. Tryggvadóttir, R. Schubring, M. Kroeger, K. Heia, M. Esaiassen, A. Macagnano, and B. M. Jørgensen. Multisensor for fish quality evaluation. *Trends in Food Science and Technology*, 15:86–93, 2004.
- [88] L. Otero and P. D. Sanz. Modelling heat transfer in high pressure food processing: a review. *Innovative Food Science and Emerging Technologies*, 4:121–134, 2003.
- [89] Q. T. Pham. Extension to Planck’s equation for predicting freezing times of foodstuffs of simple shapes. *International Journal of Refrigeration*, 7(6):377–383, 1984.
- [90] Q. T. Pham. A fast, unconditionally stable finite-difference scheme for heat conduction with phase change. *International Journal of Heat and Mass Transfer*, 28: 2079–2085, 1985.
- [91] Q. T. Pham. Analytical method for predicting freezing times of rectangular blocks of foodstuffs. *International Journal of Refrigeration*, 8(1):43–47, 1985.
- [92] Q. T. Pham. Modelling heat and mass transfer in frozen foods: a review. *International Journal of Refrigeration*, 29:876–888, 2006.
- [93] Q. T. Pham. Mathematical modeling of freezing processes. In *Handbook of Frozen Food Processing and Packaging*, chapter 7. Taylor & Francis Group, LLC, 2006.
- [94] R. Plank. Beiträge zur Berechnung und Bewertung der Gefriereschwindigkeit von Lebensmitteln. *Beihefte zur Zeitschrift für die gesamte Kälte-Industrie*, 3(10), 1941.
- [95] J. Prüss, J. Saal, and G. Simonett. Existence of analytic solutions for the classical Stefan problem. *Mathematische Annalen*, 338:703–755, 2007.

- [96] J. Rouillé, A. LeBail, H. S. Ramaswamy, and L. Leclerc. High pressure thawing of fish and shellfish. *Journal of Food Engineering*, 53:83–88, 2002.
- [97] N. Sakai and T. Hanzawa. Applications and advances in far-infrared heating in Japan. *Trends in Food Science and Technology*, 5:357–362, November 1994.
- [98] S. A. Sallberg, P. S. Maybeck, and M. E. Oxley. Infinite-dimensional sampled-data Kalman filtering and the stochastic heat equation. In *Proceedings of the 49th IEEE Conference on Decision and Control*, Atlanta, GA, USA, 2010.
- [99] M. G. Sandberg, K. Henriksen, S. Aspaas, H. Bull-Berg, and U. Johansen. Verdiskaping og sysselsetting i norsk sjømatnæring - en ringvirkningsanalyse med fokus på 2012, 2014.
- [100] R. Schubring, C. Meyer, O. Schlüter, S. Boguslawski, and D. Knorr. Impact of high pressure assisted thawing on the quality of fillets from various fish species. *Innovative Food Science and Emerging Technologies*, 4:257–267, 2003.
- [101] P. O. Skjervold, A. M. B. Røra, S. O. Fjæra, A. Vegusdal, A. Vorre, and O. Einen. Effects of pre-, in-, or post-rigor filleting of live chilled Atlantic salmon. *Aquaculture*, 194:315–326, 2001.
- [102] A. Smyshlyaev and M. Krstić. *Adaptive Control of Parabolic PDEs*. Princeton University Press, Princeton, New Jersey, USA, 2010.
- [103] C. Sophocleous. Transformation properties of a variable-coefficient Burgers’ equation. *Chaos, Solitons and Fractals*, 20(5):1047–1057, 2004.
- [104] G. D. Stroud. *Rigor in Fish - The Effect on Quality*. Torrey Advisory Note. Ministry of Technology, Torrey Research Station, 1969.
- [105] N. Sugimoto and T. Kakutani. ‘Generalized Burgers’ equation’ for nonlinear viscoelastic waves. *Wave Motion*, 7(5):447–458, 1985.
- [106] V. A. Vaclavik and E. W. Christian. Food preservation and processing. In *Essentials of Food Science*, Food Science Text Series, pages 425–446. Springer New York, 2008.
- [107] Y. Wang, T. D. Wig, J. Tang, and L. M. Hallberg. Dielectric properties of foods relevant to RF and microwave pasteurization and sterilization. *Journal of Food Engineering*, (57):257–268, 2003.
- [108] B. Woinet, J. Andrieu, and M. Laurent. Experimental and theoretical study of model food freezing. Part 1. heat transfer modelling. *Journal of Food Engineering*, 35: 381–393, 1998.
- [109] Q. Zhang. Adaptive observer for multiple-input-multiple-output (mimo) linear time-varying systems. *IEEE Transactions on Automatic Control*, 47(3):525–529, March 2002.

- [110] Y. Zhao, B. Flugstad, E. Kolbe, J. W. Park, and J. H. Wells. Using capacitive (radio frequency) dielectric heating in food processing and preservation – a review. *Journal of Food Process Engineering*, (23):25–55, 2000.
- [111] S. Zhu, H. S. Ramaswamy, and B. K. Simpson. Effect of high-pressure versus conventional thawing on color, drip loss and texture of Atlantic salmon frozen by different methods. *LWT - Food Science and Technology*, 37:291–299, 2004.